



# FRIEDRICH-SCHILLER- UNIVERSITÄT JENA

## Crustal structure and fluids along the Leipzig-Regensburg fault zone

Dissertation  
(kumulativ)

zur Erlangung des akademischen Grades  
doctor rerum naturalium (Dr. rer. nat)

vorgelegt dem Rat der Chemisch-Geowissenschaftlichen Fakultät der  
Friedrich-Schiller-Universität Jena

von M. Sc. Marcel van Laaten

geboren am 22.06.1988 in Bremen

**Gutachter:**

1. Prof. Dr. Ulrich Wegler, Friedrich-Schiller-Universität Jena
2. Prof. Dr. Michael Korn, Universität Leipzig

Tag der Verteidigung: 22.01.2025

## **Erklärung zu den Eigenanteilen der Promovendin/des Promovenden sowie der weiteren Doktorandinnen/Doktoranden als Co-Autorinnen/-Autoren an den Publikationen und Zweitpublikationsrechten bei einer kumulativen Dissertation**

Für alle in dieser kumulativen Dissertation verwendeten Manuskripte liegen die notwendigen Genehmigungen der Verlage („Reprint permissions“) für die Zweitpublikation vor.

Die Co-Autorinnen/-Autoren der in dieser kumulativen Dissertation verwendeten Manuskripte sind sowohl über die Nutzung, als auch über die unten angegebenen Eigenanteile der weiteren Doktorandinnen/Doktoranden als Co-Autorinnen/-Autoren an den Publikationen und Zweitpublikationsrechten bei einer kumulativen Dissertation informiert und stimmen dem zu.

Die Anteile der Promovendin/des Promovenden sowie der weiteren Doktorandinnen/Doktoranden als Co-Autorinnen/Co-Autoren an den Publikationen und Zweitpublikationsrechten bei einer kumulativen Dissertation sind in der Anlage aufgeführt.

Jena, 9. Juli 2024

---

Marcel van Laaten

Ich bin mit der Abfassung der Dissertation als publikationsbasierte Dissertation, d.h. kumulativ, einverstanden und bestätige die vorstehenden Angaben.

Jena, 9. Juli 2024

---

Prof. Dr. Ulrich Wegler

## Tabelarische Auflistung der Eigenanteile des Promovenden

|   |            |          |          |
|---|------------|----------|----------|
| Publikation 1: <b>van Laaten, M.</b> , Eulenfeld, T. and Wegler, U. (2022), Comparison of Multiple Lapse Time Window Analysis and Qopen to determine intrinsic and scattering attenuation, Geophys. J. Int., 228, p. 913-926, <a href="https://doi.org/10.1093/gji/ggab390">https://doi.org/10.1093/gji/ggab390</a> |            |          |          |
|   | Autor 1:   | Autor 2: | Autor 3: |
| Konzeption des Forschungsansatzes   | x          | x        | x        |
| Planung der Untersuchung  | x          |          |          |
| Datenerhebung   | x          |          |          |
| Datenanalyse und -interpretation  | x          | x        | x        |
| Schreiben des Manuskripts   | x          | x        | x        |
| <b>Vorschlag Anrechnung Publikationsäquivalente</b>   | <b>1.0</b> |          |          |

|  |            |          |          |
|--|------------|----------|----------|
| Publikation 2: <b>van Laaten, M.</b> , Wegler, U. and Eulenfeld, T. (2023), On the trail of fluids in the northernmost intracontinental earthquake swarm areas of the Leipzig-Regensburg fault zone, Germany, J. Seismol., 27, p. 573-597, <a href="https://doi.org/10.1007/s10950-023-10146-8">https://doi.org/10.1007/s10950-023-10146-8</a> |            |          |          |
|  | Autor 1:   | Autor 2: | Autor 3: |
| Konzeption des Forschungsansatzes  | x          | x        |          |
| Planung der Untersuchung   | x          | x        |          |
| Datenerhebung  | x          |          |          |
| Datenanalyse und -interpretation   | x          | x        | x        |
| Schreiben des Manuskripts  | x          | x        | x        |
| <b>Vorschlag Anrechnung Publikationsäquivalente</b>  | <b>1.0</b> |          |          |

|  |            |          |  |
|--|------------|----------|--|
| Publikation 3: <b>van Laaten, M.</b> and Wegler, U. (2024), Non-linear inversion for a multi-layer seismic S-wave attenuation model using radiative transfer theory, eingereicht in J. Geophys. Res. Solid Earth |            |          |  |
|  | Autor 1:   | Autor 2: |  |
| Konzeption des Forschungsansatzes  | x          | x        |  |
| Planung der Untersuchung   | x          | x        |  |
| Datenerhebung  | x          |          |  |
| Datenanalyse und -interpretation   | x          | x        |  |
| Schreiben des Manuskripts  | x          | x        |  |
| <b>Vorschlag Anrechnung Publikationsäquivalente</b>  | <b>1.0</b> |          |  |

## Selbstständigkeitserklärung

Ich erkläre, dass ich die vorliegende Arbeit selbständig und unter Verwendung der angegebenen Hilfsmittel, persönlichen Mitteilungen und Quellen angefertigt habe.

Jena, 9. Juli 2024

---

Marcel van Laaten



# Zusammenfassung

Die Mehrheit der Erdbeben in Deutschland konzentriert sich auf einige wenige Regionen. Eine dieser Regionen ist Ost-Thüringen/West-Sachsen. Die Erdbeben verteilen sich entlang eines Nord-Süd ausgerichteten, etwa 150 km langen Streifens zwischen dem tschechischen Cheb-Becken im Süden und Leipzig im Norden. Die Verteilung der Erdbeben, das regionale Spannungsfeld sowie das Vorhandensein einiger Nord-Süd verlaufender Störungselemente im südlichen Teil führten zur Hypothese eines transregionalen Störungssystems, das nach den Städten benannt wurde, über die es sich erstreckt: Rostock-Leipzig-Regensburg-Störungszone. Die genaue Lage und Struktur der Rostock-Leipzig-Regensburg-Störungszone ist nach wie vor nicht geklärt und Gegenstand aktueller Forschung. Die Störungszone erstreckt sich über eine Länge von etwa 700 km und eine Breite von 40 km und soll aus zahlreichen en échelon segmentierten Verwerfungen bestehen. Die Schwierigkeiten bei der Erfassung des Störungszonensystems resultieren daraus, dass es bis auf wenige Ausnahmen keine Verwerfungen an der Oberfläche gibt. Es wird angenommen, dass es sich um ein reaktiviertes, gescheitertes Rift-System handelt, das während der variszischen Orogenese angelegt wurde. Die Rostock-Leipzig-Regensburg-Störungszone gilt als tiefgreifende, sinistrale Blattverschiebung. Hinweise darauf geben die Erdbeben, die sich im mittleren Teil der Rostock-Leipzig-Regensburg-Störungszone befinden, welcher auch als Leipzig-Regensburg-Störungszone bezeichnet werden kann. Die Erdbebenfrequenz entlang des 150 km langen Nord-Süd-Streifens ist im Süden deutlich höher und die Erdbeben treten meistens in Tiefen zwischen 5 und 15 km auf, während Erdbeben im Norden weniger frequent sind und typischerweise in Tiefen zwischen 10 und 25 km vorkommen. Eine Besonderheit der Störungszone sind die zahlreichen Schwarmbebenregionen. Diese befinden sich nahezu ausschließlich im südlichen Teil zwischen dem Cheb-Becken und dem sächsischen Vogtland. Die Ursache der Schwarmbeben sind sehr wahrscheinlich aufsteigende Fluide aus einer partiellen Schmelze an der Lithosphären-Asthenosphären-Grenze.

Die vorliegende, kumulative Dissertation zielt darauf ab, ein besseres Verständnis der Krustenstruktur und geologischer Prozesse entlang der Rostock-Leipzig-Regensburg-Störungszone zu erzielen. Zu diesem Zweck wird der Untergrund hinsichtlich der seismischen Geschwindigkeit und

der seismischen Dämpfung analysiert. Die kombinierte Betrachtung der beiden Parameter soll Einblicke in die Prozesse des Untergrundes liefern und die Ursachen von Erdbeben und Erdbebenschwärmen aufklären. Zusätzlich wird die frequenzabhängige intrinsische Dämpfung und Streudämpfung auch tiefenabhängig aufgelöst. Die Datengrundlage bilden der Erdbebenkatalog und die Stationen des Seismoverbund Mitteldeutschland. Die Beantwortung der Fragen erfolgt in drei Forschungsarbeiten, von denen zwei bereits veröffentlicht und eine zur Veröffentlichung eingereicht wurden.

Die erste Veröffentlichung mit dem Titel „Comparison of Multiple Lapse Time Window Analysis and Qopen to determine intrinsic and scattering attenuation“ stellt in mehrfacher Hinsicht eine Vorarbeit für eine spätere Veröffentlichung dar. Gegenstand der Untersuchung ist die Bestimmung der frequenzabhängigen intrinsischen und Streudämpfung der Kruste im Bereich sächsisches Vogtland bis Leipzig unter Annahme eines homogenen streuenden Untergrundes. Dazu werden zwei unterschiedliche Methoden verwendet. Einerseits wird die Dämpfung mit der sogenannten „Multiple Lapse Time Window Analysis“ bestimmt, andererseits mit dem sogenannten „envelope fitting“. Der Vergleich zeigt, dass beide Methoden ähnliche Ergebnisse liefern. Ebenso wird in der Veröffentlichung der Einfluss verschiedener Parameter auf die Ergebnisse getestet. Die ermittelte intrinsische Dämpfung und Streudämpfung in dem Bereich sächsisches Vogtland bis Leipzig ist dabei geringer als die Dämpfung in NW-Bohemia. Trotz der Annahme eines homogenen Untergrundes kann somit bereits eine heterogene Kruste entlang der Leipzig-Regensburg-Störungszone nachgewiesen werden. Ebenso zeigt der Vergleich, dass beide Methoden innerhalb ihrer Fehlerbalken die gleichen Ergebnisse liefern. Das envelope fitting ist dabei leicht besser, da die Fehlerbalken geringfügig kleiner sind.

Die zweite Veröffentlichung mit dem Titel „On the trail of fluids in the northernmost intracontinental earthquake swarm areas of the Leipzig-Regensburg fault zone, Germany“ analysiert die seismische Geschwindigkeit des Untergrundes entlang der Leipzig-Regensburg-Störungszone. Die seismische Geschwindigkeit der Kruste wird mittels Laufzeittomographie abgebildet, während Geschwindigkeitsdiskontinuitäten der Lithosphäre und oberen Asthenosphäre mittels Receiver Functions bestimmt werden. Die Tomographie erlaubt Rückschlüsse auf die Krustenstruktur und ermöglicht die Identifikation von Bereichen, die potenziell

Fluide enthalten. Anhand erhöhter  $v_p/v_s$ -Verhältnisse konnten Bereiche identifiziert werden, die sehr wahrscheinlich Fluide enthalten. Diese Fluide sind sehr wahrscheinlich für die Schwarmbeben bei Schöneck und Werdau verantwortlich. Des Weiteren kann die Fluidquelle der beiden Schwarmbebenregionen mittels Receiver Functions nachgewiesen werden. Hierbei handelt es sich um dieselbe Quelle, die für die aufsteigenden Fluide unter NW-Böhmen/Vogtland verantwortlich ist.

Die dritte Veröffentlichung mit dem Titel „Non-linear inversion for a multi-layer seismic S-wave attenuation model using radiative transfer theory“ präsentiert eine methodische Weiterentwicklung zur Bestimmung der intrinsischen Absorption und Streudämpfung. Die Studie berücksichtigt nicht nur die Frequenzabhängigkeit, sondern auch die Tiefenabhängigkeit der seismischen Dämpfung. Mittels Monte-Carlo-Simulation wird die seismische Dämpfung einmal für den südlichen und einmal für den nördlichen Teil der Leipzig-Regensburg-Störungszone bestimmt. Die Ergebnisse zeigen eine geringe Tiefenabhängigkeit für beide Regionen. Es gibt jedoch Unterschiede in der Stärke der seismischen Dämpfung. Die intrinsische Dämpfung ist für beide Regionen ähnlich, der Süden ist dafür aber stärker streuend. Ein weiteres Ergebnis dieser Veröffentlichung ist die mögliche Erklärung der Erdbebentiefenverteilung entlang der Störungszone. Die Erdbeben entlang der Störungszone treten insbesondere in Bereichen mit geringer intrinsischer Dämpfung auf.

Ein weiteres Ergebnis der Dissertation ist die Abschätzung des Spannungsabfalls. Die Energietransfergleichung erlaubt nicht nur die Bestimmung der seismischen Dämpfung, sondern auch der Quellspektren von Erdbeben. Anhand des seismischen Moments und der Eckfrequenz, die aus den Quellspektren bestimmt werden können, lässt sich der Spannungsabfall in der Kruste nach einem Erdbeben bestimmen. Bereits mit der geringen Anzahl an verwendeten Erdbeben ist hier eine Abschätzung des Spannungsabfalls möglich. Es zeigt sich, dass die Erdbeben im nördlichen Teil der Störungszone selbstähnlich sind und der Spannungsabfall unabhängig von der Magnitude ist. Im Süden hingegen neigen stärkere Erdbeben zu einem stärkeren Spannungsabfall.

Die Ergebnisse dieser Dissertation demonstrieren, dass die Kombination aus der Analyse der seismischen Geschwindigkeit und der seismischen Dämpfung einen vielfältigen Einblick in die Prozesse des Untergrundes ermöglicht. Durch die Untersuchung beider Materialeigenschaften wird deutlich, dass sie sich gegenseitig ergänzen, um die Eigenschaften der

Kruste aufzuzeigen. Zusammengefasst zeigen diese Analysen, dass die Kruste entlang der Leipzig-Regensburg-Störungszone heterogen ist. Diese Ergebnisse unterstreichen die Bedeutung eines vielschichtigen Ansatzes bei der Untersuchung von Prozessen im Untergrund und ermöglichen so ein umfassenderes Verständnis der seismotektonischen Bedingungen in der Region.

# Summary

The majority of earthquakes in Germany are concentrated in a few regions. One of these regions is eastern Thuringia/western Saxony, where earthquakes occur along a north-south band spanning approximately 150 km between the Cheb Basin in the Czech Republic in the south and Leipzig (Germany) in the north. The distribution of these earthquakes, the regional stress field and the presence of some north-south striking fault elements in the southern part have led to the hypothesis of a transregional fault system. This system has been named the Rostock-Leipzig-Regensburg fault zone, extending over a length of 700 km and a width of 40 km consisting of multiple segmented en échelon faults. The precise location and structure of the Rostock-Leipzig-Regensburg fault zone are still unknown and currently under investigation. The challenges in mapping this fault system stem from the fact that, with a few exceptions, there are no visible faults on the surface. It is assumed that the fault zone is a reactivated, failed rift system that was created during the Variscan orogeny. The Rostock-Leipzig-Regensburg fault zone is considered to be a deep-seated sinistral fault zone system. This is indicated by the earthquakes located in the central part of the Rostock-Leipzig-Regensburg fault zone, which can be referred as the Leipzig-Regensburg fault zone. The earthquake frequency along this 150 km long north-south strip is significantly higher in the south, with earthquakes occurring typically at depths between 5 and 15 km. In contrast, earthquakes in the north are less frequent and typically occur at depths between 10 and 25 km. A distinct feature of the fault zone is the prevalence of numerous earthquake swarm regions. These are concentrated in the southern part, situated between the Cheb Basin and the Saxon Vogtland. The earthquake swarms are triggered by uprising fluids from a partial melt at the lithosphere-asthenosphere boundary. The objective of this cumulative dissertation is to gain a deeper understanding of the crustal structure and geological processes along the Rostock-Leipzig-Regensburg fault zone. To achieve this, the subsurface is analyzed in terms of seismic velocity and seismic attenuation. The combined observation of these two parameters provide insights into subsurface processes and help explain the causes of earthquakes and earthquake swarms. The analysis of seismic attenuation is accompanied by a methodological development in which the frequency-dependent in-

trinsic and scattering attenuation is also resolved as a function of depth. Data for this analysis is derived from the earthquake catalog and the stations of the Seismoverbund Mitteldeutschland. The research questions are addressed in three research articles, two of which have already been published and one that has been submitted for publication.

The first publication, titled "Comparison of Multiple Lapse Time Window Analysis and Qopen to Determine Intrinsic and Scattering Attenuation" serves as a preliminary study for a subsequent publication. The study focuses on determining the frequency-dependent intrinsic and scattering attenuation of the crust between the Saxon Vogtland and Leipzig under the assumption of a homogeneous scattering subsurface. Two methods are used for this purpose: "Multiple Lapse Time Window Analysis" and "envelope fitting". The comparison shows that both methods yield comparable outcomes. The publication also explores the impact of various parameters on the results. Comparing intrinsic and scattering attenuation values for the northern and southern part of the fault zone reveals that the northern region exhibits less attenuation than the southern region. Despite the assumption of a homogeneous subsurface, the results indicate that the Leipzig-Regensburg fault zone is heterogeneous. The findings also indicate that both methods produce similar results within their respective error bars, with envelope fitting showing slightly smaller error bars.

The second publication, titled "On the trail of fluids in the northernmost intracontinental earthquake swarm areas of the Leipzig-Regensburg fault zone, Germany" examines the seismic velocity of the subsurface along the Leipzig-Regensburg fault zone. The seismic velocity of the crust is imaged using traveltime tomography, while velocity discontinuities of the lithosphere and upper asthenosphere are determined using receiver functions. Tomography enables conclusions about the crustal structure. Additionally, areas in the crust that potentially contain fluids can be identified. They are likely the cause of the earthquake swarms at Schöneck and Werdau. Moreover, the fluid source of the two earthquake swarm regions can be determined using receiver functions. The source is the same source that is responsible for the uprising fluids below NW-Bohemia/Vogtland.

The third publication, titled "Non-linear inversion for a multi-layer seismic S-wave attenuation model using radiative transfer theory" presents a methodological advancement for determining intrinsic and scattering at-

tenuation. The study takes into account not only frequency dependence, but also depth dependence. Using Monte Carlo simulation, attenuation is determined once for the southern part and once for the northern part of the Leipzig-Regensburg fault zone. The results show low depth dependence for both regions. However, there are discrepancies in the degree of seismic attenuation. Intrinsic attenuation is comparable between the two regions, yet the southern region exhibits greater scattering. Furthermore, this publication offers a potential explanation for the distribution of earthquakes along the fault zone. By assuming that the crust behaves like a Maxwell body, intrinsic attenuation is proportional to inverse viscosity. In regions where the crust exhibits low intrinsic attenuation, earthquakes occur due to high viscosity or differential stress.

Another outcome of the dissertation is the estimation of stress drop. Radiative transfer theory allows not only the determination of seismic attenuation, but also the source spectra of earthquakes. From the seismic moment and corner frequency, obtained from the source spectra, the stress drop of an earthquake can be determined. Even with the limited number of earthquakes used an estimate of stress drop is possible here. It is evident that earthquakes in the northern region exhibit self-similarity. The stress drop remains constant regardless of magnitude. In contrast, stronger earthquakes in the southern region tend to have a higher stress drop.

The results of this dissertation demonstrate that combining the analysis of seismic velocity and seismic attenuation provides a diverse insight into processes of the subsurface. By examining both material properties, it becomes evident that they complement each other in revealing the characteristics of the crust. Together, these analyses show that the crust along the Leipzig-Regensburg fault zone is heterogeneous. These findings underscore the importance of employing a multi-layered approach to study subsurface processes, thereby providing a more comprehensive understanding of the seismotectonic conditions in the region.



# List of Figures

|     |   |     |
|-----|---|-----|
| 1.1 | Seismic hazard map of Germany with the expected mean PGA at each location for a return period of 475 years. . . . . | 2   |
| 1.2 | Simplified geological map of the study area. . . . .  | 3   |
| 2.1 | Plate tectonic development in the Central European segment of the Variscides. . . . .                               | 8   |
| 2.2 | Geological map and paleogeographic affiliation of Central Germany and the Bohemian Massif. . . . .                  | 9   |
| 2.3 | Regional geological units of Saxony. . . . .  | 11  |
| 2.4 | Overview map of the localized earthquakes and major faults. . . . .   | 13  |
| 3.1 | Temporal distribution of detected earthquakes from January 2009 to April 2024. . . . .                              | 16  |
| 3.2 | Gravity anomalies and selected structural elements of the LRZ. . . . .  | 20  |
| 3.3 | Overview map with the faults and existing seismic profiles in the study area. . . . .                               | 22  |
| 3.4 | Seismic profile EV01 and EV02. . . . .  | 23  |
| 3.5 | Reflection seismic profile DEKORP3/MVE90. . . . .   | 24  |
| 3.6 | Geological model of the 9Hr profile. . . . .  | 25  |
| 3.7 | Pseudo 3-D illustration of the P-wave velocity along the Granu95A and Granu95B profile. . . . .                     | 26  |
| 3.8 | Tectonic interpretation of the CEL09 profile. . . . .   | 28  |
| 4.1 | Tomography illustrated by the example of computed tomography. . . . .   | 30  |
| 4.2 | Theoretical waveform of the receiver function of a two-layer model. . . . .   | 34  |
| 4.3 | Seismic envelope of an earthquake. . . . .  | 36  |
| 4.4 | Energy propagation simulation of a seismic wave in a multi-layer model using Monte Carlo simulation. . . . .        | 40  |
| 7.1 | Schematic differential stress profile of the crust. . . . .   | 152 |
| 7.2 | Earthquake depth distribution and depth profiles of the intrinsic attenuation. . . . .                              | 153 |
| 7.3 | Stress drop analysis. . . . .   | 155 |



# List of Symbols

|                      |  |
|----------------------|--|
| $\Delta\sigma$       | Stress drop                              |
| $\Delta l$           | Path element                             |
| $\eta$               | Viscosity                                |
| $\theta$             | Polar angle                              |
| $\kappa$             | Hurst exponent                           |
| $\lambda$            | Damping factor                           |
| $\omega$             | Circular frequency                       |
| $\Phi$               | Scalar wave field                        |
| $\phi$               | Azimuthal angle                          |
| $A$                  | Amplitude                                |
| $b$                  | Absorption coefficient                   |
| $d$                  | Data vector                              |
| $d\Omega_{\hat{k}'}$ | Solid angle element                      |
| $dl$                 | Infinitesimal wavelength                 |
| $f$                  | Frequency                                |
| $f_c$                | Corner frequency                         |
| $G$                  | Green's function                         |
| $g$                  | Angular dependent scattering coefficient |
| $g^*$                | Transport scattering coefficient         |
| $g_0$                | Total scattering coefficient             |
| $g_{fwd}$            | Forward modeling operator                |
| $H$                  | Heaviside step function                  |
| $I$                  | Intensity                                |
| $I_n$                | identity matrix                          |
| $J$                  | Jacobian matrix                          |
| $\hat{k}$            | (Incoming) unit vector                   |
| $\hat{k}'$           | Outgoing unit vector                     |
| $L$                  | Discrete model parameters                |
| $m$                  | Model parameters                         |
| $M_0$                | Seismic moment                           |
| $N$                  | Particle density                         |
| $n$                  | High-frequency fall-off                  |
| $p$                  | Phase function                           |
| $Q^{-1}$             | Quality factor                           |
| $Q_i^{-1}$           | Intrinsic attenuation                    |
| $Q_{sc}^{-1}$        | Scattering attenuation                   |

|                       |                                  |
|-----------------------|----------------------------------|
| $s$                   | Path between source and receiver |
| $T$                   | Seismic wave traveltime          |
| $t$                   | Time                             |
| $t_0$                 | Earthquake origin time           |
| $t_s$                 | Relative traveltime              |
| $T_{obs}$             | Observed traveltime              |
| $T_{syn}$             | Synthetic traveltime             |
| $u$                   | Slowness                         |
| $v$                   | Seismic velocity                 |
| $v_p$                 | P-wave velocity                  |
| $v_s$                 | S-wave velocity                  |
| $x$                   | Location                         |
| $x_1^0, x_2^0, x_3^0$ | Source coordinates               |
| $x_1, x_2, x_3$       | Receiver coordinates             |

# List of Abbreviation

|               |   |
|---------------|---|
| ART           | Approximate ray tracing   |
| BG            | Bergen granite intrusion  |
| BKZ           | Bergen-Klingenthal-Chodov fault zone  |
| EB            | Eibenstock granite intrusion  |
| ELZ           | Eichigt-Adorf-Luby fault zone   |
| FZ            | Flöha-Halle fault zone  |
| GBZ           | Gefell-Bad Brambach fault zone  |
| GJZ           | Gera-Jáchymov fault zone  |
| IASP91        | 1-D Earth velocity model of the International Association of Seismology and Physics of the Earth's Interior |
| KB            | Kirchberg granite intrusion   |
| L(-component) | Longitudinal component  |
| LRZ           | Leipzig-Regensburg fault zone   |
| $M_L$         | Local magnitude   |
| $M_w$         | Moment magnitude  |
| Moho          | Mohorovičić discontinuity   |
| NLRZ          | Northern part of the LRZ  |
| P(-wave)      | Primary wave or pressure wave   |
| Q(-component) | Vertical shear wave component (Q for German "quer")   |
| RF            | Receiver function   |
| RTT           | Radiative transfer theory   |
| S(-wave)      | Secondary wave or shear wave  |
| SLRZ          | Southern part of the LRZ  |
| SV-wave       | Vertical polarized shear wave   |
| T(-component) | Tangential component  |
| TWT           | Two way traveltime  |



# Contents

|                                     |             |
|-------------------------------------|-------------|
| <b>Zusammenfassung</b>              | <b>vii</b>  |
| <b>Summary</b>                      | <b>xi</b>   |
| <b>List of Symbols</b>              | <b>xvii</b> |
| <b>List of Abbreviation</b>         | <b>xix</b>  |
| <b>1 Introduction</b>               | <b>1</b>    |
| 1.1 Motivation . . . . .            | 1           |
| 1.2 Aim of this work . . . . .      | 3           |
| <b>2 Geological setting</b>         | <b>7</b>    |
| 2.1 Geological evolution . . . . .  | 7           |
| 2.2 Geological structure . . . . .  | 10          |
| 2.3 Major faults . . . . .          | 12          |
| <b>3 Geophysical knowledge</b>      | <b>15</b>   |
| 3.1 Seismology . . . . .            | 15          |
| 3.2 Gravimetry . . . . .            | 19          |
| 3.3 Seismics . . . . .              | 21          |
| 3.3.1 EV01 and EV02 . . . . .       | 21          |
| 3.3.2 DEKORP3/MVE-90 East . . . . . | 21          |
| 3.3.3 9Hr . . . . .                 | 23          |
| 3.3.4 GRANU95 . . . . .             | 26          |
| 3.3.5 CEL09 . . . . .               | 27          |
| <b>4 Methods</b>                    | <b>29</b>   |
| 4.1 Traveltime tomography . . . . . | 29          |
| 4.1.1 Inversion . . . . .           | 30          |
| 4.1.2 Forward modeling . . . . .    | 32          |
| 4.2 Receiver functions . . . . .    | 33          |
| 4.3 Seismic attenuation . . . . .   | 35          |
| <b>5 Publication summary</b>        | <b>41</b>   |

---

|   |              |
|---|--------------|
| <b>6 Publications</b>                               | <b>43</b>    |
| 6.1 Publication 1 . . . . .                         | 43           |
| 6.2 Publication 2 . . . . .                         | 58           |
| 6.3 Publication 3 . . . . .                         | 84           |
| <b>7 Results and discussion</b>                     | <b>149</b>   |
| 7.1 Fluids and their origin . . . . .               | 149          |
| 7.2 Schöneck and Werdau earthquake swarms . . . . . | 150          |
| 7.3 Earthquakes along the LRZ . . . . .             | 151          |
| 7.4 Stress drop . . . . .                           | 153          |
| <b>8 Conclusions</b>                                | <b>157</b>   |
| <b>References</b>                                   | <b>159</b>   |
| <b>Acknowledgments</b>                              | <b>xxiii</b> |

# 1 | Introduction

## 1.1 Motivation

Seismic activity in Germany is relatively low compared to regions that lie on active plate boundaries or have volcanic activity (Leydecker, 2011). In Germany, the following areas are known to exhibit increased seismic activity (Fig. 1.1): Alpine region, Lower Rhine Bay, Swabian Alp, Rhine Rift Valley and East-Thuringia/West-Saxony (Grünthal et al., 1998). This thesis takes a closer look at the East-Thuringia/West-Saxony region and examines the seismic activity and its causes. The earthquakes along the East-Thuringian and West-Saxon border are distributed along a north-south oriented band, extending between Leipzig (Germany) in the north and the Cheb Basin in NW-Bohemia (Czech Republic) in the south (Fig. 1.2).

The distribution of earthquakes and the existence of numerous north-south trending fault elements, which have been proven by local and regional geological and geophysical studies, led Grünthal et al. (1985) to hypothesize a north-south striking transregional fault zone system called the Rostock-Leipzig-Regensburg Fault Zone (originally the Rostock-Desau-Regensburg Photolineation). The fault zone extends over a length of 700 km and a width of 40 km stretching from Rostock in the north to Regensburg in the south (Bankwitz et al., 2003). However, only the central part (Leipzig to NW-Bohemia) of the fault zone system exhibits seismic activity. Various studies have already addressed the controversial Rostock-Leipzig-Regensburg fault zone (e.g. Bankwitz et al., 2003; Dahm et al., 2018; Hemmann et al., 2003; Korn et al., 2008; Müller, 2022; Pohl et al., 2006; Sonnabend, 2022). Despite this, there are still many unanswered questions regarding the system, such as the exact location of the fault zones or the heterogeneous earthquake distribution. With a few exceptions in the southern part, the fault zone system is not visible on the surface and direct observation is not possible. The seismic activity in the region indicates the presence of two fault directions. The first is the northwest-southeast striking Hercynian faults, while the second is a deep-seated, north-south striking sinistral fault system. (Bankwitz et al., 2003; Behr et al., 2002; Müller, 2022; Sonnabend, 2022).

This dissertation primarily regards the seismically active portion of the Rostock-Leipzig-Regensburg fault zone. For this reason, the Rostock-Leipzig-Regensburg fault zone will only be referred in the following as

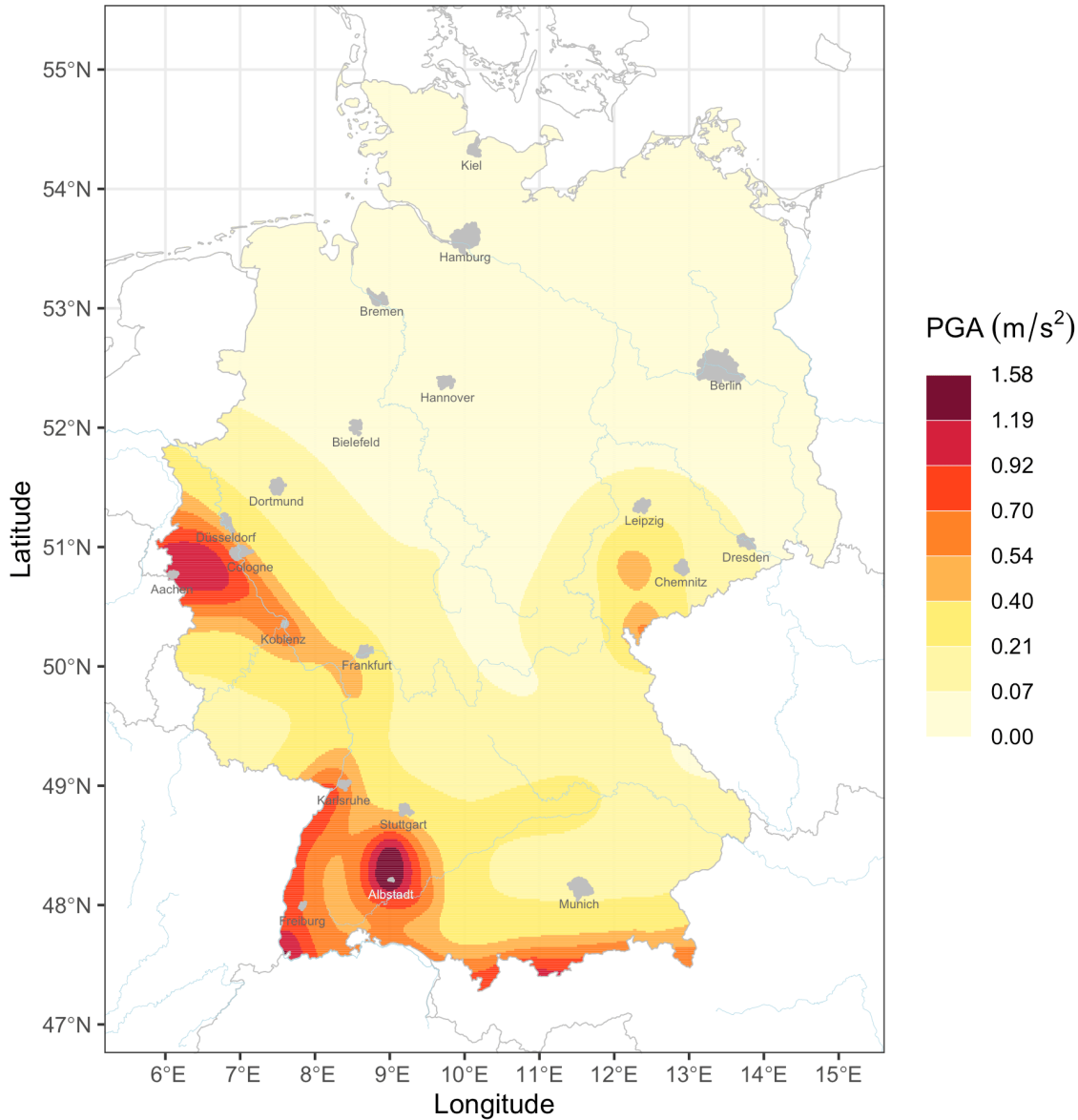


Figure 1.1: Seismic hazard map of Germany with the expected mean PGA at each location for a return period of 475 years (Schneider et al., 2023).

the Leipzig-Regensburg fault zone (LRZ). The LRZ can be divided into three areas: the northern (Leipzig area), central (East-Thuringian/West-Saxon border area) and southern area (NW-Bohemia/Vogtland) (Fig. 1.2).

The seismic hazard map (Grünthal et al., 2018) classifies the region between Vogtland and Leipzig as earthquake risk zone (DIN EN 1998-1/NA), as stronger earthquakes have repeatedly occurred in the region over the course of time (Fig. 1.1). The strongest documented earthquake was the Central German earthquake on March 6, 1872 near Gera with an estimated moment magnitude of  $M_w$  5.2, which could still be

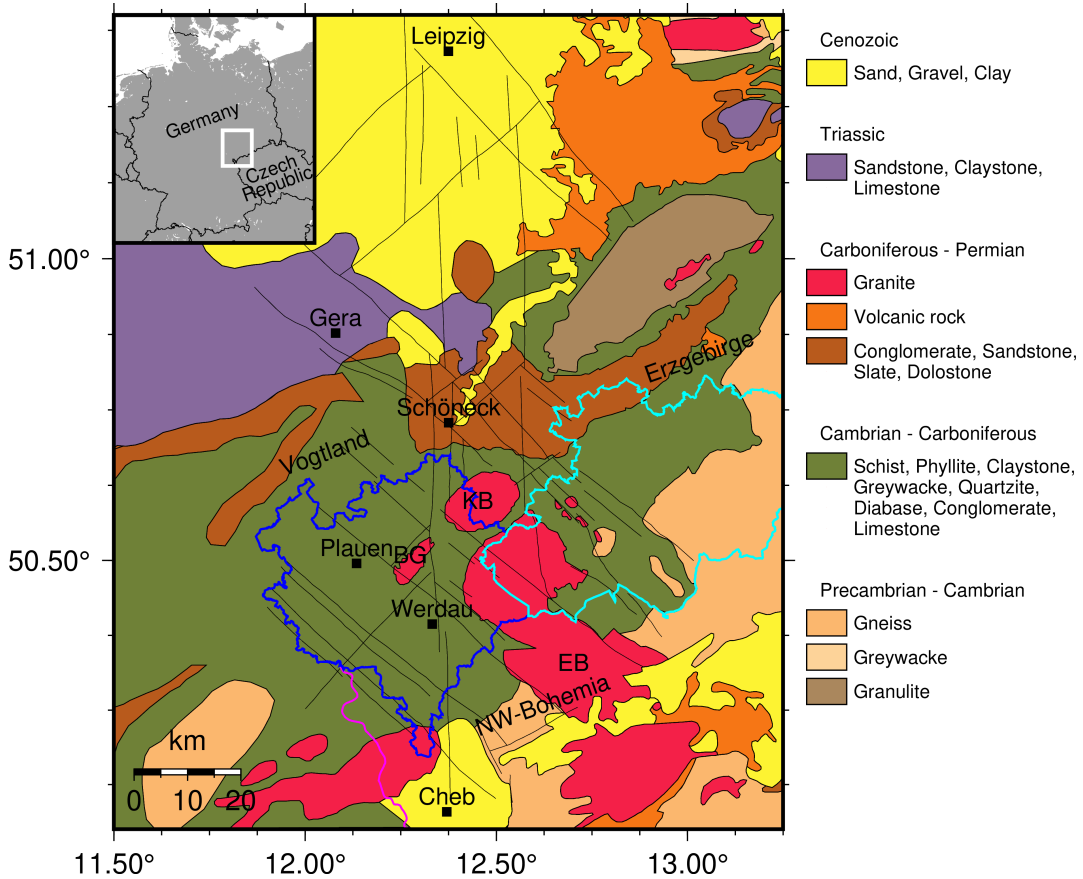


Figure 1.2: Simplified geological map (after LfULG - Sächsisches Landesamt für Umwelt, Landwirtschaft und Geologie, 2018) of the study area and its location within Europe with important areas and cities. Faults are shown as thin black lines and the Vogtland, Erzgebirge and NW-Bohemia regions are marked in blue, cyan and magenta, respectively. The Eibenstock, Kirchberg and Bergen granite intrusions are labeled EB, KB and BG.

felt at a distance of several 100 km (von Seebach, 1873). Other significant earthquakes occurred in 1985 and 1986 near Nový Kostel ( $M_L$  5.1 and  $M_L$  4.8) and in 1908 near Klingenthal ( $M_L$  4.6) (Leydecker, 2011). Another noteworthy feature of the LRZ is the occurrence of earthquake swarms (Fischer et al., 2014; Grünthal et al., 1985; Korn et al., 2008), with up to 10,000 earthquakes in a few weeks. The earthquake swarm activity is mainly concentrated in the southern part of the LRZ, an area that is subject of current research (see Fischer et al., 2014). The driving process that govern the evolution of earthquake swarms is high-pressure fluid migration within the crust (e.g. Fischer et al., 2014). However, the exact trigger mechanism remains uncertain.

## 1.2 Aim of this work

The objective of this thesis is to investigate the subsurface along the LRZ. To this end, seismic velocity and seismic attenuation in this re-

gion are analyzed. The combined consideration of velocity and attenuation allows conclusions to be drawn about the seismotectonic conditions and the causes of earthquakes and earthquake swarms along the LRZ. Another objective is the further development of the method for determining seismic attenuation. Similar to seismic velocity, the frequency-dependent attenuation is spatially resolved. The earthquake catalog of the "Seismoverbund Mitteldeutschland", containing over 19,000 localized earthquakes in the region, along with a large number of broadband seismometers from various networks, serves as the data basis for this thesis. The key research questions addressed in this thesis are:

### **Where are fluids located along the LRZ and can they be imaged?**

Several areas with earthquake swarm activity can be identified in the southern part of the LRZ (Korn et al., 2008). The main trigger for these earthquake swarms are most likely uprising fluids from the asthenosphere (Geissler et al., 2005; Heuer et al., 2006). As the fluids traverse the crust, they trigger earthquake swarms and eventually emerge at the surface at mofettes. In the northern area of the Saxon Vogtland and further north, earthquake swarms occur, but there are no fluids emerging at the surface. The objective of this investigation is to determine whether there are also fluids in the northern area and to identify possible fluid pathways. This is achieved through travelttime tomography, receiver function analysis and determining seismic attenuation.

### **Why are there earthquake swarm areas in the Vogtland region of Saxony?**

Earthquake swarm areas are identified in the Saxon Vogtland and near Werdau (e.g. Hemmann et al., 2003; Korn et al., 2008), indicating the presence of fluids in the subsurface. Fluids are the primary driving force behind earthquake swarms, although they are not the sole trigger of the NW-Bohemia/Vogtland earthquake swarms (Mousavi et al., 2015). Using seismic travelttime tomography and seismic attenuation, the crust in the Saxon Vogtland and its northern region is examined to determine if the earthquake swarms in the Saxon Vogtland are triggered by the same mechanisms as those in NW-Bohemia/Vogtland. If fluids are found in the north, their origin will be investigated using receiver function analysis. Given the close proximity of NW-Bohemia/Vogtland and the Saxon

Vogtland, it is possible that the two regions share the same fluid source. However, Werdau is much further north and the source of the fluids remains unknown.

### **Why does earthquake behavior differ along the LRZ?**

The seismic activity along the LRZ exhibits distinct characteristics. The southern region is subject to a greater frequency of earthquakes compared to the northern region (Seismoverbund Mitteldeutschland, 2024). Additionally, earthquakes in the south occur at shallower depths. The typical earthquake depth for NW-Bohemia/Vogtland is 5 to 15 km. In the northern part of the LRZ, earthquakes in the first few kilometers of the crust are more rare. Earthquakes typically occur at a depth of 10 to 25 km in the northern part. To explain this difference in behavior, the crust along the LRZ is investigated.

### **Can seismic attenuation, determined with radiative transfer equation, also be resolved as a function of depth?**

The spatial distribution of material properties in rocks can provide valuable information about subsurface structures, processes and composition. Seismic attenuation is sensitive to porosity, viscosity, fluid content, temperature and heterogeneities in the medium. The spatial distribution of seismic attenuation can provide new insights into the subsurface and the processes taking place there. This thesis aims to determine if resolving seismic attenuation as a function of depth is possible using radiative transfer theory. Achieving this goal requires further development of the energy transfer equation application to invert a 1-D multi-layer model that differentiates between frequency-dependent scattering and absorption. This marks the initial step towards 3-D attenuation tomography utilizing radiative transfer theory, which should provide new insights into the subsurface.



## 2 | Geological setting

The geological structure of Central Europe is a complex mosaic of various crustal fragments that have formed over different geological periods. The north-south orientation of the LRZ intersects several of these fragments. The southern part of the LRZ is primarily composed of metamorphic and magmatic hard rocks near the surface, while the northern part is mainly made up of solid sedimentary rocks or loose sediments. The different structures and the deposition history are described in more detail in the following.

### 2.1 Geological evolution

The breakup of the supercontinent Rodinia into two large blocks, North Rodinia and South Rodinia, during the Neoproterozoic sets the initial foundations for the formation of the Variscan orogeny. Continental rifting caused both blocks to collide with the Congo Craton merging to create the supercontinent Pannotia (Murphy et al., 2021; Nance et al., 2022). The collision led to the Cadomian orogeny in the late Neoproterozoic. At the end of its brief existence, Pannotia broke apart into Gondwana, Laurentia, Baltica and possibly Sibiria (Murphy et al., 2021). The disintegration caused Laurentia, Baltica, and Sibiria to move northwards. During the Ordovician, Avalonia and Armorica separated from Gondwana through rift processes and moved northwards. The individual subcontinents were separated from each other by ocean basins, such as Iapetus between Laurentia and Baltica or the Tornquist Ocean between Baltica and Avalonia (Murphy et al., 2021; Nance et al., 2022). By the Upper Ordovician, Avalonia collided with Baltica, closing the Tornquist Ocean. In the Silurian period, the collision of Avalonia and Baltica with Laurentia formed the new large continent Laurussia, leading to the Caledonian orogeny and the closure of the Iapetus Ocean (McKerrow et al., 2000; Murphy et al., 2021). During the Middle Silurian to the Upper Devonian period, Gondwana and the newly formed large continent Laurussia came into closer proximity once again (Fig. 2.1). This convergence led to the Variscan orogeny in the Devonian, which was caused by the collision of various microplates and the convergence of the two large continents. The Caledonian and Variscan orogenies ultimately led to the formation of the supercontinent Pangaea, which was essentially complete at the end of the Carboniferous (e.g.

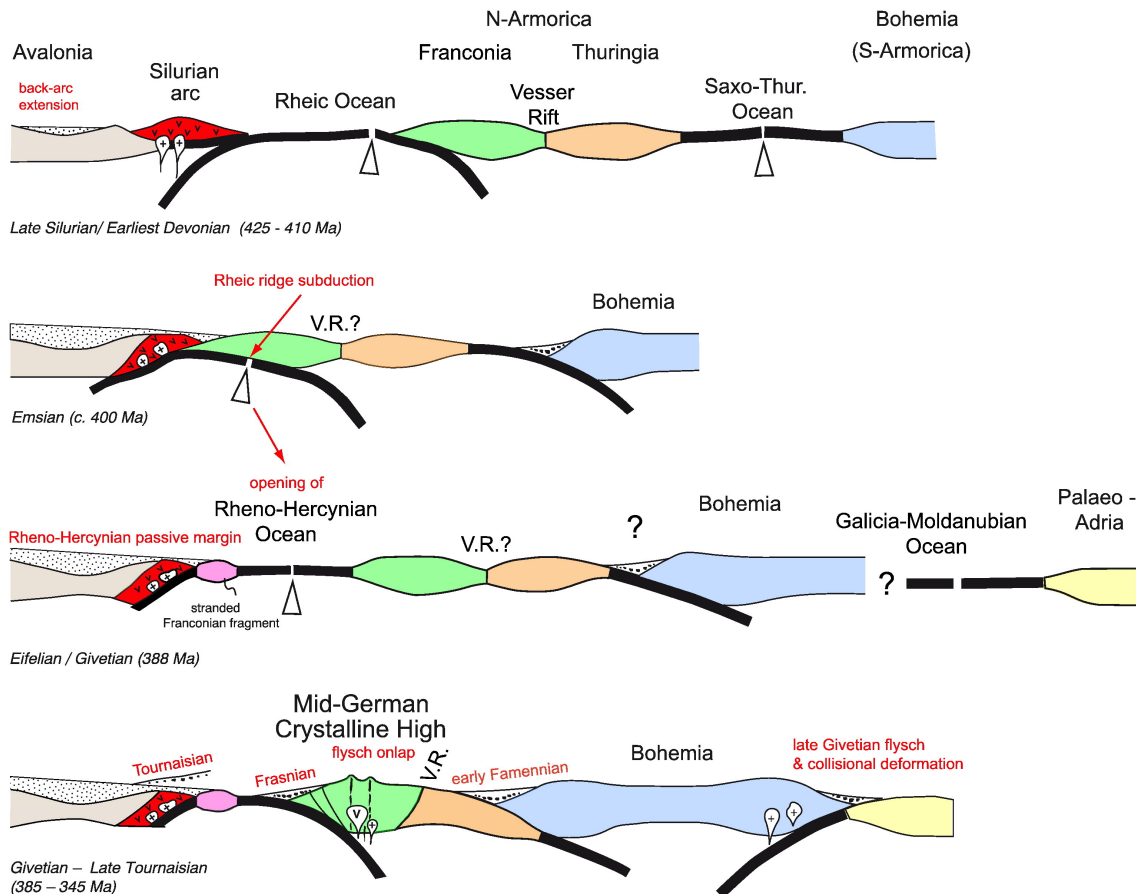


Figure 2.1: Plate tectonic development in the Central European segment of the Variscides (Wolfgang et al., 2017).

Franke, 2000). The convergence of Gondwana and Laurussia in the late Carboniferous period led to a shift from a north-south collision to an east-west movement, resulting in dextral continental shears (McCann, 2008). During the late Carboniferous and Permian periods, plate detachments caused a thinning of the crust, leading to increased heat flow and intense volcanism (Pälchen & Walter, 2008). The continuous erosion of the Variscan mountains resulted in the formation of a peneplain, which was subsequently covered by sedimentary deposits. Following the resumption of tectonic uplift by the Alpine orogeny, the mountains were preserved as Variscan islands among younger Mesozoic rocks (Pälchen & Walter, 2008).

According to Kossmat (1927), the Variscan orogeny can be divided from north to south in the area of the LRZ as follows (see also Fig. 2.2): The Mid-German-Crystalline High, Saxothuringian, and Moldanubian. The subdivisions are based on the rock type and degree of metamorphism. In the Tertiary, the northern area of the LRZ was situated on the pe-

riphery of the Paleo-North Sea due to the retreat of the Cretaceous sea. Over the course of lengthy periods, fluctuations in sea level resulted in the deposition of a various sediments that still overlay the bedrock today. These sediments were later deformed by glaciotectonic activity caused by repeated ice advances (e.g. Ehlers et al., 2011; Eissmann, 1987, 1996, 2002).

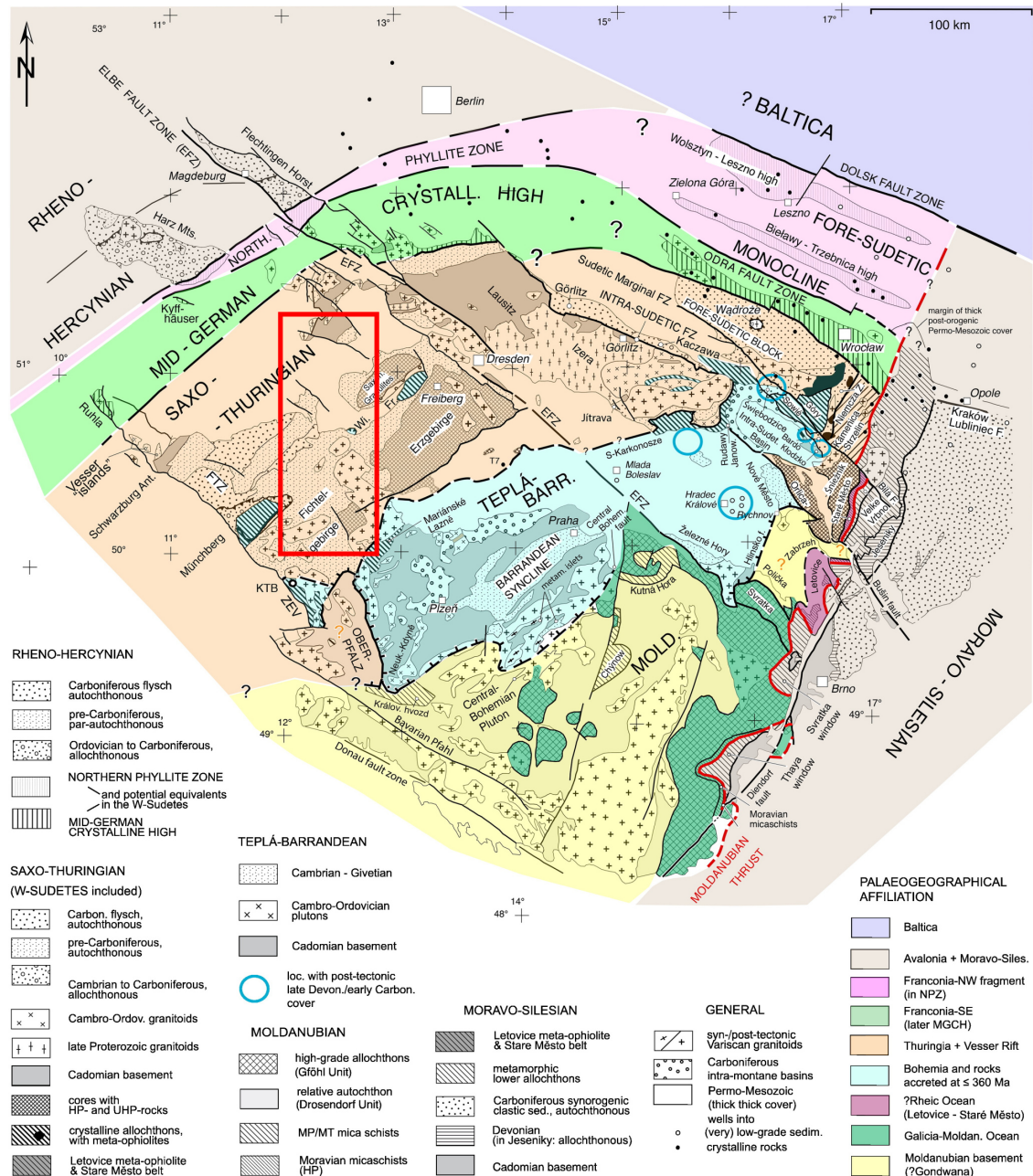


Figure 2.2: Geological map and paleogeographic affiliation of Central Germany and the Bohemian Massif (modified from Wolfgang et al., 2017). The red box marks the investigation area.

## 2.2 Geological structure

The deposition periods of the rocks are distinct, resulting in their deposition in close proximity to and upon one another (Fig. 2.2). The geology along the LRZ can be divided vertically into storeys and horizontally into regional units. In terms of regional geology, the LRZ area can be divided from south to north as follows (Fig. 2.3): The Fichtelgebirge and Erzgebirge anticlinal zones, the Vogtland and Central Saxonian anticlinal zones, the North Saxonian anticlinal zone, and the Lower Lusatian anticlinal zone. These structures predominantly strike southwest-northeast. The different storeys can be divided into three categories based on their age of formation, composition, and tectonic origin (Pälchen & Walter, 2008): basement, transitional, and overburden. Along the LRZ, all three storeys are present at the surface (Fig. 2.2). If the overlying layer is missing, it indicates that the upper layer has either not been formed or has already eroded. The seismically active part of the LRZ is bordered to the south by the Eger Graben and to the east by the Eibenstock-Nejdek granite massif of the Erzgebirge (Pälchen & Walter, 2008).

The basement is composed of rocks that are characterized by intensive deformation, regional metamorphism and magmatic intrusions. The rocks were formed during the Cadomian and Variscan orogeny (Franke, 2000). The Cadomian rocks were partially overprinted again during the Variscan orogeny. They consist of low-grade metamorphic deformed sediments and metamorphic rocks that formed under different pressure-temperature conditions, such as phyllite and flysch. The igneous rocks were either incorporated into the mountain formation or formed immediately after a mountain formation as a result of it (Pälchen & Walter, 2008), such as the Eibenstock granite intrusion. In the Saxon Vogtland, the basement is exposed at the surface. Towards the north, the basement is covered by progressively thicker units of transitional and overburden (Fig. 2.2). Nevertheless, the basement can still be identified at greater depths using geophysical methods (see Chapter 3), even though the exact lithology remains unknown.

The transitional basement, lies discordant on the bedrock. It is composed of deposits from volcanic eruptions and sediments from eroded Variscan rocks (Pälchen & Walter, 2008). Due to the uplift of the prehistoric Erzgebirge in the Upper Carboniferous, it was subjected to

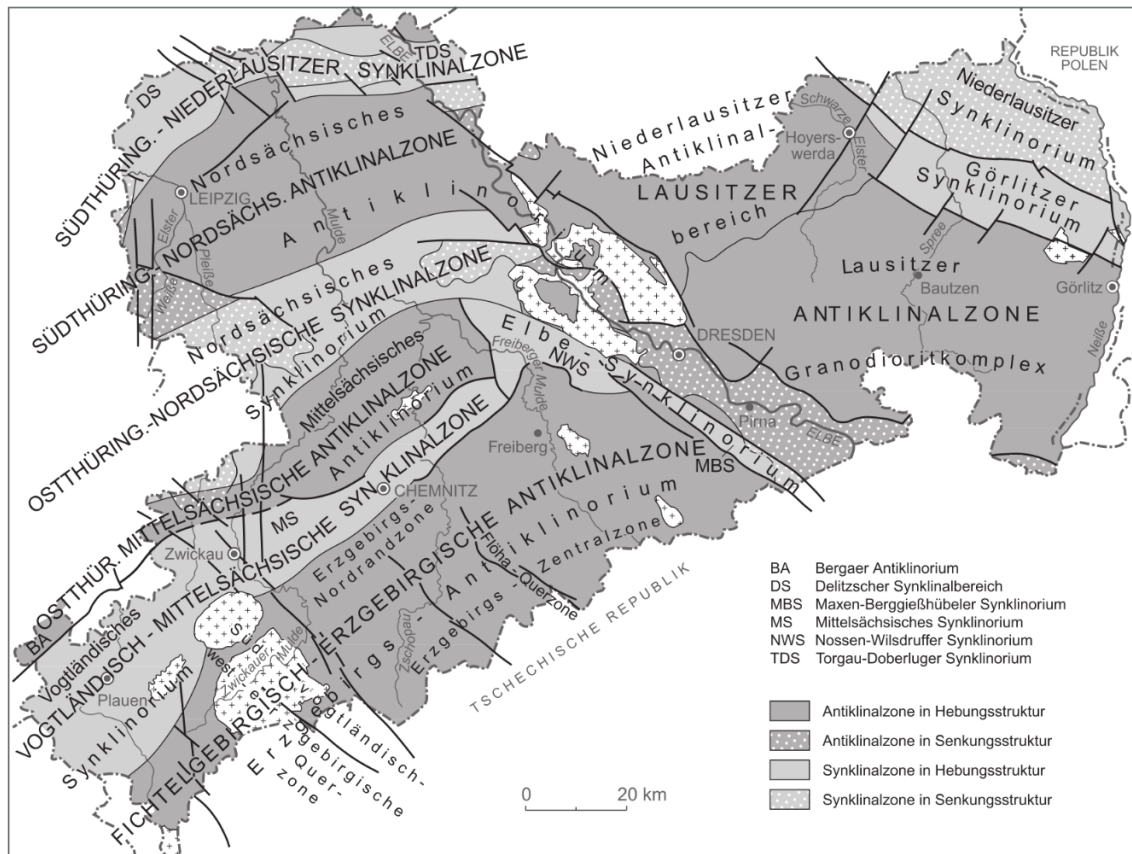


Figure 2.3: Regional geological units of Saxony (Pälchen & Walter, 2008)

increased weathering and erosion (Linnemann & Romer, 2010). The eroded material from the Erzgebirge was sedimented together with volcanic debris in basin structures such as the Vorerzgebirgs depression. The overburden consists of sedimentary rocks that formed after the Variscan orogeny was leveled in the late Permian (Linnemann & Romer, 2010). These rocks were deposited by both marine and terrestrial processes. The deposition of sediments was influenced by numerous transgressions and regressions of the sea level, especially in northern Saxony and in the Thuringian Basin (Pälchen & Walter, 2008). Erosion relics in the Erzgebirge indicate that sediments from the overburden were also deposited there, but have already been largely eroded (Pälchen & Walter, 2008). Sediments deposited up to the end of the Mesozoic era mainly exist as bedrock and have been preserved in several basins and depressions. These are superimposed by Cenozoic sediments, which are predominantly unconsolidated rocks and discordantly overlie underlying rocks of all levels.

## 2.3 Major faults

The study area encompasses several regional tectonic fault zones, that are partially exposed to the surface (Fig. 2.4). The dominant strike direction of the fault zones is northwest-southeast, which is attributed to the large number of Hercynian faults, such as the Bergen-Klingenthal-Chodov fault zone, Gera-Jáchymov fault zone (GJZ), or Halle fault (FZ). These faults were created during the Variscan orogeny. Based on photolineations derived from orthophotos, digital elevation models, and gravity anomalies, there are also indications of a deep-seated, north-south and east-west striking structure (e.g. Bankwitz et al., 2003; Behr et al., 2002; Bram & Hirschmann, 1992; Grünthal et al., 1985; Kämpf et al., 1991; Pohl et al., 2006). In the study area, the faults of the different directions intersect and form a complex mosaic. In particular, intersections of the northwest-southeast and north-south striking fault zones occur in the Cheb basin, Zwickau, Gera, and Leipzig. Earthquakes occur along both fault directions (Korn et al., 2008; Sonnabend, 2022) and the strongest earthquake in the past century occurred in the vicinity of the Gera intersection (see Section 3.1).

The Leipzig-Regensburg fault zone is a transregional sinistral strike-slip fault zone system with a length of 700 km and a width of 40 km (Bankwitz et al., 2003; Kämpf et al., 1991). The exact location, structure, and history of the fault zone are subject of current research. According to Grünthal et al. (2009), the LRZ could be a reactivated failed rift system created during the Variscan orogeny (Meschede, 2018). Several volcanic structures are identified along the LRZ, including the Delitzsch complex north of Leipzig, the Weißenbrunn and Ebersbrunn diatreme near Zwickau, and the Plesná and Velký Luh Maar in the NW-Bohemia region (Nickschick et al., 2014). The age of the volcanoes varies, with the oldest being Cretaceous in the north and the youngest being Oligocene and Miocene in the Vogtland area and Cenozoic in the south (Nickschick et al., 2014). The LRZ has a seismically active central part of 150 km in length between Leipzig in the north and the Cheb Basin in the south. The fault zone consists of numerous north-south oriented sub-parallel faults, each composed of en échelon segments of a few kilometers length (Bankwitz et al., 2003; Bram & Hirschmann, 1992; Fischer et al., 2014). Due to the segmentation of several short lineaments, Pohl et al. (2006) dismissed the possibility of a strike-slip

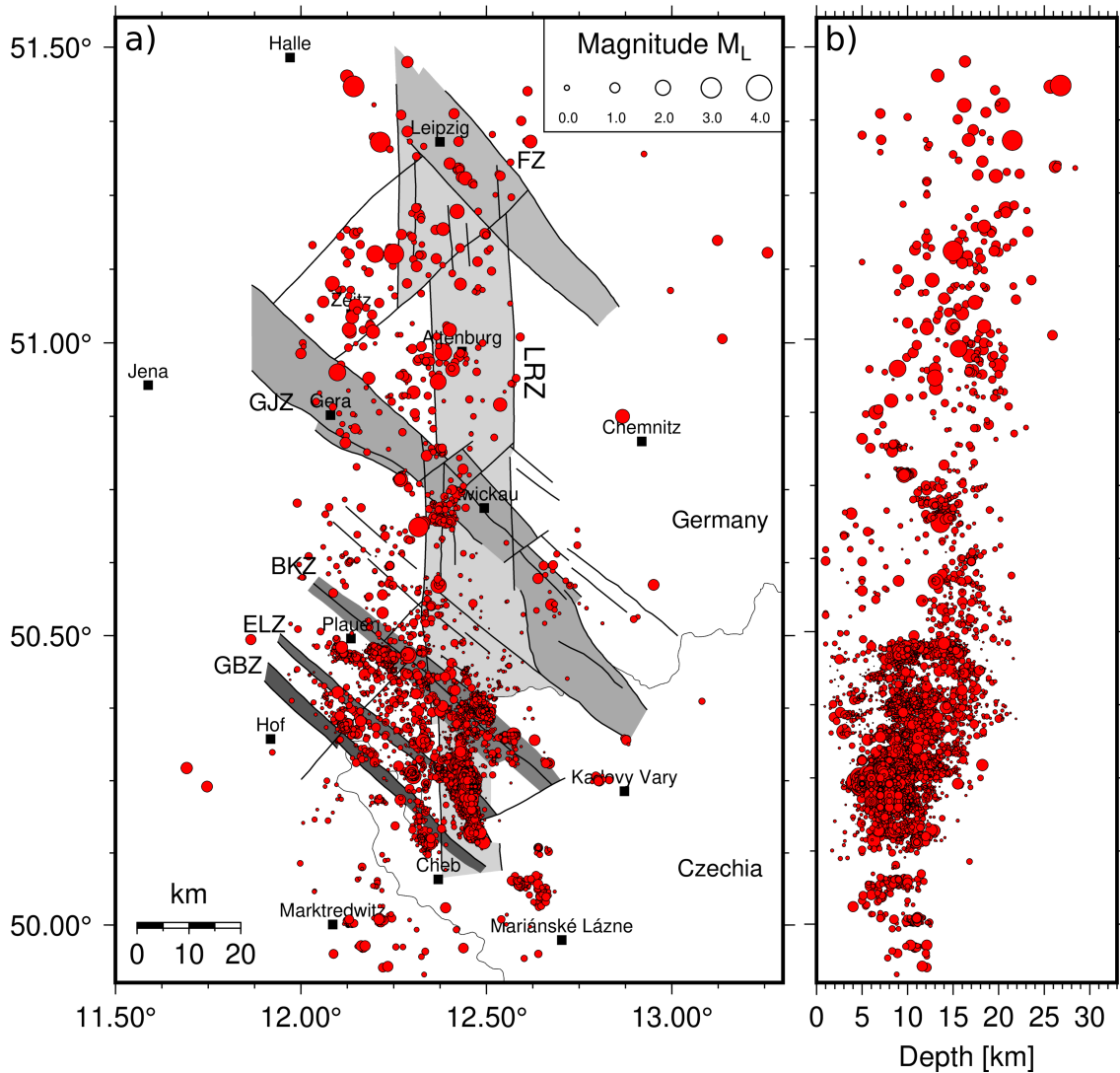


Figure 2.4: Overview map of the localized earthquakes of the Seismoverbund Mitteldeutschland earthquake catalog from January 2009 to April 2024. The area of the north-south striking LRZ (Leipzig-Regensburg fault zone) is shown in light gray and the areas of the northwest-southeast striking Hercynian fault zones (from north to south: FZ - Flöha-Halle fault zone, GJZ - Gera-Jáchymov fault zone, BKZ - Bergen-Klingenthal-Chodov fault zone, ELZ - Eichigt-Adorf-Luby fault zone, GBZ - Gefell-Bad Brambach fault zone) as dark gray (after LfULG - Sächsisches Landesamt für Umwelt, Landwirtschaft und Geologie, 2018). b) Depth distribution of seismicity along the Leipzig-Regensburg fault zone.

zone, instead proposing normal fault kinematics with oblique components. The zone cannot be delineated by geological mapping, as the active faults do not reach the surface (Müller, 2022). Sonnabend (2022) attributed the lack of surface manifestation to the young age of the fault zone system. Since it is still in its embryonic stage, it did not have time to manifest on the surface, or, at least in the northern part, the fault is covered by sediments. Paleoseismic investigations by Müller (2022) also revealed no geological evidence near the surface in the northern

area of the LRZ. Some studies that analyzed photolineations of satellite data claimed the observation of the LRZ at the surface (Bankwitz et al., 2003; Grünthal et al., 1985; Krull, 1984; Pohl et al., 2006). The results of these studies have been questioned by subsequent studies using modern satellite-based data (Dahm et al., 2018; Grünthal et al., 2018).

The GJZ is an approximately 200 km long fault zone, that follows the northwest-southeast Hercynian strike direction and was most likely created during the Variscan orogeny (Bankwitz et al., 2003). The fault continues to the west as the Finne fault. The GJZ consists of numerous individual faults that form a complex system. Gravimetric, magnetic and seismic data indicate the presence of a pronounced, deep-seated fault system (Bankwitz & Bankwitz, 1994). Near Gera, the GJZ crosses the north-south striking LRZ.

The Halle fault is approximately 40 km long, strikes in a northwest-southeast direction as well and is part of the Flöha-Halle fault zone (FZ). The fault has undergone several phases during its tectonic evolution. The strike direction also indicates that the fault was created during the Variscan orogeny. According to Rappsilber (2003), the Halle fault was a strike-slip fault in the Early Permian and later reactivated as a reverse fault in the Late Cretaceous (Kley & Voigt, 2008; Rappsilber, 2003). The fault is still considered active today. Two earthquakes with a magnitude of approximately 3 occurred in 2015 and 2017 between Leipzig and Halle and were attributed to the Halle fault (Dahm et al., 2018). Both earthquakes occurred at great depths (26 and 29 km), suggesting a fault in the lower crust near the Moho (Dahm et al., 2018).

## 3 | Geophysical knowledge

Due to the lack of visible faults on the surface, it is difficult to precisely localize the LRZ, but various geophysical investigations, such as focal mechanisms of the earthquakes, indicate that a deep-seated fault zone exists in the region. Furthermore, there are gravimetric indications as well as several reflection and refraction seismic studies investigating the crust in the area.

### 3.1 Seismology

The earthquakes along the LRZ are constrained to a narrow, north-south oriented band with a length of approximately 150 km and a width of 40 km between the Cheb Basin in the Czech Republic in the south and Leipzig, Germany in the north (Bankwitz et al., 2003; Kämpf et al., 1991) (Fig. 2.4). There is no historical evidence of seismic activity north of Leipzig and south of Schwandorf (Bavaria) over the centuries (Leydecker, 2011). With the current seismic networks, it has only been possible to locate isolated, stronger earthquakes south of Schwandorf. However, it is uncertain whether these are related to the LRZ. North of Leipzig, even with the current seismic networks, no earthquake has been detected.

The earthquake catalog of the "Seismoverbund Mitteldeutschland" (Seismoverbund Mitteldeutschland, 2024), which is based on the evaluation of the Thuringian Seismological Network and the University of Leipzig, respectively the "Observatorium Collm", contains a total of 19,832 tectonic earthquakes in the LRZ area between January 2009 and April 2024 (Fig. 2.4 and Fig. 3.1). The local magnitudes of these earthquakes range from  $M_L$  -1.5 to 4.2 (Fig. 3.1). The largest historical earthquake in the region occurred near the intersection of the LRZ and GJZ on March 6, 1872 with an estimated magnitude of  $M_w$  5.2 (von Seebach, 1873). Most earthquakes in recent times occur in the southern part of the LRZ, in the NW-Bohemia/Vogtland region, leading to more studies in the southern part compared to the rest. A detailed overview of the various studies conducted in the southern part, has been given by Fischer et al. (2014). Despite the uneven distribution of currently located earthquakes (Fig. 2.4), the seismic hazard near Gera is comparable to that in the NW-Bohemia/Vogtland area (Fig. 1.1). Several strong historical earthquakes have occurred in the vicinity of Gera, including the

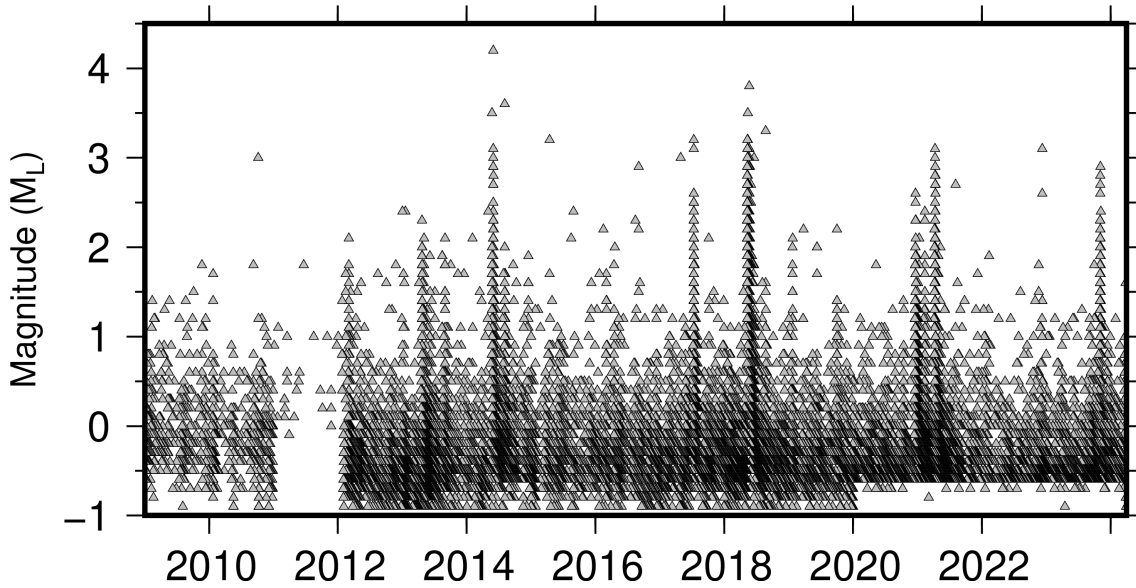


Figure 3.1: Temporal distribution of detected earthquakes from January 2009 to April 2024 (Seismoverbund Mitteldeutschland, 2024).

Central German earthquake of 1872 and an earthquake in 1857 with  $M_w$  4.2 (Leydecker, 2011). Therefore, the area around Gera is seismically endangered for historical reasons.

The majority of earthquakes in the southern region occur at depths between 5 and 15 km, occasionally reaching up to 20 km. As one moves northward, the frequency of earthquakes in the earthquake catalog of the Seismoverbund Mitteldeutschland decreases and the depth increases, resulting in a typical earthquake depth of between 10 and 25 km in the northern portion of the LRZ (Fig. 2.4). The reactivation analysis of pre-existing faults by Švancara et al. (2008) indicates that steep north-northwest-south-southeast to north-south fault structures can be easily reactivated in the NW-Bohemia/Vogtland area. However, faults with an east-northeast-west-southwest orientation (e.g. Eger Graben) have a relatively high resistance, which explains the lack of seismicity along these faults. Similarly, reactivation of northwest-southeast striking faults (e.g., Hercynian fault zone) is also rather unfavorable in the recent stress field (Švancara et al., 2008).

Korn et al. (2008) and Sonnabend (2022) analyzed the focal mechanism of earthquakes along the LRZ. Korn et al. (2008) used P-polarities and P/SV amplitude ratios to determine the fault plane solution, while Sonnabend (2022) employed moment tensor inversion. In both studies, the north-south direction was confirmed in the NW-Bohemia/Vogtland area and along the LRZ. Sonnabend (2022) divide the LRZ into an in-

ner and outer part. The inner part of the LRZ is a 5 to 10 km wide band with north-south striking focal mechanisms. In contrast, in the outer band, earthquakes are primarily active on Hercynian structures with a northwest-southeast strike direction. The existence of the LRZ is therefore considered very probable, even if only a few surface manifestations were found. According to Sonnabend (2022), there is also the possibility that both rupture directions cross each other or that different focal mechanisms are activated at different depths. It is also possible that deep earthquakes on north-south faults could manifest coexisting ruptures in northwest-southeast directions at the surface (Sonnabend, 2022). This stress relief can cause earthquakes or lead to aseismic displacements, which is also referred to as slow-creep and has been postulated for the GJZ outside of the intersection area (Ellenberg, 1992). The seismic stress caused by the north-south displacement at the northwest-southeast structures then discharges in the intersection area, resulting in a greater seismic hazard potential at the intersection area of the Hercynian faults and the LRZ (Sonnabend, 2022).

A distinct feature of the LRZ is the prevalence of earthquake swarm regions (Fischer et al., 2014; Korn et al., 2008). The majority of swarm areas are concentrated in the southern part of the fault zone system. In contrast, the northern part of the LRZ is devoid of earthquake swarms. The northernmost earthquake swarm region is Werdau, located in the central part of the LRZ, and has been the subject of only a few studies (e.g. Hemmann et al., 2003).

The term earthquake swarm was coined by Credner (1876) and describes a specific earthquake sequence. In a classic earthquake sequence, the strongest earthquake, the so-called mainshock, occurs immediately at the beginning of the sequence. This is followed by several weaker aftershocks. In contrast, the strongest earthquake in an earthquake swarm can occur at any time during the swarm. The swarm-like nature of seismic activity in NW-Bohemia/Vogtland has been documented in historical macroseismic reports dating back to 1552 (Grünthal, 1989). During a swarm, over 1000 earthquakes can occur in a very small area within several hours or days. In general, the large number of equally strong earthquakes during a swarm does not exceed magnitude 5.

The periodic occurrence of earthquake swarms along the LRZ is characterised by a significantly higher frequency of earthquake swarms in the south than in the north. In the NW-Bohemia/Vogtland region, nine

earthquake swarms (1997, 2000/2001, 2008, 2011, 2014, 2018, 2020/2021, 2023 and 2024) have been recorded between Nový Kostel and Klingenthal in recent years. A total of five earthquake swarms (1998, 2001, 2010, 2012/13, and 2017) have been recorded for Schöneck in the Vogtland region and three earthquake swarms (1997/98, 2006, and 2016) have been documented for the northernmost region of Werdau (Seismoverbund Mitteldeutschland, 2024). Fluids are believed to be a primary cause of earthquake swarms, yet the precise mechanism of how fluids trigger earthquake swarms remains unclear. One possible explanation could be elastic stress transfer (Fischer et al., 2014). Supercritical fluids enter an existing fault system and relieve the fracture, decreasing the effective normal stress and thus the resistance to slip (Hubbert & Rubey, 1959). The movement results in an earthquake, which in turn opens up new faults, creating new pathways for the fluids to move on and trigger earthquakes again. This cycle can be repeated several times, which could explain the frequency of earthquakes during a swarm. For the earthquake swarms of NW-Bohemia/Vogtland, there are several indications that uprising mantle-derived magmatic fluids (Bräuer et al., 2009; Hofmann et al., 2003; Hrubcová et al., 2017; Mousavi et al., 2015; Špičák & Horálek, 2001; Vlček et al., 2022; Weise et al., 2001) trigger the earthquake swarms on their way to the surface, where they emerge at mofettes (Mousavi et al., 2015). The source of the fluids is believed to be in the asthenosphere (Heuer et al., 2006). Geochemical analyses support the assumption of mantle-derived magmatic fluids, as the emitted mofette gases at the surface contain components from the Earth's mantle (Weinlich et al., 1999). However, the hypothesis that hydrological events are responsible for the onset of earthquake swarms (Heinicke et al., 2017) cannot be proven (Vlček et al., 2022).

Using teleseismic tomography to image the lithosphere and asthenosphere, Plomerová et al. (2007) were able to prove that the area does not contain a mantle plume. The tomography revealed no evidence of a narrow and ascending velocity anomaly, such as can be observed below the Eifel (Ritter et al., 2001). Instead, partial melting in the asthenosphere and at the base of the lithosphere is thought to be responsible for the uprising fluids (Geissler et al., 2005; Heuer et al., 2006). The melting has elevated the lithosphere-asthenosphere boundary to approximately 65 km, while the boundary in the surrounding area lies at a depth of approximately 100 km (Geissler et al., 2010). Consequently, the crust

below NW-Bohemia/Vogtland has been thinned, so that the Moho can already be encountered at a depth of less than 28 km (Geissler et al., 2005; Heuer et al., 2006). However, for the northern earthquake swarm regions, such as Werdau, the fluid source remains unknown. Hemmann et al. (2003) proposes that fluids rise along the LRZ and GJZ intersection and trigger the Werdau earthquake swarms.

### 3.2 Gravimetry

In addition to seismic activity, the Bouger anomaly map also provides indications of a north-south trending zone (Fig. 3.2). The western boundary of the LRZ is marked by gravity maxima anomalies and the east by gravity minima anomalies. Specifically, the southern part of the LRZ is bordered to the east by the Eichigt, Bergen, Kirchberg gravity minimum, as well as the Erzgebirge gravity minimum, which is the largest gravimetric minimum by area and amplitude in the Central European Variscids (Pälchen, 2009). In the west of the southern part lies the Hof gravity maximum, caused by two high-density bodies at depths of 3 to 6 km and 12 to 15 km (Hofmann, 2003). North of Leipzig, the LRZ is bounded to the east by the Delitzsch-Wurzen gravity minimum, resulting from the granodiorites of the Delitzsch plutonite massif, and to the west by the Halle gravity maximum, which is caused by the Halle volcanite complex. The central area of the LRZ is also bounded by the Gera-Borna gravity maximum in the east, caused by the denser rock masses of the pre-Variscan basement. The overall picture shows a north-south orientation which Bram and Hirschmann (1992) interpreted as a deep-seated north-south and east-west striking structure. Using Linsser filtering, Behr et al. (2002) were able to create tomographic images of the Bouguer gravity field at certain depths. In the tomographic images of Behr et al. (2002), east-west striking structures can be detected at depths of 2.5 to 20 km and north-south striking structures in Saxony and eastern Thuringia at a depth of 20 km. The number of north-south striking structures also increases with depth. Švancara et al. (2008) analyzed the same data set and derived the gravity effect of the seismogenic zone confining the top 18 km of the crust. The resulting residual gravity map shows potential stress concentration structures that can cause seismicity, if they lie within the existing zones of weakness. During their investigation, three dominant strike directions were identified in the study area: northwest-southeast (Hercynian), north-

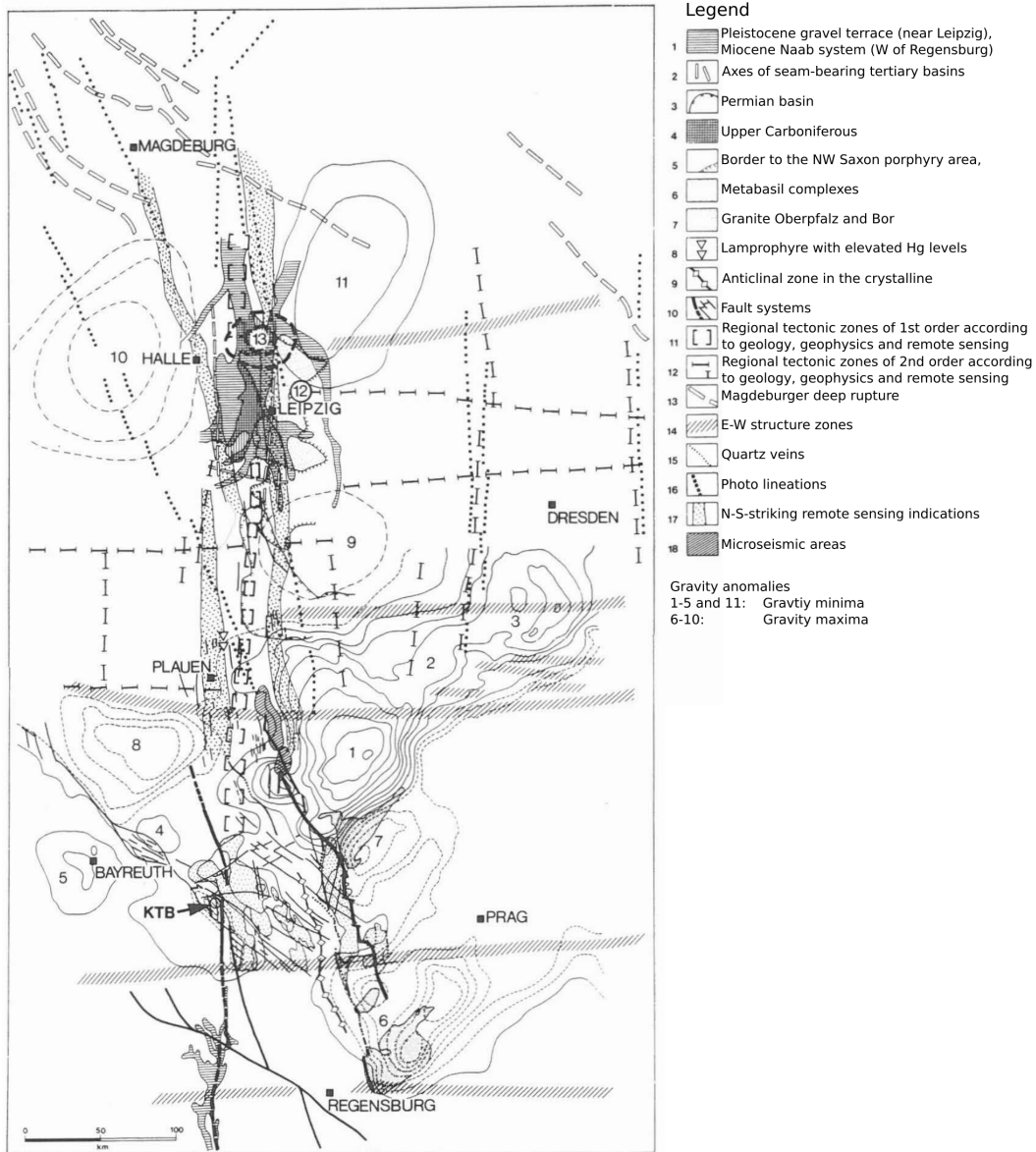


Figure 3.2: Gravity anomalies and selected structural elements of the LRZ (after Bram & Hirschmann, 1992).

northeast-south-southwest (Rhenish) and east-northeast-west-southwest (Erzgebirge). The north-south striking structure, interpreted by Bram and Hirschmann (1992), manifested itself in the results as a consistent anomaly. As a potential explanation, Švancara et al. (2008) state that the north-south striking structure is either not a deep-seated structure or, more likely, may not be accompanied by a significant density contrast.

### 3.3 Seismics

Active seismic measurement campaigns were carried out in the study area to investigate the deep crustal structures in the Saxothuringian and NW-Bohemia regions (Fig. 3.3). One of the first profiles to cross the study area was EV01, which was initially recorded in 1976 between Vogtland and Olbernhau and later extended in 1978 to EV02. The DEKORP3/MVE-90 East profile was recorded 1990 between Untersteinach and Bautzen as part of the DEKORP project. The objective of the project was to investigate the deep crustal structure of Germany. Between 1991 and 1993, the 9Hr profile was recorded between Klingenthal and Prachatice in the Czech Republic. In 1995, two additional profiles were recorded: GRANU95A, from Leipzig to Olbernhau and GRANU95B between Bamberg and Großenhain. The aim of these profiles was to correlate the near-surface geology and the deep structures. In 2000, the CELEBRATION2000 project was carried out with several seismic profiles to investigate the structural and tectonic evolution of the crust and upper mantle. The following section presents the results of the different surveys that fall within the boundaries of the study area.

#### 3.3.1 EV01 and EV02

The EV01 and EV02 profile (Fig. 3.4) traverse the Vogtland Synclinal Zone, the Erzgebirgs Anticline and the Lausitzer Scholle. The seismic profile interpretation was conducted by Conrad et al. (1994). Different velocities and densities were determined at different depths, whereby the velocity values in the depth range from 18 to 20 km and below 28 km remain constant due to continuous discontinuities. The Moho is not clearly visible, but appears to be interrupted by several faults (Conrad et al., 1994).

#### 3.3.2 DEKORP3/MVE-90 East

The DEKORP (Deutsches Kontinentales Reflexionsseismisches Programm) was designed to investigate the deep structures of Germany. The MVE-90 section (Münchberg Massif-Vogtland-Erzgebirge) of the DEKORP3 profile is a 390 km long seismic profile that runs parallel to the southern boundary of the Saxothuringian. The location is roughly the same as EV01 and EV02 and should traverse all Hercynian structures in central Germany. The profile passes the Münchberg gneiss mas-

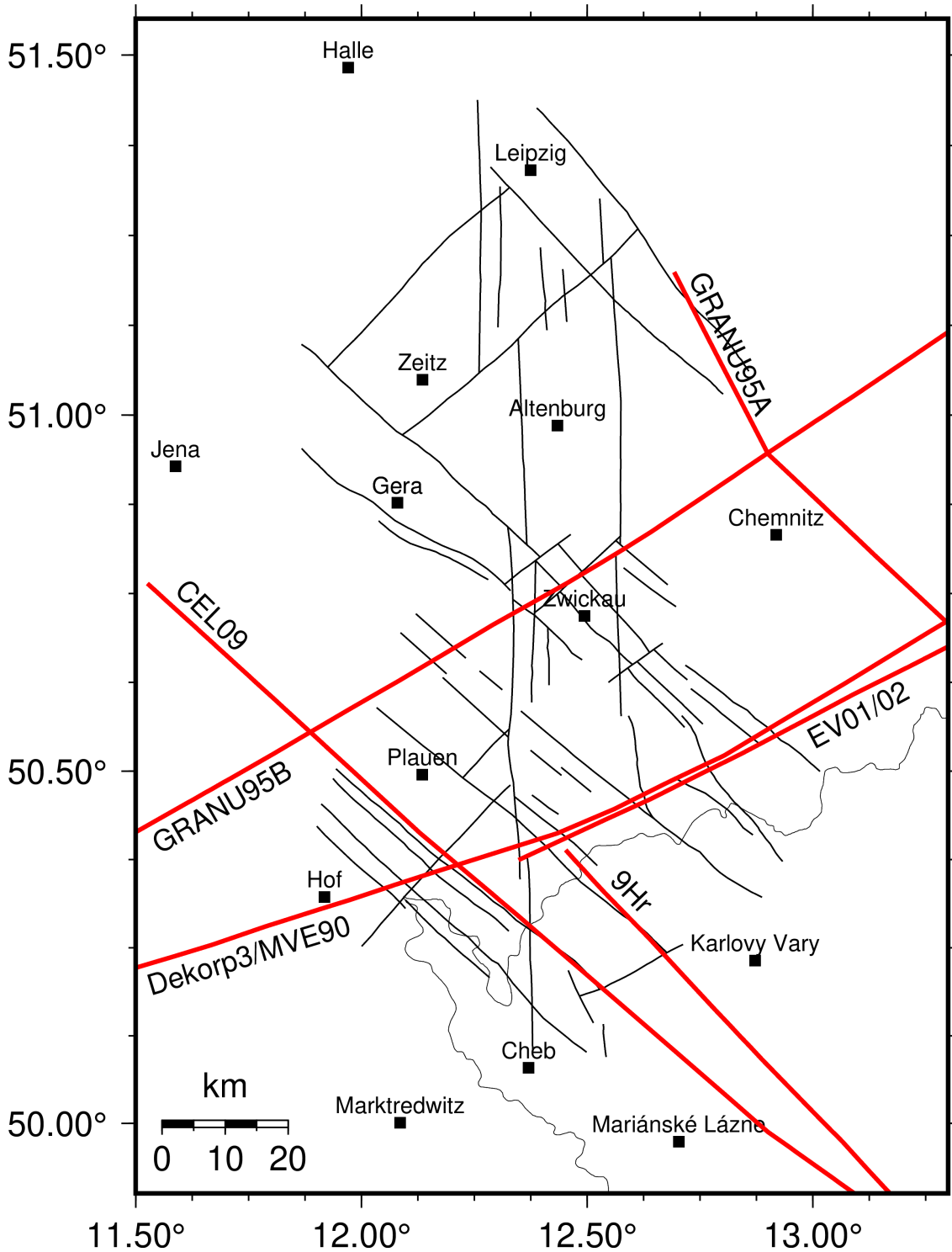


Figure 3.3: Overview map with the faults (black lines) and existing seismic profiles (red lines) in the study area.

sif, the Vogtland syncline zone, and the Erzgebirge. In the LRZ area, a bow-like structure can be observed in the reflection seismic evaluation near the surface up to 2.5 s TWT (approximately 8 km), which can be attributed to the Vogtland syncline. The majority of structures

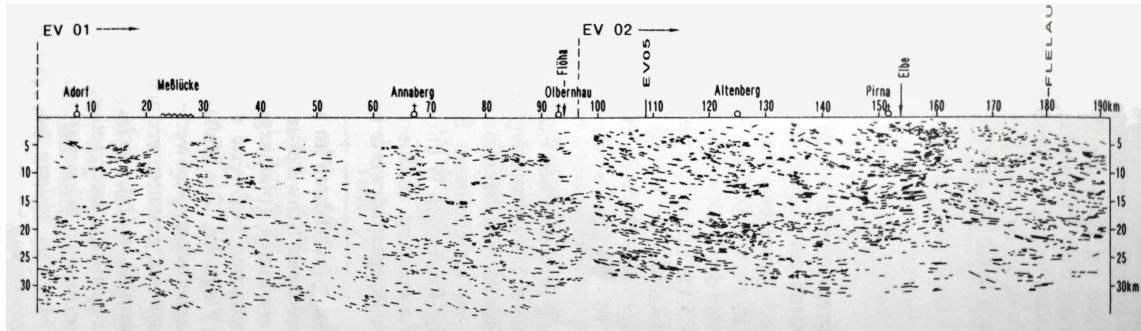


Figure 3.4: Deep seismic regional profile EV: Selected reflection elements (Conrad et al., 1994).

in the profile dip to the west, with some exceptions. An east dipping deep fault was identified between profile kilometers 260 and 280 km. Between 2.5 and 6 s TWT (approximately 8 to 18 km), the middle crust is characterized by lens-like structures with a long axis between 20 and 50 kilometers (DEKORP Research Group, 1994). The lower part of the middle crust is characterized by a weakly reflecting zone with reflectors dipping to the southwest. Between 8 s (approximately 24 km) and the Moho, the lower crust is distinguished by sub-horizontal to flat reflectors. The Moho reflection is located in the profile between 28 and 30 km. A reprocessing of the profile (Fig. 3.5) was conducted by Bleibinhaus et al. (2003). In the study, the central area between profile kilometers 270 and 290 was examined in greater detail. The study proposed the potential continuation of the Mariánské Lázně fault zone with a dip of  $57^\circ$  to the west. The highly reflective layers near the surface, which were already known, are also clearly visible in Bleibinhaus et al. (2003) at a depth of 10 km. Further reprocessing was conducted by Schimschal (2013) using Fresnel volume migration. With a thickness of 10 km, the synclinorium exhibits clear reflections in the near-surface area, thereby confirming the fundamental dip of the geological units to the west. In the central area of the analyzed profile, highly reflective units are visible at a depth of approximately 15 km. In the easternmost extent of these highly reflective layers, between 15 and 25 km, and in the westernmost extent between 8 and 13 km, the reflectivity of the crust is diminished. A pronounced Moho updoming is also visible in the profile, which is not as clearly evident in the original evaluation.

### 3.3.3 9Hr

The 9Hr profile (Tomek et al., 1997) is an approximately 200 km long seismic profile between Klingenthal and Prachatice in southern Bo-

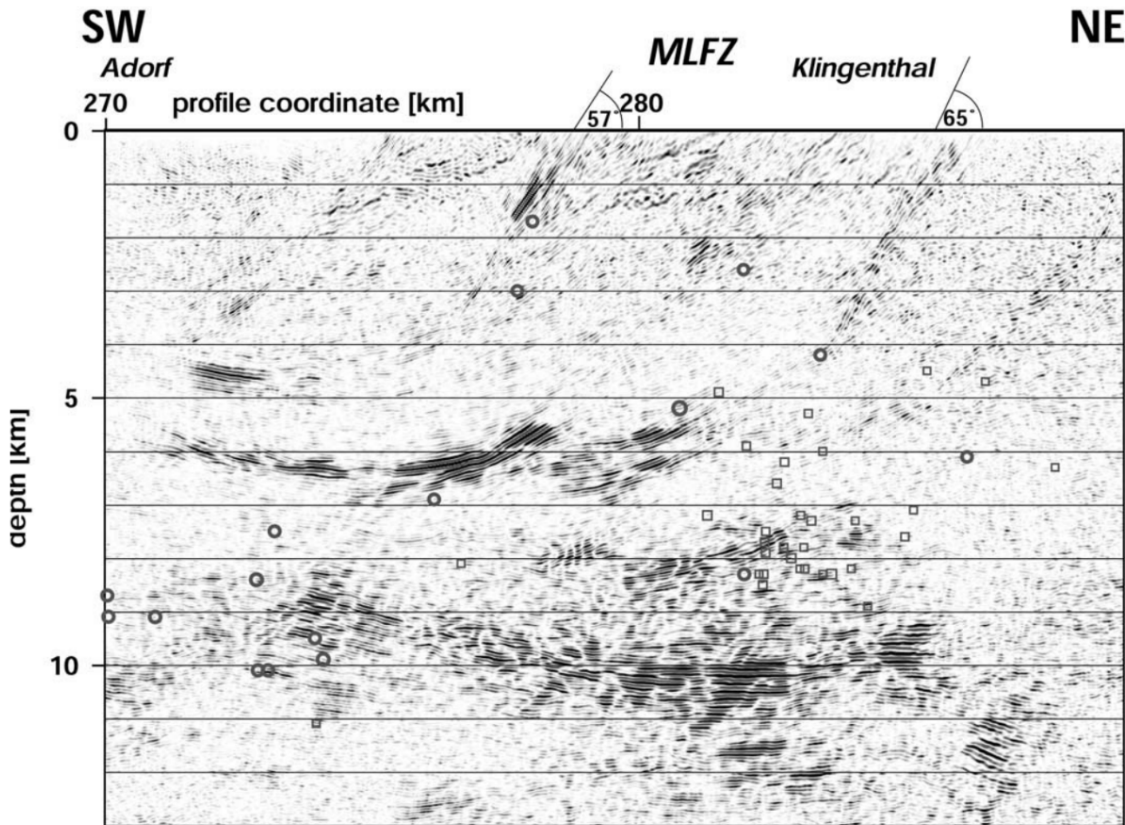


Figure 3.5: Reflection seismic profile DEKORP3/MVE90 reprocessed by Bleibinhaus et al. (2003).

hemia. The profile crosses the Saxothuringian, Teplá-Barrandian, and Moldanubian. The goal of the seismic survey campaign was to image the internal structures of the Bohemian Massif (Fig. 3.6). Alongside the seismic exploration, additional geophysical and geological investigations were carried out in the West Bohemian region, which are summarized in Vrána and Štědrá (1998). Within the Saxothuringian area, reflection structures in the seismogram indicate a delaminated lower and middle crust (Vrána & Štědrá, 1998). Furthermore, information on the possible location of basalt intrusions in the area of the crust-mantle boundary could be identified as a deep manifestation of volcanic activity during the Tertiary (Vrána & Štědrá, 1998). Also, a system of horizontal reflections at a depth of approximately 10 km was identified in the northern part of the profile. Tomek et al. (1997) interpreted this as the primary overthrust of the Variscan orogen in western Bohemia. Above the faults are allochthonous units of the Saxothuringian and rocks of the Mariánské Lázně Complex (Tomek et al., 1997).

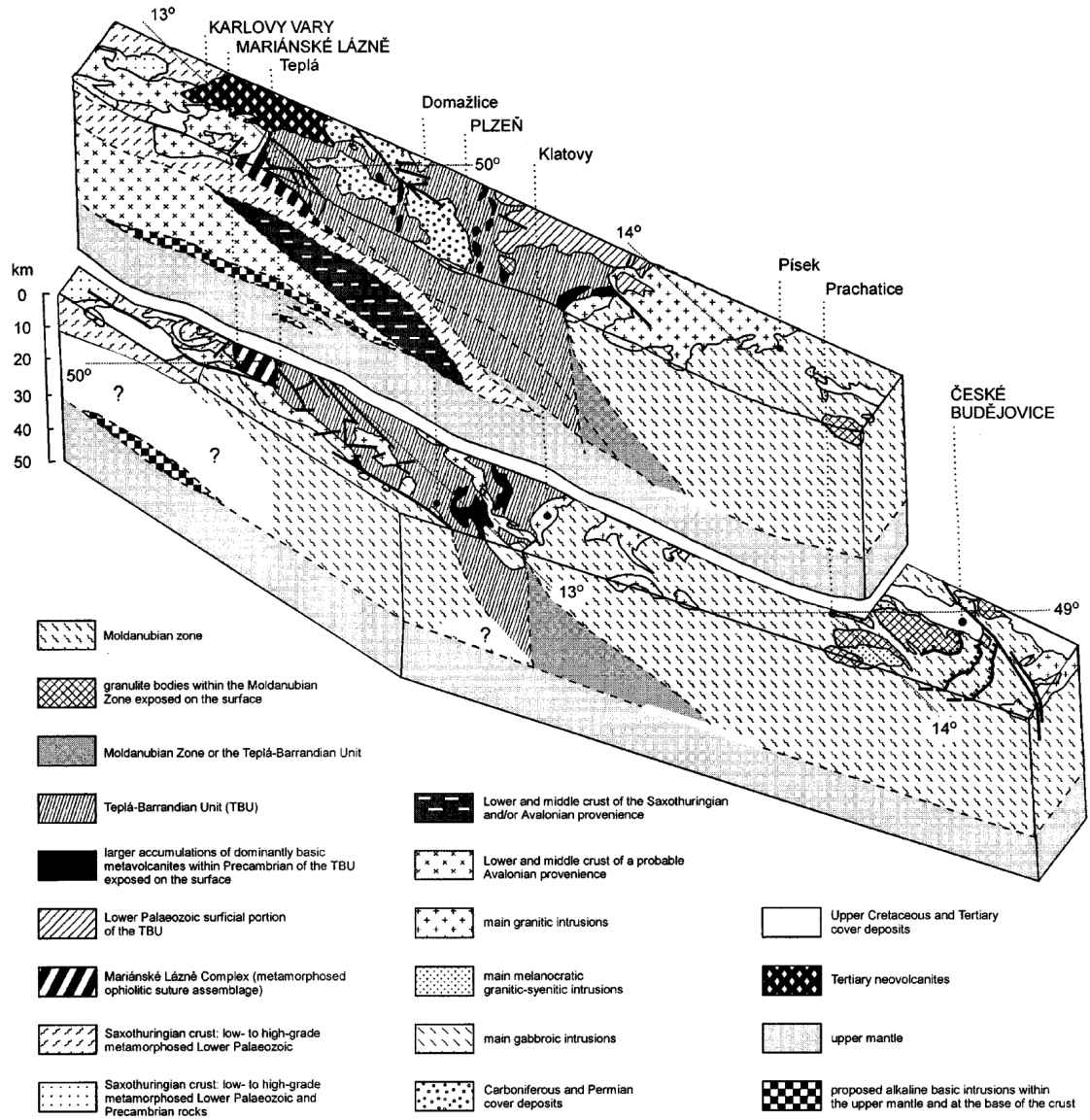


Figure 3.6: Geological model of the 9Hr profile (Vrána & Štědrá, 1998).

### 3.3.4 GRANU95

The GRANU95 project aimed to answer questions about the tectonic structure and geodynamic evolution of the eastern Saxothuringian region. The investigation focused on the deep structures beneath the Saxonian granulite mountains, with a particular focus on their origin. Additionally, the project aimed to correlate the near-surface geology with the deep structures and to elucidate the southwest extension of the Saxothuringian and its relationship to the Münchberg gneiss mass. Two seismic profiles were recorded: one stretching from Leipzig to Olbernaue, covering a length of 90 km (95A) and the other from Bamberg to Großenhain with a length of 260 km (95B). The evaluation and interpretation of these profiles was carried out by Enderle et al. (1998). A 2-D velocity model was employed to divide the crust into four layers (Fig. 3.7): upper, middle, and lower crust, with a further subdivision of the

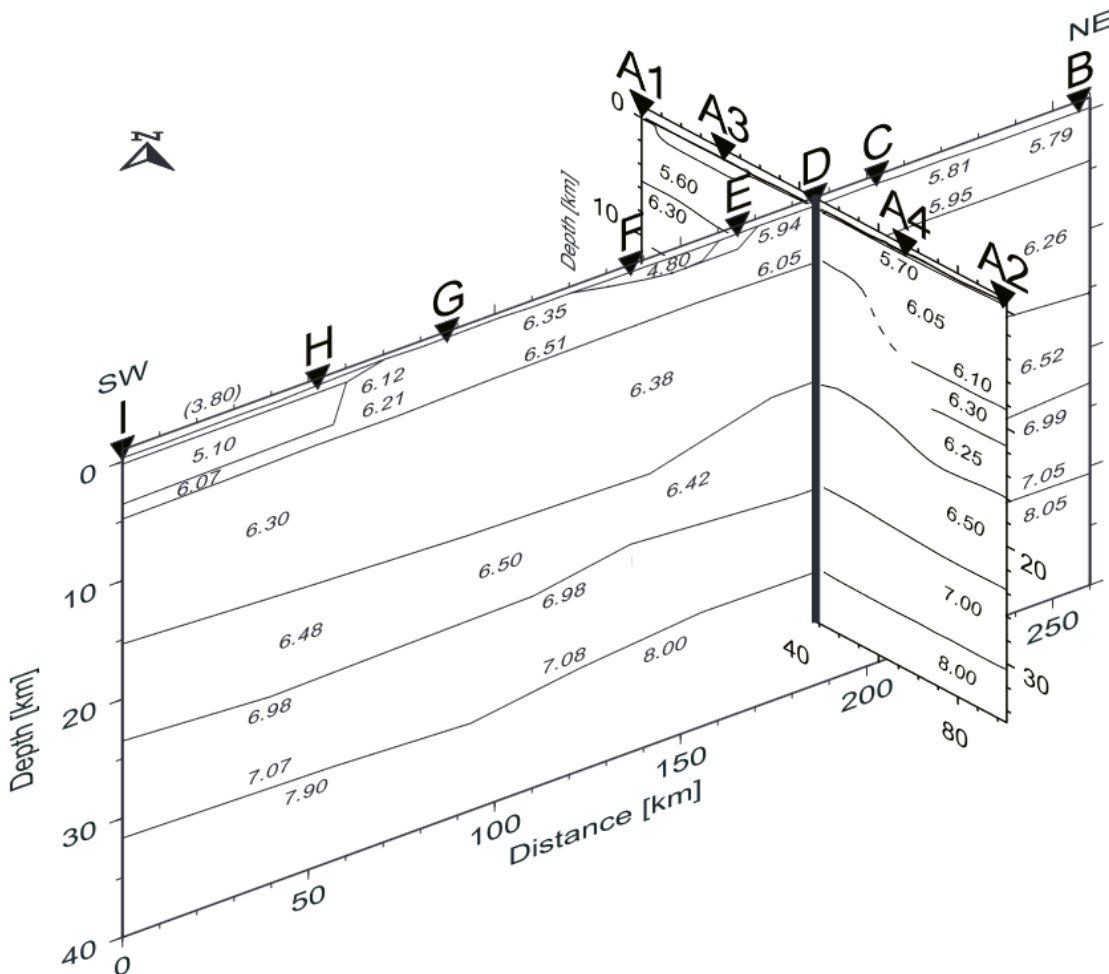


Figure 3.7: Pseudo 3-D illustration of the P-wave velocity along the Granu95A and Granu95B profile (Enderle, 1998).

lower crust. The upper crust is composed of well-known sedimentary basins with low velocities (approximately 5 km/s) and the crystalline basement (approximately 6 km/s), with thicknesses of approximately 5 and 2 km, respectively. The middle crust has velocities ranging from 6.2 to 6.4 km/s. This layer is in line with the Variscan strike direction (southwest-northeast) to an average depth of 15 km and extends perpendicular to the Variscan strike direction (northwest-southeast) to a depth of 11-16 km (dipping to the southeast). Overall, the middle crust is only weakly reflective. The upper part of the lower crust (22 to 24 km), is also weakly reflective, with velocities of 6.4 to 6.6 km/s. The lower part of the lower crust, however, shows increased velocities (7 km/s). According to Enderle et al. (1998), the increased velocity can be explained by the intercalation of mafic granulites. The Moho along the profile is located at a depth between 30 and 32 km and does not show any significant uplift.

### 3.3.5 CEL09

The CELEBRATION2000 project (Central European Lithospheric Experiment Based on Refraction 2000) was designed to investigate the major tectonic features and deep lithospheric structure in the Trans-European Suture Zone, southern Baltica, Carpathian Mountains, Pannonian basin, and Bohemian Massif. The refraction and wide-angle reflection CEL09 profile, with a length of 450 km, is part of the CELEBRATION 2000 experiment. It crosses the entire Bohemian Massif in a north-south direction, starting in the Saxothuringian. Hrubcová et al. (2005) analyzed the data (Fig. 3.8). The initial 6 km of the crust in the area of the Saxothuringian exhibited a high-velocity gradient. The velocities determined are consistent with the near-surface Carboniferous flysch as reported by Hrubcová et al. (2005). Subsequently, the velocity gradient is minimal up to a depth of approximately 13 km. The CEL09 profile also crosses the NW-Bohemia earthquake swarm region. The hypocenters of the earthquakes are located in the upper and middle crustal regions and exhibit low velocities (5.9 km/s). Hrubcová et al. (2005) suggested that the low velocity of the crust in this area is due to fluids released by ongoing magmatic activity and/or fracturing of the crust. Similar to the DEKORP3/MVE-90 profile and Granu95 profiles, highly reflective layers above the Moho are visible in the lower crust between 26 and 35 km depth in the area of the Saxothuringian

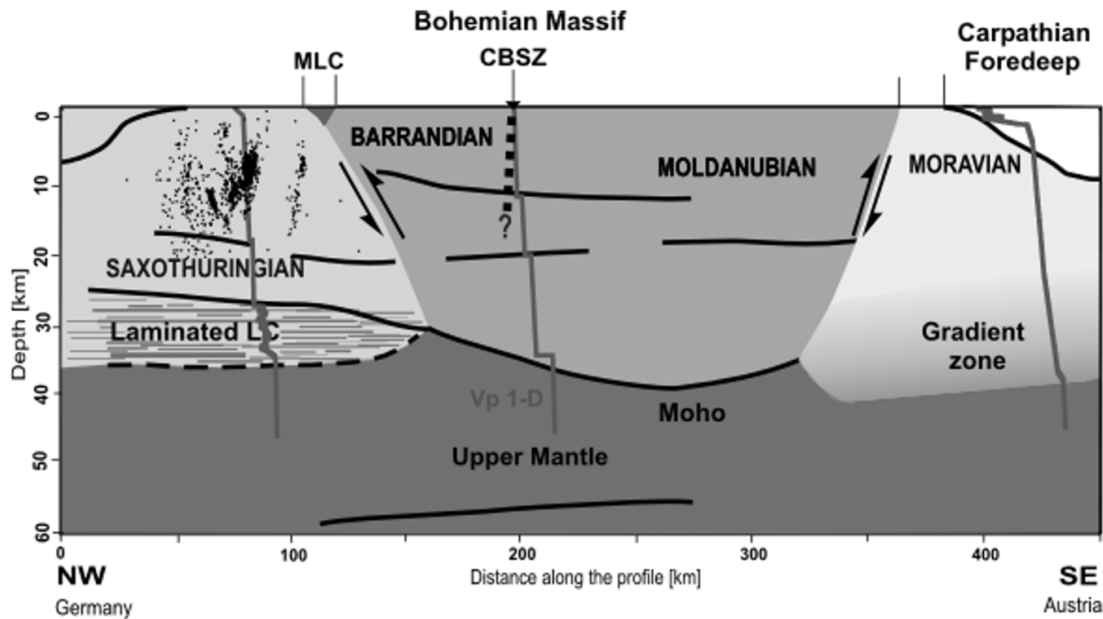


Figure 3.8: Tectonic interpretation of the CEL09 profile (Hrubcová et al., 2005). The hypocenters of the earthquake swarms in NW-Bohemia/Vogtland are shown as dots.

of the CEL09 profile. Additionally, the layers exhibit a pronounced velocity contrast at the upper boundary of the lower crustal layer. The Moho is represented by a narrow, 1 km wide zone of rapid velocity increase between 34 and 35 km depth, as observed by Hrubcová et al. (2005). This depth is somewhat deeper than that of the Granu95 and DEKORP3/MVE-90 profiles (30 and 33 km, respectively).

In summary, the seismic profiles shows a complex crustal structure with several common characteristics. The initial few kilometers of the crust are characterized by near-surface geology, such as sedimentary basins or the crystalline basement. In the middle crust, structures dipping to the southwest can be observed, but in the area of the LRZ east-dipping structures are also visible. In the lower crust, above the Moho, strongly reflective layers are visible in almost all profiles. These layers are interpreted as mafic intrusions, possibly stretched and arranged horizontally during post-orogenic extension. The Moho itself lies at a depth of between 28 and 35 km, depending on the profile.

## 4 | Methods

Three different methods were used to investigate earthquakes and the subsurface. Two of them are based on evaluating seismic velocity, while one is based on evaluating seismic attenuation. The methods used are only briefly explained below; a more detailed description can be found in the publications.

### 4.1 Travelttime tomography

The term tomography is derived from the Greek words *tomos* (slice, section) and *grapho* (to write). The method is an imaging procedure that enables the visualization of an object in layers using a penetrating wave (Fig. 4.1). Different types of waves enable a wide range of possible applications. One of the earliest applications of tomography was in medicine, specifically in the form of X-ray computed tomography and magnetic resonance tomography in the mid-1950s. By combining 2-D slices, a 3-D image of the human body could be created (e.g. Hounsfield, 1973). In the present era, tomography is a routine procedure for imaging internal structures like the human body for diagnostic purposes in medicine, for testing the integrity of materials, and for imaging the subsurface of the earth. A comprehensive introduction to seismological tomography and detailed descriptions can be found in e.g. Iyer and Hirahara (1993); Kissling (1988); Nolet (1987); Spakman et al. (1988). Various methods have been created utilizing either teleseismic events or local earthquakes, but they all rely on the same tomography principle (Fig. 4.1). For this thesis, only local earthquakes have been used for tomography.

Travelttime tomography is based on measuring the time it takes for a seismic wave to travel from an earthquake in the subsurface to a seismic station at the surface. As the wave propagates through the subsurface, it encounters different materials with different properties, such as seismic velocity. Because a wave can be viewed as a ray, the velocity can be determined using the travelttime and distance. Then, the velocity can be distributed along the ray's path. With a large number of rays and travelttimes, tomography can be conducted to image the subsurface. The seismic velocity at a location in the model corresponds to the average velocity over all ray path segments contributing to the solution at that location, with direction and weighting taken into account (Haslinger,

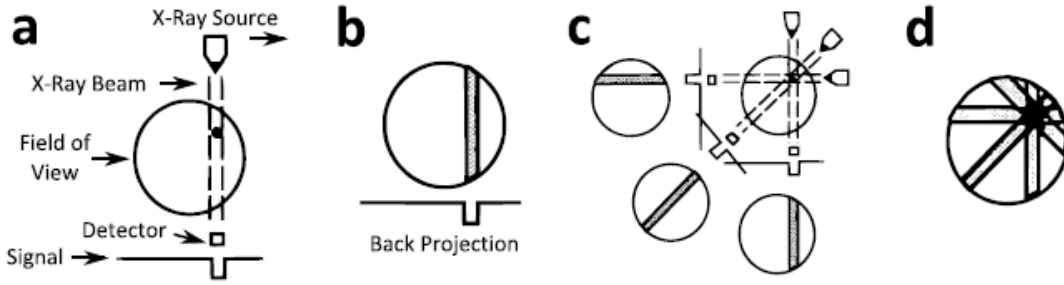


Figure 4.1: Tomography illustrated by the example of computed tomography after Stewart (1991). (a) Geometry of the CT with an X-ray source and detector position. The source generates a beam that propagates through a sample and is detected by the detector. (b) The absorption of the X-ray results in the measured amplitude along the beam path and is thus distributed on the measured distance (gray area). (c) By varying the acquisition geometry, different running paths of X-rays and thus a variety of information of the absorption within the body is obtained. (d) Superposition of different acquisition geometries results in an increase of sensitivity for the overlapping region (black) and therefore enables with adequate measurements to create an image of the interior of the sample.

1998). The spatial distribution can then be used to infer structures or the composition of the subsurface. Essentially, the creation of a velocity model consists of two steps: forward modeling to generate synthetic data from a velocity model, and inversion to fit synthetic data to observed data and adjust the subsurface model based on the differences.

#### 4.1.1 Inversion

For the traveltime tomography, the code SIMULPS (Eberhart-Phillips, 1993; Thurber, 1983, 1993) was used. The code has been continuously developed over time (e.g. Eberhart-Phillips, 1986; Rietbrock, 2001) and allows the use of P- and S-traveltimes to perform the iterative and simulated inversion for 3-D velocity structures and hypocenter parameters using parameter separation and a 3-D ray tracer.

The arrival time of a seismic wave emitted by an earthquake can be described by the equation:

$$T = t_0 + t_s(x_1^0, x_2^0, x_3^0, v(s), x_1, x_2, x_3) \quad (4.1)$$

with  $t_0$  the origin time of the earthquake,  $t_s$  the traveltime of the seismic wave along the path  $s$  from the source  $(x_1^0, x_2^0, x_3^0)$  to the seismic station  $(x_1, x_2, x_3)$  and the velocity  $v(s)$  along the path  $s$ . The traveltime  $T$  is non-linear, as the four hypocenter parameters  $(t_0, x_1^0, x_2^0, x_3^0)$  cannot normally be represented as a linear combination of four independent functions, each of which in turn depends on only one hypocenter pa-

parameter. The traveltime difference between an observed phase  $T_{obs}$  and a synthetically calculated phase  $T_{syn}$  can be calculated as follows:

$$\Delta T = T_{obs} - T_{syn} \quad (4.2)$$

where for  $T_{syn}$  the hypocenter parameters  $(t_0, x_1^0, x_2^0, x_3^0)$  are estimated from the earthquake location and the path  $s$  resulting from the forward ray tracing of a given velocity model. The goal is to minimize the difference  $\Delta T$  by modifying the velocity model so that the synthetic traveltimes  $T_{syn}$  correspond to the observed traveltime  $T_{obs}$ .

The non-linear problem can be written as:

$$g_{fwd}(m) = d \quad (4.3)$$

Here  $m$  contains both the velocity parameters of the model and the hypocenter parameters of all earthquakes, whereby all parameters of  $m$  are basically unknown. The data vector  $d$  contains all traveltimes and  $g_{fwd}$  is a function describing the relationship between  $m$  and  $d$ . The function  $g_{fwd}$  is non-linear because the ray path and thus the travel-time depend on the velocity model. Taylor expansion results in a linear relationship between traveltime residuals and model parameters:

$$\Delta T \equiv \Delta t_0 + \sum_{k=1}^3 \frac{\partial t_s}{\partial x_k^0} \Delta x_k^0 + \sum_{l=1}^L \frac{\partial t_s}{\partial v_l} \Delta v_l \quad (4.4)$$

with  $L$  discrete model parameters. The partial terms are calculated via forward modeling and  $\Delta x_k^0$  and  $\Delta v_l$  are the parameters that are searched for by model fitting. The equation 4.3 can be rewritten in matrix notation with many observations:

$$\Delta \mathbf{d} \equiv \mathbf{J} \Delta \mathbf{m} \quad (4.5)$$

with  $\Delta \mathbf{d}$  the vector of traveltime residuals,  $\mathbf{J}$  the Jacobian matrix containing all partial derivatives and  $\Delta \mathbf{m}$  the vector of model corrections. The non-linear problem is solved iteratively using a least-squares inversion, as the ray paths and travel times change when the velocity model is modified. Additionally, a damping factor  $\lambda$  is often used for the mixed-deterministic problem to provide further constraints on the model parameters, thereby reducing the non-uniqueness of the solution:

$$\Delta \mathbf{m} = (\mathbf{J}^T \mathbf{J} + \lambda \mathbf{I}_n)^{-1} \mathbf{J}^T \Delta \mathbf{d} \quad (4.6)$$

with  $\mathbf{I}_n$  the identity matrix.

### 4.1.2 Forward modeling

Forward modeling can be used to calculate synthetic traveltimes for a given velocity model. A simple method for calculating traveltimes is ray theory. Ray theory is a high-frequency approximation of the equation of motion and is only valid when the seismic wavelength is much smaller than the scale length of the velocity structure. Forward modeling is the most time-consuming part of tomography, but the resolution of tomography depends largely on forward modeling (Zhang & Toksöz, 1998). More specifically, it depends on the accuracy of the calculation of the ray path and the calculation of the traveltimes. The scalar equation of wave propagation in an isotropic heterogeneous medium can be expressed as:

$$\Delta^2 \Phi(x, t) = \frac{1}{v(x)^2} \frac{\partial^2 \Phi(x, t)}{\partial t^2} \quad (4.7)$$

with  $\Phi(x, t)$  the scalar wave field,  $t$  the time and  $v(x)$  the 3-D velocity model. For high frequencies, a harmonic solution is obtained with the above equation:

$$\Phi(x, t) = A(x) \exp(i\omega(t - T(x))) \quad (4.8)$$

with  $A(x)$  the amplitude and  $\omega$  the circular frequency. Using the solution 4.8 in 4.7 results in the eikonal equation:

$$\Delta^2 T(x) = u^2 = \frac{1}{v^2} \quad (4.9)$$

with  $u$  the slowness. The wavefronts can be calculated with  $T(x) = \text{const}$ . The ray paths result as normals to the wavefront pointing in the direction of propagation. With the parameterization  $x = x(s)$  with  $s$  the arc length along the ray, the eikonal equation can be rewritten to the ray equation:

$$\frac{d}{ds} \left( \frac{1}{v} \frac{dx}{ds} \right) = \Delta \frac{1}{v} \quad (4.10)$$

The ray equation can be solved numerically and the solution results in a ray path. Integrating over the ray path results in the traveltime.

In SIMULPS ray paths are calculated in two steps. The first step, the approximate ray tracing (ART) method (Thurber, 1983), is a rough approximation and is used to define the initial condition for the second, more time consuming step. The simplicity of the ART method

allows for quick and discrete sampling of the solution space, preventing it from converging to a local minimum. In the ART method, ray paths are computed as circular arcs. This is achieved by forming an initial ray path assuming a constant velocity gradient perpendicular to the source-receiver connection. Further ray paths can then be calculated by multiplicatively stretching the initial ray path. The set of paths or arcs created in this way are all in one plane, and are then additionally rotated around the source-receiver axis so that all paths in a 3-D space are covered as far as possible. The fastest path is then selected from all these arcs and improved in the second step. The second step consists of the pseudo-bending of Um and Thurber (1987), which can be derived from Fermat's principle: The curvature of a ray is proportional to the component of the local gradient perpendicular to the ray tangent. For the pseudo-bending method, the center of three neighboring ray points is numerically shifted so that a circular arc through the points has a given radius of curvature. The points must be close enough so that the velocity gradient in that region can be considered constant to a first approximation. This is done sequentially for all inner ray points of a ray. However, adjusting the following points will also change the boundary condition of the previously calculated points. This necessitates an iterative process, which continues until a certain number of iterations is reached or the runtime along a new ray path does not change significantly.

## 4.2 Receiver functions

Receiver function (RF) is a time series that can be calculated from seismograms to visualize velocity discontinuities, allowing the study of crust and mantle structures (e.g. Bostock et al., 2002; Kind et al., 2002). The RF method images velocity discontinuities by taking advantage of reflections and transmissions at layer boundaries (Fig. 4.2), as well as conversions to the complementary body wave types (P-to-S or S-to-P). Teleseismic data is used to calculate receiver functions since stations and earthquakes are far apart. As a result, the teleseismic wave has to travel long distances and arrives from a great depth below the station, ensuring the far-field assumption of a plane wave. For P-waves, earthquakes between  $30^\circ$  and  $90^\circ$  can be used, while for S-waves the distance must be between  $55^\circ$  and  $85^\circ$ , as the S-to-P conversion at the Moho only occurs for events with a distance greater than  $55^\circ$ . At larger distances ( $>90^\circ$ ), the wave field becomes more complicated as it interacts with

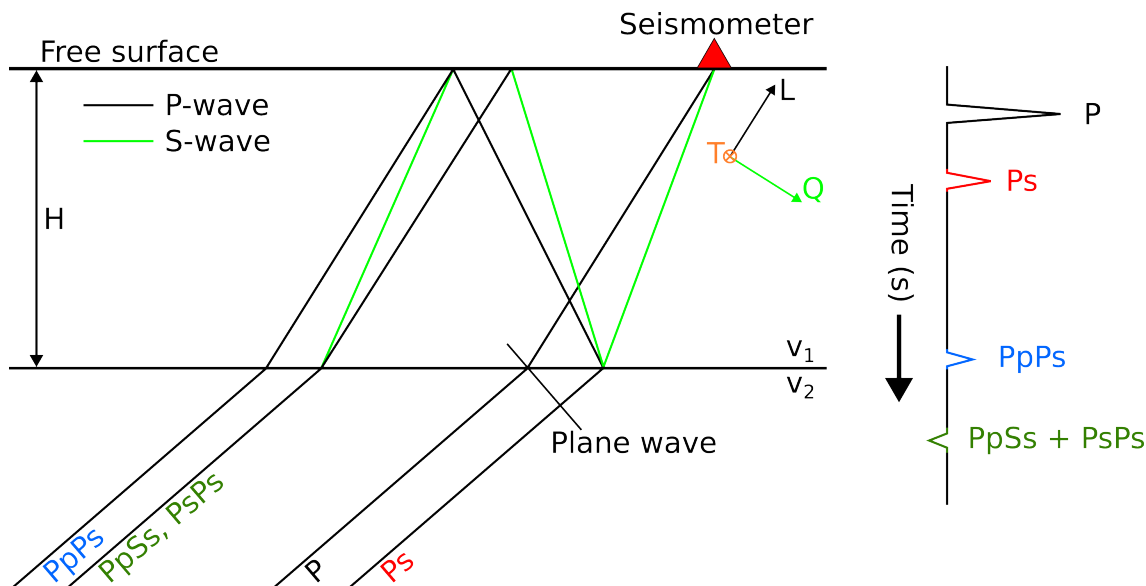


Figure 4.2: In a layered half-space model with thickness  $H$ , the incoming teleseismic P-wave is converted to S-wave at the layer boundary. On the left is a simplified Q-component receiver function corresponding to the two-layer model. Major phases are labeled.

the core-mantle boundary at these distances.

RFs are defined to produce positive amplitudes when the velocity in the layer above the discontinuity is slower than the velocity in the layer below (e.g. Moho). Conversely, negative amplitudes occur when the slower layer is below the discontinuity and the faster layer is above, such as at the lithosphere-asthenosphere boundary. All three components of a seismometer are used to calculate the RFs, because both P- and S-waves are important. The RFs utilize the principle that S-wave velocity is smaller than P-wave velocity, resulting in the converted S-wave arriving later at the seismometer. To identify the converted phase and the corresponding primary phase, the P- and S-waves must first be separated. This is achieved through a rotation in the LQT system requiring only the incidence angle and back azimuth for each event separately. Theoretical angles can be assumed, which can be calculated directly from the data using event and receiver locations and a global Earth model like IASP91 (Kennett & Engdahl, 1991). The newly obtained components register the longitudinal (L) and vertical wave (Q) particle motion.

After separating the primary and converted phases, the next step is to determine the arrival time of the converted phase. The relative time difference between, for instance, the P-wave and the converted S-wave contains information about the depth of the boundary layer as well as the P- and S-wave velocity. To identify the arrival time, the time se-

ries of the converted phase is compared to the signature of the primary phase. In the case of P-RF, the P-to-S converted wave is identified on the Q-component by deconvoluting the P-wave characteristics recorded on the L-component from the signal. The source time function of the L-component is used to determine the inverse, which is folded to both, the L- and Q-component. Ideally, the waveform should produce a spike on the L-component. On the Q-component, the P-to-S converted phase has the same waveform as the P-wave on the L-component, but with a smaller amplitude and a time shift that depends on the depth of the discontinuity. All P-wave signatures on the Q-component can be converted to spikes by applying  $L^{-1}$ , resulting in positive and negative spikes based on the velocity contrast. Summing records from different source regions at a station can improve the RFs (Kumar et al., 2010), since the amplitudes caused by different source regions interfere destructively, while the receiver-side signals are the same for all events and interfere constructively. To determine the depth of the discontinuity, the arrival time of the converted P-to-S wave on the Q-component is calculated relative to the arrival time of the main phase on the L-component. A velocity model can then be used to convert time to depth.

### 4.3 Seismic attenuation

A wave generated by an earthquake propagates through the subsurface and interacts with the medium as it travels. The wave can be reflected or transmitted through layer boundaries, waves can be converted or the wave is attenuated by the medium as it propagates. The attenuation characteristics of the subsurface can be determined by analyzing the waveform of the first arrival and the coda (Fig. 4.3). The coda is the part of the seismogram that follows the direct body wave (P- or S-wave). For simplicity, the acoustic case of the S-wave is discussed below. The S-wave coda is easier to identify, because it is free of other body waves and the proportion of the converted wave (S-to-P) is less than 1/10 of the coda (Aki & Chouet, 1975; Sato et al., 2012). The main factors that cause the coda to decay over time are absorption, scattering and geometric spreading. Absorption or intrinsic attenuation describes the conversion of seismic energy into heat or other forms of energy by anelastic processes such as friction. On the other hand, scattering attenuation describes the scattering of energy of a wave field in different phases due to material changes such as layer boundaries or small-scale

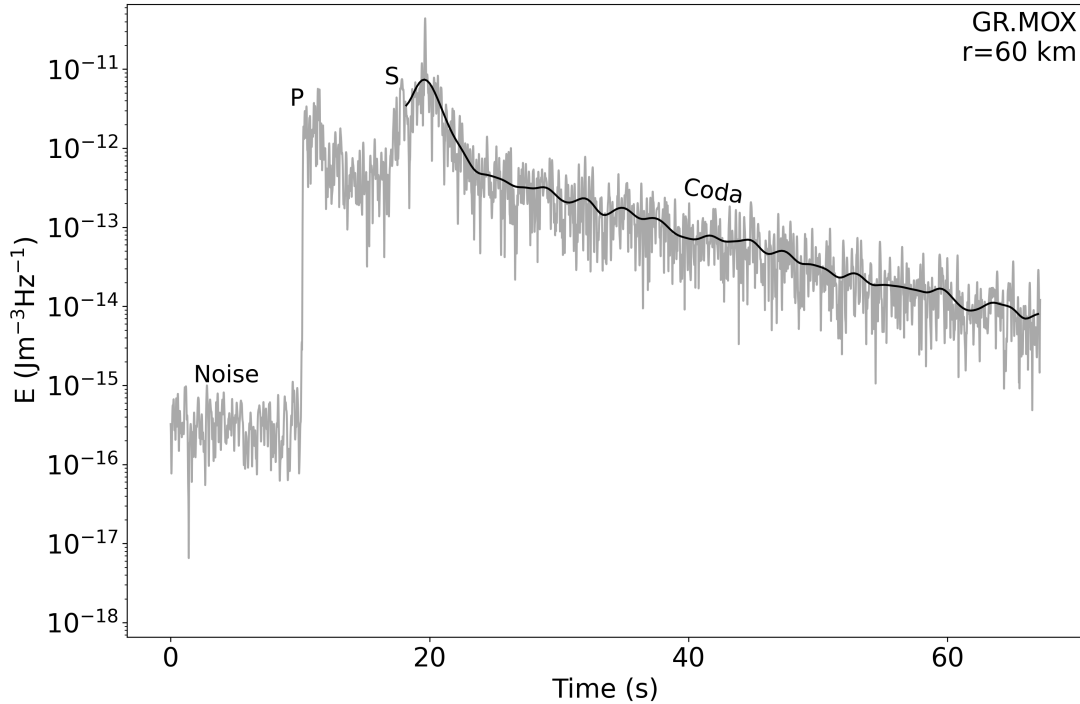


Figure 4.3: Observed envelope (gray line) and smoothed envelope (black line) of the spectral energy density of the station MOX in the frequency range 11 - 22 Hz for a  $M_L$  1.8 earthquake at a distance of 60 km. The P- and S-wave arrivals are marked with P and S, respectively. Before the arrival of the P-wave the station records noise and after the arrival of the S-wave the recorded incoming earthquake waves are called coda.

3-D heterogeneities, causing the seismic wave to change direction. The average distance at which a particle is scattered can be described by the inverse total scattering coefficient  $1/g_0$ . In cases of multiple scattering, the wave can lose its initial direction and can travel in a completely different direction. The average distance for this phenomenon can be expressed by the inverse transport scattering coefficient  $1/g^*$ . Assuming isotropic scattering, the total scattering coefficient  $g_0$  equals the transport scattering coefficient  $g^*$ . Abubakirov and Gusev (1990) showed that seismic waves in the Earth are not scattered isotropically, but anisotropically. In the case of isotropic scattering, the change of direction after a scattering process is equally likely in all directions, whereas in the case of anisotropic scattering, the probability that the wave is scattered in the approximate direction of initial propagation is greater.

However, deterministic methods of wave propagation are insufficient to explain scattering processes, necessitating the use of stochastic methods to describe wave propagation. Scattering occurs in particular when waves interact with structures of the same size as their wavelength, mak-

ing it impossible to resolve the heterogeneities themselves. The scattering coefficient as a function of frequency follows a power-law, indicating that frequency-dependent scattering either remains constant or increases as frequency increases.

A suitable method for determining both intrinsic and scattering attenuation is the radiative transfer theory (RTT), originally developed for astrophysics to describe the propagation of light through the scattering atmosphere (Chandrasekhar, 1960; Schuster, 1905). Later, the RTT was adapted for seismology (Gusev & Abubakirov, 1996; Wu, 1985; Zeng et al., 1991) to describe the late part of high-frequency seismograms. RTT neglects information about individual phases of the wave, such that the phase information is replaced by a statistical average. The quantity described by the RTT is the specific intensity of the wave  $I$  and not the wave field itself. The acoustic 3-D RTT can be described as follows (after Apresyan & Kravtsov, 1996):

$$\begin{aligned} \frac{\partial I(\mathbf{x}, \hat{\mathbf{k}}, t, f)}{v(\mathbf{x}) \partial t} + \hat{\mathbf{k}} \nabla_r I(\mathbf{x}, \hat{\mathbf{k}}, t, f) = & \\ - g_0(\mathbf{x}, f) I(\mathbf{x}, \hat{\mathbf{k}}, t, f) - \frac{b(\mathbf{x}, f)}{v(\mathbf{x})} I(\mathbf{x}, \hat{\mathbf{k}}, t, f) & \quad (4.11) \\ + \frac{1}{4\pi} \iint g(\mathbf{x}, \hat{\mathbf{k}}, \hat{\mathbf{k}}', f) I(\mathbf{x}, \hat{\mathbf{k}}', t, f) d\hat{\mathbf{k}}' & \\ + Q_{int}(\mathbf{x}, \hat{\mathbf{k}}, t, f) & \end{aligned}$$

with  $I$  the intensity,  $\mathbf{x}$  the location,  $f$  the frequency,  $b$  the absorption coefficient,  $g$  the angular dependent scattering coefficient and  $Q_{int}$  the source intensity. The equation is an energy balance and can be explained as follows: the left-hand side represents the temporal and spatial changes in intensity, while the right-hand side represents the effects of scattering, absorption and sources. The change in intensity  $I$  is equal to the loss of energy flux due to absorption  $b$  and scattering  $g_0$  from direction  $\hat{\mathbf{k}}$  to  $\hat{\mathbf{k}}'$  and the gain of energy in direction  $\hat{\mathbf{k}}$  due to scattering  $g$  from direction  $\hat{\mathbf{k}}'$ , as well as the gain of energy due to sources  $Q_{int}$ .

The RTT equation is a first-order integro-differential equation in space, time and propagation direction  $\hat{\mathbf{k}}$  and corresponds to the Boltzmann equation of the kinetic theory of gases. The solution of the RTT is non-trivial and analytical solutions can only be found for special cases, like the diffusion model (energy travels long distances with multiple scat-

tering), the Markov approximation (only forward scattering and energy travels short distances), or the Paaschens equation (Paaschens, 1997). The Paaschens equation is an analytical solution and can be used to calculate the resulting energy density of a point source with the Green's function  $G$ :

$$G(t, \mathbf{x}, g^*) = \exp(-vtg^*) \left[ \frac{\delta(x - vt)}{4\pi x^2} + \left(\frac{4\pi v}{3g^*}\right)^{-\frac{3}{2}} t^{-\frac{3}{2}} \right. \\ \left. \times \left(1 - \frac{x^2}{v^2 t^2}\right)^{\frac{1}{8}} K\left(vtg^* \left(1 - \frac{x^2}{v^2 t^2}\right)^{\frac{3}{4}}\right) H(vt - x) \right]$$

with

$$K(x') = e^{x'} \sqrt{1 + \frac{2.026}{x'}} \quad (4.12)$$

with  $t$  the time and  $H$  the Heaviside step function. The intrinsic attenuation can be taken into account with the term  $\exp(-bt)$ . The Paaschens equation assumes a homogeneous and isotropic random medium, isotropic scattering, and an isotropic source. The equation provides a simple distinction between scattering and absorption attenuation in the context of RTT (Fehler et al., 1992), but overall it is only an approximation and a strong simplification of reality. For instance, isotropic scattering does not account for envelope broadening. Envelope broadening refers to a temporal shift of the maximum of an envelope due to strong scattering, resulting in waves being slightly diverted from their original propagation direction (Sato, 1989). Envelope broadening is essential to accurately describe the first arrival of body waves. Instead, the first arrival in the Paaschens equation is described by the  $\delta$ -function. The entire envelope of an S-wave was first used by Hoshiya (1991) using Multiple Lapse Time Window Analysis to determine the scattering and intrinsic attenuation of the subsurface.

To solve the general case (Eq. 4.11), numerical methods can be used, such as Monte Carlo simulations. While Monte Carlo simulations are more computationally intense, they can account for the depth dependence of the attenuation, focal mechanism of earthquake and anisotropic scattering. The acoustic RTT (Eq. 4.11) can be rewritten (after Gusev

& Abubakirov, 1996):

$$\begin{aligned} \frac{dI(\mathbf{x}, \hat{\mathbf{k}}, t, f)}{dl} &= -I(\mathbf{x}, \hat{\mathbf{k}}, t, f) \int g(\mathbf{x}, \hat{\mathbf{k}}, \hat{\mathbf{k}}', f) d\Omega_{\hat{\mathbf{k}}'} \\ &- \frac{b(\mathbf{x}, f)}{v(\mathbf{x})} I(\mathbf{x}, \hat{\mathbf{k}}, t, f) + \int g(\mathbf{x}, \hat{\mathbf{k}}', \hat{\mathbf{k}}, f) I(\mathbf{x}, \hat{\mathbf{k}}', t, f) d\Omega_{\hat{\mathbf{k}}} \end{aligned} \quad (4.13)$$

with  $d\Omega_{\hat{\mathbf{k}}'}$  the solid angle element. The left-hand side describes the change in intensity on an infinitesimal wavelength  $dl$ . The wavelength is discretized to convert it into a Monte Carlo scheme (after Gusev & Abubakirov, 1996):

$$\begin{aligned} \frac{\Delta N(\mathbf{x}, \hat{\mathbf{k}}, t, f)}{N(\mathbf{x}, \hat{\mathbf{k}}, t, f)} &= -g_0(\mathbf{x}, f) \Delta l \int p(\hat{\mathbf{k}}, \hat{\mathbf{k}}', f) d\Omega_{\hat{\mathbf{k}}'} \\ &- \frac{b(\mathbf{x}, f)}{v(\mathbf{x})} \Delta l + \frac{g_0(\mathbf{x}, f) \Delta l}{N(\mathbf{x}, \hat{\mathbf{k}}, t, f)} \int p(\hat{\mathbf{k}}', \hat{\mathbf{k}}, f) N(\mathbf{x}, \hat{\mathbf{k}}', t, f) d\Omega_{\hat{\mathbf{k}}} \end{aligned} \quad (4.14)$$

with the phase function  $p$  (Gusev & Abubakirov, 1996):

$$p(\hat{\mathbf{k}}', \hat{\mathbf{k}}, f) = p(\theta, \phi, f) = \frac{g(\theta, \phi, f)}{g_0(f)} \quad (4.15)$$

In equation 4.14, the intensity of the waves is now represented by the particle density  $N$ . The left-hand side of the equation describes the change in particle density at the path element  $\Delta l$ , and the right-hand side can be divided into three parts. The first term describes the part of the particle density that leaves the direction  $\hat{\mathbf{k}}$  due to scattering, the second term describes the part that is absorbed, and the last term describes the part that leads to an increase in particle density due to scattering from the direction  $\hat{\mathbf{k}}'$  to the direction  $\hat{\mathbf{k}}$ . The Monte Carlo simulation thus mimics the motion of energy particles emitted by an earthquake (Fig. 4.4). When a particle propagates along the path length  $\Delta l$ , only the first two terms on the right-hand side need to be modeled in the Monte Carlo simulation, as the last term is automatically accounted for. The energy particles are simulated based on to the physical properties of the different layers. It is important to note that the Monte Carlo simulation describes the process of energy propagation using a first-order Markov chain. First-order Markov chains are a stochastic model, where the outcome of the current step depends solely on the directly preceding step

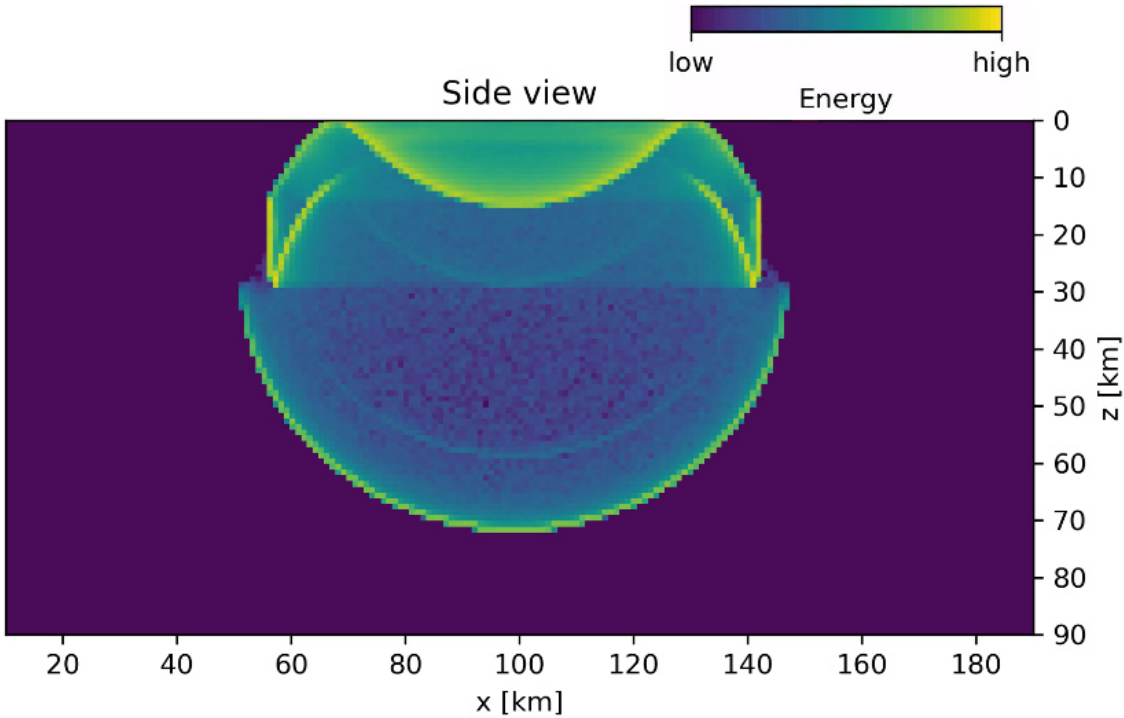


Figure 4.4: Energy propagation simulation of a seismic wave in a multi-layer model using Monte Carlo simulation.

and not on steps further back. In a scattering event, the new direction of the particle is determined by its previous direction. If particles are simulated long enough or a large number of particles are simulated, a fraction of them will reach the surface during the simulation, and can be recorded by stations.

Seismic attenuation can be described by the quality factor  $Q^{-1}$ . It is a measure of the energy lost to the medium during seismic wave propagation. The scattering attenuation  $Q_{sc}^{-1}$  can be determined by the equation:

$$Q_{sc}^{-1}(x, f) = \frac{v(x) g^*(x)}{2\pi f} \quad (4.16)$$

and the intrinsic attenuation can be determined with:

$$Q_i^{-1}(x, f) = \frac{b(x)}{2\pi f} \quad (4.17)$$

Seismic attenuation depends on porosity, fluids, elasticity and other rock properties (Aizawa et al., 2008; Chapman et al., 2015; Jackson et al., 2002) that do not necessarily affect seismic velocity. Thus, seismic attenuation analysis complements seismic velocity analysis and can provides new insight into subsurface processes.

## 5 | Publication summary

The scientific questions are outlined in section 1.2. The research questions were investigated in three individual publications submitted to international peer-reviewed journals. The results of these publications are briefly summarized below.

### **Publication 1:**

Comparison of Multiple Lapse Time Window Analysis and Qopen to determine intrinsic and scattering attenuation

by Marcel van Laaten, Tom Eulenfeld, Ulrich Wegler, published in *Geophysical Journal International* (2022), 228, p. 913-926, <https://doi.org/10.1093/gji/ggab390>.

This publication examines the seismic attenuation properties of the crust in the Saxon Vogtland region up to Leipzig. The S-wave and seismic coda of earthquakes are investigated using the radiative transfer theory. Two methods are employed: Multiple Lapse Time Window Analysis and envelope fitting with the Paaschens equation. Both methods can be used to determine the frequency-dependent scattering and absorption for a homogeneous subsurface. Nevertheless, the Multiple Lapse Time Window Analysis is more established, and we compare if envelope fitting provides similar results. The results indicate that both methods are identical within the error bars, although the envelope fitting has smaller error bars. Furthermore, the parameter dependencies of the results for both methods are examined. The determined attenuation values indicate that both the scattering and intrinsic attenuation in the central and northern parts of the LRZ are lower than in NW-Bohemia/Vogtland.

### **Publication 2:**

On the trail of fluids in the northernmost intracontinental earthquake swarm areas of the Leipzig-Regensburg fault zone, Germany

by Marcel van Laaten, Ulrich Wegler, Tom Eulenfeld, published in *Journal of Seismology* (2023), 27, p. 573-597, <https://doi.org/10.1007/s10950-023-10146-8>.

This publication investigates the seismic velocity along the LRZ. Local earthquakes are used to employ travelttime tomography to investigate the upper and middle crust. Teleseismic earthquakes are used for receiver function analysis to examine the lower crust and upper mantle in terms of their structural and spatial characteristics. In particular, the Schöneck and Werdau earthquake swarm region is examined. Potential fluid pathways in the crust are indicated by high  $v_p/v_s$  ratios, which, in conjunction with faults and presumed granite intrusions, are believed to be the underlying cause of the Schöneck and Werdau earthquake swarms. The Moho can be identified through receiver functions in the 25 to 33 km range, and two north-dipping seismic reflectors are observed at depths of 55 and 68 km. The 68 km depth anomaly is a partial melt, emitting fluids. These uprising fluids travel along fault zones to the surface and trigger on their way the earthquake swarms of the LRZ.

**Publication 3:**

Non-linear inversion for a multi-layer seismic S-wave attenuation model using radiative transfer theory

by Marcel van Laaten, Ulrich Wegler, submitted to Journal of Geophysical Research - Solid Earth

This manuscript examines not only the frequency-dependent absorption and scattering, but also the depth dependence of seismic attenuation. S-waves and the coda of local earthquakes are utilized for this purpose. The LRZ is divided into two distinct regions, the southern and northern LRZ, and for both regions, the attenuation is determined. Results indicate that the seismic attenuation of the crust is only slightly depth-dependent in both regions. In general, the southern region exhibits stronger scattering than the northern region, while both regions exhibit similar absorption properties.

## 6 | Publications

### 6.1 Publication 1

**Comparison of Multiple Lapse Time Window Analysis and Qopen to determine intrinsic and scattering attenuation**

Marcel van Laaten<sup>1</sup>, Tom Eulendorf<sup>1</sup>, Ulrich Wegler<sup>1</sup>

<sup>1</sup> Institute of Geosciences, Friedrich Schiller University Jena, Burgweg 11, 07749 Jena

Published in 2022 in Geophysical Journal International, 228, pp. 913-926

<https://doi.org/10.1093/gji/ggab390>

## Comparison of Multiple Lapse Time Window Analysis and Qopen to determine intrinsic and scattering attenuation

M. van Laaten , T. Eulenfeld and U. Wegler

*Institute of Geosciences, Friedrich Schiller University Jena, Burgweg 11, 07749 Jena, Germany. E-mail: marcel.vanlaaten@uni-jena.de*

Accepted 2021 September 21. Received 2021 September 17; in original form 2021 May 4

### SUMMARY

This study compares the results of Multiple Lapse Time Windows Analysis (MLTWA) and full envelope inversion (Qopen) to determine intrinsic and scattering attenuation of the crust using the region around the central part of the Leipzig–Regensburg fault zone in Germany as an example. We use 18 of the region’s strongest earthquakes from 2008 to 2019 with a magnitude between 1.4 and 3.0 in the frequency band range between 3 and 34 Hz. The determined attenuation values of both methods are similar within their error bars. The inverse quality factors of the shear wave are relatively low compared to other regions, with values of  $3.2 \times 10^{-4}$  to  $8.7 \times 10^{-4}$  for  $Q_i^{-1}$  and  $1.4 \times 10^{-4}$  to  $2.8 \times 10^{-4}$  for  $Q_{sc}^{-1}$ , respectively. As a by-product of Qopen, we also obtain the energy site amplification of the stations used in the inversion as well as source displacement spectra and moment magnitudes of the inverted earthquakes. Several combinations of inversion parameters were tested for MLTWA, with  $Q_i^{-1}$  and  $Q_{sc}^{-1}$  providing the lowest trade-off. Likewise, we investigated the influence of window length on the results of Qopen. We found a dependency of the results on the length, if the windows are shorter than 30 s. For longer time windows, the dependence disappears, and the result becomes independent of window length.

**Key words:** Europe; Inverse theory; Coda waves; Seismic attenuation.

### 1 INTRODUCTION

Seismic attenuation provides valuable information about the structure of the crust and is important to analyse earthquakes. Over time, different methods have been developed to calculate seismic attenuation (e.g. Shearer & Earle 2004; Saito et al. 2005; Calvet et al. 2013; Mayor et al. 2016; Shito et al. 2020), each with its advantages and disadvantages. Various studies have already drawn a comparison between some of these methods, for example, Bachura & Fischer (2016), Gaebler et al. (2015) or Eulenfeld & Wegler (2017). However, a comparison between the two commonly used methods of Multiple Lapse Time Window Analysis (MLTWA) and Separation of intrinsic and scattering Q by envelope inversion (Qopen) with the same data does not yet exist. In this study, we focus on the determination of S-wave scattering  $Q_{sc}^{-1}$  and the intrinsic attenuation  $Q_i^{-1}$  to obtain information about small-scale heterogeneities of the subsurface in the central area of the Leipzig–Regensburg fault zone (LRZ), Germany (Fig. 1) and compare the two methods concerning their results. Both methods are shown as examples in Fig. 2. The dimensionless quality factor  $Q$  describes the loss of relative energy per oscillation cycle. The greater challenge is the distinction between  $Q_i^{-1}$  and  $Q_{sc}^{-1}$ . Besides the geometrical spreading, both are main contributors to the total seismic attenuation  $Q_t^{-1}$ .

$$Q_t^{-1} = Q_i^{-1} + Q_{sc}^{-1} \quad (1)$$

Intrinsic attenuation describes the conversion of seismic energy into heat or other forms of energy by inelastic processes such as friction while scattering attenuation describes the process of changing the direction of wave propagation or phase shift due to heterogeneities. Another approach to determining attenuation is to measure  $Q$  based on coda waves (Aki & Chouet 1975). The resulting  $Q_c^{-1}$  is easy to measure, but the physical meaning of  $Q_c^{-1}$  is controversial since  $Q_c^{-1}$  depends simultaneously on the scattering and anelastic properties of the crust (Calvet et al. 2013). Only in the multiple scattering regime, for example, at sufficiently long lapse-times,  $Q_c^{-1}$  is an approximation of  $Q_i^{-1}$  (Aki & Chouet 1975). In contrast, the attenuation values  $Q_i^{-1}$  and  $Q_{sc}^{-1}$  depend only on the transport scattering coefficient  $g^*$  and the absorption coefficient  $b$ , respectively. The relation is given by (Eulenfeld & Wegler 2016):

$$Q_{sc}^{-1} = \frac{g^* v_0}{2\pi f} \quad Q_i^{-1} = \frac{b}{2\pi f} \quad (2)$$

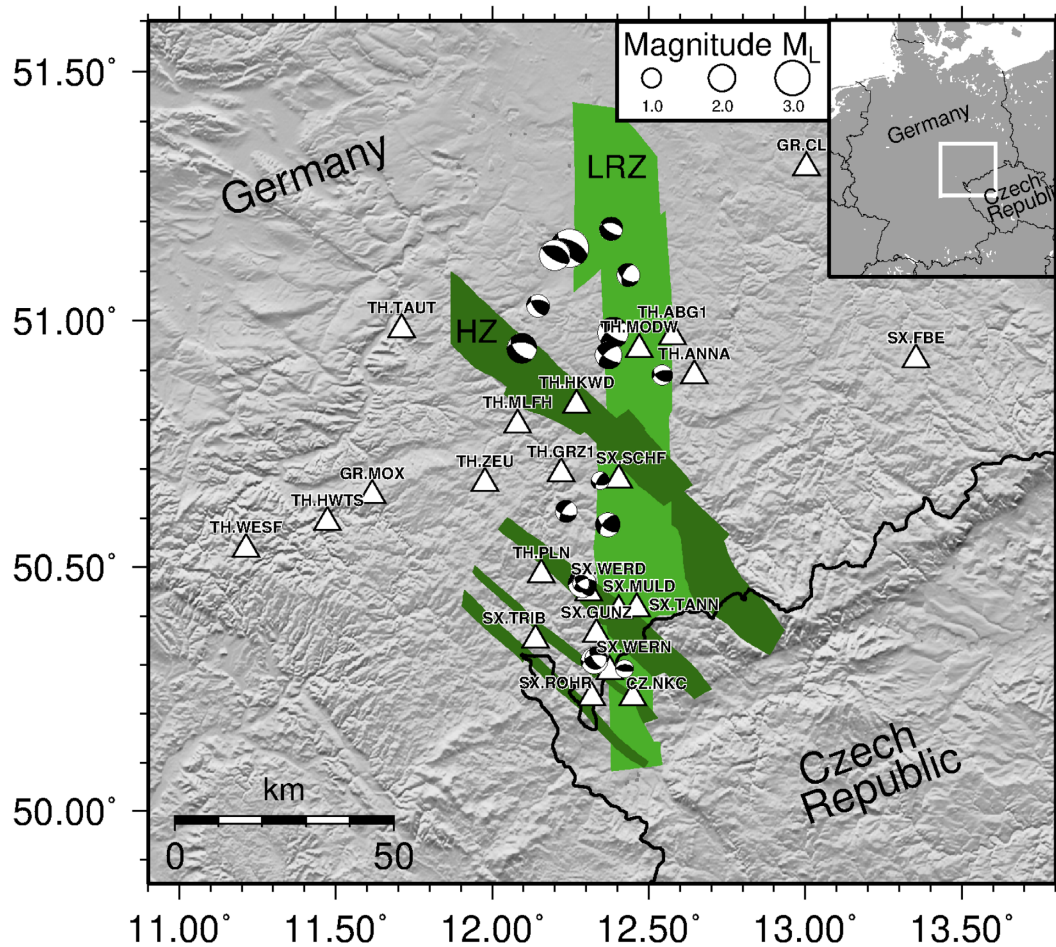


**Figure 1.** Overview map with hillshade of the survey area. The 18 tectonic earthquakes used for this study are shown with their focal mechanisms, obtained with Grond (Heimann *et al.* 2018), and with a size corresponding to their magnitude. The area of the N-S striking LRZ is shown in light green and the areas of the NW-SE striking Herzyn fault zones (HZ) as dark green (after LfULG 2018). White triangles display the position of the stations.

with the mean velocity  $v_0$  and frequency  $f$ . A power law can often describe the frequency dependence of  $Q^{-1}$ :

$$Q^{-1} = Q_0^{-1} f^n \quad (3)$$

## 2 INVESTIGATION AREA

The investigation focuses on the crustal structure in the central area of the LRZ (Grünthal *et al.* 1985). Several NW-SE striking Hercynian fault zones cross the N-S striking LRZ (Pitzsch 1963). A band of seismic activity with an area of about 150 km length and 40 km width (Bankwitz *et al.* 2003) characterize the middle part of the LRZ, with most earthquakes occurring at depths between 4 and 17 km. The southern earthquakes are mainly located in the shallower crustal area, while the northern earthquakes also occur at greater depths. There are also numerous areas of intracontinental earthquake swarms along the southern part of the LRZ (Korn *et al.* 2008), while the north has no such earthquake swarm areas. In contrast to normal earthquakes with a strong main earthquake and weaker aftershocks, the strongest earthquake of an earthquake swarm does not occur at the beginning but usually later on. Another unique aspect of earthquake swarms is that they actually only occur in areas of extensional tectonics such as mid-ocean rifts or active volcanic areas. However, both phenomena do not occur in this area (Fischer *et al.* 2014). An analysis of the magnitude distribution and temporal evolution has shown that swarms of the LRZ correspond to the typical values of an earthquake swarm (Neunhöfer 1998; Hemmann *et al.* 2003). The  $b$ -values of 73 swarms in the period 1903 to 1999 were analysed by Neunhöfer & Hemmann (2005) and are in the range of 0.5–1.5. The intensive swarms of 1908, 1962, 1985/86 as well as 1997 and 2000 are very close to a  $b$ -value of 1 (Neunhöfer & Hemmann 2005). This value agrees with the observation of Ibs-von Seht *et al.* (2008), who determined a  $b$ -value of 0.8 for intracontinental earthquake swarms in non-volcanic areas. Ascending fluids from the subsurface are assumed to be the source of these earthquake swarms (Špičák & Horálek 2001; Weise *et al.* 2001; Hofmann *et al.* 2003; Bräuer *et al.* 2009; Mousavi *et al.* 2015). The study area also borders the southern NW-Bohemia/Vogtland region at the German–Czech border, where a large variety of different investigations and methods have been carried out to obtain information on the earthquake swarm activity and crustal structure (Fischer *et al.* 2014).

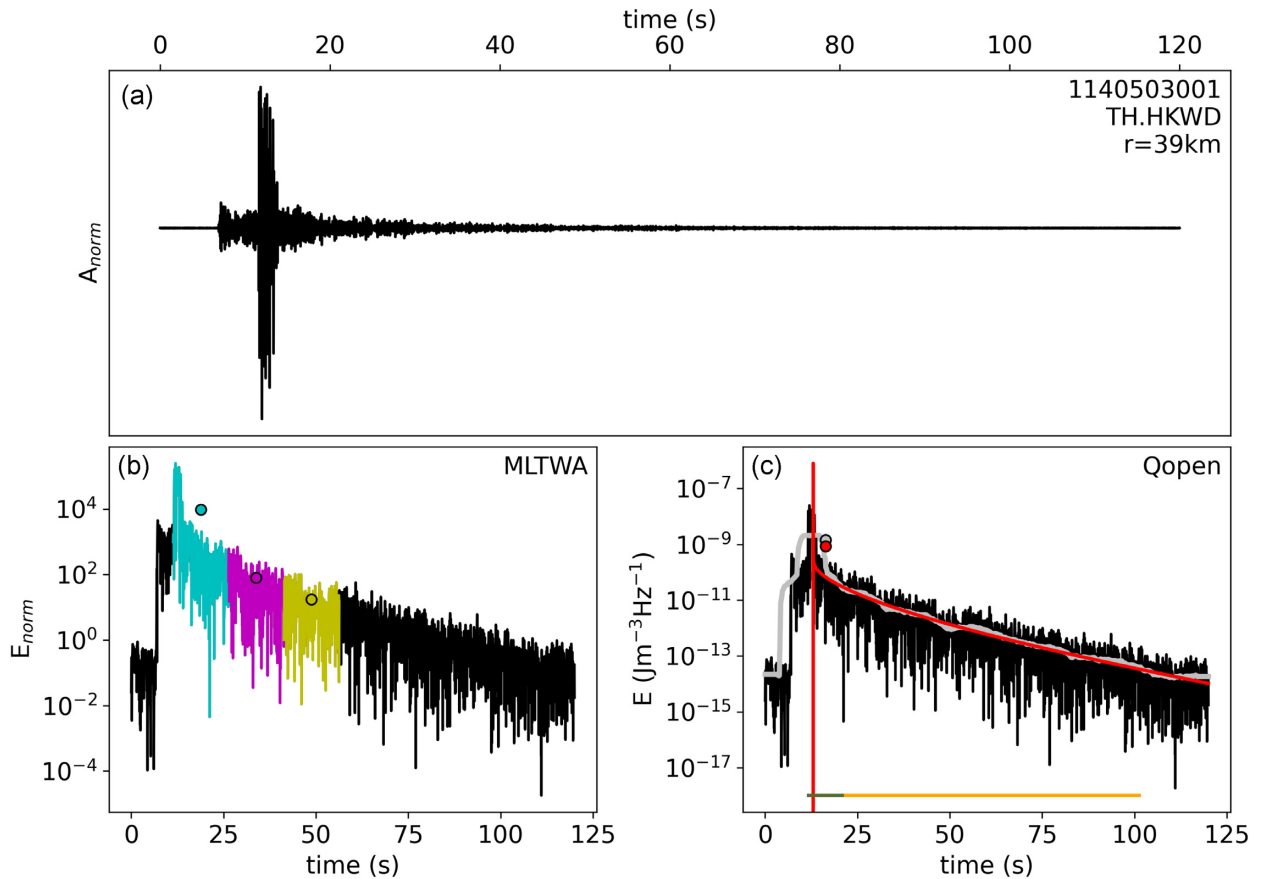


**Figure 2.** (a) Processed E-component of station HKWD in 39 km distance to an event (origin time: 2014-05-03T03:46:01.2). The displayed data are tapered, detrended, filtered (4.25–12.75 Hz) and normalized. Bottom: three-component envelope (black) of the station and exemplary representation of the two methods used for this study. (b) MLTWA method with three time windows (cyan, magenta and yellow) of 15 s length starting from the *S*-arrival time and the corresponding integrated energy (circles). (c) Qopen with the smoothed envelope over 2 s (grey), the time window of the direct wave (olive) and the coda window (orange) for which the synthetic energy density (red) is calculated using the Green's function. The envelope in the direct wave time window is averaged (circles).

### 3 DATA AND METHOD

#### 3.1 Data

We use 18 of the strongest earthquakes (Fig. 1) of the Thüringer Seismologisches Netz (TSN) earthquake catalogue from the period 2008–2019 and within the coordinates of latitude  $50.30^{\circ}$ – $51.19^{\circ}$  and longitude  $12.0^{\circ}$ – $12.75^{\circ}$  to determine the attenuation properties in the area of the LRZ. The magnitudes range from 1.4 to 3.0 and the depths from 9.0 to 19.2 km. In total, waveform data were collected at 22 low noise stations (Fig. 1) by the networks Czech Regional Seismic Network (Czech Regional Seismic Network 2019), German Regional Seismic Network (German Regional Seismic Network 2019), Saxon Seismic Network (Saxon Seismic Network 2019) and Thüringer Seismologisches Netz (Thüringer Seismologisches Netz 2019). Each station is equipped with a three-component seismometer, and the seismograms were sampled at a 100 or 200 Hz rate. Only stations with a distance of less than 90 km from the earthquake are selected. The seismograms were detrended, tapered to minimize boundary effects and divided by sensitivity. The data is then filtered, and the analysis was performed in eight frequency bands: 1.5–4.5, 2.1–6.3, 3–9, 4.25–12.75, 6–18, 8.5–25.5, 12–36 and 17–49.9 Hz with the corresponding central frequencies: 3, 4.2, 6, 8.5, 12, 17, 24 and 34 Hz. The data must be available at a minimum of four stations for the appropriate frequency of the event to be considered, and the picks were manually identified with SeismicHandler (Stammler 1993). We calculate the required *S*-wave velocity using the *S*-wave traveltime and distance. The following calculation of the envelopes is based on the square sum of the three components, and the Hilbert transform, as well as the correction of the free surface (Eulenfeld & Wegler 2016). The last step for Qopen is to smooth the envelope over 2 s. Only seismograms with a good signal-to-noise ratio (SNR) of at least two and sufficient coda length of at least 45 s starting from the *S*-pick were used for analysis. We used the mean value of a reference time window between 0 and 4 s before the origin time to calculate the noise level.

### 3.2 Multiple Lapse Time Window Analysis

Fehler *et al.* (1992) introduced the MLTWA method for calculating the attenuation property of the subsurface. Further studies have already successfully applied the method (Hoshiya *et al.* 2001; Giampiccolo *et al.* 2006; Carcolé & Sato 2010; Meirova & Pinsky 2014; Bachura & Fischer 2016). Since the two attenuation parameters  $Q_i^{-1}$  and  $Q_{sc}^{-1}$  have a different influence on the envelope, the relative energy change of several time windows and over different distances can be used to determine the respective attenuation. The scattering attenuation  $Q_{sc}^{-1}$  is mainly responsible for the ratio of energy in different time windows over different distances. For example, strong scattering ensures that most of the energy ends up in the later time windows, while weak scattering ensures that most of the energy ends up in the first time window (Carcolé & Sato 2010). Intrinsic attenuation  $Q_i^{-1}$ , on the other hand, is responsible for the exponential decay with time of the energy of the seismic wavefield, regardless of the distance (Carcolé & Sato 2010).

The  $S$ -wave energy density  $E_{syn}$  in a given frequency band can be described with the equation (Sens-Schönfelder & Wegler 2006):

$$E_{syn}(t, \mathbf{r}) = WR(\mathbf{r})G(t, \mathbf{r}, g^*)e^{-bt} \quad (4)$$

with  $t$  the lapse time,  $\mathbf{r}$  a vector pointing from the hypocentre to the location of the station,  $W$  the spectral  $S$ -wave source energy of the event,  $R(\mathbf{r})$  the energy site amplification of the station,  $G(t, \mathbf{r}, g^*)$  the energy density Green's function and the exponent  $e^{-bt}$  which describes the intrinsic attenuation with time and depends only on the absorption coefficient  $b$ . The Green's function considers the direct  $S$ -wave and the scattered wavefield, assuming a homogeneous  $S$ -wave velocity, homogenous attenuation parameters, isotropic scattering and isotropic source radiation pattern. It can be calculated with the analytical approximation solution of the 3-D isotropic energy transfer equation of Paasschens (Paasschens 1997; Eulenfeld & Wegler 2016):

$$G(t, \mathbf{r}, g^*) = \exp(-v_0 t g^*) \left[ \frac{\delta(r - v_0 t)}{4\pi r^2} + \left( \frac{4\pi v_0}{3g^*} \right)^{-\frac{3}{2}} t^{-\frac{3}{2}} \right. \\ \left. \times \left( 1 - \frac{r^2}{v_0^2 t^2} \right)^{\frac{1}{8}} K \left( v_0 t g^* \left( 1 - \frac{r^2}{v_0^2 t^2} \right)^{\frac{3}{4}} \right) H(v_0 t - r) \right]$$

with

$$K(x) = e^x \sqrt{1 + \frac{2.026}{x}} \quad (5)$$

with the Heaviside step function  $H$  and  $r = |\mathbf{r}|$ . The Dirac delta function term  $\delta$  of the equation describes the direct wave and the other term the scattered waves. The assumption of isotropic scattering instead of anisotropic scattering is invalid. However, a scattering coefficient  $g_0$  determined under the assumption of isotropic scattering in an anisotropic scattering medium can be equated to the transport scattering coefficient  $g^*$  (Gaebler *et al.* 2015).

By coda normalization of the observed data, the terms  $W$  and  $R(\mathbf{r})$  of eq. (4) are removed (Aki 1980) and the synthetic energy depends only on the Green's function and the exponent of intrinsic attenuation. The coda normalization factor is the mean value of the energy in a reference time window between 60 and 65 s after origin time and is calculated separately for each seismogram. The normalization window was chosen as late in the coda as possible but still fulfills the SNR criterion. Afterwards, the envelope is divided into three consecutive time windows of 15 s, starting from the  $S$ -wave arrival time  $t_s$  and integrated within the time window:

$$E_1(\mathbf{r}) = \int_{t_s}^{t_s+15s} E(t, \mathbf{r}) dt, \quad E_2(\mathbf{r}) = \int_{t_s+15s}^{t_s+30s} E(t, \mathbf{r}) dt, \quad E_3(\mathbf{r}) = \int_{t_s+30s}^{t_s+45s} E(t, \mathbf{r}) dt \quad (6)$$

Subsequently, the three energy integrals are corrected for the hypocentral distance by multiplying with  $4\pi r^2$  resulting in the misfit function  $M$  (Bachura & Fischer 2016) between observed and synthetic data over the three time windows  $i$ :

$$M(Q_{sc}^{-1}, Q_i^{-1}) = \sum_{k=1}^N \sum_{i=1}^3 w_i (\log_{10}(4\pi r^2 E_{obs_i}(\mathbf{r}_k)) - \log_{10}(4\pi r^2 E_{syn_i}(\mathbf{r}_k)))^2 \quad (7)$$

with  $N$  the number of stations of an event. The misfit function is used individually for each event and frequency band. To minimize the influence of the source radiation characteristics in the direct wave (Bachura & Fischer 2016), the two later time windows  $E_2(\mathbf{r})$  and  $E_3(\mathbf{r})$  are weighted stronger in the inversion with the weighting factor  $w = (0.5, 1, 1)$ . We use the brute force method to minimize the misfit function over a range of  $Q_{sc}^{-1} = [10^{-5}, 10^{-3}]$  and  $Q_i^{-1} = [10^{-4}, 10^{-2}]$  with 200 points in both dimensions. The final attenuation result is the median of all events and as an error measure, the interquartile range (75th and 25th percentile) was calculated.

### 3.3 Qopen

The software Qopen is provided by Eulenfeld & Wegler (2016) and calculates attenuation, source displacement spectra and site amplifications. The programme is based on the radiative transfer theory (RTT) and uses Paasschens equation (Paasschens 1997) to calculate the Green's function. The inversion proceeds as follows: first, the parameters  $b$ ,  $g^*$ ,  $R(\mathbf{r})$  and  $W$  from eq. (4) are inverted individually for each frequency

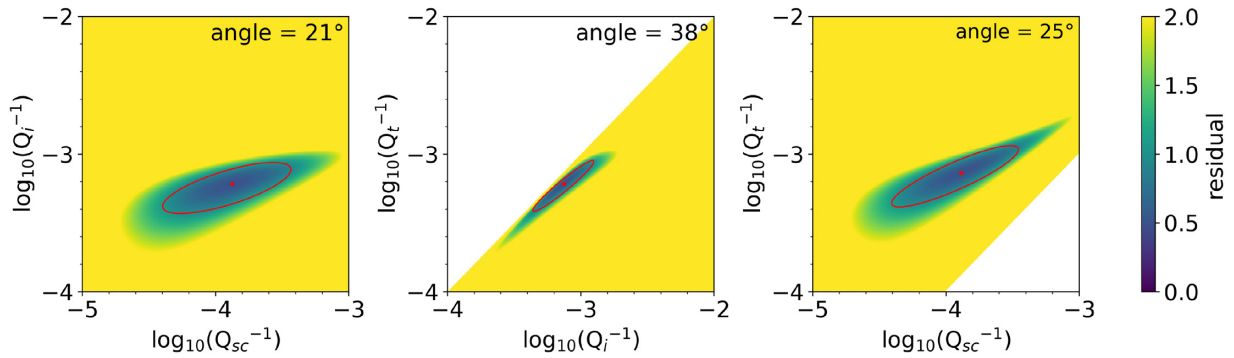


**Figure 3.** Comparison of the misfit functions of the MLTWA inversion of one event between 6 and 18 Hz using different inversion parameters. The red dot shows the minimal residual. The red ellipse represents all points with residual  $< 1$  and a standard deviation of  $2\sigma$ . The angle of the ellipse in relation to the  $x$ -axis results in the trade-off of the inversion parameters, which is lowest for the combination  $Q_{sc}^{-1}$  and  $Q_i^{-1}$ .

band and earthquake using the least-squares linear equation system. In the next step, we fix the parameters  $b$  and  $g^*$  and eq. (4) is solved again only for  $R(\mathbf{r})$  and  $W$  for each frequency band and earthquake individually. To fix the collinearity between  $W$  and  $R(\mathbf{r})$  from eq. (4), the site amplification of a single station or the geometric mean of site amplification of all stations needs to be fixed and is set to 1 in this study (Eulenfeld & Wegler 2016). Finally, the source displacement spectra, source parameters and the moment magnitudes are calculated. The further details of the inversion are described in Eulenfeld & Wegler (2016). The boundaries used for the inversion are  $g^* = [10^{-8}, 10^{-2}] \text{ m}^{-1}$  and  $b = [10^{-6}, 1] \text{ s}^{-1}$ . The direct  $S$ -wave window starts 1 s before the  $S$ -wave arrival time and ends 10 s afterwards. The coda window starts at the end of the direct  $S$ -wave window and has a maximum length of 120 s considering an  $\text{SNR} > 2$ , where the  $\text{SNR}$  is determined for each frequency band separately. The length of the time window corresponds to the weighting of the station in the inversion. Station data with a coda shorter than 35 s was not considered for the inversion. The separation of the envelope into two different time windows (direct wave and coda) is necessary because the effects of anisotropic scattering near the  $S$ -wave cannot be described correctly by the acoustic Green's function assuming isotropic scattering. The problem can be solved by more complex methods, such as elastic Monte-Carlo simulation with Born scattering coefficients (Przybilla *et al.* 2006; Sens-Schönfelder *et al.* 2009; Gaebler *et al.* 2015).

We added the option of coda normalization to Qopen to better compare to coda normalized MLTWA. In this case, only the parameters  $b$  and  $g_0$  are inverted, and this step eliminates information about source displacement spectra and site amplifications.

## 4 RESULTS

### 4.1 MLTWA

We tested various combinations of inversion parameters to identify the lowest trade-off between  $Q_i^{-1}$ ,  $Q_{sc}^{-1}$  and  $Q_t^{-1}$ . Fig. 3 shows the misfit functions for three different combinations, providing information about model validity and data processing suitability. The misfit function should be parallel to one of the axes to restrict at least one inversion parameter. The more parallel the misfit function is, the lower the trade-off between the two inversion parameters is in the end. Still, one of the two inversion parameters remains stable over a wide range, resulting in uncertainty for this parameter. As a result, the combination of  $Q_i^{-1}$  and  $Q_{sc}^{-1}$  gives the least trade-off compared to the parameter combinations of  $Q_i^{-1}$  and  $Q_t^{-1}$  and  $Q_{sc}^{-1}$  and  $Q_t^{-1}$ .

The comparison between observed and synthetic data is shown in Fig. 4 averaged over all events. Due to the direct  $S$ -wave's strong influence on the first time window, the observed values scatter strongly for  $E_1$ , and the radiation pattern behaviour of the earthquake becomes notable here as the coda normalization cannot completely eliminate the effect. However, the radiation pattern's influence on the attenuation's determination is minimal since the station distribution covers a wide azimuthal range. In contrast, the time windows  $E_2$  and  $E_3$  show a good agreement between observed and synthetic data.

### 4.2 Qopen

An essential point in the inversion of Qopen is the choice of the time window length of the coda window. Short time windows result in an imprecise estimation of attenuation parameters and trade-off. Long time windows possibly might not be realized due to the noise level. Therefore, it is crucial to find a balance between these two aspects. We have investigated the window length's influence on the inversion (Fig. 5). For this purpose, the data were inverted several times with coda time windows of various lengths, and the mean values of all events were compared. We fixed all inversion parameters with a direct wave window of 10 s. The coda window successively increases in steps of 5 s, starting from a coda window length of 10 s up to 65 s. The length of the longest coda window was chosen in a way to extend until the normalization time window in MLTWA. The window's length always corresponds exactly to the specified value, even if the  $\text{SNR}$  would allow a longer coda time window. Seismograms with shorter time windows due to low  $\text{SNR}$  were removed from this test. As a result, less and less

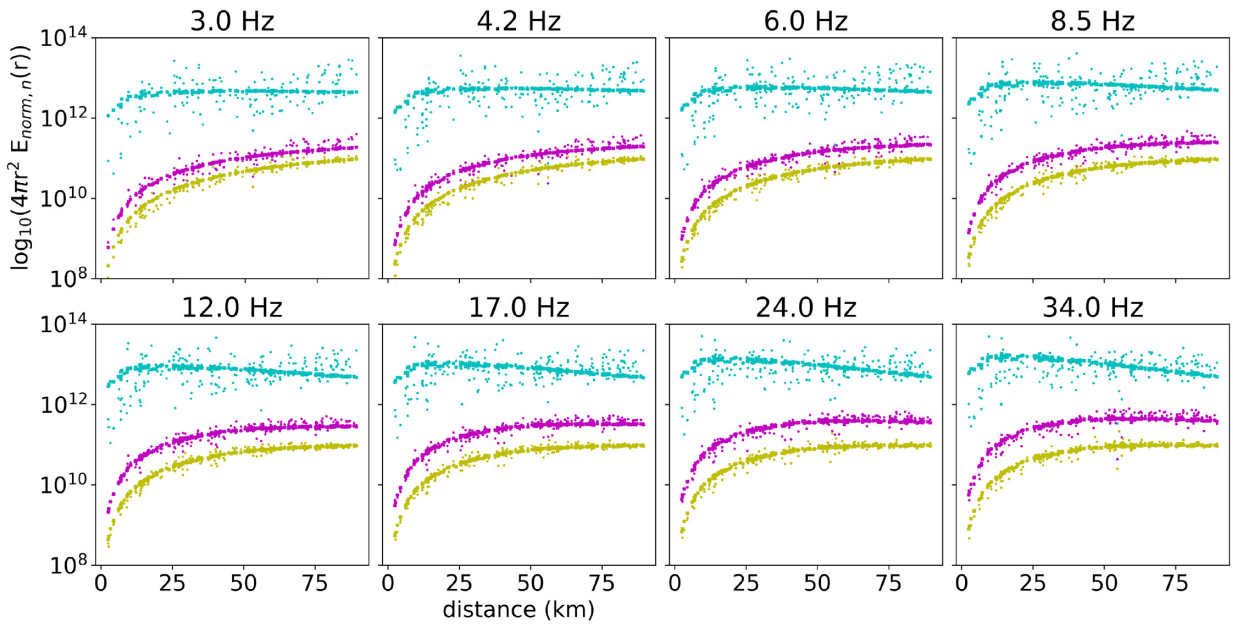


**Figure 4.** Comparison of synthetics (crosses) and observed (dots) energy versus hypocentral distance of all events of the MLTWA. The colours cyan, magenta and yellow represents the three time windows  $E_1$ ,  $E_2$  and  $E_3$  respectively.

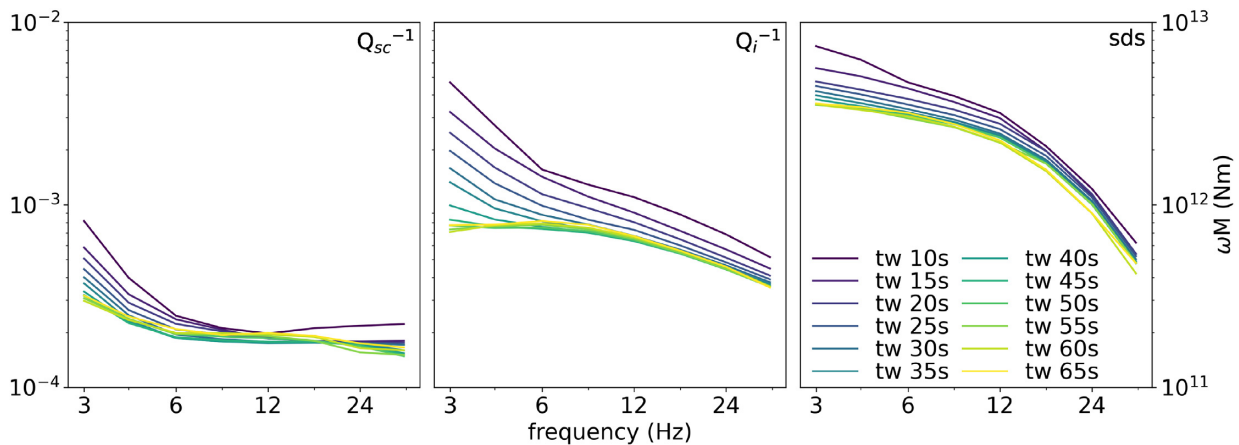


**Figure 5.** Comparison of  $Q_{sc}^{-1}$ ,  $Q_i^{-1}$  and source displacement spectrum (sds) calculated with Qopen and averaged over eight events for different time window (tw) lengths. Since long coda time windows are required, we reduced the data set to the strongest events. The start time of the time windows is always the same. For short time windows, there is a trade-off between increased source displacement spectra and  $Q_i^{-1}$ . With sufficiently long time windows of about 30 s, the trade-off disappears, and  $Q_i^{-1}$  and source displacement spectrum become independent of the window length.

data were available for the inversion as the length increased. The data set of 18 events was reduced to the eight strongest events for this specific analysis to ensure that in the end, all events are inverted, and the data remains comparable. Thus, the same number of seismograms is inverted in all time windows and only in the last two time windows, the number of seismograms reduced from 64 to 62. The analysis of the different time windows shows a trade-off between  $Q_i^{-1}$  and the source displacement spectra. With a sufficient coda length of about 30 s, the trade-off disappears, and the results of Qopen remain stable and are independent of the window length. The influence of the coda window length on  $Q_{sc}^{-1}$  is minimal, only for very short time windows of 10 and 15 s the inversion provides larger  $Q_{sc}^{-1}$  values compared to the other time windows. The reason for the different results between short and long coda time windows is exemplified in Fig. 6. The inverted parameters  $g^*$  and  $b$  differs greatly (10 s coda window (red):  $g^* = 9.2 \times 10^{-6} \text{ m}^{-1}$  and  $b = 9.6 \times 10^{-2} \text{ s}^{-1}$ ; 120 s coda window (blue):  $g^* = 3.3 \times 10^{-6} \text{ m}^{-1}$  and  $b = 3.6 \times 10^{-2} \text{ s}^{-1}$ ) and explain the discrepancy in attenuation values between the different length of coda time windows. Examining the short time window of 10 s (red bar), one can see that the two synthetic envelopes correspond to the real data about equally well, the envelope of the short time window is slightly above, while the envelope of the long time window slightly below the observed data. However, looking at the later part of the coda, the envelope of the short time window decreases more than the observed data, while the envelope of the long coda time window still fits the observed data. The shorter coda time windows are too short to determine an independent  $Q_i^{-1}$  and source displacement spectra.

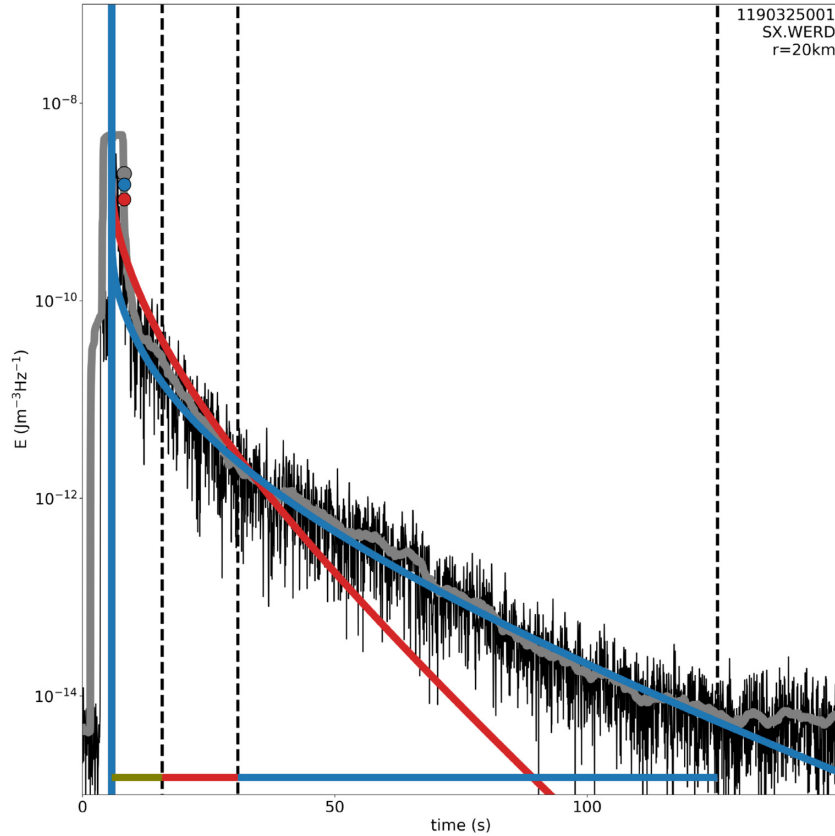


**Figure 6.** Fit at Station SX.WERD out of 13 stations between observed (black), smoothed observed envelope (grey) and synthetic energy densities of Qopen with different coda window lengths (red 10 s and blue 120 s). The dots show the energy of the direct wave in the respective colour. The bar below the envelope represents the section used for Qopen, respectively.

The increase of  $Q_{sc}^{-1}$  and the flattening of  $Q_i^{-1}$  at low frequencies between 3 and 6 Hz at Fig. 5 can be explained by an imprecise fit of the envelope in this frequency range and a smaller amount of available data. Therefore, the error is much larger than the high frequencies values, which explains the deviation at the low frequencies from the expected power law for  $Q_i^{-1}$ . We suggest to configure Qopen to use a long coda time window, that is, extend until 100 s after  $S$ -onset, and cut the time window earlier depending on SNR ratio. The suggested 100 s long coda window is an upper limit for studies on a regional scale (e.g. Eulenfeld & Wegler 2017). For local studies with shorter event-station distances, the coda window should be around 30–50 s long. The direct wave window should be chosen sufficiently long to include the onset and forward scattered waves. Depending on the extent of the study region, its length should be around 4–10 s.

As a by-product of the Qopen inversion, the source displacement spectra (Fig. 7), the moment magnitude  $M_W$  (Fig. 8) and the site amplification (Fig. 9) are determined. According to Sato *et al.* (2012), the source displacement spectra  $\omega M(f)$  of a double-couple in the far-field can be calculated by:

$$\omega M(f) = \sqrt{\frac{5\rho_0 v_0^5 W(f)}{2\pi f^2}} \quad (8)$$

with the density  $\rho_0$ . The average corner frequency of all events is 11.4 Hz, and the average high-frequency fall-off is 1.8. Thereby, the corner frequency corresponds to the typical corner frequency of local earthquakes and the high-frequency fall-off matches approximately the  $\omega^2$ -model.

The relationship between  $M_0$  (in Nm) and  $M_W$  can be described by (Hanks & Kanamori 1979):

$$M_W = \frac{2}{3} \log_{10} M_0 - 6.07 \quad (9)$$

The inverted moment magnitudes  $M_W$  mostly correspond well to the local magnitudes  $M_L$  of the earthquake catalogue (Fig. 8). Nevertheless, with decreasing magnitude, the difference between the determined  $M_W$  and the given  $M_L$  increases. Various studies have shown that the local magnitude starting at  $M_L < 2$  does not correspond to  $M_W$  (e.g. Deichmann 2006; Bethmann *et al.* 2011), a linear fit is needed to convert the magnitudes. Deichmann (2006) conducted a theoretical study on this and concluded that systematic and random errors in the determination of  $M_L$  lead to the difference between  $M_L$  and  $M_W$ , while the study by Bethmann *et al.* (2011) proves this with real data and uses the modified ray theoretical representation for the displacement of a heterogeneous elastic medium to determine the seismic moment.

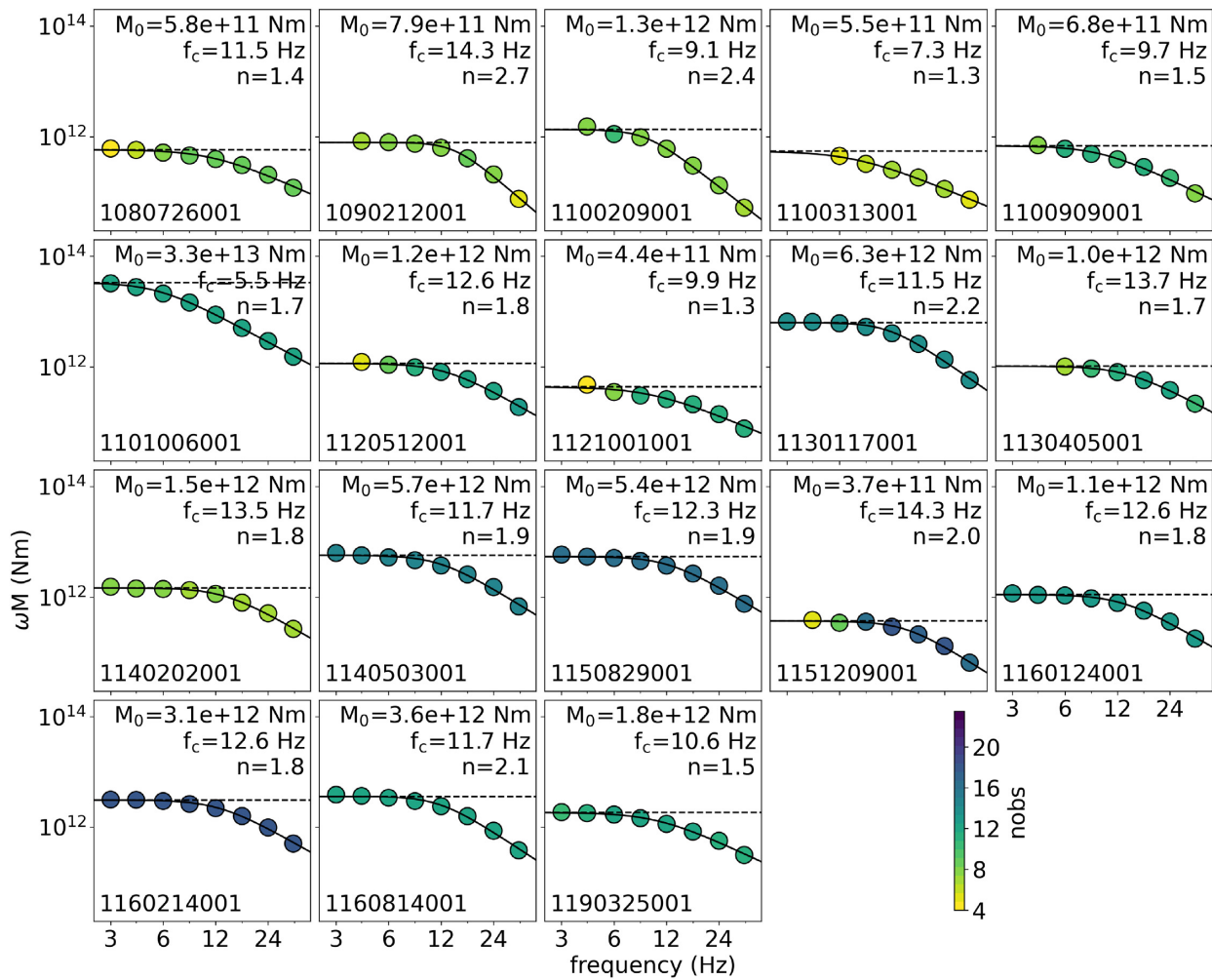


**Figure 7.** Observed source displacement spectra, displayed as circles depending on the number of observations (nobs) and fitted source model (black lines) for each inverted event. Also, the seismic moment  $M_0$ , the corner frequency  $f_c$  and the high-frequency fall-off  $n$  were determined.

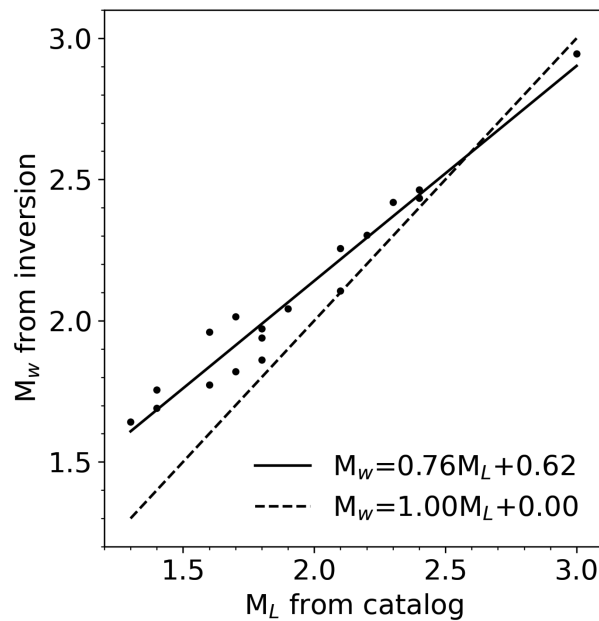


**Figure 8.** Comparison of catalogue local magnitude  $M_L$  and moment magnitude  $M_W$  estimated during the inversion.

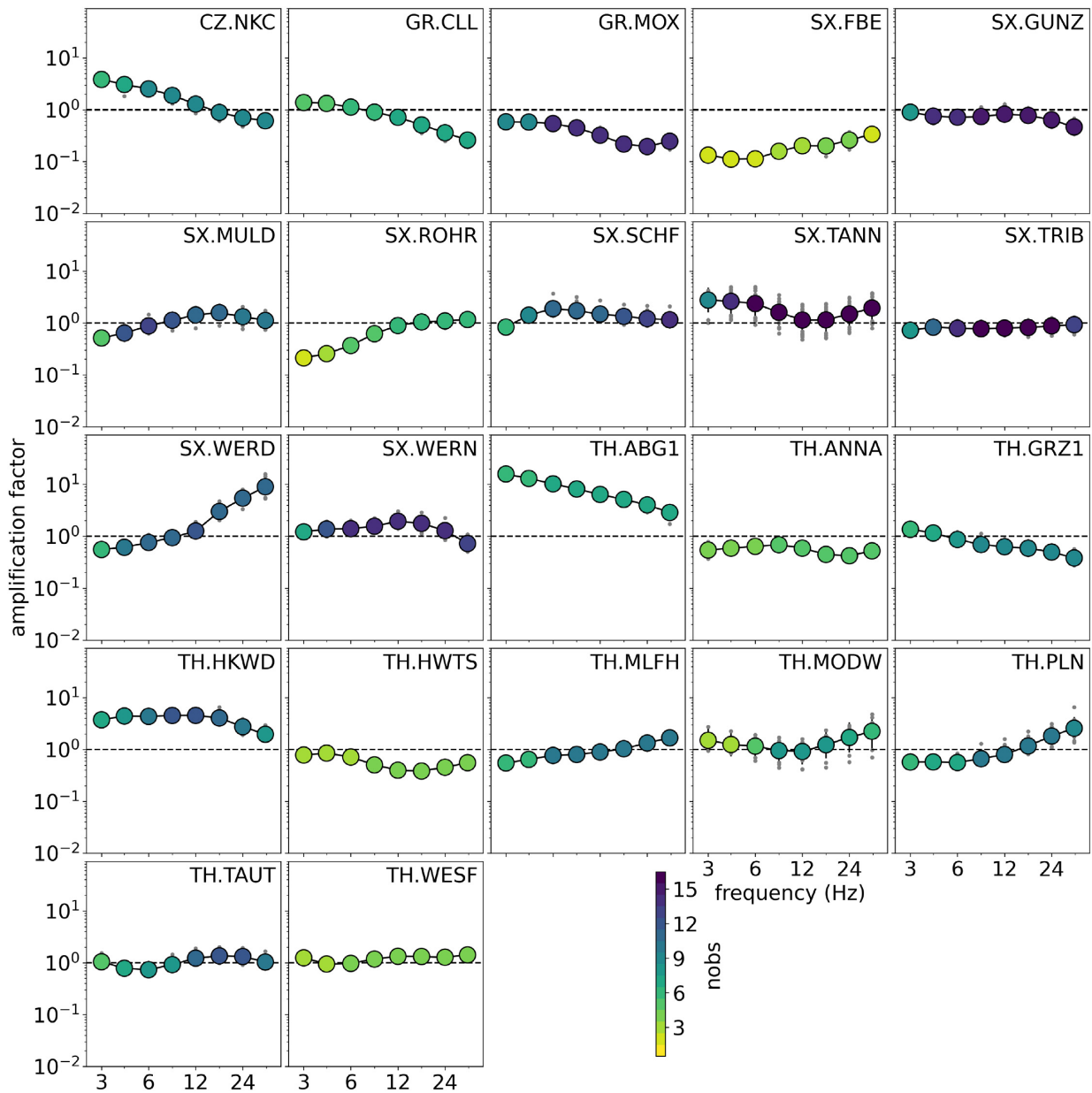


**Figure 9.** Inverted site amplification of each station. Grey dots indicate the result for individual measurements of one event. The coloured circles represent the median and the number of events used in the corresponding frequency.

The site amplification (Fig. 9) depends on the material near the surface and can vary greatly over short distances. Stations located on sedimentary rocks usually have a site amplification factor greater than 1, whereas stations located below the surface usually exhibit a factor below 1. Especially the stations AGB1, FBE, HKWD, MOX and WERD stand out among the site amplification. Station AGB1 is located on sediments, explaining the much larger site amplification factor. MODW, which is also on sediment, has a much smaller value in the range of 1. The low values of ANNA, FBE and MOX can be explained by the location in an adit below the surface, while TANN, which is also in an adit, shows higher values. The location of all other stations is on the surface. The reasons for the last two conspicuous site amplification, at station WERD, where site amplification increases strongly at high frequencies, and at station HKWD, which generally shows high values, are unknown. It should also be noted that MODW and TANN’s values are largely scattered, leading to errors greater than those for other stations.

### 4.3 Comparison of methods and other studies

A fit between synthetic and observed data of an event with  $M_L = 2.4$  and the central frequency of 8.5 Hz is shown in Fig. 10 for the nine closest stations. Eq. (4) was used to calculate the synthetic envelopes. The envelope of the MLTWA was normalized using the mean value of the time window 60–65 s after the origin time of the observed data. The energy of the direct wave of the MLTWA was calculated analogously

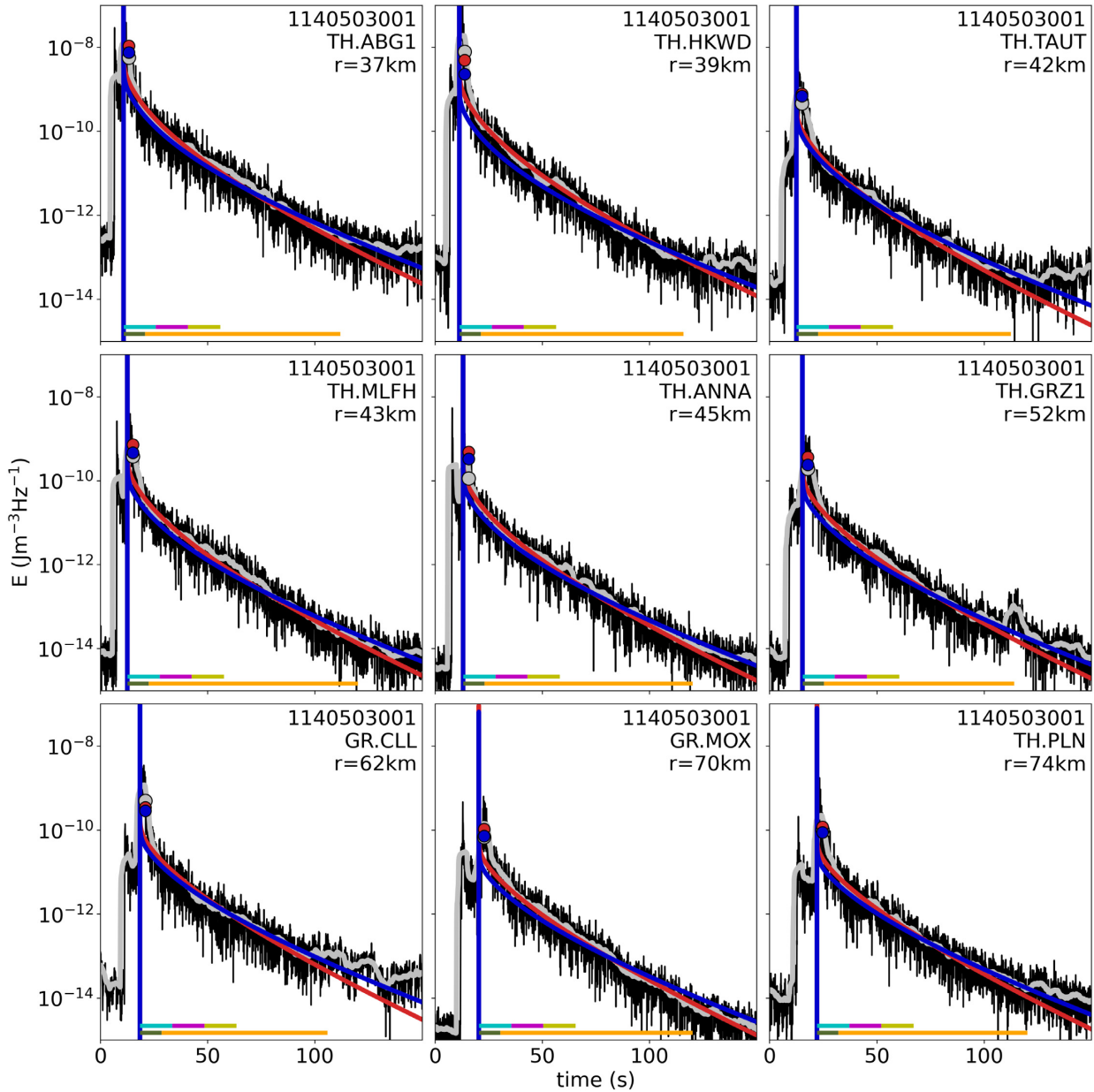


**Figure 10.** Fits between observed (black), smoothed observed envelope (grey) and synthetic energy densities of the inversion of MLTWA (blue line) and Qopen (red line) of an event ( $M_L$  2.4,  $M_W$  2.45) in the frequency band 4.25–12.75 Hz. The dots show the energy of the direct wave in the respective colour. The bar below the envelope represents the section used for the MLTWA and Qopen, respectively. Cyan, magenta and yellow indicate the three energy windows of the MLTWA and olive and orange the direct wave and coda window used for Qopen. Only the nine stations closest to the event are shown here.

to Qopen. The attenuation values were determined using only data from this event and are  $6.5 \times 10^{-4}$  and  $8.5 \times 10^{-4}$  for  $Q_i^{-1}$  and  $1.2 \times 10^{-4}$  and  $1.6 \times 10^{-4}$  for  $Q_{sc}^{-1}$  for MLTWA and Qopen, respectively. Both methods show equally good fits, both for the direct wave window and the coda window. Depending on the station, sometimes Qopen and sometimes the MLTWA provides the best result. Overall, the observed data can be described well by the modelled data under the assumption of RTT with multiple isotropic scattering with the exception of the direct wave. The determined scattering attenuation and intrinsic attenuation of the different methods are shown in Fig. 11 and Table 1. Qopen and the coda normalized version of Qopen,  $Qopen^{cn}$ , provide similar results. Likewise, the results of MLTWA and Qopen are similar within their errors. However, a comparison of the error bars shows that the error of Qopen at  $Q_{sc}^{-1}$  are smaller than for the MLTWA. For  $Q_i^{-1}$ , both methods have errors of about the same size. A further reduction of the error would be achieved using the elastic wave theory or the elastic energy transfer theory instead of the acoustic energy transfer theory (e.g. Gaebler et al. 2015; Emoto et al. 2017). However, these may take much more computation time. An equal weighting of all three time windows of the MLTWA inversion would result in about 4 per cent lower values for  $Q_i^{-1}$  and  $Q_{sc}^{-1}$  and a coda normalized Qopen inversion with 45 s time window length and weighting of the bulk window of 0.5

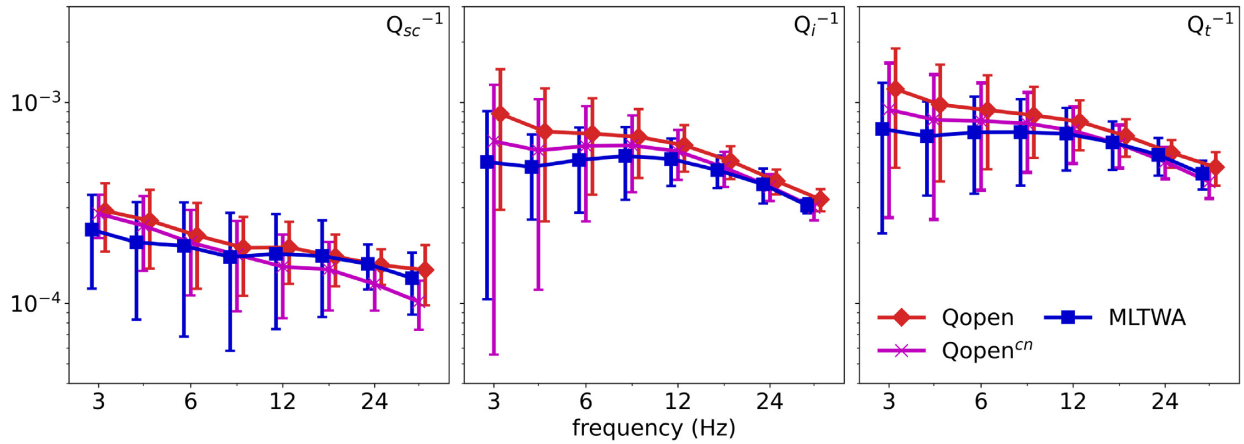


**Figure 11.** Comparison of the results of  $Q_{sc}^{-1}$ ,  $Q_i^{-1}$  and  $Q_t^{-1}$  with the interquartile range (75th and 25th percentile) as error of the different methods. The frequency values are slightly shifted for better presentation.

**Table 1.** Crustal scattering and intrinsic attenuation parameters.

| Frequency (Hz) | MLTWA                |                      | Qopen                |                      |
|----------------|----------------------|----------------------|----------------------|----------------------|
|                | $Q_i^{-1}$           | $Q_{sc}^{-1}$        | $Q_i^{-1}$           | $Q_{sc}^{-1}$        |
| 3              | $5.0 \times 10^{-4}$ | $2.3 \times 10^{-4}$ | $8.7 \times 10^{-4}$ | $2.8 \times 10^{-4}$ |
| 4.2            | $4.7 \times 10^{-4}$ | $2.0 \times 10^{-4}$ | $7.1 \times 10^{-4}$ | $2.5 \times 10^{-4}$ |
| 6              | $5.1 \times 10^{-4}$ | $1.9 \times 10^{-4}$ | $6.9 \times 10^{-4}$ | $2.1 \times 10^{-4}$ |
| 8.5            | $5.4 \times 10^{-4}$ | $1.7 \times 10^{-4}$ | $6.7 \times 10^{-4}$ | $1.8 \times 10^{-4}$ |
| 12             | $5.2 \times 10^{-4}$ | $1.8 \times 10^{-4}$ | $6.1 \times 10^{-4}$ | $1.8 \times 10^{-4}$ |
| 17             | $4.6 \times 10^{-4}$ | $1.7 \times 10^{-4}$ | $5.1 \times 10^{-4}$ | $1.7 \times 10^{-4}$ |
| 24             | $3.9 \times 10^{-4}$ | $1.5 \times 10^{-4}$ | $4.0 \times 10^{-4}$ | $1.5 \times 10^{-4}$ |
| 34             | $3.0 \times 10^{-4}$ | $1.3 \times 10^{-4}$ | $3.2 \times 10^{-4}$ | $1.4 \times 10^{-4}$ |

would result in 8 per cent lower values of  $Q_i^{-1}$  and 13 per cent lower values for  $Q_{sc}^{-1}$ . Therefore, although the difference between the methods is slightly larger, the systematic errors are still smaller than the error bars.

The inverse quality factor is monotonically decreasing for both the scattering attenuation and the intrinsic attenuation, only at low frequencies of  $Q_i^{-1}$  there is a slight flattening. In this context, the results of Qopen are more in line with the power law than the results of MLTWA. The reason for the slight flattening at low frequencies might be, on the one hand, an imprecise fitting of the envelope due to shorter time windows and, on the other hand, a small amount of data due to the SNR criterion. As a result, the error bars at low frequencies are significantly larger than at high frequencies. A comparison between the two attenuations also shows that the error bars of  $Q_i^{-1}$  are significantly smaller than the error bars of  $Q_{sc}^{-1}$  for both methods. The comparison of the absolute values of the attenuation shows that in the study area,  $Q_i^{-1}$  has significantly larger values than  $Q_{sc}^{-1}$ , implying intrinsic attenuation dominates in the study area. Gaebler *et al.* (2015) provide a similar result for the NW-Bohemia/Vogtland region (Fig. 12) which lies only a few kilometres south of our investigation area. Again, intrinsic attenuation dominates over scattering attenuation. However, the inverse quality factors of Gaebler *et al.* (2015) are higher than the values of this study by a factor between 2 and 8, indicating some spatial heterogeneity of attenuation within the region. The frequency dependence of the total attenuation is described by the power law (eq. 3) and yields the best fit at  $Q_{sc}^{-1} \propto f^{-0.28}$ ,  $Q_i^{-1} \propto f^{-0.37}$  and  $Q_t^{-1} \propto f^{-0.35}$  for Qopen and  $Q_{sc}^{-1} \propto f^{-0.20}$ ,  $Q_i^{-1} \propto f^{-0.17}$  and  $Q_t^{-1} \propto f^{-0.18}$  for MLTWA. Comparing the power laws of both methods, they provide similar values for  $Q_{sc}^{-1}$ . However, there are differences for  $Q_i^{-1}$ , due to the flattening of the intrinsic attenuation at low frequencies of MLTWA. Compared to the LRZ, the values of the NW-Bohemia/Vogtland region are  $Q_{sc}^{-1} \propto f^{-0.71}$ ,  $Q_i^{-1} \propto f^{-0.93}$  and  $Q_t^{-1} \propto f^{-0.86}$ , respectively. Using the exponent  $n$  of the frequency dependence (eq. 3) of  $Q_{sc}^{-1}$  the Hurst parameter  $\kappa$  can be calculated with  $n = -2\kappa$ , describing the roughness of a medium (Sato *et al.* 2012). With Qopen, this parameter is  $\kappa = 0.14$  and thus only about half as large as the result of Gaebler *et al.* (2015) of the neighbouring NW-Bohemia/Vogtland region with  $\kappa = 0.36$ . The difference in the Hurst parameter between NW-Bohemia/Vogtland and LRZ has the same cause as the difference in the power law between Qopen and MLTWA. The study of Gaebler *et al.* (2015) uses low frequencies which have a strong influence on the slope of the power law (Fig. 12). Looking only at the mid and high frequencies above 6 Hz, the decrease of the attenuation values over the frequencies is similar to the LRZ region.

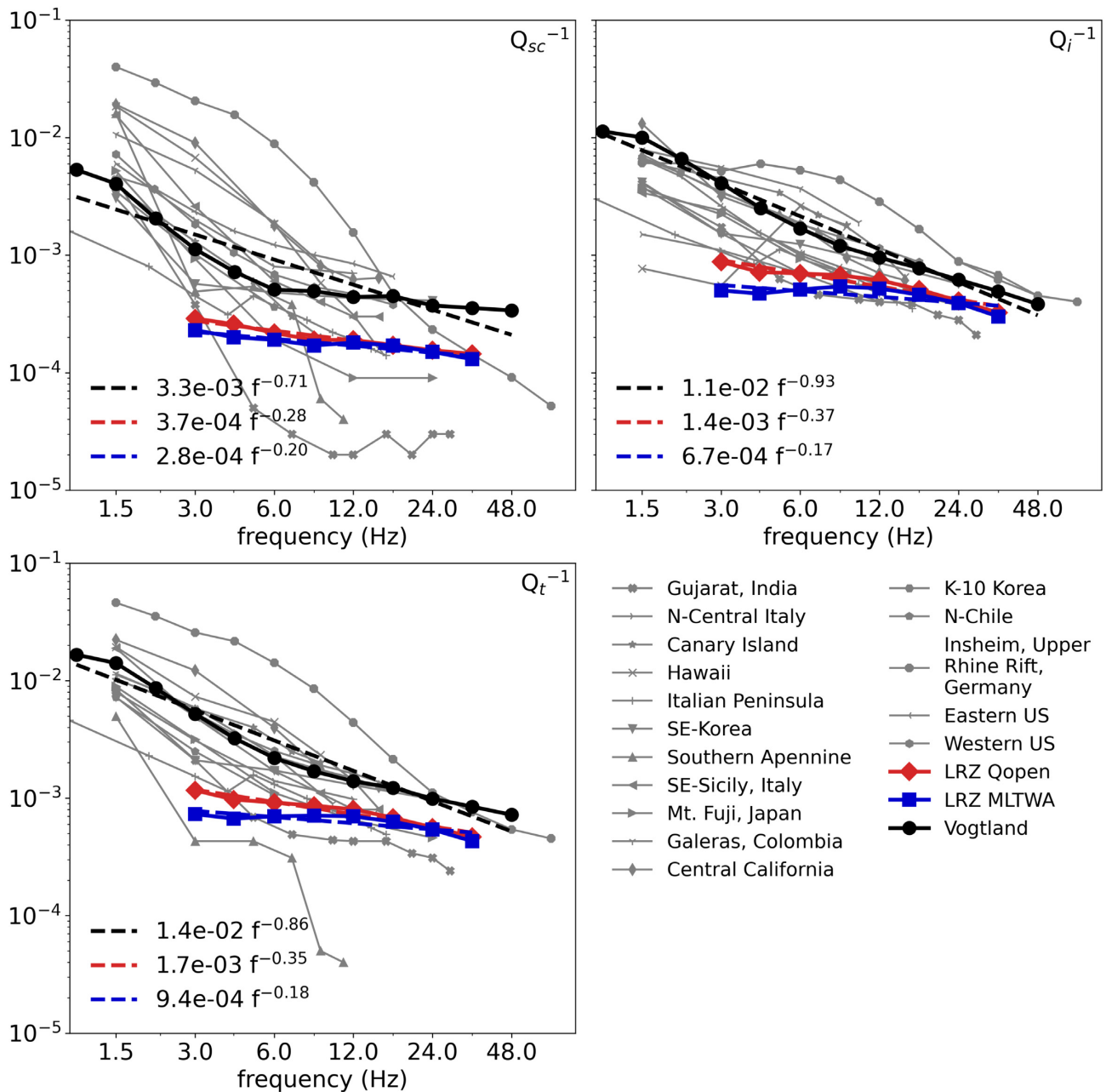


**Figure 12.** Qopen (red) and MLTWA (blue) results of this study and the results of Gaebler *et al.* (2015) of the neighbouring Vogtland region (black) and some other studies for comparison [Gujarat, India: Ugalde *et al.* (2007); N-Central Italy: Del Pezzo *et al.* (2011); Canary Island: Canas *et al.* (1998); Hawaii: Mayeda *et al.* (1992); Italian Peninsula: Bianco *et al.* (2005); SE-Korea: Chung (2014); Southern Apennine: Bianco *et al.* (2002); SE-Sicily, Italy: Giampiccolo *et al.* (2006); Mt. Fuji, Japan: Chung *et al.* (2009); Galeras, Colombia: Ugalde *et al.* (2010); Central California: Mayeda *et al.* (1992); K-10 Korea: Chung & Asep (2013); N-Chile: Hoshiba *et al.* (2001); Insheim: Eulenfeld & Wegler (2016); Eastern & Western US: Eulenfeld & Wegler (2017)]. The dashed lines display the fit of the power law.

## 5 CONCLUSION

Two methods were applied to determine intrinsic and the scattering attenuation of the central LRZ region in the frequency band range between 3 and 34 Hz. The MLTWA uses the average of three consecutive time windows of the envelope to determine the attenuation values. Qopen, on the other hand, uses the entire envelope to determine the attenuation values, as far as the SNR allows. Care should be taken when selecting the window lengths in Qopen to avoid a trade-off between  $Q_i^{-1}$  and source displacement spectra. The time window of the direct wave should include the *S*-onset and the forward scattered waves and should be in the range of 4–10 s for local studies. For the coda time window, we recommend a minimum length of 30 s to avoid trade-offs. The results show that both methods provide identical values within their error bars. On closer examination of the data, the Qopen method is more consistent with the power law of the frequency-dependent attenuation parameters for our data set than the MLTWA. In addition, Qopen can also be used to determine the site amplification of the stations and

source spectra of the earthquakes, as well as the moment magnitude (Eulenfeld *et al.* 2021), which is not possible with the coda normalized MLTWA. The determined intrinsic as well as the scattering attenuation are lower in the central part of the LRZ than in its southern part. This correlates well with higher swarm earthquake activity and ascending fluids in the south. A 3-D inversion of attenuation parameters is required to image this in more detail.

## ACKNOWLEDGEMENTS

We thank two anonymous reviewers whose comments contributed significantly to the improvement of the manuscript. We would also like to thank the operators of the networks TSN, SXNET, GR and CZ and the BGR. SeismicHandler was funded by the German Research Foundation (DFG) within the framework of SPP-1066. Data processing and plotting were performed with ObsPy (Krischer *et al.* 2015), NumPy (Harris *et al.* 2020) and Matplotlib (Hunter 2007).

## DATA AVAILABILITY

The waveform data are available via <https://eida.bgr.de/> and <http://eida.gfz-potsdam.de>. The topographical data can be found at <https://earthexplorer.usgs.gov/> (SRTM 2021). The MLTWA-Python code used in this work is available on request from the author. Qopen is available at: <https://github.com/trichter/qopen> (Eulenfeld 2021).

## REFERENCES

- Aki, K. & Chouet, B., 1975. Origin of coda waves: source, attenuation and scattering effects, *J. geophys. Res.*, **80**, 3322–3342.
- Aki, K., 1980. Attenuation of shear-waves in the lithosphere for frequencies from 0.05 to 25 Hz, *Phys. Earth Planet. Inter.*, **21**, 50–60.
- Bachura, M. & Fischer, T., 2016. Coda attenuation analysis in the West Bohemia/Vogtland Earthquake Swarm Area, *Pure appl. Geophys.*, **173**, 425–437.
- Bankwitz, P., Schneider, G., Kämpf, H. & Bankwitz, E., 2003. Structural characteristics of epicentral areas in Central Europe: study case Cheb basin (Czech Republic), *J. Geodyn.*, **35**, 5–32.
- Bethmann, F., Deichmann, N. & Mai, P.M., 2011. Scaling relations of local magnitude versus moment magnitude for sequences of similar earthquakes in Switzerland, *Bull. seism. Soc. Am.*, **101**, 515–534.
- Bianco, F., Del Pezzo, E., Castellano, M., Ibanez, J.M. & Di Luccio, F., 2002. Separation of intrinsic and scattering seismic attenuation in the Southern Apennine zone, Italy, *Geophys. J. Int.*, **150**, 10–22.
- Bianco, F., Del Pezzo, E., Malagnini, L., Di Luccio, F. & Akinci, A., 2005. Separation of depth-dependent intrinsic and scattering seismic attenuation in the northeastern sector of the Italian Peninsula, *Geophys. J. Int.*, **161**, 130–142.
- Bräuer, K., Kämpf, H. & Strauch, G., 2009. Earthquake swarms in non-volcanic regions: what fluids have to say, *Geophys. Res. Lett.*, **36**, L17309.
- Calvet, M., Sylvander, M., Margerin, L. & Villaseñor, A., 2013. Spatial variations of seismic attenuation and heterogeneity in the Pyrenees: Coda Q and peak delay time analysis, *Tectonophysics*, **608**, 428–439.
- Canas, J.A., Ugalde, A., Pujades, L.G., Carracedo, J.C., Soler, V. & Blanco, M.J., 1998. Intrinsic and scattering seismic wave attenuation in the Canary Islands, *J. geophys. Res.*, **103**, 15037–15050.
- Carcolé, E. & Sato, H., 2010. Spatial distribution of scattering loss and intrinsic absorption of short-period S waves in the lithosphere of Japan on the basis of Multiple Lapse Time Window Analysis of Hi-net data, *Geophys. J. Int.*, **180**, 268–290.
- Czech Regional Seismic Network, 2019. Institute of Geophysics, Academy of Sciences of the Czech Republic, International Federation of Digital Seismograph Networks, doi:10.7914/SN/CZ.
- Chung, T.W., Lees, J.M., Yoshimoto, K., Fujita, E. & Ukawa, M., 2009. Intrinsic and scattering attenuation of the Mt Fuji Region, Japan, *Geophys. J. Int.*, **177**, 1366–1382.
- Chung, T.W. & Asep, N.R., 2013. Multiple Lapse Time Window Analysis of the Korean Peninsula considering focal depth, *J. Korean Soc. Earth Explor. Geophys.*, **16**, 293–299 (in Korean).
- Chung, T.W., 2014. Quantitative study of the separation of intrinsic and scattering seismic attenuation in southeastern Korea using the Monte Carlo simulation method, *Disaster Adv.*, **7**(3), 7–17.
- Deichmann, N., 2006. Local magnitude, a moment revisited, *Bull. seism. Soc. Am.*, **96**, 1267–1277.
- Del Pezzo, E., Bianco, F., Marzorati, S., Augliera, P., D’Alema, E. & Massa, M., 2011. Depth-dependent intrinsic and scattering seismic attenuation in north central Italy, *Geophys. J. Int.*, **186**, 373–381.
- Emoto, K., Saito, T. & Shiomi, K., 2017. Statistical parameters of random heterogeneity estimated by analysing coda waves based on finite difference method, *Geophys. J. Int.*, **211**, 1575–1584.
- Eulenfeld, T. & Wegler, U., 2016. Measurement of intrinsic and scattering attenuation of shear waves in two sedimentary basins and comparison to crystalline sites in Germany, *Geophys. J. Int.*, **202**, 744–757.
- Eulenfeld, T. & Wegler, U., 2017. Crustal intrinsic and scattering attenuation of high-frequency shear waves in the contiguous United States, *J. geophys. Res.*, **122**, 4676–4690.
- Eulenfeld, T., 2021. *trichter/qopen* (Zenodo), doi:10.5281/zenodo.3953654.
- Eulenfeld, T., Dahm, T., Heimann, S. & Wegler, U., 2021. Fast and robust earthquake source spectra and moment magnitudes from envelope inversion, *Bull. seism. Soc. Am.*, <https://arxiv.org/abs/2107.11083>.
- Fehler, M., Hoshihara, M., Sato, H. & Obara, K., 1992. Separation of scattering and intrinsic attenuation for the Kanto-Tokai region, Japan, using measurements of S-wave energy versus hypocentral distance, *Geophys. J. Int.*, **108**, 787–800.
- Fischer, T., Horálek, J., Hrubcová, P., Vavryčuk, V., Bräuer, K. & Kämpf, H., 2014. Intra-continental earthquake swarms in West-Bohemia and Vogtland: a review, *Tectonophysics*, **611**, 1–27.
- Gaebler, P.J., Eulenfeld, T. & Wegler, U., 2015. Seismic scattering and absorption parameters in the W-Bohemia/Vogtland region from elastic and acoustic radiative transfer theory, *Geophys. J. Int.*, **203**, 1471–1481.
- Giampiccolo, E., Tuvè, T., Gresta, S. & Patanè, D., 2006. S-waves attenuation and separation of scattering and intrinsic absorption of seismic energy in southeastern Sicily (Italy), *Geophys. J. Int.*, **165**, 211–222.
- German Regional Seismic Network, 2019. Federal Institute for Geosciences and Natural Resources (BGR), doi:10.25928/MBX6-HR74.
- Grünthal, G., Bankwitz, P., Bankwitz, E., Bednarek, J., Guterch, B., Schenk, V., Schenková Z. & Zeman, A., 1985. Seismicity and geological features of the eastern part of the West European Platform, *Gerlands Beiträge zur Geophys.*, **94**, 276–289.
- Hanks, T.C. & Kanamori, H., 1979. A moment magnitude scale, *J. geophys. Res.*, **84**, 2348–2350.
- Harris, C.R. *et al.*, 2020. Array programming with NumPy, *Nature*, **585**, 357–362.
- Heimann, S. *et al.*, 2018. Grond — a probabilistic earthquake source inversion framework, GFZ Dat Services, doi:10.5880/GFZ.2.1.2018.003.
- Hemmman, A., Meier, T., Jentzsch, G. & Ziegert, A., 2003. Similarity of waveforms and relative relocalisation of the earthquake swarm 1997/1998 near Werdau, *J. Geodyn.*, **35**, 191–208.

- Hunter, J.D., 2007. Matplotlib: a 2D Graphics Environment, *Comput. Sci. Eng.*, **9**, 90–95.
- Hofmann, Y., Jahr, T. & Jentzsch, G., 2003. Three-dimensional gravimetric modelling to detect the deep structure of the region Vogtland/NW-Bohemia, *J. Geodyn.*, **35**, 209–220.
- Hoshiaba, M., Rietbrock, A., Scherbaum, F., Nakahara, H. & Haberland, C., 2001. Scattering attenuation and intrinsic absorption using uniform and depth dependent model - Application to full seismogram envelope recorded in Northern Chile, *J. Seismol.*, **5**, 157–179.
- Ibs-von Seht, M., Plenefisch, T. & Klinge, K., 2008. Earthquake swarms in continental rifts—a comparison of selected cases in America, Africa and Europe, *Tectonophysics*, **452**, 66–77.
- Krischer, L., Megies, T., Barsch, R., Beyreuther, M., Lecocq, T., Caudron, C. & Wassermann, J., 2015. ObsPy: a bridge for seismology into scientific Python ecosystem, *Comput. Sci. Discov.*, **8**(1), 014003.
- Korn, M., Funke, S. & Wendt, S., 2008. Seismicity and seismotectonics of West Saxony, Germany—new insights from recent seismicity observed with the Saxonian seismic network, *Stud. Geophys. Geod.*, **52**, 479–492.
- LfULG - Sächsisches Landesamt für Umwelt, Landwirtschaft und Geologie, 2018. Digitales geologisches und seismologisches Kartenmaterial des Freistaates Sachsen, Available at: <https://www.lfulg.sachsen.de/karte-n-und-daten-13433.html>.
- Mayeda, K., Koyanagi, S., Hoshiaba, M., Aki, K. & Zeng, Y., 1992. A comparative study of scattering, intrinsic, and coda  $Q^{-1}$  for Hawaii, Long Valley, and central California between 1.5 and 15.0 Hz, *J. geophys. Res.*, **97**, 6643–6659.
- Mayor, J., Calvet, M., Margerin, L., Vanderhaeghe, O. & Traversa, P., 2016. Crustal structure of the Alps as seen by attenuation tomography, *Earth planet. Sci. Lett.*, **439**, 71–80.
- Meirova, T. & Pinsky, V., 2014. Seismic wave attenuation in Israel region estimated from the multiple lapse time window analysis and S-wave coda decay rate, *Geophys. J. Int.*, **197**, 581–590.
- Mousavi, S., Bauer, K., Korn, M. & Hejrani, B., 2015. Seismic tomography reveals a mid-crustal intrusive body, fluid pathways and their relation to the earthquake swarms in West Bohemia/Vogtland, *Geophys. J. Int.*, **203**, 1113–1127.
- Neunhöfer, H., 1998. Das Bulletin der lokalen Erdbeben im Vogtland 1962–1997, *DGG Mitteilung*, **4**, 2–7 (n German).
- Neunhöfer, H. & Hemmann, A., 2005. Earthquake swarms in the Vogtland/Western Bohemia region: spatial distribution and magnitude-frequency distribution as an indication of the genesis of swarms?, *J. Geodyn.*, **39**, 361–385.
- Paasschens, J., 1997. Solution of the time-dependent Boltzmann equation, *Phys. Rev. E*, **56**, 1135–1141.
- Pitzsch, K., 1963. *Geologie von Sachsen*, Dt. Verl. Wiss., Berlin, in German.
- Przybilla, J., Korn, M. & Wegler, U., 2006. Radiative transfer of elastic waves versus finite difference simulations in two-dimensional random media, *J. geophys. Res.*, **111**, 148–227.
- Saito, T., Sato, H., Ohtake, M. & Obara, K., 2005. Unified explanation of envelope broadening and maximum-amplitude decay of high-frequency seismograms based on the envelope simulation using the Markov approximation: forearc side of the volcanic front in northeastern Honshu, Japan, *J. geophys. Res.*, **110**, B01304, doi:10.1029/2004JB003225.
- Sato, H., Fehler, M.C. & Maeda, T., 2012. *Seismic Wave Propagation and Scattering in the Heterogeneous Earth*, 2nd edn., Springer, Berlin.
- Sens-Schönfelder, C. & Wegler, U., 2006. Radiative transfer theory for estimation of the seismic moment, *Geophys. J. Int.*, **167**, 1363–1372.
- Sens-Schönfelder, C., Margerin, L. & Campillo, M., 2009. Laterally heterogeneous scattering explains Lg blockage in the Pyrenees, *J. geophys. Res.*, **114**, 148–227.
- Shearer, P.M. & Earle, P.S., 2004. The global short-period wavefield modelled with a Monte Carlo seismic phonon method, *Geophys. J. Int.*, **158**, 1103–1117.
- Shito, A. *et al.*, 2020. 3-D intrinsic and scattering seismic attenuation structures beneath Kyushu, Japan, *J. geophys. Res.*, **125**, e2019JB018742, doi:10.1029/2019JB018742.
- Shuttle Radar Topography Mission (SRTM) Non-Void Filled, 2021, doi:10.5066/F7K072R7.
- Špičák, A. & Horálek, J., 2001. Possible role of fluids in the process of earthquake swarm generation in the West Bohemia/Vogtland seismoactive region, *Tectonophysics*, **336**, 151–161.
- Stammler, K., 1993. SeismicHandler: programmable multichannel data handler for interactive and automatic processing of seismological analyses, *Comput. Geosci.*, **19**, 135–140.
- Saxon Seismic Network, 2019. *University of Leipzig, International Federation of Digital Seismograph Networks*, doi:10.7914/SN/SX.
- Thüringer Seismologisches Netz, 2019. *Institut für Geowissenschaften, Friedrich-Schiller-Universität Jena, International Federation of Digital Seismograph Networks*, doi:10.7914/SN/TH.
- Ugalde, A., Tripathi, J.N., Hoshiaba, M. & Rastogi, B.K., 2007. Intrinsic and scattering attenuation in western India from aftershocks of 26 January, 2001 Kachchh earthquake, *Tectonophysics*, **429**, 111–123.
- Ugalde, A., Carcolé, E. & Cargas, C.A., 2010. S-wave attenuation characteristics in the Galeras volcanic complex (south western Colombia), *Phys. Earth planet. Inter.*, **181**, 73–81.
- Weise, S., Bräuer, K., Kämpf, H., Strauch, G. & Koch, U., 2001. Transport of mantle volatiles through the crust traced by seismically released fluids: a natural experiment in the earthquake swarm area Vogtland/NW-Bohemia, Central Europe, *Tectonophysics*, **336**, 137–150.

## 6.2 Publication 2

### **On the trail of fluids in the northernmost intra-continental earthquake swarm areas of the Leipzig-Regensburg fault zone**

Marcel van Laaten<sup>1</sup>, Ulrich Wegler<sup>1</sup>, Tom Eulenfeld<sup>1</sup>

<sup>1</sup> Institute of Geosciences, Friedrich Schiller University Jena, Burgweg 11, 07749 Jena

Published in 2023 in *Journal of Seismology*, 27, pp. 573-597  
<https://doi.org/10.1007/s10950-023-10146-8>



RESEARCH

# On the trail of fluids in the northernmost intracontinental earthquake swarm areas of the Leipzig-Regensburg fault zone, Germany

Marcel van Laaten · Ulrich Wegler ·  
Tom Eulenfeld

Received: 2 May 2022 / Accepted: 12 April 2023 / Published online: 6 July 2023  
© The Author(s) 2023

**Abstract** The Leipzig-Regensburg fault zone is documented as a band of seismic activity extending northwards from the earthquake swarm region NW-Bohemia/Vogtland at the Czech-German border area and is intersected by several Hercynian fault zones. Along the fault zone, there are several earthquake swarm areas, the northernmost of which are Schöneck and Werdau. In this study, we investigate the presumably fluid-induced earthquake swarm activity of the Schöneck and Werdau area. For this purpose, we apply two methods: local earthquake tomography and receiver functions to identify the structural composition of the crust, the areas affected by fluids and the

origin of the fluids. We detected potential fluid paths characterised by high  $V_p/V_s$  ratios and granite intrusions nearby the swarms characterised by low  $V_p/V_s$  anomalies. Receiver function analysis yields the Moho at 25 to 33 km depth and two seismic discontinuities at 55 km and 68 km depth.

**Keywords** Seismic tomography · Body waves · Receiver functions · Seismicity and tectonics · Crustal imaging · Europe

## Highlights

- Tomography reveals the crustal structure in the central part of the Leipzig-Regensburg fault zone
- Fluids trigger earthquake swarms in the vicinity of intrusive bodies
- Fluid source is an anomaly in the uppermost mantle that reaches up to Werdau.

M. van Laaten (✉) · U. Wegler · T. Eulenfeld  
Institute of Geosciences, Friedrich Schiller University Jena,  
Burgweg 11, Jena 07749, Germany  
e-mail: marcel.vanlaaten@uni-jena.de

U. Wegler  
e-mail: ulrich.wegler@uni-jena.de

T. Eulenfeld  
e-mail: tom.eulenfeld@uni-jena.de

## 1 Introduction

Earthquake swarms are sequences of seismic earthquakes that occur within a local area without a discernible main shock and are therefore distinct from normal earthquake sequences that include a main earthquake and aftershocks. Earthquake swarms are common in volcanic and hydrothermal areas (e.g. Zaliapin and Ben-Zion 2013; Shelly et al. 2016; White et al. 2019; Bachura et al. 2020) or in relation to the injection of industrial fluids (Horton 2012). Magma and fluid movement are suspected of causing seismicity by decreasing the effective normal stress and thus reducing resistance to slip (Hubbert and Rubey 1959). In contrast, intracontinental tectonic earthquake swarms without volcanic or geothermal activity are rare. In this study, we investigate the source of the northernmost

earthquake swarm areas of the Leipzig-Regensburg fault zone (LRZ) and the reason for the absence of earthquake swarms further north. For this purpose, we use two different techniques to investigate earthquake swarms. Local earthquake tomography (LET) is used to image the crustal volume; receiver functions (RFs) are used to image the crust and uppermost mantle. Since the  $V_p/V_s$  is very sensitive to fluids (O'Connell and Budiansky 1974; Schmeling 1985; Mavko and Mukerji 1995; Takei 2002), the LET can be used to identify areas affected by fluids, such as the earthquake swarm areas, while RFs provide information about the source of the fluids. Previous attenuation studies along the LRZ have shown differences in attenuation behaviour between the central/northern (van Laaten et al. 2022a) and southern parts of the LRZ (Gaebler et al. 2015; Eulenfeld et al. 2021). The fluid-sensitive intrinsic attenuation in the southern part is larger, by a factor of 2 to 8, than in the central/northern part depending on the frequency, indicating a certain level of heterogeneity along the fault zone (van Laaten et al. 2022a).

### 1.1 Earthquake swarms in NW-Bohemia/Vogtland

The earthquake swarms occur in several known clusters along the LRZ (Korn et al. 2008; Fischer et al. 2014). Some of these have been well studied (Horálek and Fischer 2008; Fischer et al. 2014), such as the earthquake swarms in the NW-Bohemia/Vogtland region (Fig. 1). Various observations indicate that uprising mantle-derived magmatic fluids trigger the earthquake swarms of NW-Bohemia/Vogtland (Špičák and Horálek 2001; Weise et al. 2001; Hofmann et al. 2003; Bräuer et al. 2009; Mousavi et al. 2015; Hrubcová et al. 2017; Vlček et al. 2022) coming from an updomed Moho below NW-Bohemia/Vogtland (Geissler et al. 2005; Hrubcová et al. 2017). A low-velocity zone in the upper mantle around 65 km in depth, interpreted as partial melts or asthenospheric updoming, may be the initial source of these ascending fluids (Heuer et al. 2006). Another connection between fluids and earthquake swarm activity is the spatial distribution of epicentres, which roughly overlaps with gas escapes (Fischer et al. 2014). In contrast to the well-studied NW-Bohemia/Vogtland region, the northern earthquake swarm areas of the LRZ are not yet well-studied. The

region Werdau is known as the northernmost earthquake swarm area in the Saxothuringian Seismotectonic Province with the peculiarity of an increased intracontinental seismicity (Neunhöfer 1998). The main differences between the northern and southern earthquake swarm areas are the frequency of occurrence and the focal depths. The earthquakes in NW-Bohemia/Vogtland are much more frequent and shallower, with depths ranging from 6 to 10 km, compared to the northern earthquake swarm areas, which have depths ranging from 10 to 16 km.

### 1.2 Schöneck and Werdau earthquake swarm areas

The earthquake swarm areas Schöneck and Werdau (Fig. 1), named after nearby cities, are located in Germany. Most earthquakes in the Werdau area occur at the intersection of the fault zones (Fig. 1). Outside of the intersection, the seismic activity is largely prevented by aseismic creep along the GJZ (Ellenberg 1992), leading to an accumulation of energy at the intersection (Hemmann et al. 2003). As a result, the released energy is higher compared to other earthquakes in NW-Bohemia/Vogtland, leading to an increased seismic hazard. The largest historical earthquake in the region in the past 700 years occurred near the GJZ/LRZ intersection on March 6, 1872, with an estimated moment magnitude of  $M_w = 5.2$ , and was felt at a distance of several hundred kilometres (von Seebach 1873).

From the period 1903 to 1999, 73 swarms from the LRZ region were analysed by Neunhöfer and Hemmann (2005). The b-values range from 0.5 to 1.5, with the intensive swarms of 1908, 1962, 1985/86, 1997 and 2000 being very close to 1. This value agrees with the observation of Ibs-von Seht et al. (2008), who determined a b-value of 0.8 for intracontinental earthquake swarms in non-volcanic areas. Recent swarm activities were observed in 1998, 2001, 2010, 2012/13, and 2017 for Schöneck and 1997/98, 2006, and 2016 for Werdau, with the 2016 swarm taking place northeast of Werdau rather than south of Werdau. The Schöneck earthquake swarm area can be divided into three smaller clusters (Fig. 1), the western cluster with focal depths between 13 and 17 km, the central cluster with focal depths between 8 and 13 km and the eastern cluster with focal depths between 8 and 13 km and occasionally depths

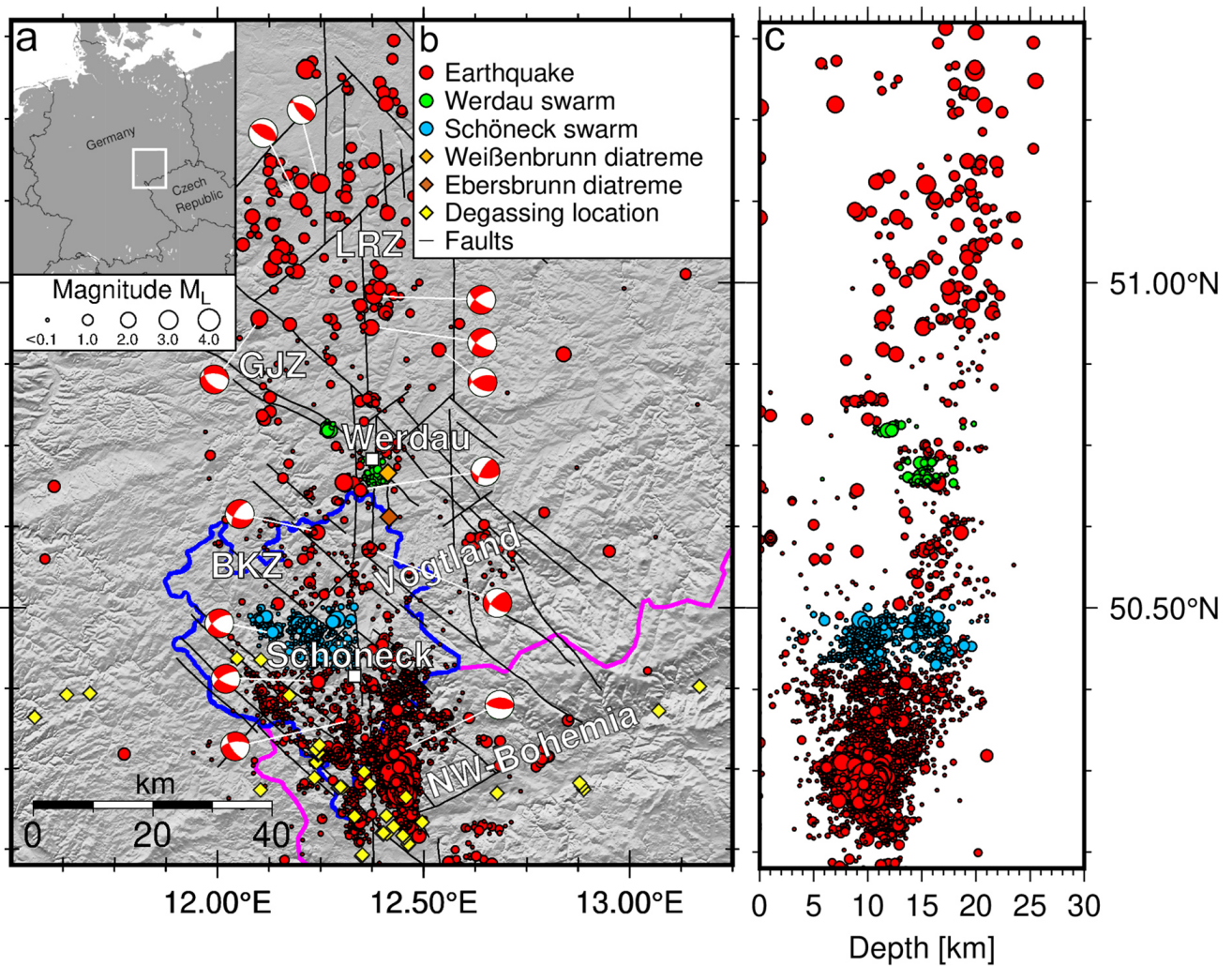


**Fig. 1** a) Overview map of the survey area and its location within Europe. b) Hillshade of the survey area. c) N-S section. Major fault zones are shown as black lines, such as the Leipzig-Regensburg fault zone (LRZ), the Gera-Jáchymov fault zone (GJZ) and the Bergen-Klingenthal-Chodov fault zone (BKZ). The tectonic earthquakes are shown as red circles, size representing their magnitude, while the earthquake swarms of the Schöneck area are shown in blue and the earthquake swarms of Werdau as green circles. Degassing locations (Mofette/Spring) are

marked as yellow and the diatremes of Weißenbrunn and Ebersbrunn as orange and brown diamonds, respectively. In addition, the focal mechanisms of some earthquakes along the LRZ are shown. The areas of Vogtland (blue outline) and NW-Bohemia (pink outline) as well as the locations of the cities of Schöneck and Werdau are indicated. Earthquake locations after Thüringer Seismologisches Netz (2021). Focal mechanisms were obtained with Grond (Heimann et al. 2018). Faults after LfULG (2018) and degassing locations after Geissler et al. (2005)

between 16 and 20 km. The focal depth of the Werdau earthquake swarms is ~16 km, except for the 2016 swarm northeast of Werdau, which had a focal depth of ~12 km. The swarm duration of Werdau and Schöneck was about one to two months, with approximately 40 to 70 located events. The maximum magnitudes of the swarms were in the range of 1.1 to 1.3 for Schöneck

and 1.7 to 2.8 for Werdau, respectively. In contrast to the NW-Bohemia/Vogtland region, CO<sub>2</sub> degassing near Schöneck and Werdau is not observed (Fischer et al. 2014; Heinicke et al. 2019). Since the Schöneck and Werdau earthquakes show a clear swarm character (Hemmam et al. 2003; Korn et al. 2008; Fischer et al. 2014), fluids might play an important role

in the swarm generation. The origin of these fluids is unknown since there is no detected escape at the surface and, therefore, the fluids cannot be analyzed. Hemmann et al. (2003), who investigated the waveform and relocation of the Werdau earthquake swarm, suggested that the fluids rise along the intersection of LRZ and GJZ within the crust. However, no hydro-chemical or younger volcanic activities like those known for the NW-Bohemia/Vogtland region have been observed for the region of Werdau (Hemmann et al. 2003). Only two smaller diatremes (Schmidt et al. 2013) near Werdau indicate past upper mantle fluid activity. Schüller et al. (2012) performed (U-Th)/He age determination test measurements on apatite and determined an age of  $\sim 113$ –96 Ma for one of the two diatremes, while the exact age of the other diatreme is still unknown. According to Alexowsky et al. (2007) the second diatrem is assumed to be Tertiary or Cretaceous in age.

### 1.3 Geological setting

The Vogtland area is part of the Saxothuringian Zone of the Variscan orogen (Pietzsch 1963). The area formed in several periods (Cambrian to Permian) and consists primarily of metamorphic rocks. It is bordered to the east by intrusions that were emplaced during the Variscan orogeny (Förster et al. 1999). Within the survey area, several Hercynian fault zones (Pietzsch 1963) also strike NW-SE, such as the GJZ located in the northern part and several parallel faults in the south, such as the Bergen-Klingenthal-Chodov fault zone (BKZ). Furthermore, the LRZ (Grünthal et al. 1985) crosses the survey area and is a N-S striking fault zone between the German cities of Leipzig and Regensburg with a seismically active middle part of about 150 km in length and 40 km in width between the Cheb basin in the Czech Republic and Leipzig (Kämpf et al. 1991; Bankwitz et al. 2003). The LRZ cannot be observed with geological methods as no corresponding geological displacements are visible in the investigated area. Older studies based on photolineations of satellite images claimed the observation of the LRZ at the surface (Bankwitz et al. 1979; Krull 1984; Grünthal et al. 1985; Bankwitz et al. 2003; Pohl et al. 2006), but these results were questioned by recent studies using modern satellite-

based data (Dahm et al. 2018; Grünthal et al. 2018). Therefore, the existence of the LRZ is mainly proven by the observation of an N-S trending seismicity (Fig. 1). A bundle of short N-S trending geophysical potential field structures provides further evidence for the LRZ (Becker et al. 1989).

## 2 Local earthquake tomography

### 2.1 Data

We used recordings from 2001 to 2018 at several seismic stations of the BW, CZ, GR, SX, SXNET and TH networks (Fig. 2). For the inversion, we considered earthquakes from the TH catalogue (Thüringer Seismologisches Netz 2021) between latitudes of 50.35°N and 51.08°N and longitudes of 12.0°E and 12.75°E. We divided the region into several cubes of 2 km in side length to ensure a balanced distribution of identical sources. We calculated the mean magnitude of all events in each cell and considered only events for the inversion whose magnitude was greater than the mean magnitude. In addition, we used several criteria to filter the events further. Each event must fulfil an azimuthal gap criterion of 160°, the magnitude of the event was required to be greater than  $-0.7$ , a minimum of five arrival times each for P- and S-waves were necessary for an event to be used for the inversion, the depth of the earthquake could not be greater than twice the distance to the nearest station and the maximum epicentral distance must be 110 km. After applying the criteria, the number of events decreased from about 2013 to 419 (Fig. 2).

All events were manually re-picked using SeismicHandler (Stammler 1993). Based on the scheme proposed by Evans et al. (1994), we used arrival time weightings to improve the quality of the data. Regardless of the wave type, each pick is given a quality class. These classes range from 0 (highest quality) to 2 (lowest quality) to account for the picking accuracy of 0.025, 0.05 and 0.1 s. For P-waves, 77, 22 and 1 per cent were in classes 0, 1 and 2, respectively; for S-waves, the proportions were 68, 30 and 2 per cent. The average uncertainty is 27 ms for P-waves and 30 ms for S-waves. This results in 4406 P-phase and 3910 S-phase picks for the

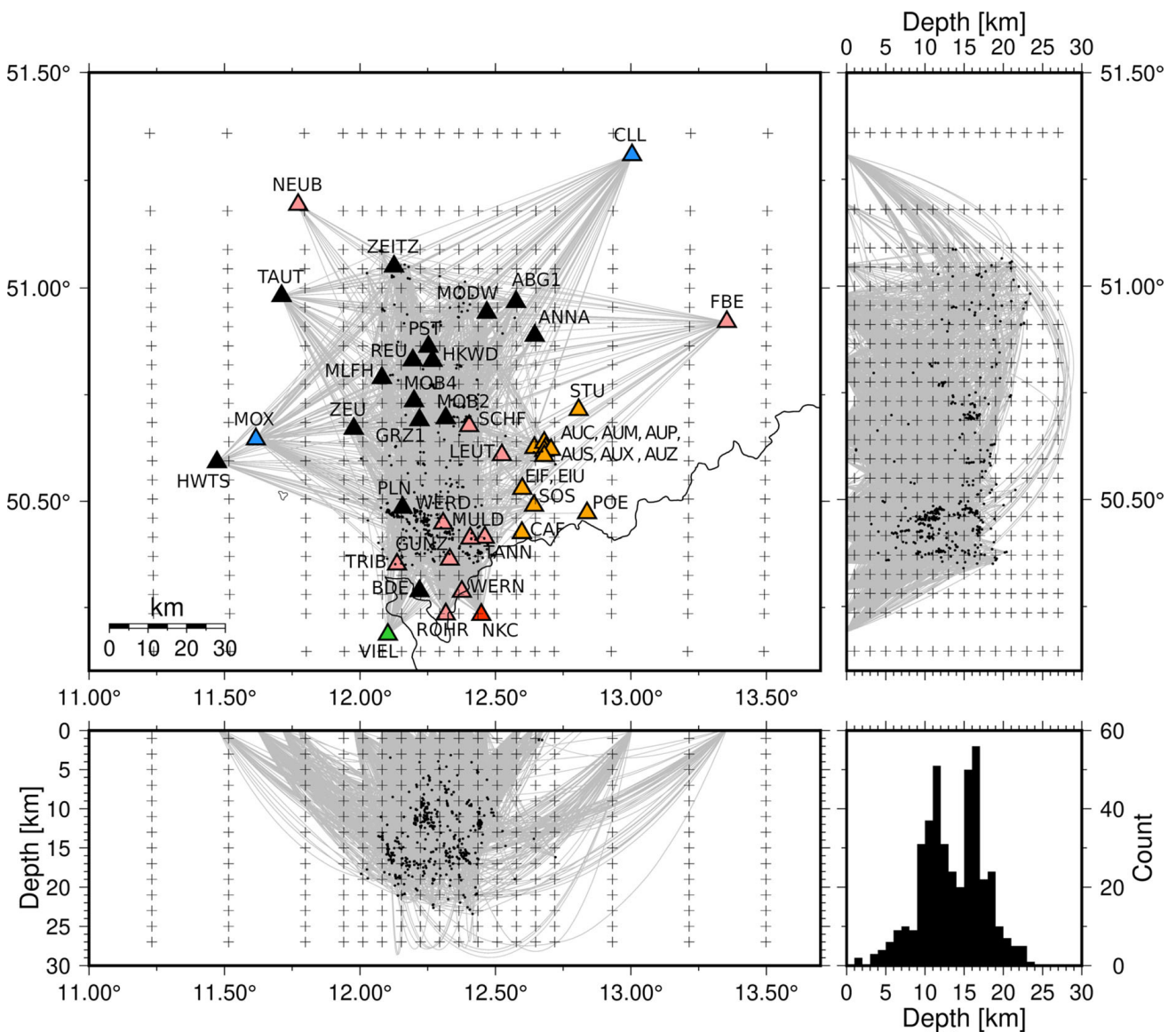


**Fig. 2** Map view and vertical sections with the ray coverage and the distribution of stations (triangles), selected and relocated seismic events (black dots) and grid nodes (black crosses) used in the inversion of SIMULPS14. The data were compiled

using different station networks: TSN (black), SXNET (pink), GR (blue), BayernNetz (green), WEBNET (red) and SXNET-offline (orange). The histogram plot shows the depth distribution of earthquakes

419 events used in the inversion with an average distance of 31 km.

### 2.2 1-D inversion

VELEST (Kissling et al. 1995) was used to invert for a minimum 1-D model. In order to obtain a reliable starting model and relocate the earthquakes for the 3-D inversion, it is necessary to first invert in 1-D to tackle

the non-uniqueness of the non-linearized inverse problem’s solution. The inversion depends on the starting model and initial hypocenters, so a trial-and-error procedure is necessary (Kissling et al. 1994). We used a wide range of starting models, beginning with a random velocity value for the surface and a random velocity gradient, resulting in several realistic and unrealistic models, as suggested by Boncio et al. (2004). A total of 1000 randomly generated starting models were produced, with a layer thickness of 1 km and a depth

extent to the approximate Moho depth of 30 km. To sufficiently relocate the earthquakes and better narrow the solution space of the inversion, the origin time and location of each event varied realistically and unrealistically with randomly Gaussian distributed error in the range of  $\pm 10$  km for latitude and longitude,  $\pm 0.1$  s for arrival time and  $\pm 5$  km for depth for each inversion. We used station SCHF as a reference station for VELEST due to its central location within the survey area and the high number of event recordings. Based on the Wadati diagram, the  $V_p/V_s$  ratio was fixed at 1.71, which is a comparable value to the adjacent region of NW-Bohemia (Málek et al. 2005; Mousavi et al. 2015). The final 1-D velocity model with the lowest RMS residual is displayed as a red line in Fig. 3. The inversion reduced the RMS error from 2.6 s in the starting model to 83 ms in the final model, which is still high compared to the average picking uncertainty. Most of the inverted models are similar to the best-fit model, but there are significant differences in the velocity of the near-surface layers. These layers are difficult to resolve with VELEST because of significant deviations from 1D layering near the surface. In addition to the accumulation of models around the best-fit model, there is another area of higher velocities where inverted models accumulate.

These models result from unrealistically high-velocity starting models ( $V_p$  at surface  $\geq 8$  km/s), which run into a local minimum during the inversion process. However, the RMS of these models with more than 160 ms is significantly higher than the best-fit model's RMS.

In addition, VELEST calculates the station corrections, indicating lateral variations of data fitting within the minimum 1-D velocity model (Kissling et al. 1995). Large-scale velocity variations and near-surface heterogeneity cause these variations. The station corrections sign represents the velocity variation compared to the 1-D velocity model at the reference station. Positive values indicate that the true velocities are lower compared to the 1-D velocity model and negative values indicate that the true velocity is higher. Figure 4 shows the calculated station corrections for the stations used in this study relative to the reference station SCHF ranging from  $-0.50$  to  $+0.48$  s. The P-wave corrections show similar values at stations with similar geology, with stations close to the reference station showing lower values than stations farther away. Relative positive station corrections of the P-wave can be observed in the north-west of SCHF, which can be explained by the sediments in that area. On the other

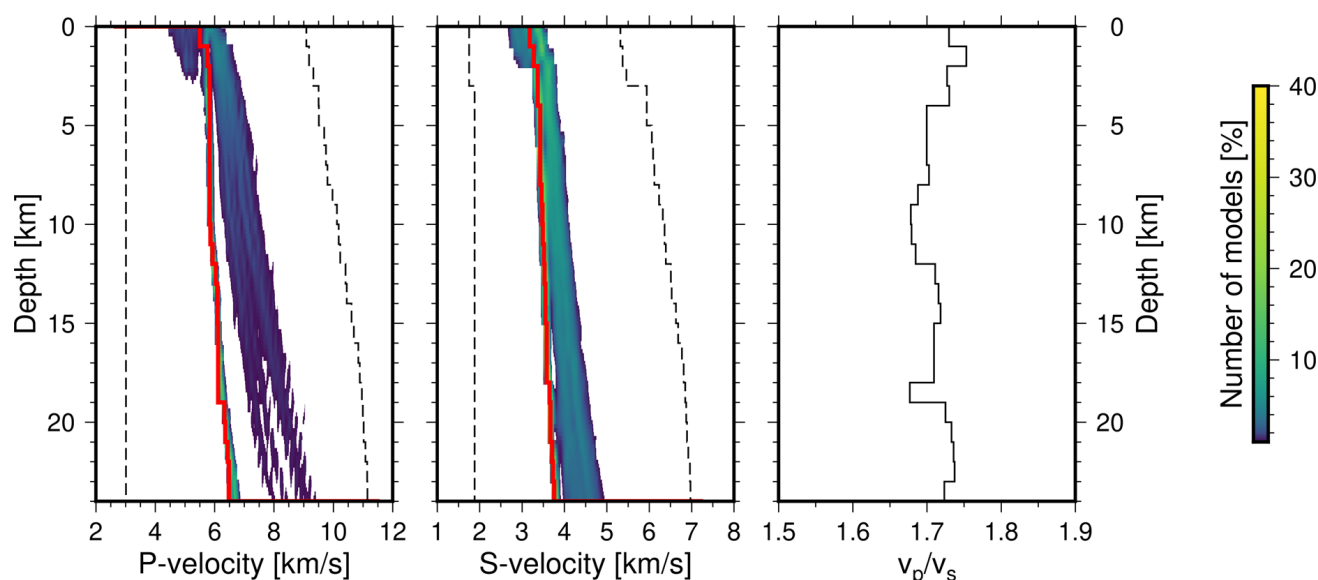


**Fig. 3** Final minimum 1-D velocity model for P-wave, S-wave and  $V_p/V_s$  ratio of the best model. The range of input models is indicated by the black dashed lines. The colour scale reflects the

number of 1000 inverted models passing each dot. The solid red line indicates the best model with the lowest RMS

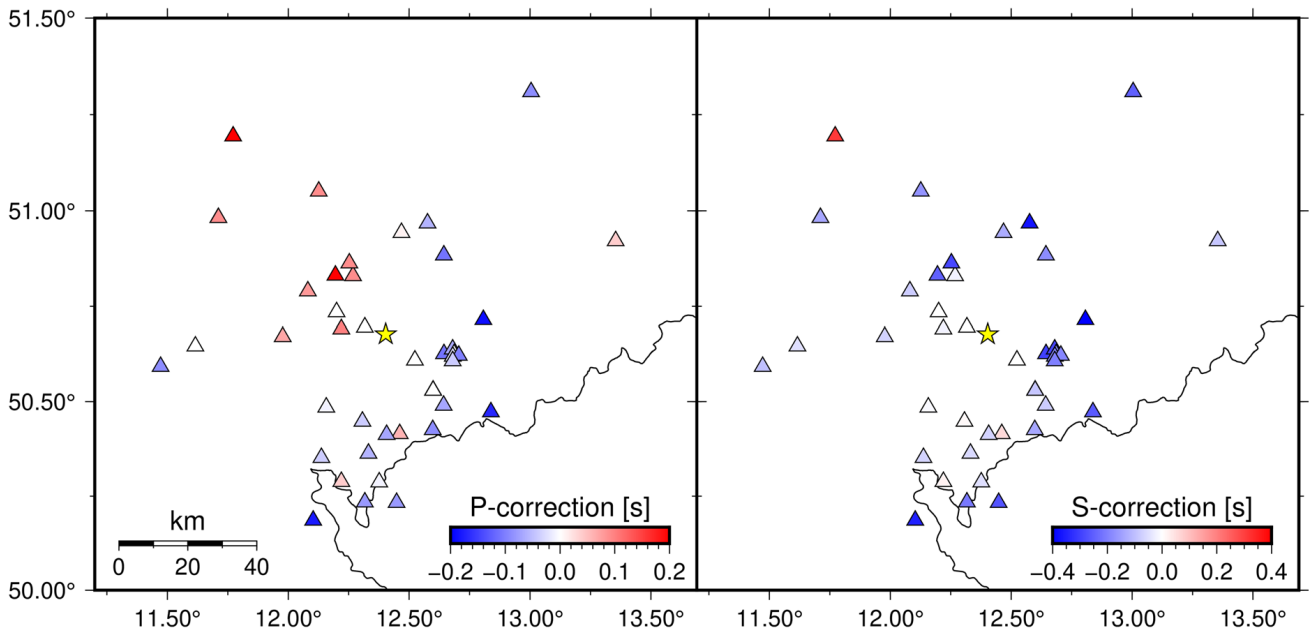


**Fig. 4** Station delay times for P- and S-wave based on the result of the best 1-D velocity inversion. The reference station SCHF is marked as yellow star

hand, hard-rock geology causes negative values in the south-east.

VELEST does not provide information about the absolute uncertainty of event locations. Therefore, we used HYPOINVERS (Klein 2002) to relocate 183 of the 419 events with at least 15 P- and 10S-picks, using the new velocity model. The mean location uncertainty was 0.4km and 1 km for latitude and longitude and 3 km for depth. The uncertainty in longitude was about twice that of latitude and can be explained by the lack of stations in the east and northeast of the survey area. A detailed presentation of the hypocentre change through relocalization can be found in the Appendix (Fig. 14).

### 2.3 3-D inversion

After inverting for the minimum 1-D velocity model, SIMULPS14 (Thurber 1983, 1993; Eberhart-Phillips 1993) was used to invert simultaneously for hypocentre locations and 3-D velocity structure. The forward modelling uses the pseudo-bending method to calculate the ray paths. SIMULPS14 uses the least-squares algorithm to update the velocity model and hypocentre locations. The inversion of the velocity model can be

performed individually or simultaneously for  $V_p$  and  $V_p/V_s$ . The  $V_s$  model generally tends to have a lower resolution than the  $V_p$  model, due to the more difficult determination of the S-wave arrival time. Here we directly invert for the ratio of  $V_p/V_s$  since this value is sensitive to fluids. According to Thurber (1993) and Thurber and Eberhart-Phillips (1999) the direct inversion for  $V_p/V_s$  is more stable than the inversion for  $V_s$  and a subsequent computation of  $V_p/V_s$ .

The lowest RMS 1-D velocity model was used as the starting model and the inversion was performed first for the  $V_p$  model and then jointly with  $V_p/V_s$ . As suggested by Evans et al. (1994), the inversion was initially carried out with a large horizontal grid spacing of 30 km and then successively reduced. We used up to 10 iterations before the grid spacing was reduced to a final grid spacing of 5 km in the investigation area’s centre. The outer region has a greater spacing to address the heterogeneous ray coverage. Throughout the inversion process, the vertical nodes are fixed at a spacing of 2 km. The damping values of the inversion were determined by a L-curve analysis (Hansen 1992). Damping of 15 for  $V_p$  and 25 for  $V_p/V_s$  (Fig. 5) was used in the inversion to provide a balance between data misfit reduction and a low model variance. The damping

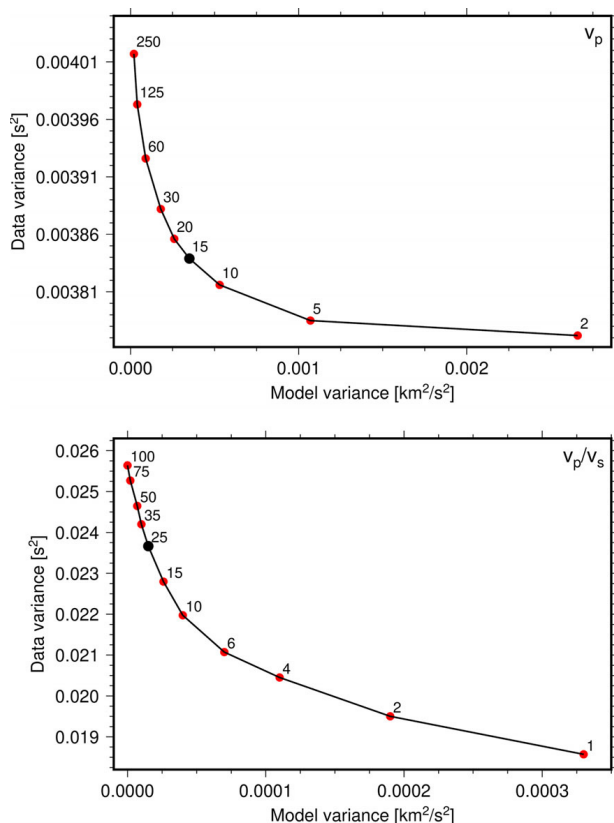


**Fig. 5** L-curve test used for the determination of the best damping parameter values used in the damped least-squares inversion. Values of 15 and 25 for  $V_p$  and  $V_p/V_s$  (black dots), respectively, were chosen

value of  $V_p/V_s$  is slightly higher compared to the L-curve result (around 6) to achieve a smoother result.

#### 2.4 Resolution tests

A quantitative analysis of the quality is the resolution matrix. The matrix's rows describe the dependency of the solution for one model parameter on all the other model parameters. The diagonal elements of the resolution matrix (RDE) indicate how the corresponding model parameter's solution depends on any other parameter, especially on its neighbours (Evans et al. 1994). The RDE ranges between 0 and 1, with 0 indicating no resolution and 1 indicating perfect resolution. However, high damping values and larger numbers of model parameters reduce the RDE (Eberhart-Phillips and Reyners 1997). The RDE values are calculated within SIMULPS14 and are shown in Fig. 6. Good

resolution, defined as RDE values greater than 0.15 for  $V_p$  and 0.3 for  $V_p/V_s$ , is achieved in the central and southern areas of the  $V_p$  model, where a large number of earthquakes are located. With increasing depth, parts of the northern model are also well resolved due to the deeper earthquakes in this area. In the case of  $V_p/V_s$ , the resolved area is smaller and only includes the southern part of the model. Additional figures of the RDE can be found in the Appendix (Fig. 15).

A second evaluation of the resolution can be obtained by a checkerboard test (Hearn and Ni 1994; Zelt 1998). For the checkerboard test, a defined pattern with a specific size and perturbation is applied to a velocity model. Forward modelling is performed with the perturbed velocity model, generating synthetic travel times with the same source-receiver distribution used in the real data set's inversion. According to the pick accuracy, we added Gaussian noise to the data, and the synthetic travel times are inverted using the same parameterization and starting model used for the real data inversion. The checkerboard test is successful if the inversion can reconstruct the checkerboard pattern and the perturbation. During the inversion process for the synthetic test, the hypocenters were fixed to get the same ray distribution. This may enable a slightly easier recovery of the original model (Mousavi et al. 2015), but due to the good relocalization of the earthquakes, this will not be of significant importance. We tested a 5 per cent perturbation with different cell sizes. The smallest pattern that could be reconstructed, and thus the best result of the checkerboard test, is shown in Fig. 7, with a cell size of  $15 \times 15 \times 5$  km. The slices from 7 to 11 km depth show a good result, and the  $V_p$  inversion can reconstruct the pattern except for the corner areas of the model. At 15 km, the sign of the checkerboard pattern is neutral, which explains the diffuse reconstructed pattern. In contrast, the 3 km depth section pattern shows partial smearing effects in the central and southern areas, indicating a lower resolution. A comparison with the RDE confirms the results of the checkerboard test. Areas of reconstructed patterns have a higher RDE value ( $\geq 0.15$ ), and vice versa, areas without reconstructed patterns have a lower RDE value ( $< 0.15$ ). The  $V_p/V_s$  checkerboard pattern can be reconstructed in the model's southern and some central areas at depths of 3 to 11 km. Comparing the  $V_p/V_s$  checkerboard test to the RDE confirms that the resolu-

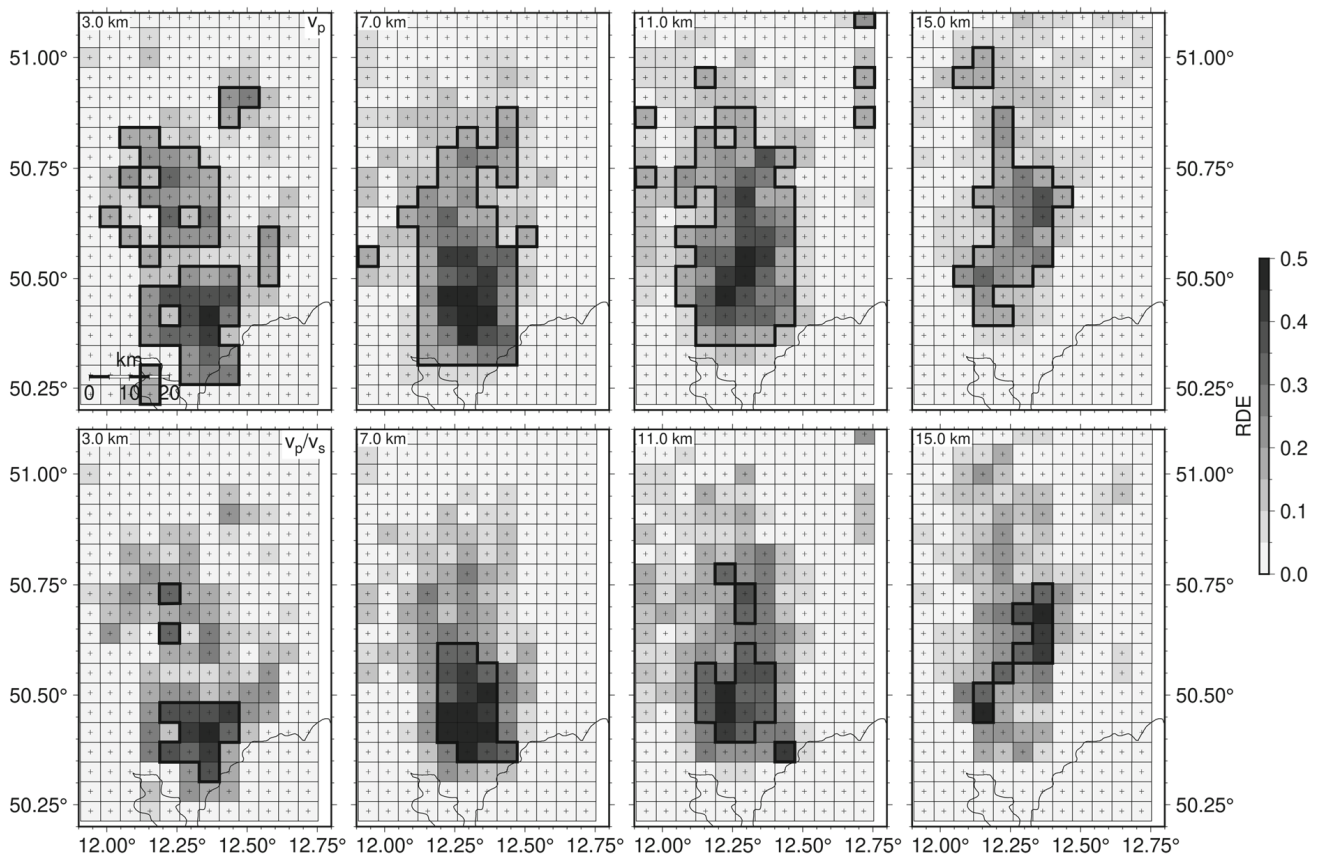


**Fig. 6** RDE (Resolution of Diagonal Elements) values of the inverted velocity models. The upper row belongs to the  $V_p$  model, the lower row to the ratio of  $V_p/V_s$ . The areas of reliable resolution ( $RDE > 0.15$  for  $V_p$  and  $RDE > 0.30$  for  $V_p/V_s$ ) are sur-

rounded by a black bold contour line. The position of the grid nodes for the inversion is shown with crosses. For reference, thin continuous black lines indicate political borders between Czech Republic and Germany, respectively

tion is high in the centre and the southern part, whereas the north has no or low resolution. Additional figures of the checkerboard test can be found in the Appendix (Fig. 16). In some areas of the slices there is a high RDE value but no reconstructed checkerboard pattern. In these areas, interpretation should be done with caution.

### 2.5 Results

Figures 8 and 9 show the inversion results for  $V_p$  and  $V_p/V_s$ .  $V_p$  values range from 5.4 to 6.4 km/s, while  $V_p/V_s$  varies from 1.63 to 1.75. Horizontal slices of  $V_p$  and  $V_p/V_s$  (Fig. 8) are displayed at the nodes of the

inversion grid from 3 km to 15 km depth in 4 km steps. Black dots display the earthquakes within 1 km of the corresponding depth slices.

In addition, three vertical sections are displayed (Fig. 9) along the profiles P1, P2 and P3 crossing the earthquake swarm area Schöneck (P1) and Werdau (P2, P3). For orientation, the vertical slices are displayed in the velocity models (Fig. 8). Earthquakes used in the inversion and occurring near the vertical sections are perpendicularly projected and displayed if the projection distance is less than 5 km. The final RMS error of both models was about 54 ms. The 3-D inversion can better explain the residual between observed and calculated travel times (see Fig. 17) over the entire distance range than the 1-D inversion. In particular, the residuals of the P-wave show a clear reduction.

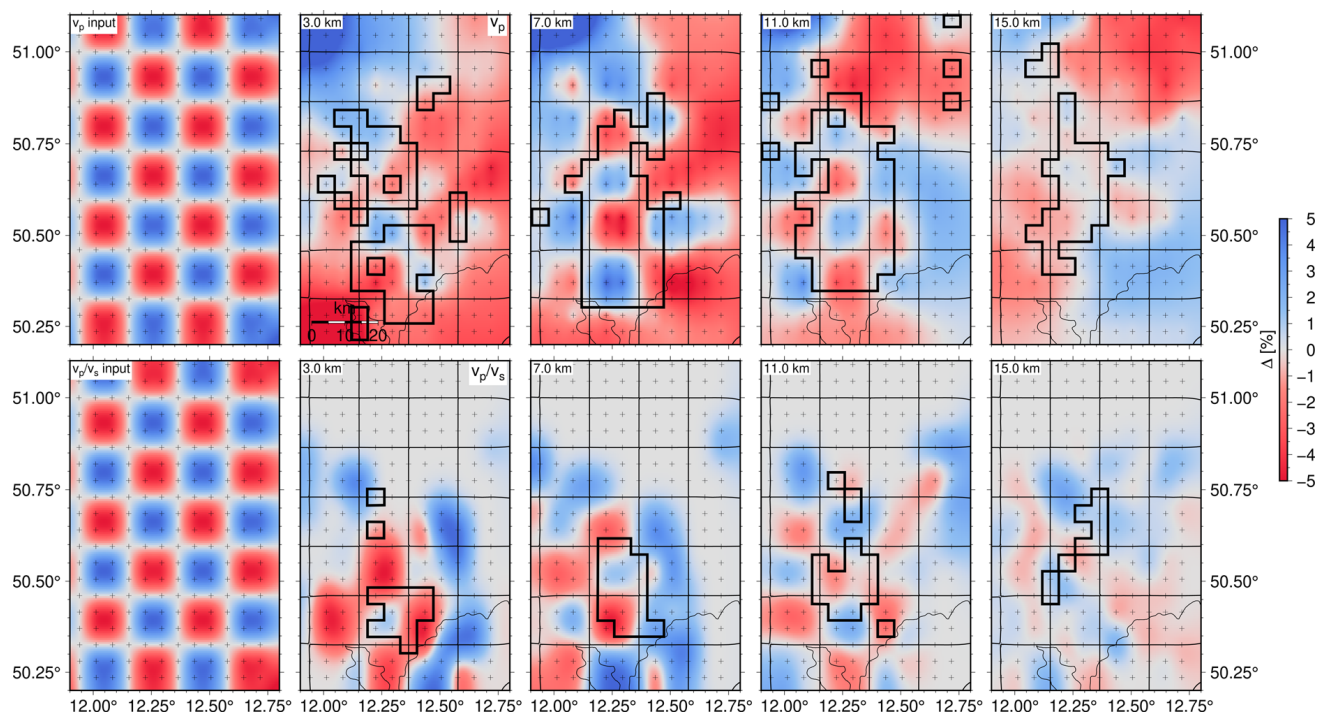


**Fig. 7** Checkerboard resolution test for  $V_p$  model (upper row) and  $V_p/V_s$  model (bottom row). The synthetic pattern used for the inversion is in the left column. RDE values of reliable resolution are displayed as black bold contour lines. Synthetic times were computed from the 1-D starting velocity model with 5% perturbation.

The cell size of the pattern is  $15 \times 15 \times 5$  km and is indicated by black lines. The position of the grid nodes for the inversion is shown with crosses. Thin continuous black lines indicate political borders between Czech Republic and Germany

### 3 Receiver function

Receiver functions (RFs) allow us to observe the seismic discontinuities of the Earth within the crust and upper mantle below a station (Vinnik 1977). The method of P-wave RFs is based on the effect that a portion of the incident P-wave is converted into a S-wave at a discontinuity. As a result, the propagation velocity of this converted phase is slower and arrives at the station after the primary phase. This time difference can be used to detect discontinuities and determine their depths.

#### 3.1 Data and method

All broadband seismic stations that were openly accessible within the latitude range of  $49.95^\circ\text{N}$  to  $51.04^\circ\text{N}$

and longitude range of  $12.0^\circ\text{E}$  to  $12.6^\circ\text{E}$  were used. A total of 18 stations from different networks with network codes BW, CZ, GR, SX and TH are available in the area, distributed along a N-S aligned strip. The P-receiver functions were calculated with the software *rf* by Eulenfeld (2020). We selected all available earthquakes of the Geofon catalogue (Quinteros et al. 2021) with a moment magnitude  $M_W$  larger than 5.5 and an epicentral distance between  $30^\circ$  and  $90^\circ$  from 2011 to 2020 (Fig. 10). The waveform data was then filtered between 0.05 Hz and 1 Hz. Waveforms with a signal-to-noise ratio smaller than 2 compared to a time window  $-20$  s to  $-15$  s prior to the P-wave were removed. Finally, the data were trimmed to 0 s to 100 s relative to the P-onset, rotated into the LQT system and subsequently deconvolved using iterative time-domain deconvolution (Ligorria and Ammon 1999). We calculated a total of 6844 RFs. Figure 11a) shows the stacked RFs of the Q-component of each station.

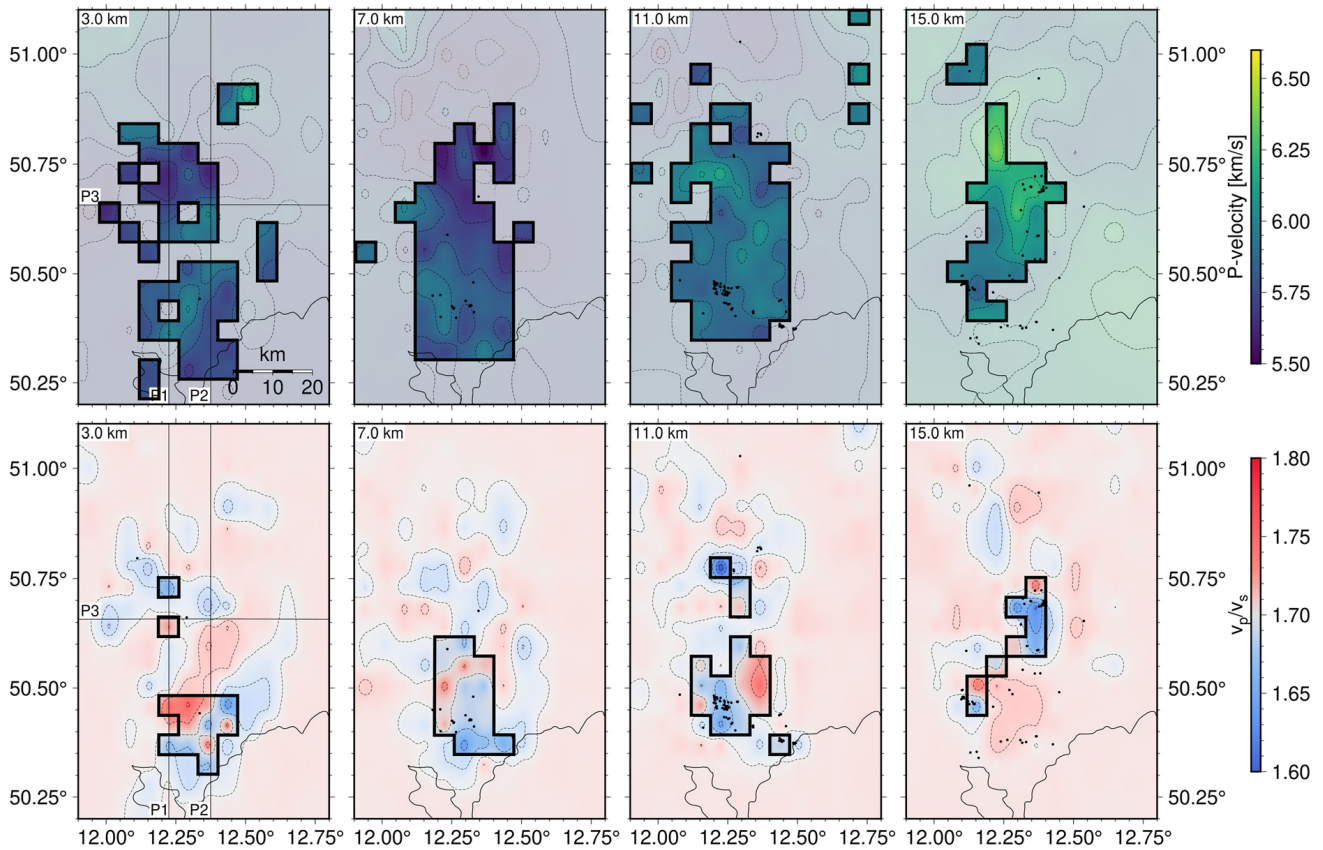


**Fig. 8** Horizontal slices of the  $V_p$  velocity model (top row) and  $V_p/V_s$  ratio (bottom row) derived from the 3-D inversion from 3 km up to 15 km depth. Contour lines are displayed as dashed lines. Areas with low RDE values ( $< 0.15$  for  $V_p$  and  $< 0.3$  for  $V_p/V_s$ ) are kept transparent. Thin continuous black lines indicate borders between Czech Republic and Germany, respectively.

Earthquakes in the range of 1 km of the corresponding depth are displayed as black dots. The location of profiles P1, P2 and P3 are given for orientation in the 3 km depth slice. The phyllite (S1), the graywacke (S2), presumably fluid pathways (F) and quartz-rich granitic composition intrusions (I1–I3) mentioned in the discussion section are highlighted

### 3.2 Results

At all stations, a strong positive amplitude is visible between 2.5 and 4.5 s, which can be interpreted as the Ps-conversion of the Moho. The weaker Moho multiples are partly visible at about 12.5 to 13.5 s (positive PpSs) and between 14 and 15 s (PpPs+PsPs). Figure 11b) shows a detailed example of individual RFs of the station SCHF. Noticeable differences between the RFs between 60 and 325 degrees back-azimuth and the RFs outside this range are visible at the station SCHF. This effect is also visible at some other stations. Affected stations are slightly south and north of SCHF (MULD to GRZ1) and the effect is always visible at RFs coming from the same back-azimuth range.

According to Cossette et al. (2016), the difference can be explained by two effects. Either there is a large-scale structural heterogeneity below the affected stations, which should be visible in the tomography, or elastic anisotropy in the crust causes the effect.

### 3.3 Moho depth and $V_p/V_s$ ratio

Using the method of Zhu and Kanamori (2000), the delay times of the Moho Ps conversion and their multiples can be used to determine the depth of the Moho and the  $V_p/V_s$ -ratio (Table 1). For the grid search, an average crustal P-wave velocity of 6.3 km/s was assumed. We estimated the uncertainty by the 95% margin of the

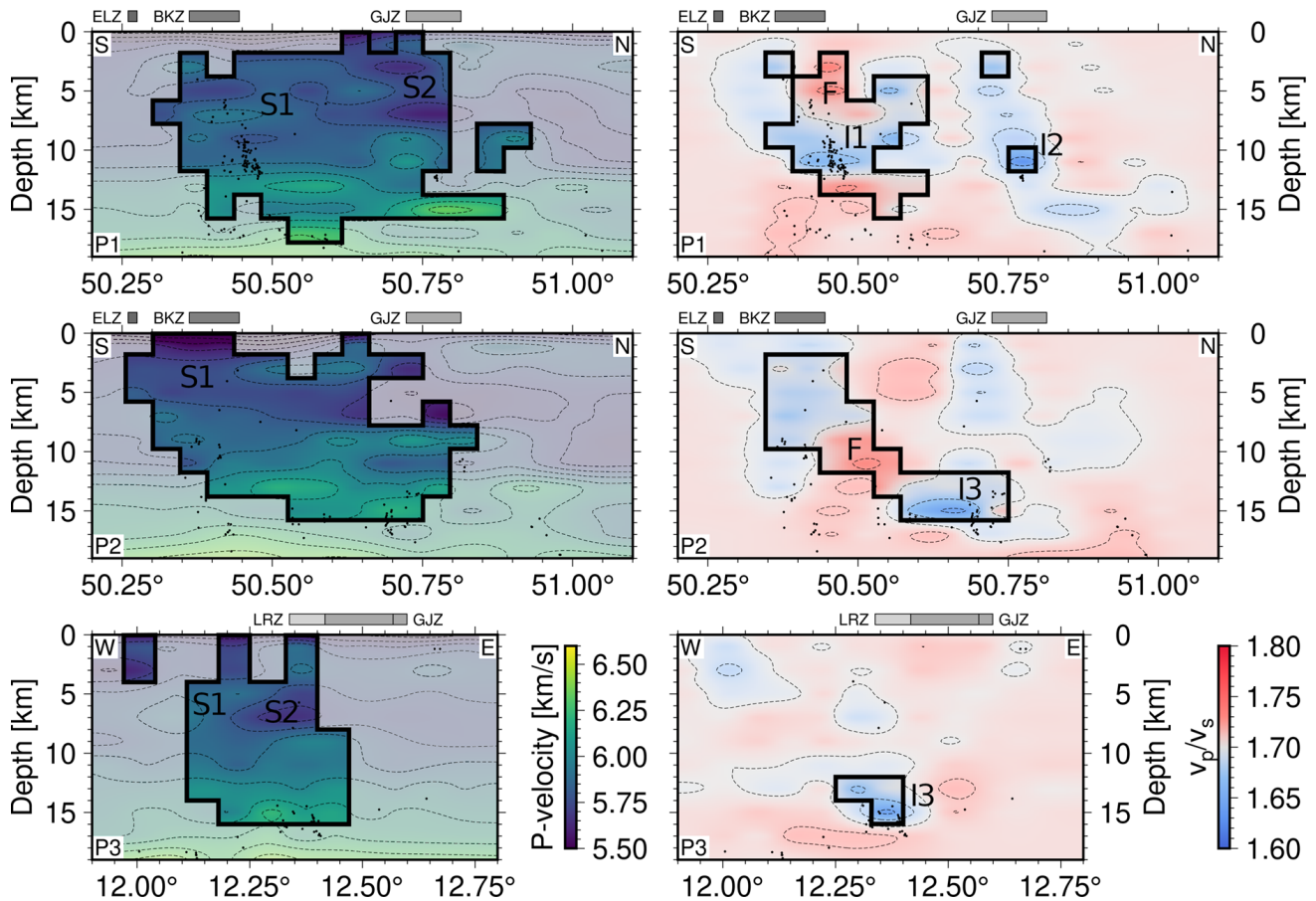


**Fig. 9** Vertical sections of the  $V_p$  and  $V_p/V_s$  velocity model along the profiles P1, P2 and P3. For orientation the location of the profiles are given in Fig. 8. Contour lines are displayed as dashed lines. Areas with low RDE values ( $< 0.15$  for  $V_p$  and  $< 0.3$  for  $V_p/V_s$ ) are kept transparent. Seismic events (black dots) are plotted in the slices, if the horizontal projection distance is smaller than 5 km. Profile P1 crosses the earthquake swarm

area of Schöneck at  $50.45^\circ\text{N}$  and Profile P2 and P3 the earthquake swarm area of Werdau at  $50.70^\circ\text{N}$  and  $12.40^\circ\text{E}$ , respectively. In addition above the models, the intersecting areas of the fault zones are marked. The phyllite (S1), the graywacke (S2), presumably fluid pathways (F) and quartz-rich granitic composition intrusions (I1–I4) mentioned in the discussion section are highlighted

maximal stacked amplitude (see Appendix Fig. 18). For the station MGBB it was impossible to determine the depth and  $V_p/V_s$ , because the Ps-conversion and the multiples did not join together at one point. The grid search yields an average Moho depth of  $30.5 \pm 1.5$  km and an average  $V_p/V_s$  value of  $1.73 \pm 0.07$  for the study area. Overall, the results, within the error bars, are consistent with the results of Geissler et al. (2005) and Heuer et al. (2006).

Beneath the NW-Bohemia area, the Moho domes up to 25.0 to 30.0 km. For the Vogtland area, the Moho depth increases to 30.0 to 32.8 km. North of it, the Moho domes up again to 29.1 to 30.9 km. The  $V_p/V_s$  ratios

follow a slight north–south gradient, with the exception of ROHR. The  $V_p/V_s$  values for the southern area are normal to very high (1.69 – 1.92) and, with the exception of HKWD where the error interval is significantly larger, the northern area shows normal  $V_p/V_s$  values (1.68 – 1.74). A systematic error in determining the Moho is caused by using a constant velocity for the crust. Increasing or decreasing the average velocity by 0.2 km/s, the Moho depth increases or decreases by 1 km on average, whereas the  $V_p/V_s$  ratio is almost independent of the P-wave velocity. Since this systematic error is smaller than the error estimate at most stations, we can neglect it.

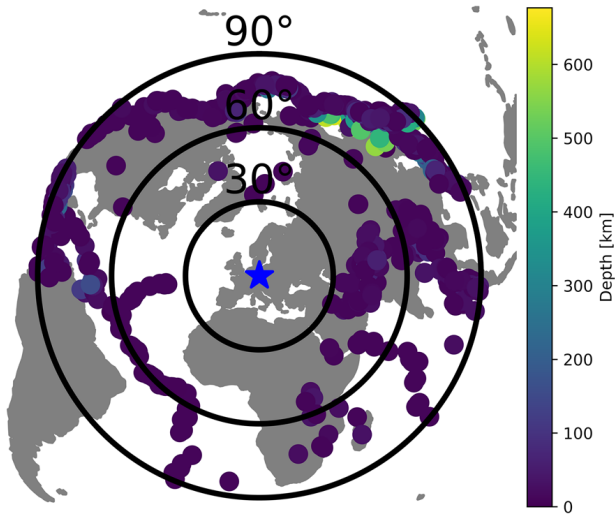


**Fig. 10** Distribution of the teleseismic events used for the P-RF analysis

### 3.4 Migration

To create a depth section from the time traces, a migration (Yuan et al. 2000) was carried out. For the migration, we used a modified version of the IASP91 model (Kennet and Engdahl 1991), with the velocities of the first 20 km depth taken from our 1-D velocity model obtained in Section 2.2. Using the velocity model, the RFs are back-projected along the range of Fresnel zones and stacked within a 2-D plane. To estimate the migration uncertainty, we compare the migration once with the modified and unmodified version of the IASP91 model. Using the modified IASP91 model, the anomalies are 2 km deeper than when using the unmodified IASP91 model. Therefore, we propose the 2 km as an uncertainty for the migration. Figure 12 shows the resulting migrated N-S profile calculated from 6844

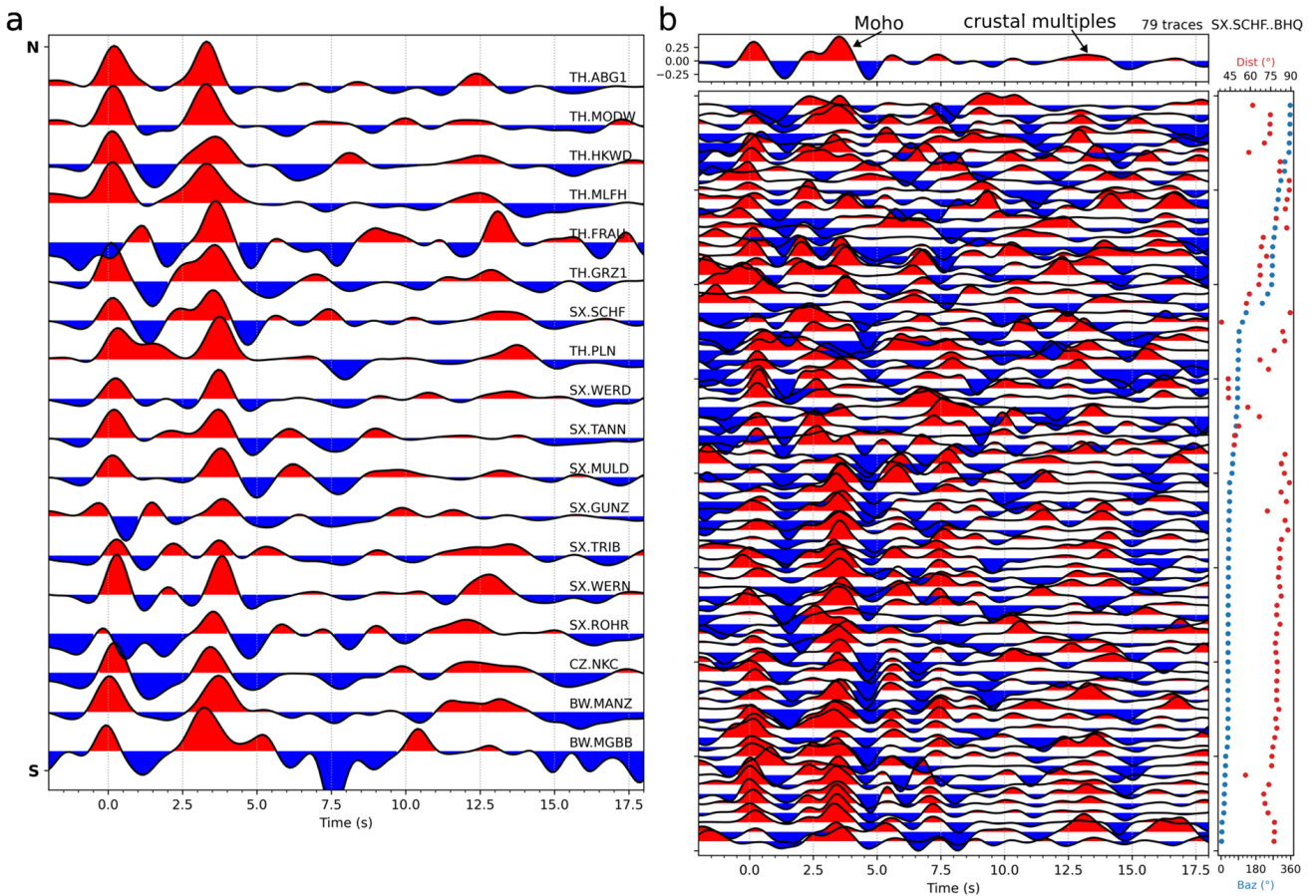


**Fig. 11** a) Q Component of stacked RF of all stations sorted by the station latitude. b) Q component of RF for the seismic station SCHF sorted by back-azimuth. Back-azimuth (blue dots) and distance (red dots) of the used earthquakes are displayed in

the right panel. Only 1/8 of all calculated RF at this station are displayed. Stacked RF of the station SCHF is displayed at the top

RFs. The gap in the migrated section at about 50.60°N occurs because there are no seismic stations in this area. A distinct positive phase (R1) is visible between 27 and 31 km depth, another positive phase (R2) at 55 km depth which dips to 65 km depth towards the north, and below a negative phase (R3) at about 68 km depth. The positive phase R2 displaces the negative phase R3 at about 50.7°N and then disappears at 50.8°N. The reflectors R2 and R3 are not visible north of 50.8°N. The R2 and R3 phase can also be observed in the single station RFs. The positive R2 phase is visible between GUNZ and PLN at about 6 to 6.5 s and the negative R3 phase is visible between NKC and PLN at about 7.5 to 8 s.

## 4 Discussion

### 4.1 Crustal structure in the area of investigation

A schematic representation of the interpretation is shown in Fig. 13. The depth slices of the velocity models reveal a three-layered crustal structure (Fig. 9), with an upper heterogeneous crust that extends down to 6–8 km, a middle crust that extends down to a depth of about 17 km and a lower crust underneath. The velocity anomalies within the upper crust can be related to the geology of the surface. Following Christensen (1996), the low P-velocities of 5.4 to 5.6 km/s and Vp/Vs-values of 1.65–1.68 in the 3–7 km depth range can be assigned to a graywacke (S2) and the higher P-velocities of 5.9–6.1 km/s and high Vp/Vs-values of 1.71–1.74 represent phyllite and/or granite (S1). Since the seismic properties of phyllite and granite are similar and both are present in the area, we cannot further distinguish. The S1 and S2 anomalies are exposed at the surface and follow the NE-SW trend of the Saxothuringian (Pietzsch 1963), which is also visible in the velocity model at 3 km depth (Fig. 8). The thickness of the upper crust of 6–8 km also fits with the indicated thickness of the Saxothuringian (Pietzsch 1963).

Below the upper crust is the middle crust at depth of 8–17 km. The study of Enderle et al. (1998) determined a P-wave velocity of 6.3 km/s for the depth range of 7–15 km using an active seismic refraction study and proposed a felsic granulite composition for the

depth range. For the range from 8 to 17 km depth, our velocity model shows Vp values of 5.85–6.25 km/s, whereas the Vp/Vs ratio shows values between 1.64 and 1.73. Assuming a lithostatic pressure of around 200–425 MPa for the depths of 8–17 km, the Vp and Vp/Vs values would, according to Christensen (1996), correspond to a granite gneiss composition rather than the felsic granulite composition proposed by Enderle et al. (1998).

Below 17 km, the velocity increases to more than 6.3 km/s, representing the transition from the middle to the lower crust. Thus, the crustal structure of the study area corresponds to the typical structure of the Central European crust (Tesauro et al. 2008). Furthermore, the brittle-ductile transition (Fig. 13) can be determined with the earthquake distribution. Since very few to no earthquakes occur in the ductile part of the crust (Ellis and Stöckhert 2004), the boundary is 14 km in the NW-Bohemia area and 24 km in the northern part of the LRZ.

### 4.2 Seismic properties of the Schöneck and Werdau earthquake swarm areas

The two earthquake swarm areas Schöneck and Werdau show similar properties in the tomographic models. Both areas (Fig. 9) are inconspicuous in the Vp model and cannot be distinguished from the respective surrounding. In the Vp/Vs ratio, however, there are low Vp/Vs anomalies (I1, I3, I4) of approximately 1.67 near the earthquake swarm areas. Besides these low Vp/Vs anomalies, there is another low Vp/Vs anomaly (I2) in the northwest of Werdau where the 2016 Werdau swarm occurred.

The velocities and ratios (Vp 5.8 km/s and Vp/Vs of 1.67 for all Schöneck clusters and Vp 6.1 km/s and Vp/Vs of 1.68 for Werdau) can be explained by a quartz-rich granitic composition intrusion in the granite gneiss environment of the middle crust. Since we cannot determine the age of the Werdau intrusions, they could be related to the intrusions that emplaced to the east of the study area during the Variscan orogeny (Förster et al. 1999) or, to the diatreme of Ebersbrunn and Weißenbrunn, which lie only a few kilometres

**Table 1** Seismic station coordinates used for the RF analysis and sorted by latitude, Moho depth values H and Vp/Vs ratio obtained by the grid search method of Zhu and Kanamori (2000) and n number of stacked traces

| Station | Lat. [°N] | Long. [°E] | Elevation [m] | H [km]   | Vp/Vs     | n   |
|---------|-----------|------------|---------------|----------|-----------|-----|
| TH.ABG1 | 50.967    | 12.576     | 203           | 28.7±1.3 | 1.72±0.06 | 445 |
| TH.MODW | 50.942    | 12.468     | 240           | 30.4±1.4 | 1.68±0.08 | 512 |
| TH.HKWD | 50.829    | 12.268     | 308           | 29.1±2.2 | 1.77±0.12 | 444 |
| TH.MLFH | 50.789    | 12.080     | 231           | 30.9±0.8 | 1.68±0.05 | 522 |
| TH.GRZ1 | 50.690    | 12.219     | 203           | 30.7±1.3 | 1.74±0.09 | 410 |
| SX.SCHF | 50.677    | 12.403     | 435           | 32.8±1.6 | 1.68±0.05 | 631 |
| TH.PLN  | 50.485    | 12.157     | 432           | 32.8±1.4 | 1.70±0.07 | 178 |
| SX.WERD | 50.448    | 12.307     | 589           | 31.7±1.4 | 1.72±0.06 | 471 |
| SX.TANN | 50.415    | 12.461     | 836           | 32.2±1.3 | 1.74±0.07 | 544 |
| SX.MULD | 50.411    | 12.403     | 678           | 32.4±1.3 | 1.69±0.06 | 643 |
| SX.GUNZ | 50.363    | 12.331     | 669           | 30.3±1.5 | 1.84±0.07 | 479 |
| SX.TRIB | 50.352    | 12.137     | 510           | 31.9±1.6 | 1.69±0.04 | 273 |
| SX.WERN | 50.287    | 12.376     | 672           | 29.0±1.9 | 1.81±0.07 | 598 |
| SX.ROHR | 50.234    | 12.317     | 629           | 30.0±1.6 | 1.65±0.06 | 158 |
| CZ.NKC  | 50.233    | 12.447     | 564           | 27.6±1.8 | 1.76±0.09 | 491 |
| BW.MANZ | 49.986    | 12.108     | 635           | 25.0±1.2 | 1.92±0.07 | 36  |

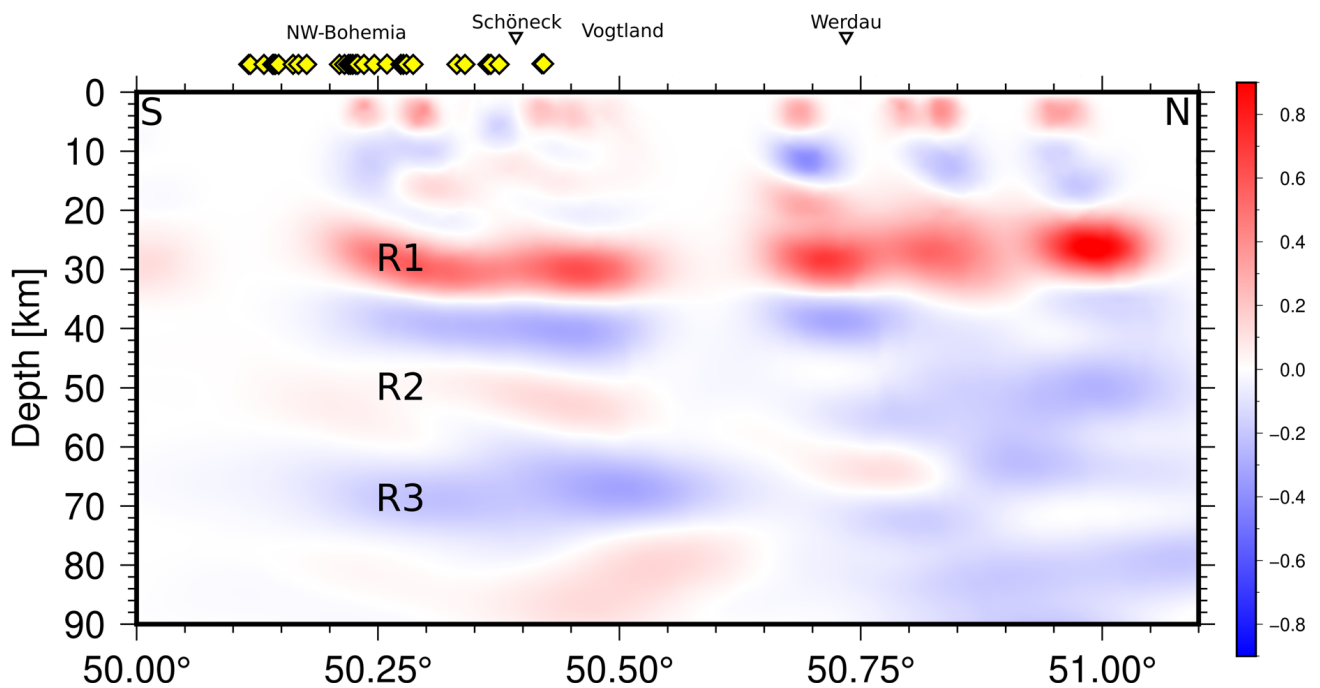


**Fig. 12** Migration image of the Q component RF along the N-S profile with RFs stacked in the Fresnel zone range. The red colour corresponds to positive velocity contrasts, while the blue colour corresponds to negative velocity contrasts. The three anomalies Moho (R1), seismic reflector (R2) and partial melting (R3) are

marked. Mineral springs and moffettes are marked as yellow diamonds. Due to the station distribution, the central and southern area is less well resolved. Degassing locations after Geissler et al. (2005)

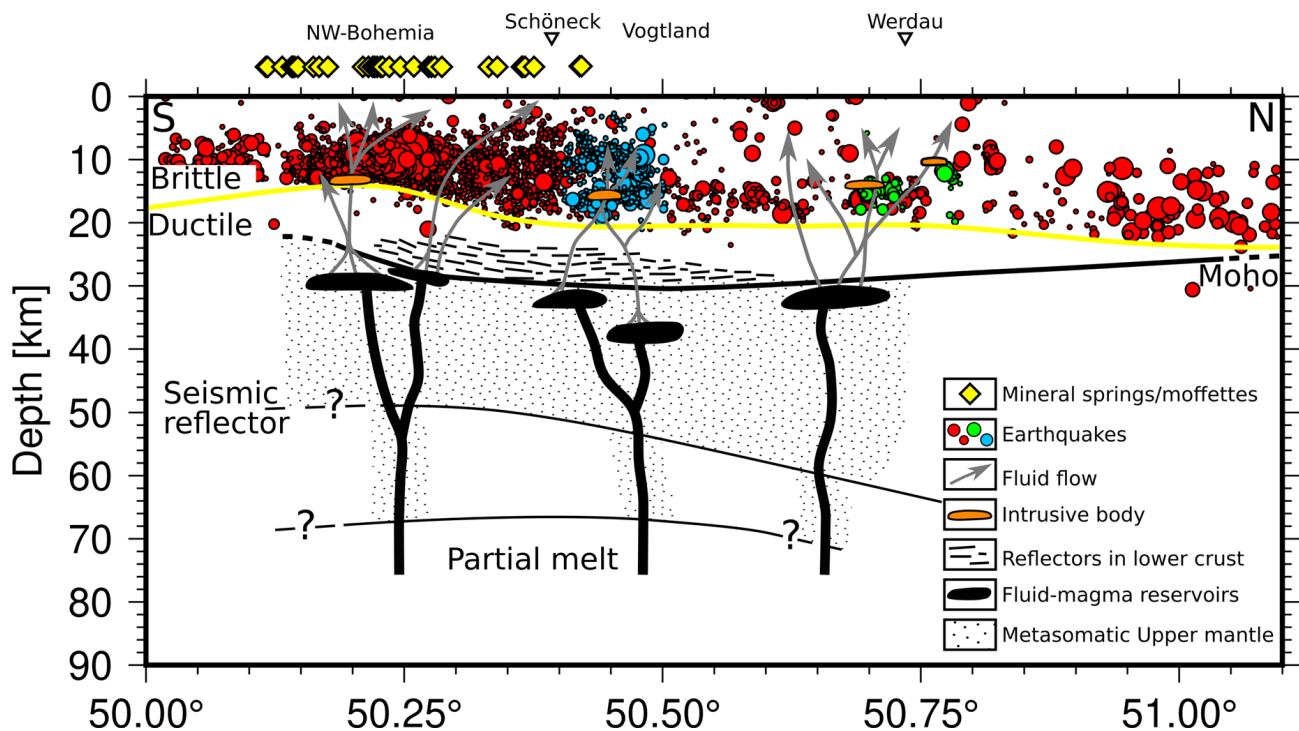


**Fig. 13** Schematic interpretation based on the results of this and previous studies. Magmatic processes in the mantle cause rising melt that transport fluids (black channels). Fluids dissolve from the melt in the upper mantle and continue to rise (grey arrows). If the fluids pass an intrusion body (orange bodies) in the area of a fault zone, the fluids trigger earthquake swarms. The fluids

continue to rise and emerge in the NW-Bohemia area on the surface in form of mineral springs or mofettes (yellow diamonds), while in the northern area they spread diffusely in the upper crust and at the surface. Modified from Heuer et al. (2006); Geissler et al. (2005); Mousavi et al. (2015) and degassing locations after Geissler et al. (2005)

south of Werdau (Schmidt et al. 2013). Further investigations are necessary.

Geodynamic modelling has shown for the Vogtland area that the deformation and the shear stress caused by the regional stress field are too low to generate earthquake swarms (Kurz et al. 2003). The regional stress field is only responsible for the prestressing of the crust (Kurz et al. 2003) and an additional physical process in the form of fluids triggers the earthquake swarms (Parotidis et al. 2005). The additional periodic pore pressures and temperature changes caused by ascending magmatic fluids ultimately trigger earthquakes in the Vogtland (Kurz et al. 2003). Since the earthquake swarm areas Schöneck and Werdau are directly adjacent to the Vogtland earthquake swarm area, we assume a similar situation where the regional stress field cannot trigger the earthquake swarms on its own. More-

over, the earthquakes at Schöneck and Werdau show swarm character, so fluids must also be present. Numerous studies have shown that high  $V_p/V_s$  ratios image fluid pathways (Husen et al. 2004; Kato et al. 2010; Muskin et al. 2013). In the Vogtland area, the potential fluid path passing through the earthquake swarm area could already be imaged by Mousavi et al. (2015) by means of a channel-like increased  $V_p/V_s$  structure. A similar structure passing through the Schöneck or Werdau earthquake swarm area is not visible in our study. Instead, we see larger areas (F) of presumably high  $V_p/V_s$  ratio (1.72 - 1.73) around the earthquake swarm areas and the low  $V_p/V_s$  anomalies (1.67 - 1.68), indicating the presence of fluids (Fig. 9). Since the checkerboard test could not reconstruct the pattern for the area of the fluids, a clear interpretation about the presence of fluids is not possible. Thus we suggest that fluids rise

from the lower crust and presumably emerge diffusely at the surface, since in this area, in contrast to NW-Bohemia/Vogtland, there are no known concentrated degassing sites e.g. in the form of mofettes.

Similar to the Vogtland earthquake swarm (Mousavi et al. 2015), the relocated earthquake swarms are distributed along an axis that runs through the low  $V_p/V_s$  anomaly in the case of Schöneck and slightly north of the anomaly of Werdau. We assume that smaller fractures, which we cannot resolve with the tomography, run through the intrusive body and fluids rise along these fractures. The fractures, in turn, could be related to the BKZ and GJZ. Therefore we assume the combination of a regional stress field prestressing the crust, fault zones that accumulate stress in the intersection, magmatic fluids ascending along these fault zones and a change in the material property in the form of a quartz-rich granitic intrusiva are the cause of the Schöneck and Werdau earthquake swarms.

#### 4.3 Crustal mantle transition and fluid migration

Based on the receiver function analysis (Fig. 12), the deeper area of the crust and the transition to the upper mantle can be analysed. The method of Zhu and Kanamori (2000) and the migration, where a strong positive phase (R1) is visible, yield a Moho depth of 25 -  $33 \pm 2.0$  km. We can observe an updoming of the Moho below NW-Bohemia, which previous studies had already observed (e.g. Geissler et al. 2005; Heuer et al. 2006; Hrubcová et al. 2013). The attenuation values of the crust in the southern part of the LRZ (Gaebler et al. 2015; Eulenfeld et al. 2021) are higher than in the northern part (van Laaten et al. 2022a), which already indicates an increased magma/fluid/heat transport in the southern part of the LRZ, which in turn can be attributed to the updoming Moho (Heuer et al. 2006).

Geissler et al. (2005) and Heuer et al. (2006) had already observed the positive phase (R2) at a depth of  $55 \pm 2.0$  km below NW-Bohemia. According to Heuer et al. (2006), it is a seismic reflector below NW-Bohemia extending further north and south, while Geissler et al. (2005) suggest that the seismic disconti-

nity is related to the base of a metasomatic uppermost mantle containing a few per cent melt. In our study, we can trace the R2 reflector to the GJZ/LRZ intersection, with the reflector dipping to the north. The negative phase (R3) at  $68 \pm 2.0$  km is more prominent than the R2 anomaly, indicating a stronger velocity contrast. Heuer et al. (2006) also observed the R3 anomaly in their study. According to their modelling, it may be a velocity decrease of  $3.7 \pm 1.0\%$  at about 65 km depth or a 5 km thick gradual velocity decrease between 65 and 70 km. Heuer et al. (2006) interpret the velocity decrease as a local uplift of the lithosphere-asthenosphere boundary below NW-Bohemia. An upwelling of the lithosphere-asthenosphere boundary was also interpreted by Plomerová et al. (2007), based on the results of their teleseismic P-velocity tomography study in the Bohemian Massif. The updoming could account for increased partial melt in the lithospheric mantle (Heuer et al. 2006). This in turn may lead to mantle-induced degassing of  $\text{CO}_2$ , which rises and causes the earthquake swarms in the NW-Bohemia area. We can also observe the same anomaly and trace it northward up to the GJZ/LRZ intersection. At the intersection, the R3 anomaly is then bounded by the R2 reflector. A schematic interpretation is shown in Fig. 13. The same melting that causes the NW-Bohemia earthquake swarms, thus causing fluids to rise along the region's fault zones and trigger the Schöneck and Werdau earthquake swarms as well.

## 5 Conclusion

This study presents the results of LET and RFs to image the crustal and upper mantle structure. The LET shows the transitions from upper to middle and middle to lower crust and that the near-surface geology matches the near-surface velocity models. Magmatic fluids, characterised by increased  $V_p/V_s$  ratios, ascend and diffuse towards the surface. The swarms gather in small areas and are always near low  $V_p/V_s$  anomalies which we interpret as individual intrusion bodies. This intrusion body is probably a granite of older origin, as recent volcanic activity has not been observed in the area. In sum, the earthquake swarms are triggered

by various factors: the regional stress field, which is responsible for the prestressing of the crust, intersecting fault zones causing an accumulation of stress and ascending mantle fluids. Thus, the earthquake swarms of Schöneck and Werdau are subject to a similar trigger mechanism as the earthquake swarms of NW-Bohemia/Vogtland. The RFs results provide the Moho depth, a seismic reflector at 55 km depth dipping to the north, and a zone of partial melting below 65 km depth as the origin of fluids. Werdau is thus the northernmost swarm earthquake area of the LRZ, as the melt zone does not extend further north.

**Acknowledgements** We thank Wolfram Geissler and another anonymous reviewer whose comments contributed significantly to the improvement of the manuscript. Thanks to all the helpers and staff running the networks BW (BayernNetz 2014), CZ (Czech Regional Seismic Network 1973), GR (German Regional Seismic Network (GRSN) 2019), SX (SXNET Saxon Seismic Network 2019) and TH (Thüringer Seismologisches Netz 2019) and the BGR (German Regional Seismic Network (GRSN) 2019) and the GFZ (Quinteros et al. 2021) for providing the waveform and earthquake data. We wish to thank Falk Hänel of TU Freiberg for providing the SXNET-offline waveform data and the LfULG (LfULG 2018) for the free access of geological data. Also we would like to thank Xiaohui Yuan and Felix Schneider for providing the RFs migration code and Thomas Burghardt for his support in the usage of SeismicHandler. SeismicHandler was funded by the Deutsche Forschungsgemeinschaft (DFG) within the framework of SPP-1066. We used the rf code from <https://github.com/trichter/rf> (Eulenfeld 2020). Figures were generated with Generic Mapping Tools (Wessel et al. 2013) or Python using ObsPy (Krischer et al. 2015), NumPy (Harris et al. 2020) and Matplotlib (Hunter 2007). The focal mechanisms were obtained with Grond (Heimann et al. 2018).

**Author contributions** Marcel van Laaten and Ulrich Wegler contributed to the study conception and design. The data processing was performed by Marcel van Laaten. All authors contributed to the data analysis and interpretation. The first draft of the manuscript was written by Marcel van Laaten. Ulrich Wegler and Tom Eulenfeld commented on previous versions of the manuscript. All authors read and approved the final manuscript.

**Funding** The authors did not receive support from any organization for the submitted work. Open Access funding enabled and organized by Projekt DEAL.

**Availability of data and material** The receiver function profile and velocity models are available in the Zenodo repository <https://doi.org/10.5281/zenodo.6511543> (van Laaten et al. 2022b).

**Compliance with ethical standards**

**Conflict of interest** The authors declare no competing interests.

**Open Access** This article is licensed under a Creative Commons Attribution 4.0 International License, which permits use, sharing, adaptation, distribution and reproduction in any medium or format, as long as you give appropriate credit to the original author(s) and the source, provide a link to the Creative Commons licence, and indicate if changes were made. The images or other third party material in this article are included in the article's Creative Commons licence, unless indicated otherwise in a credit line to the material. If material is not included in the article's Creative Commons licence and your intended use is not permitted by statutory regulation or exceeds the permitted use, you will need to obtain permission directly from the copyright holder. To view a copy of this licence, visit <http://creativecommons.org/licenses/by/4.0/>.

Appendix A: Figures

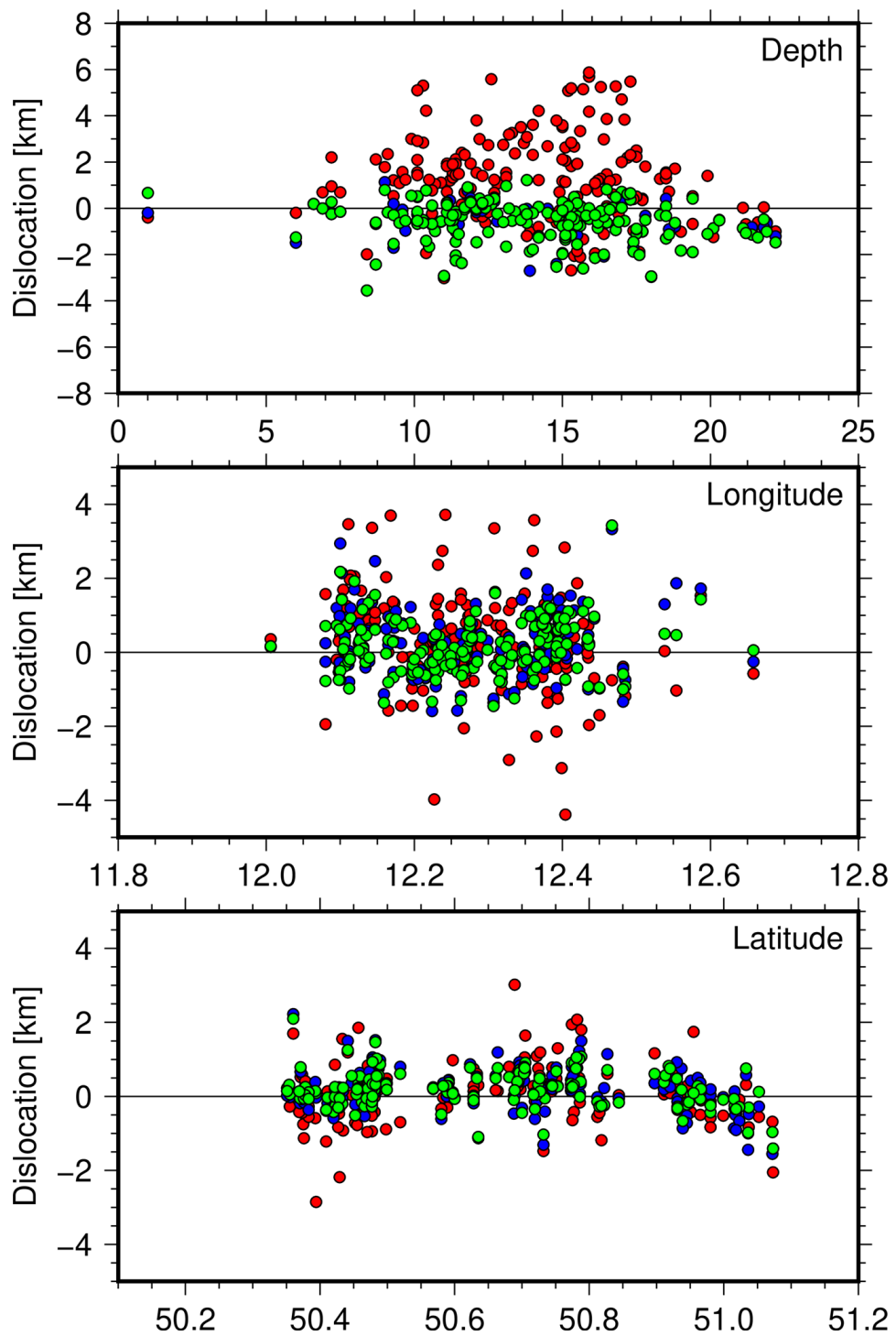


**Fig. 14** Dislocation after relocalization compared to the initial hypocentre. The green dots correspond to the relocalization of VELEST, the blue dots to the relocalization of SIMULPS and the red dots to the relocalization of HYPOINVERS

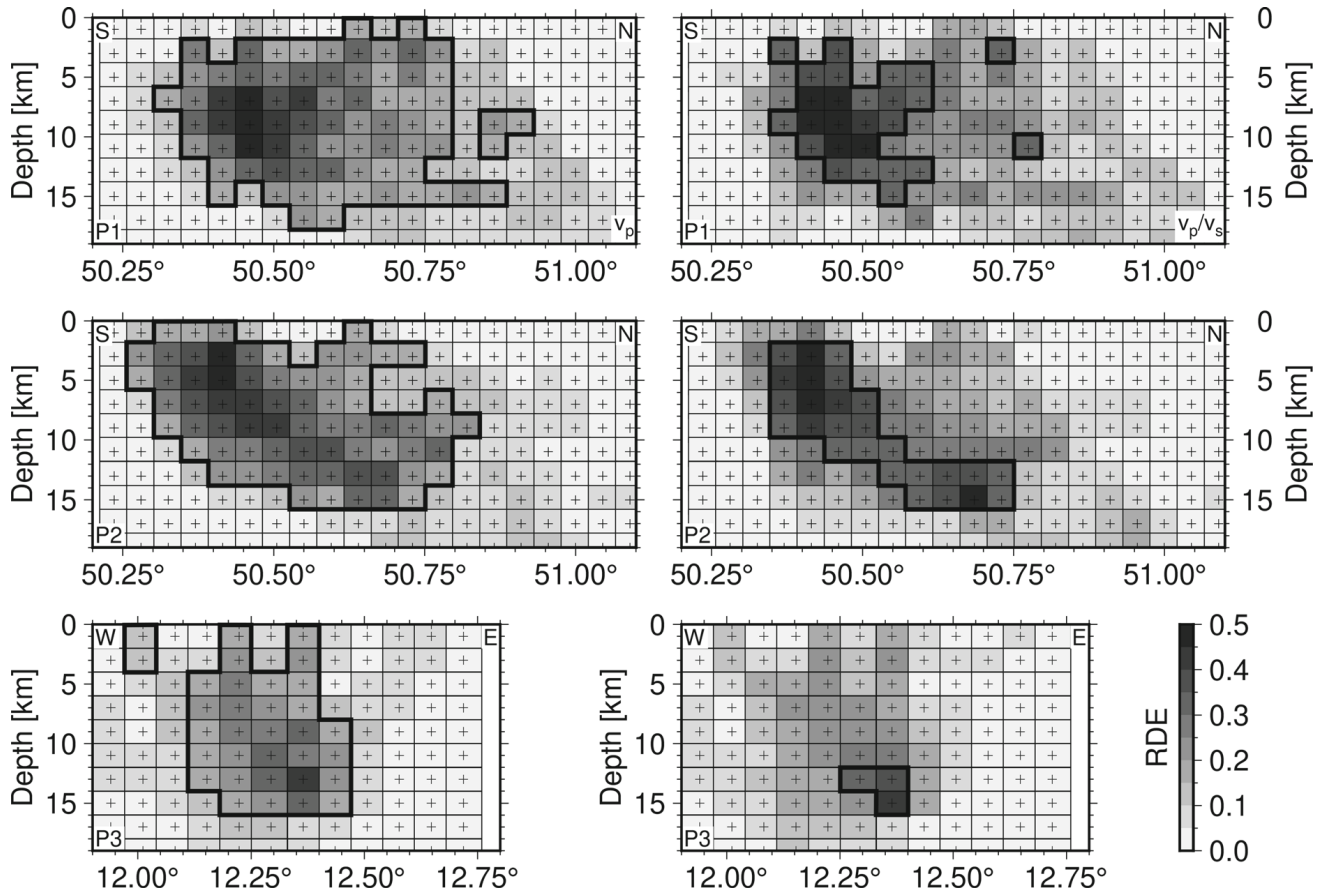


**Fig. 15** Vertical sections of the RDE (Resolution of Diagonal Elements) along the profiles P1, P2 and P3. For orientation the location of the profiles are given in Fig. 8. The areas of reliable

resolution ( $RDE > 0.15$  for  $V_p$  and  $RDE > 0.30$  for  $V_p/V_s$ ) are surrounded by a black bold contour line. The position of the grid nodes for the inversion is shown with crosses

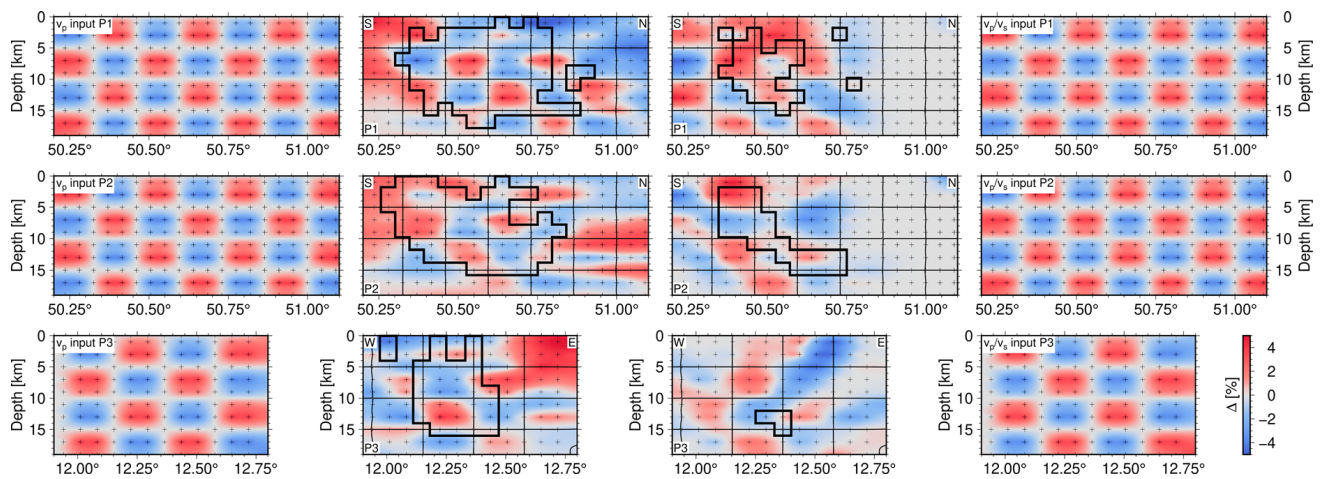


**Fig. 16** Vertical sections of the Checkerboard resolution test along the profiles P1, P2 and P3. For orientation the location of the profiles are given in Fig. 8. Synthetic times are computed from the 1-D starting velocity model with 5% perturbations. The

cell size of the pattern is 15x15x5 km and is indicated by black lines. The areas of reliable resolution are surrounded by a black bold contour line. The position of the grid nodes for the inversion is shown with crosses

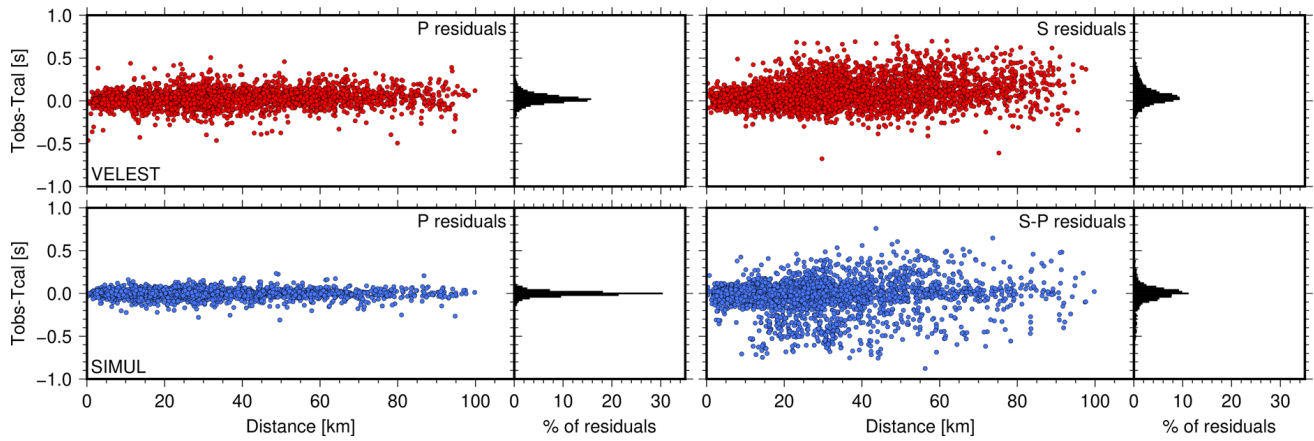


**Fig. 17** Traveltime residuals between observed and calculated traveltimes as a function of the hypocentral distance and as histogram. The residuals of the P-wave are on the left and the residuals of the S-wave (VELEST) or S-P (SIMUL) are on the right

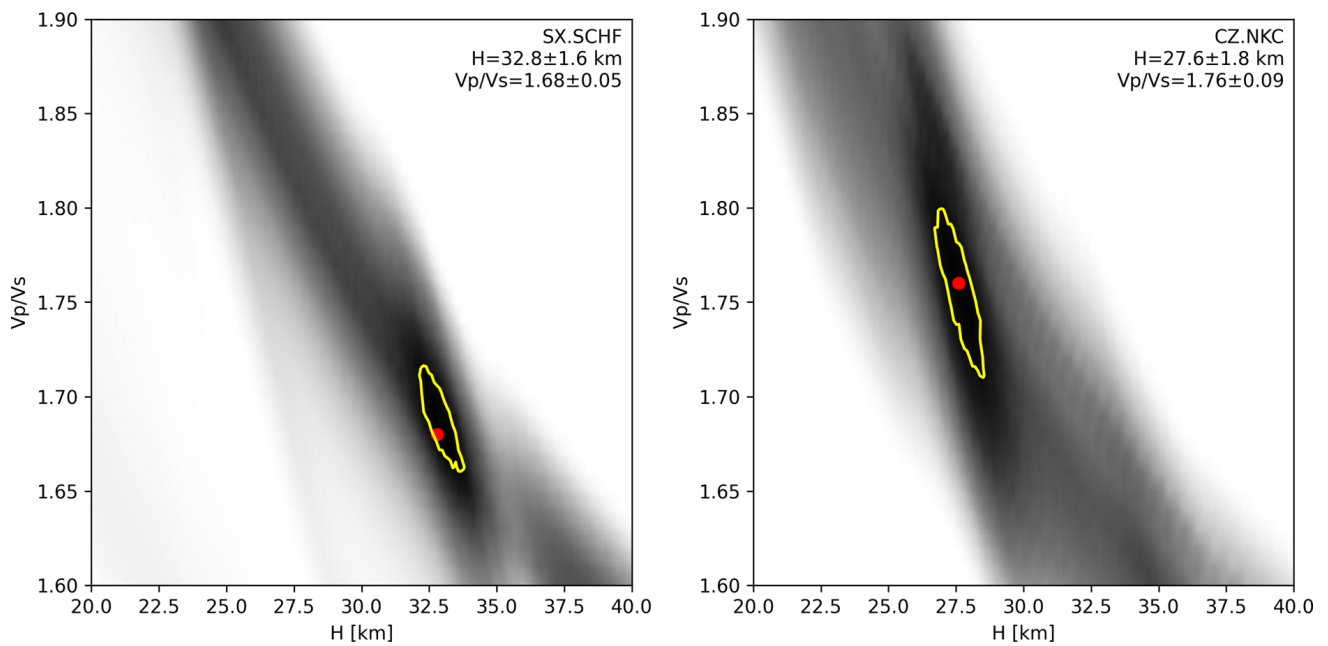


**Fig. 18** Inversion results for estimating the Moho depth and  $V_p/V_s$  ratio for the stations SCHF and NKC with an average crustal P-wave velocity of 6.3 km/s. The yellow line is used for

the error estimation and marks the area of 95% of the maximal stacked amplitude

## References

- Alexowsky W, Berger H, Goth K, et al (2007) Geologische Karte des Freistaates Sachsen 5240 Zwickau und 5241 Zwickau Ost
- Bachura M, Fischer T, Doubravová J et al (2020) From earthquake swarm to a main shock-aftershocks: the 2018 activity in West Bohemia/Vogtland. *Geophys J Int* 224:1835–1848. <https://doi.org/10.1093/gji/ggaa523>
- Bankwitz P, Bankwitz E, Frischbutter A (1979) Fototektonische Interpretation von Mitteleuropa nach Aufnahmen der sowjetischen Wettersatelliten Meteor 25 und 28. Veröffentlichungen des Zentralinstituts für Physik der Erde Beiträge zur Fernerkundung:37–60. In German
- Bankwitz P, Schneider G, Kämpf H et al (2003) Structural characteristics of epicentral areas in Central Europe: study case Cheb basin (Czech Republic). *J Geodyn* 35:5–32. [https://doi.org/10.1016/S0264-3707\(02\)00051-0](https://doi.org/10.1016/S0264-3707(02)00051-0)
- BayernNetz (2014) Department of Earth and Environmental Sciences, Geophysical Observatory, University of Munchen, International Federation of Digital Seismograph. Networks. <https://doi.org/10.7914/SN/BW>
- Becker H, Lindner H, Schenke G et al (1989) Mitteldeutsche Schwelle/Zentralteil - Komplexbericht. Geophysik, Leipzig (unpublished), VEB (in German)
- Boncio P, Lavecchia G, Milana G et al (2004) Seismogenesis in Central Apennines, Italy: an integrated analysis of minor earthquake sequences and structural data in the Amatrice Campotosto area. *Ann Geophys* 47:1723–1726. <https://doi.org/10.4401/AG-3371>
- Bräuer K, Kämpf H, Strauch G (2009) Earthquake swarms in nonvolcanic regions: what fluids have to say. *Geophys Res Lett* 36(L17):309. <https://doi.org/10.1029/2009GL039615>
- Christensen N (1996) Poisson's ratio and crustal seismology. *J Geophys Res* 101:3139–3156. <https://doi.org/10.1029/95JB03446>
- Cossette É, Audet P, Schneider D et al (2016) Structure and anisotropy of the crust in the Cyclades, Greece, using receiver functions constrained by in situ rock textural data. *J Geophys Res* 121:2661–2678. <https://doi.org/10.1002/2015JB012460>
- Czech Regional Seismic Network (1973) Institute of Geophysics, Academy of Sciences of the Czech Republic, International Federation of Digital Seismograph. Networks. <https://doi.org/10.7914/SN/CZ>
- Dahm T, Heimann S, Funke S, et al (2018) Seismicity in the block mountains between Halle and Leipzig, Central Germany: centroid moment tensors, ground motion simulation, and felt intensities of two M<sub>3</sub> earthquakes in 2015 and 2017. *J Seismol* 22:985–1003. <https://doi.org/10.1007/s10950-018-9746-9>
- Eberhart-Phillips D (1993) Local earthquake tomography: Earthquake source regions. Chapman and Hall, New York
- Eberhart-Phillips D, Reyners M (1997) Continental subduction and three-dimensional crustal structure: The northern South Island, New Zealand. *J Geophys Res* 102:843–861. <https://doi.org/10.1029/96JB03555>
- Ellenberg J (1992) Recent fault tectonics and their relations to the seismicity of East Germany. *Tectonophysics* 202:117–121. [https://doi.org/10.1016/0040-1951\(92\)90089-0](https://doi.org/10.1016/0040-1951(92)90089-0)
- Ellis S, Stöckhert B (2004) Elevated stresses and creep rates beneath the brittle-ductile transition caused by seismic faulting in the upper crust. *J Geophys Res* 109(B05):407. <https://doi.org/10.1029/2003JB002744>
- Enderle U, Schuster K, Prodehl C et al (1998) The refraction seismic experiment GRANU95 in the Saxothuringian belt, southeastern Germany. *Geophys J Int* 133:245–259. <https://doi.org/10.1046/j.1365-246X.1998.00462.x>
- Eulenfeld T (2020) rf: Receiver function calculation in seismology. *J Open Source Softw* 5:1808. <https://doi.org/10.21105/joss.01808>
- Eulenfeld T, Dahm T, Heimann S et al (2021) Fast and Robust Earthquake Source Spectra and Moment Magnitudes from Envelope Inversion. *Bull Seismol Soc Am* 112:878–893. <https://doi.org/10.1785/0120210200>
- Evans J, Eberhart-Phillips D, Thurber C (1994) User's Manual for Simulps12 for Imaging Vp and Vp/Vs: a derivative of the "Thurber" tomographic inversion Simul3 for local earthquakes and explosions. Tech. Rep. 94–431, U.S. Geological Survey, Washington, D.C., <https://doi.org/10.3133/ofr94431>, open File Rep
- Fischer T, Horálek J, Hrubcová P et al (2014) Intra-continental earthquake swarms in West-Bohemia and Vogtland: a review. *Tectonophysics* 611:1–27. <https://doi.org/10.1016/j.tecto.2013.11.001>
- Förster HJ, Tischendorf G, Trumbull B et al (1999) Late-Collisional Granites in the Variscan Erzgebirge, Germany. *J of Petrology* 40:1613–1645. <https://doi.org/10.1093/ptro/40.11.1613>
- Gaebler PJ, Eulenfeld T, Wegler U (2015) Seismic scattering and absorption parameters in the W-Bohemia/Vogtland region from elastic and acoustic radiative transfer theory. *Geophys J Int* 203:1471–1481. <https://doi.org/10.1093/gji/ggv393>
- Geissler W, Kämpf H, Kind R et al (2005) Seismic structure and locations of a CO<sub>2</sub> source in the upper mantle of the western Eger (Ohře) Rift, central Europe. *Tectonophysics* 24:1–23. <https://doi.org/10.1029/2004TC001672>
- German Regional Seismic Network (GRSN) (2019) Federal Institute for Geosciences and Natural Resources (BGR). <https://doi.org/10.25928/MBX6-HR74>
- Grünthal G, Bankwitz P, Bankwitz E et al (1985) Seismicity and geological features of the eastern part of the West European Platform. *Gerlands Beiträge zur Geophysik* 94:276–289
- Grünthal G, Stromeyer D, Bosse C et al (2018) The probabilistic seismic hazard assessment of Germany—version 2016, considering the range of epistemic uncertainties and aleatory variability. *Bull Earthq Eng* 16:4339–4395. <https://doi.org/10.1007/s10518-018-0315-y>
- Hansen P (1992) Analysis of discrete illposed problems by means of the L-curve. *SIAM Rev* 34:561–580. <https://doi.org/10.1137/1034115>
- Harris C, Millman K, van der Walt S et al (2020) Array programming with NumPy. *Nature* 585:357–362. <https://doi.org/10.1038/s41586-020-2649-2>
- Hearn T, Ni J (1994) Pn velocities beneath continental collision zones; the Turkish-Iranian Plateau. *Geophys J Int* 117:273–283. <https://doi.org/10.1111/j.1365-246X.1994.tb03931.x>
- Heimann S, Isken M, Kühn D et al (2018) Grond - A probabilistic earthquake source inversion framework. *GFZ Dat Services*. <https://doi.org/10.5880/GFZ.2.1.2018.003>

- Heinicke J, Stephan T, Alexandrakakis C et al (2019) Alteration as possible cause for transition from brittle failure to aseismic slip: the case of the NW-Bohemia / Vogtland earthquake swarm region. *J Geodyn* 124:79–92. <https://doi.org/10.1016/j.jog.2019.01.010>
- Hemmann A, Meier T, Jentzsch G et al (2003) Similarity of waveforms and relative relocalisation of the earthquake swarm 1997/1998 near Werdau. *J Geodyn* 35:191–208. [https://doi.org/10.1016/S0264-3707\(02\)00062-5](https://doi.org/10.1016/S0264-3707(02)00062-5)
- Heuer B, Geissler W, Kind R et al (2006) Seismic evidence for asthenospheric updoming beneath the western Bohemian Massif, central Europe. *Geophys Res Lett* 33(L05):311. <https://doi.org/10.1029/2005GL025158>
- Hofmann Y, Jahr T, Jentzsch G (2003) Three-dimensional gravimetric modelling to detect the deep structure of the region Vogtland/NW-Bohemia. *J Geodyn* 35:209–220. [https://doi.org/10.1016/S0264-3707\(02\)00063-7](https://doi.org/10.1016/S0264-3707(02)00063-7)
- Horálek J, Fischer T (2008) Role of crustal fluids in triggering the West Bohemia/Vogtland earthquake swarms: just what we know (a review). *Stud Geophys Geod* 52:455–478. <https://doi.org/10.1007/s11200-008-0032-0>
- Horton S (2012) Disposal of hydrofracking waste fluid by injection into subsurface aquifers triggers earthquake swarm in central Arkansas with potential for damaging earthquake. *Seismol Res Lett* 83:250–260. <https://doi.org/10.1785/gssrl.83.2.250>
- Hrubcová P, Vavryčuk V, Boušková A et al (2013) Moho depth determination from waveforms of microearthquakes in the West Bohemia/Vogtland swarm area. *J Geophys Res* 118:120–137. <https://doi.org/10.1029/2012JB009360>
- Hrubcová P, Geissler W, Bräuer K et al (2017) Active Magmatic Underplating in Western Eger Rift, Central Europe. *Tectonics* 36:2846–2862. <https://doi.org/10.1002/2017TC004710>
- Hubbert M, Rubey W (1959) Role of fluid pressure in mechanics of overthrust faulting: I. Mechanics of fluid-filled porous solids and its application to overthrust faulting. *Geol Soc Am Bull* 70:115–166. [https://doi.org/10.1130/0016-7606\(1959\)70\[115:ROFPIM\]2.0.CO;2](https://doi.org/10.1130/0016-7606(1959)70[115:ROFPIM]2.0.CO;2)
- Hunter J (2007) Matplotlib: A 2D Graphics Environment. *Comput Sci Eng* 9:90–95. <https://doi.org/10.1109/MCSE.2007.55>
- Husen S, Smith R, Waite G (2004) Evidence for gas and magmatic sources beneath the Yellowstone volcanic field from seismic tomographic imaging. *J Volc Geotherm Res* 131:397–410. [https://doi.org/10.1016/S0377-0273\(03\)00416-5](https://doi.org/10.1016/S0377-0273(03)00416-5)
- Ibs-von Seht M, Plenefisch T, Klinge K (2008) Earthquake swarms in continental rifts - a comparison of selected cases in America, Africa and Europe. *Tectonophysics* 452:66–77. <https://doi.org/10.1016/j.tecto.2008.02.008>
- Kämpf H, Franzke H, Neunhöfer H, et al (1991) Zur strukturellen Bedeutung der Nord-Süd-Bruchstörungszone Plauen/Klingenthal - Altenberg/Gera - Leipzig/Halle - Dessau/Bernburg. In: *Geologisch-tektonischer Bau der Gera-Jachymov (Joachimsthal)-Störungszone und die daran gebundenen Uranlagerstätten - Kurzfassungen der Vorträge und Poster*, 12–13, in German
- Kato A, Sakai S, Iidaka T et al (2010) Non-volcanic seismic swarms triggered by circulating fluids and pressure fluctuations above a solidified diorite intrusion. *Geophys Res Lett* 37(L15):302. <https://doi.org/10.1029/2010GL043887>
- Kennet B, Engdahl E (1991) Travel times for global earthquake location and phase association. *Geophys J Int* 105:429–465. <https://doi.org/10.17611/DP/9991809>
- Kissling E, Ellsworth W, Eberhart-Phillips D, et al (1994) Initial reference models in local earthquake tomography. *J Geophys Res* 99:19,635–19,646. <https://doi.org/10.1029/93JB03138>
- Kissling E, Kradolfer U, Maurer H (1995) VELEST User's Guide Short - Introduction. Tech. rep, Institute of Geophysics and Swiss Seismological Service, ETH
- Klein F (2002) User's Guide to HYPOINVERSE-2000, a Fortran Program to Solve for Earthquake Locations and Magnitudes. Tech. Rep. 02–171, U.S. Geological Survey, Washington, D.C., <https://doi.org/10.13140/2.1.4859.3602>, open File Rep
- Korn M, Funke S, Wendt S (2008) Seismicity and seismotectonics of West Saxony, Germany - new insights from recent seismicity observed with the Saxonian seismic network. *Stud Geophys Geod* 52:479–492. <https://doi.org/10.1007/s11200-008-0033-z>
- Krischer L, Megies T, Barsch R et al (2015) ObsPy: a bridge for seismology into scientific Python ecosystem. *Comput Sci Discov* 8(014):003. <https://doi.org/10.1088/1749-4699/8/1/014003>
- Krull P (1984) Kosmotektonisches Schema des Territoriums der Deutschen Demokratischen Republik. *Z Angew Geol* 30:190–194 (In German)
- Kurz J, Jahr T, Jentzsch G (2003) Geodynamic modelling of the recent stress and strain field in the Vogtland swarm earthquake area using the finite-element-method. *J Geodyn* 35:247–258. [https://doi.org/10.1016/S0264-3707\(02\)00066-2](https://doi.org/10.1016/S0264-3707(02)00066-2)
- van Laaten M, Eulenfeld T, Wegler U (2022) Comparison of Multiple Lapse Time Window Analysis and Qopen to determine intrinsic and scattering attenuation. *Geophys J Int* 228:913–926. <https://doi.org/10.1093/gji/ggab390>
- van Laaten M, Wegler U, Eulenfeld T (2022) On the trail of fluids in the northernmost intracontinental earthquake swarm areas of the Leipzig-Regensburg fault zone, Germany - data set. <https://doi.org/10.5281/zenodo.6511543>
- LfULG (2018) - Sächsisches Landesamt für Umwelt, Landwirtschaft und Geologie. Digitales geologisches und seismologisches Kartenmaterial des Freistaates Sachsen. <https://www.lfulg.sachsen.de/karten-und-daten-13433.html>
- Ligorria J, Ammon C (1999) Iterative Deconvolution and Receiver-Function Estimation. *Bull Seismol Soc Am* 89:1395–1400
- Málek J, Horálek J, Janský J (2005) One-dimensional qP-wave velocity model of the upper crust for the West Bohemia/Vogtland earthquake swarm region. *Stud Geophys Geod* 49:501–524. <https://doi.org/10.1007/s11200-005-0024-2>
- Mavko G, Mukerji T (1995) Seismic pore space compressibility and Gassman's relation. *Geophysics* 60:1743–1749. <https://doi.org/10.1190/1.1443907>
- Mousavi S, Bauer K, Korn M et al (2015) Seismic tomography reveals a mid-crustal intrusive body, fluid pathways and their relation to the earthquake swarms in West Bohemia/Vogtland. *Geophys J Int* 203:1113–1127. <https://doi.org/10.1093/gji/ggv338>

- Muskin U, Bauer K, Haberland C (2013) Seismic Vp and Vp/Vs structure of the geothermal area around Tarutung (North Sumatra, Indonesia) derived from local earthquake tomography. *J Volc Geotherm Res* 260:27–42. <https://doi.org/10.1016/j.jvolgeores.2013.04.012>
- Neunhöfer H (1998) Das Bulletin der lokalen Erdbeben im Vogtland 1962–1997. DGG Mitteilung 4:2–7 (**In German**)
- Neunhöfer H, Hemmann A (2005) Earthquake swarms in the Vogtland/Western Bohemia region: spatial distribution and magnitude-frequency distribution as an indication of the genesis of swarms? *J Geodyn* 39:361–385. <https://doi.org/10.1016/j.jog.2005.01.004>
- O'Connell R, Budiansky B (1974) Seismic velocities in dry and saturated cracked solids. *J Geophys Res* 79:5412–5426. <https://doi.org/10.1029/JB079i035p05412>
- Parotidis M, Shapiro S, Rothert E (2005) Evidence for triggering of the Vogtland swarms 2000 by pore pressure diffusion. *J Geophys Res* 110:B05S10. <https://doi.org/10.1029/2004JB003267>
- Pietzsch K (1963) *Geologie von Sachsen*. Dt. Verl. Wiss, Berlin (**in German**)
- Plomerová J, Achauer U, Babuška V et al (2007) Upper mantle beneath the Eger Rift (Central Europe): plume or asthenosphere upwelling? *Geophys J Int* 169:675–682. <https://doi.org/10.1111/j.1365-246X.2007.03361.x>
- Pohl D, Wetzel HU, Grünthal G (2006) Tektonische Untersuchung im Raum Vogtland-Leipzig mit Hilfe von Fernerkundung. In: Seyfert E (ed) *Geoinformatik und Erdbeobachtung: Vorträge*; 26. Wissenschaftlich-Technische Jahrestagung der DGPF, 11. - 13.09.2006 in Berlin. Deutschen Gesellschaft für Photogrammetrie, Fernerkundung und Geoinformation (DGPF) e.V., p 277–286
- Quinteros J, Strollo A, Evans P et al (2021) The GEOFON Program in 2020. *Seismol Res Lett* 92(3):1610–1622. <https://doi.org/10.1785/0220200415>
- Schmeling H (1985) Numerical models on the influence of partial melt on elastic, anelastic and electric properties of rocks. Part I: Elasticity and anelasticity. *Phys Earth Planet Inter* 41:34–57. [https://doi.org/10.1016/0031-9201\(86\)90080-4](https://doi.org/10.1016/0031-9201(86)90080-4)
- Schmidt A, Nowaczyk N, Kämpf H et al (2013) Origin of magnetic anomalies in the large Ebersbrunn diatreme, W Saxony, Germany. *Bulletin of Volcanology* 75. <https://doi.org/10.1007/s00445-013-0766-6>
- Schüller I, Kämpf H, Schmidt A, et al (2012) Petrographic and thermochronometric investigation of the diatreme breccia of the Ebersbrunn Diatreme-W Saxony, Germany. In: Arentsen, K., Németh, K., Smid, E. (eds) 4th International Maar Conference a multidisciplinary congress on monogenetic volcanism, Auckland New Zealand, 20–24 February 2012, Abstract Volume, pp. 139–140, ISBN: 978-1-877480-15-7
- Shelly D, Ellsworth W, Hill D (2016) Fluid-faulting evolution in high definition: Connecting fault structure and frequency-magnitude variations during the 2014 Long Valley Caldera, California, earthquake swarm. *J Geophys Res* 121:1776–1795. <https://doi.org/10.1002/2015JB012719>
- Špičák A, Horálek J (2001) Possible role of fluids in the process of earthquakeswarm generation in the West Bohemia/Vogtland seismoactive region. *Tectonophysics* 336:151–161. [https://doi.org/10.1016/S0040-1951\(01\)00099-3](https://doi.org/10.1016/S0040-1951(01)00099-3)
- Stammler K (1993) SeismicHandler: programmable multichannel data handler for interactive and automatic processing of seismological analyses. *Comput Geosci* 19:135–140. [https://doi.org/10.1016/0098-3004\(93\)90110-Q](https://doi.org/10.1016/0098-3004(93)90110-Q)
- SXNET Saxon Seismic Network (2019) University of Leipzig, International Federation of Digital Seismograph Networks. <https://doi.org/10.7914/SN/SX>
- Takei Y (2002) Effect of pore geometry on Vp/Vs: From equilibrium geometry to crack. *J Geophys Res* 107. <https://doi.org/10.1029/2001JB000522>
- Tesaro M, Kaban M, Cloetingh S (2008) EuCRUST-07: A new reference model for the European crust. *Geophys Res Lett* 35(L05):313. <https://doi.org/10.1029/2007GL032244>
- Thurber C (1983) Earthquake locations and three-dimensional crustal structure in the Coyote Lake area, central California. *J Geophys Res* 88:8226–8236. <https://doi.org/10.1029/JB088iB10p08226>
- Thurber C (1993) *Local earthquake tomography: velocities and Vp/Vs - theory*. Chapman and Hall, New York
- Thurber C, Eberhart-Phillips D (1999) Local earthquake tomography with flexible gridding. *Comput Geosci* 25:809–818. [https://doi.org/10.1016/S0098-3004\(99\)00007-2](https://doi.org/10.1016/S0098-3004(99)00007-2)
- Thüringer Seismologisches Netz (2019) Institut für Geowissenschaften, Friedrich-Schiller-Universität Jena. International Federation of Digital Seismograph Networks. <https://doi.org/10.7914/SN/TH>
- Thüringer Seismologisches Netz (2021) Institut für Geowissenschaften, Friedrich-Schiller-Universität Jena - Earthquake list, [http://www.erdbebenwahrnehmung-thueringen.uni-jena.de/aktuelle\\_Ereignisse/Bulletin\\_archiv.txt](http://www.erdbebenwahrnehmung-thueringen.uni-jena.de/aktuelle_Ereignisse/Bulletin_archiv.txt). Accessed 10 July 2021
- Vinnik L (1977) Detection of waves converted from P to SV in the mantle. *Phys Earth Planet Inter* 15:39–45. [https://doi.org/10.1016/0031-9201\(77\)90008-5](https://doi.org/10.1016/0031-9201(77)90008-5)
- Vlček J, Beránek R, Fischer T et al (2022) Earthquake swarms in West Bohemia are most likely not rain triggered. *J Geodyn* 150(101):908. <https://doi.org/10.1016/j.jog.2022.101908>
- von Seebach K (1873) *Das Mitteldeutsche Erdbeben vom 6. März, (1872)* Verlag von H. Haessel, Leipzig (**in German**)
- Weise S, Bräuer K, Kämpf H et al (2001) Transport of mantle volatiles through the crust traced by seismically released fluids: a natural experiment in the earthquake swarm area Vogtland/NW Bohemia, Central Europe. *Tectonophysics* 336:137–150. [https://doi.org/10.1016/S0040-1951\(01\)00098-1](https://doi.org/10.1016/S0040-1951(01)00098-1)
- Wessel P, Smith W, Scharroo R et al (2013) Generic Mapping Tools: Improved Version Released. *EOS Trans AGU* 94:409–410. <https://doi.org/10.1002/2013EO450001>
- White L, Rawlinson N, Lister G et al (2019) Earth's deepest earthquake swarms track fluid ascent beneath nascent arc volcanoes. *J Geophys Res* 124:25–36. <https://doi.org/10.1016/j.epsl.2019.05.048>
- Yuan X, Sobolev S, Kind R et al (2000) Subduction and collision processes in the Central Andes constrained by converted seismic phases. *Nature* 408:958–961. <https://doi.org/10.1038/35050073>

- Zaliapin I, Ben-Zion Y (2013) Earthquake clusters in southern California II: Classification and relation to physical properties of the crust. *J Geophys Res* 118:2865–2877. <https://doi.org/10.1002/jgrb.50178>
- Zelt C (1998) Lateral velocity resolution from three-dimensional seismic refraction data. *Geophys J Int* 135:1101–1112. <https://doi.org/10.1046/j.1365-246X.1998.00695.x>

- Zhu L, Kanamori H (2000) Moho depth variation in southern California from teleseismic receiver functions. *J Geophys Res* 105:2969–2980. <https://doi.org/10.1029/1999JB900322>

**Publisher's Note** Springer Nature remains neutral with regard to jurisdictional claims in published maps and institutional affiliations.

### 6.3 Publication 3

#### **Non-linear inversion for a multi-layer seismic S-wave attenuation model using radiative transfer theory**

Marcel van Laaten<sup>1</sup>, Ulrich Wegler<sup>1</sup>

<sup>1</sup> Institute of Geosciences, Friedrich Schiller University Jena, Burgweg 11, 07749 Jena

Submitted in 2024 and under review in Journal of Geophysical Research: Solid Earth

Addendum 05.02.2025:

The publication has been published in 2024 in Journal of Geophysical Research: Solid Earth, 129, e2023JB027989  
<https://doi.org/10.1029/2023JB027989>

1 **Non-linear inversion for a multi-layer seismic S-wave**  
2 **attenuation model using radiative transfer theory**

3 **Marcel van Laaten<sup>1</sup>, Ulrich Wegler<sup>1</sup>**

4 <sup>1</sup>Institute of Geosciences, Friedrich Schiller University Jena, Burgweg 11, 07749 Jena, Germany

5 **Key Points:**

- 6 • We invert for a frequency-dependent intrinsic and scattering Q with anisotropic  
7 scattering using envelope fitting in a multi-layer model  
8 • We estimate seismic moments and corner frequencies for small earthquakes using  
9 a 1-D attenuation model  
10 • We observe a strong attenuation contrast between a sedimentary basin and the  
11 underlying crystalline basement

---

Corresponding author: Marcel van Laaten, [marcel.vanlaaten@uni-jena.de](mailto:marcel.vanlaaten@uni-jena.de)

**Abstract**

We numerically solve the acoustic radiative transfer equation for seismic S-waves using Monte Carlo simulation. By assuming a von Kármán type random medium with anisotropic scattering, we are able to simulate a realistic medium and determine its attenuation properties. In this study we present an improved method, called QEST, to determine the frequency-dependent intrinsic and scattering attenuation by non-linear envelope inversion for a 1-D multi-layer model. Also, the spectral source energy of earthquakes and energy site amplification of stations are determined. The code was applied to real data from the northern and southern Leipzig-Regensburg fault zone, Germany, as well as fluid-induced earthquakes at the Insheim geothermal reservoir, Germany. The attenuation was analyzed in several frequency bands between 4.2 to 33.9 Hz and 6.0 to 67.9 Hz, respectively. The inversion results reveal that the crystalline crustal subsurface along the Leipzig-Regensburg fault zone shows little to no depth dependence, but there are differences in attenuation between the north and south. At Insheim, the near-surface sedimentary basin exhibits significantly higher absorption and scattering compared to the crystalline basement. The inversion also shows that isotropic scattering can be an oversimplification and thus underestimate attenuation.

**Plain Language Summary**

Seismic attenuation is an important property of the subsurface. It determines the amplitude decay of a seismic wave emitted by an earthquake with time and distance. Seismic attenuation can be divided into scattering and intrinsic attenuation. Scattering is caused by small-scale heterogeneities in the earth, while intrinsic attenuation is caused by anelastic processes such as internal friction. Differentiating between scattering and intrinsic attenuation poses a challenge. In this study, we present an advancement for the determination of seismic attenuation that considers the heterogeneity of the Earth's crust. We apply this new method to three distinct regions in order to assess the depth-dependent scattering and intrinsic attenuation. The findings reveal that pure crystalline rock exhibits little depth-dependence, whereas the attenuation properties of a sedimentary basin differ significantly from those of the underlying crystalline rock. Overall, quantifying the depth-dependent seismic attenuation enhances our ability to accurately estimate seismic hazard.

**1 Introduction**

Radiative transfer theory (RTT) was introduced to astrophysics to study light and its interaction with matter. It is used to understand how light propagates in different media, including the Earth's atmosphere (Chandrasekhar, 1960). The theory seeks to explain how light is absorbed, scattered and re-emitted by matter and how these processes affect the intensity, direction and spectrum of the light. RTT was later adapted for seismology, first in a scalar/acoustic approximation (Wu, 1985; Hoshiya, 1991; Zeng et al., 1991; Gusev & Abubakirov, 1996; Wegler et al., 2006) to explain the generation of seismic coda through the scattering of seismic waves at the small scale 3-D heterogeneous structure of the Earth. For a detailed derivation of RTT from wave theory, we refer to Ryzhik et al. (1996). RTT was later extended for the elastic case (e.g. Margerin et al., 2000; Shearer & Earle, 2004; Przybilla et al., 2006; Przybilla & Korn, 2008; Przybilla et al., 2009; Gaebler et al., 2015; Zhang et al., 2021). The analytical solution of Paaschens (1997) is an approximation of the analytical solution of the RTT equation for scalar waves and isotropic scattering. With isotropic scattering, the direction of propagation after a scattering event is independent of the previous direction of propagation. The probability of the new direction is the same in all directions. On the other hand, anisotropic scattering, is direction-dependent, resulting in a non-uniform distribution of probability. With forward scattering, seismic waves are likely to maintain their direction or experience only

slight deflection after a scattering event. It is well known that, isotropic scattering is an oversimplification and anisotropic scattering is more realistic (e.g. Gaebler et al., 2015; Calvet et al., 2023). Scattering of light and elastic waves with wavelength  $\lambda_w$  much larger than the size of the heterogeneities is called Rayleigh scattering and gives the Rayleigh scattering cross-section proportional to  $(1/\lambda_w)^4$  (e.g. Rayleigh, 1899). For acoustic waves in random media the condition for Rayleigh scattering is  $ak \ll 1$ . Here  $a$  is the correlation length of the random medium,  $k$  is the wave number of the S-wave and  $v$  the S-wave velocity ( $k = f/v$ ). Rayleigh scattering of scalar waves results in isotropic scattering (Sato et al., 2012, p. 132) and a frequency dependency  $g_0(f, z) = g^*(f, z) \propto f^4$  at low frequencies (Fig. 1). The total scattering coefficients  $g_0(f, z)$  is the inverse of the total mean free path  $l_0(f)$ , which in turn corresponds to the average distance at which a particle is scattered. The transport scattering coefficient  $g^*(f, z)$ , on the other hand, is the inverse of the transport mean free path  $l^*(f)$ , which can be thought of as the distance required for a particle to loose memory of its initial direction. So far, no study has measured a frequency dependency of  $g_0(f, z) = g^*(f, z) \propto f^4$  for wave propagation in real crustal material, instead a frequency dependence of  $g^*(f, z) \propto f^{-2\kappa+1}$  is always observed, which can be explained by anisotropic scattering ( $ak \gg 1$ ) in a van Kármán type random medium. Also the scattering coefficient measured from envelope inversion must be interpreted as  $g^*$  not as  $g_0$  (Gaebler et al., 2015). The relationship between  $g$  and  $g_0$  as well as  $g^*$  is that  $g_0$  is the average over all angles of  $g$  and  $g^*$  is the average over all angles of  $g$ , but forward scattering is reduced (e.g. Wegler et al., 2006). An overview of the variables used in this study can be found in Tab. S1 in Supporting Information. Nevertheless, isotropic scattering is a much simpler theory and is often used in data applications (see Sato (2019) for a review). Late coda generation in the diffusive regime is controlled by the transport scattering coefficient  $g^*(f, z)$  in both cases, isotropic and anisotropic scattering. Multiple forward scattering and envelope broadening as described by Markov approximation (Sato et al., 2012, p. 319 - 399) is also controlled by the transport scattering coefficient  $g^*(f, z)$  (Wegler et al., 2006). In summary, the effective isotropic scattering coefficient is  $g^*(f, z)$  and not  $g_0(f, z)$  if we simplify anisotropic scattering by isotropic scattering. In data applications Przybilla et al. (2009) and Gaebler et al. (2015) showed that only  $g^*(f, z)$  can be resolved from observed data. The degree of forward scattering ( $ak$ , see also Wu and Aki (1988)), the total scattering coefficient  $g_0(f, z)$  as well as the standard deviation  $\varepsilon$  and correlation length  $a$  cannot be resolved from data with currently known techniques (Wegler et al., 2006; Przybilla et al., 2009; Gaebler et al., 2015). Due to the complexity of the topic, few studies consider surface wave conversion scattering (e.g. Maeda et al., 2008; Margerin et al., 2019). In general, surface waves are often disregarded in multiple scattering theory. In this study, we ignore surface waves because we use deep earthquakes that do not directly generate surface waves. We also analyze only high frequencies where surface wave conversion scattering can be neglected due to their low energy contribution to the coda.

The attenuation can be described by the inverse quality factor  $Q^{-1}$  and is a measure of the energy lost by the direct seismic wave as it propagates. Seismic attenuation can be separated into intrinsic attenuation and scattering attenuation. Intrinsic attenuation  $Q_i^{-1}$  refers to the conversion of kinetic energy into heat or other forms of energy through anelastic processes such as friction. Scattering attenuation  $Q_{sc}^{-1}$ , on the other hand, refers to the scattering of the energy of a wave field in different directions due to velocity or density changes in small scale 3-D heterogeneities. Scattering attenuation  $Q_{sc}^{-1}$  is proportional to transport scattering coefficient  $g^*$  (Gaebler et al., 2015). In general, seismic attenuation is sensitive to fluids and other rock properties that may not necessarily affect seismic velocity (e.g. Karato, 1996; Jackson et al., 2002; Aizawa et al., 2008; Chapman et al., 2015). Therefore, attenuation imaging can provide new insights into the subsurface. Accurate quantification of seismic attenuation is also important for proper assessment of earthquake magnitudes. In seismic hazard analysis attenuation information is used in ground motion prediction equations. Many large cities, such as Istanbul, Los Angeles, Mexico City or Tokyo, are built on sediments that greatly influence the am-

117 plitude of the propagating seismic wave. The traditional technique for spatial imaging  
 118 of seismic attenuation is the so-called  $t^*$ -tomography (Rietbrock, 2001; Hauksson & P.M.,  
 119 2006; Mousavi et al., 2017), which can be used to calculate and image the total seismic  
 120 attenuation. However, this method has the drawback of being unable to differentiate be-  
 121 tween intrinsic and scattering attenuation, and the frequency dependence of attenuation  
 122 must be assumed a priori. Another method for estimating seismic attenuation is based  
 123 on the coda decay of earthquakes (e.g. Calvet & Margerin, 2013; Mayor et al., 2016; Gi-  
 124 ampiccolo & Tuvè, 2018). The decay can be used to determine  $Q_c$ , which is equated to  
 125 intrinsic attenuation by assuming the diffusion model. However,  $Q_c$  often still exhibits  
 126 significant scattering (Calvet & Margerin, 2013), making physical interpretation diffi-  
 127 cult.

128 Recent progress in methodology enables the separation of seismic attenuation into  
 129 intrinsic and scattering attenuation. Two methods have been established to determine  
 130 intrinsic and scattering attenuation based on observed seismogram envelopes: the mul-  
 131 tiple lapse-time window analysis (Hoshiya, 1991; Fehler et al., 1992) and envelope fit-  
 132 ting (e.g. Sens-Schönfelder & Wegler, 2006; Gaebler et al., 2015; Eulenfeld & Wegler, 2016,  
 133 2017; Gaebler et al., 2019; van Laaten et al., 2022; Eulenfeld et al., 2023). The outcomes  
 134 of both methods are nearly identical (van Laaten et al., 2022), although envelope fitting  
 135 tends to yield slightly better results due to lower uncertainty (van Laaten et al., 2022).  
 136 The envelope fitting can be performed with local earthquakes (e.g. Gaebler et al., 2019;  
 137 Eulenfeld et al., 2023) as well as with cross-correlation of ambient noise (e.g. Hirose et  
 138 al., 2019; van Dinther et al., 2015). Several studies have compared synthetic and observed  
 139 data using forward modeling for the 1-D case. These studies often assumed a two-layer  
 140 (Margerin et al., 1998; Lacombe et al., 2003; Sens-Schönfelder et al., 2009) model with  
 141 crust and mantle or a three-layer model (Wang & Shearer, 2017) but did not invert. Also,  
 142 the spatial distribution of intrinsic (and scattering attenuation) within a region were mapped  
 143 in two dimensions (Carcolé & Sato, 2010; Del Pezzo et al., 2016; Mayor et al., 2016; De  
 144 Siena et al., 2017; Eulenfeld & Wegler, 2017; Gabrielli et al., 2020; Ibañez et al., 2020;  
 145 Zhang et al., 2022) or three dimensions (Del Pezzo et al., 2018; Akande et al., 2019; Ogiso,  
 146 2019; Shito et al., 2020; Sketsiou et al., 2021; Gabrielli et al., 2023). Substantial simpli-  
 147 fications were often used, such as isotropic scattering, coda normalization or the assump-  
 148 tion of the diffusion model. In contrast, our QEST method performs a non-linear inver-  
 149 sion for a multi-layer attenuation model that is both depth and frequency dependent and  
 150 takes into account anisotropic scattering, spectral source energy and energy site ampli-  
 151 fication of seismic stations.

## 152 2 Method

153 The general procedure of the QEST method begins with acquiring of some a pri-  
 154 ori information, such as a 1-D velocity and density model. Next, 1-D initial attenuation  
 155 models are generated and the damping parameter  $\lambda$  for the inversion is determined from  
 156 the data using the L-curve test. Then, forward modelling is conducted on each initial  
 157 model to produce synthetic data and site amplification and source properties are deter-  
 158 mined. The misfit between the synthetic and observed data is calculated and bad atten-  
 159 uation models are discarded and new attenuation models are created based on the good  
 160 models. This cycle of forward modeling and attenuation model adjustment is repeated  
 161 multiple times until the stopping criteria are met. The objective is to minimize the mis-  
 162 fit and find an optimal attenuation model that explains the observed data while keep-  
 163 ing the model simple. The individual steps are described in detail below.

### 164 2.1 Forward modelling

165 The energy density  $E_{syn}$  in a frequency band can be described by the equation (Sens-  
 166 Schönfelder & Wegler, 2006):

$$E_{syn} = WRG \quad (1)$$

167 where  $W$  is the spectral S-wave source energy of the event,  $R$  is the S-wave energy site  
 168 amplification of the station,  $G$  is the energy density Green's function. Here, the expo-  
 169 nential intrinsic attenuation is included in the Green's function. By using Monte Carlo  
 170 simulation (Gusev & Abubakirov, 1996; Yoshimoto, 2000; Wegler et al., 2006), we can  
 171 numerically solve the equation of RTT and generate synthetic envelopes  $E_{syn}$  of the S-  
 172 wave. The simulation follows seismic ray theory in a deterministic 1-D background model  
 173 and imitates the motion of particles from the earthquake to the receiver (Fig. 2). Each  
 174 particle carries a small amount of energy through a heterogeneous medium with mul-  
 175 tiple horizontal layers. Four parameters are assigned to each layer and the particle is sim-  
 176 ulated accordingly, creating a depth dependence on the depth  $z$ : the S-wave velocity  $v(z)$ ,  
 177 the density  $\rho(z)$ , the absorption coefficient  $b(f, z)$ , and the transport scattering coeffi-  
 178 cient  $g^*(f, z)$ . Starting point is a point source and the initial direction of the particles  
 179 is randomly selected. Assuming an isotropic source, the random direction can be calcu-  
 180 lated using the equations (Yoshimoto, 2000):

$$\theta = \arccos(1 - 2U_1) \quad (2)$$

181

$$\varphi = 2\pi U_2 \quad (3)$$

182 with  $\theta$  the takeoff incidence angle and  $\varphi$  the takeoff azimuthal angle. The random num-  
 183 bers  $U_1$  and  $U_2$  are generated independently from the uniformly distributed number range  
 184 between 0 and 1, resulting in a uniform radiation pattern on a focal sphere. The par-  
 185 ticle is also given an initial energy of one. At each time step  $\Delta t$ , the particle travels the  
 186 distance  $\Delta x$ :

$$\Delta x = \Delta t v(z) \quad (4)$$

187 and the energy decreases with  $e^{-b(z)\Delta t}$ . If the medium consists of multiple layers, the  
 188 particle is transmitted or reflected at the layer boundaries according to Snell's law. To  
 189 determine if the particle is reflected at the layer boundary, the energy reflection coeffi-  
 190 cient  $R_c$  is calculated (Aki & Richards, 2002, p. 139):

$$R_c = \left( \frac{\rho_1 v_1 \cos(j_1) - \rho_2 v_2 \cos(j_2)}{\rho_1 v_1 \cos(j_1) + \rho_2 v_2 \cos(j_2)} \right)^2 \quad (5)$$

191 with  $j$  the angle of incidence and the index 1 for the current as well as index 2 for the  
 192 adjacent layer. Since we are simulating energy the amplitude reflection coefficient must  
 193 be squared. To determine whether the particle is transmitted or reflected a random num-  
 194 ber  $U_3$  is generated and if  $U_3$  is smaller than  $R_c$ , the particle is reflected. In case of trans-  
 195 mission, the particle is first projected onto the boundary and then moves the remain-  
 196 ing distance in the new direction.

197 After simulating a time step, we check if the particle is scattered and the direction  
 198 of movement changes. For each layer, we assume anisotropic scattering in a von Kármán  
 199 type random medium with the homogeneous and isotropic power spectral density func-  
 200 tion  $P(k)$  (Sato et al., 2012, p. 24):

$$P(k) = \frac{8\pi^{1.5}\varepsilon^2 a^3 \Gamma(\kappa + 1.5)}{\Gamma(\kappa) (1 + a^2 k^2)^{\kappa+1.5}} \quad (6)$$

201 with  $\Gamma$  the gamma function and  $\kappa$  the Hurst exponent. The scattering is described by  
 202 the total scattering coefficient  $g_0(f, z)$ , the transport scattering coefficient  $g^*(f, z)$  and  
 203 the angular dependent scattering coefficient  $g(\theta_{sc})$ . In the isotropic case, the total scat-  
 204 tering coefficient  $g_0$  is identical to the transport scattering coefficient  $g^*$  and it holds  $g^* =$   
 205  $g_0 = g(\theta_{sc})$ . Since we can only measure the transport scattering coefficient, we invert  
 206 only for  $g^*$  and use the transport scattering coefficient to describe the small scale 3-D  
 207 heterogeneities and calculate the scattering attenuation  $Q_{sc}^{-1}$  (Gaebler et al., 2015). With  
 208 the given condition of  $0 < \kappa < 0.5$ , typical for Earth's crust, the transport scattering  
 209 coefficient  $g^*(f, z)$  can be calculated:

$$g^*(f, z) = \frac{1}{4\pi} \int_0^{2\pi} P(k') k'^3 dk'$$

$$= \frac{\varepsilon^2}{a} \left[ (\kappa - 0.5) (1 + 4a^2k^2)^{-\kappa-0.5} - (\kappa + 0.5) (1 + 4a^2k^2)^{-\kappa+0.5} + 1 \right] \frac{\sqrt{\pi}\Gamma(\kappa + 1.5)}{\Gamma(\kappa)(\kappa + 0.5)(\kappa - 0.5)} \quad (7)$$

210 for a von Kármán type random medium and  $P(k)$  given in Eq. 6. The total scattering  
211 coefficient  $g_0(f, z)$  is:

$$\begin{aligned} g_0(f, z) &= \frac{k^2}{2\pi} \int_0^{2k} P(k') k' dk' \\ &= \frac{\varepsilon^2}{a} (ak)^2 \left[ 1 - (1 + 4a^2k^2)^{-\kappa-0.5} \right] \\ &\quad \frac{2\sqrt{\pi}\Gamma(\kappa + 1.5)}{\Gamma(\kappa)(\kappa + 0.5)} \end{aligned} \quad (8)$$

212 For large  $ak$  ( $ak \gg 1$ ) Eq. 7 and Eq. 8 can be simplified:

$$g^* = \frac{\varepsilon^2}{a} (ak)^{-2\kappa+1} \frac{2^{-2\kappa+1}\sqrt{\pi}\Gamma(\kappa + 1.5)}{\Gamma(\kappa)(-\kappa + 0.5)} \propto f^{-2\kappa+1}; \quad ak \gg 1; \quad 0 < \kappa < 0.5 \quad (9)$$

213 and

$$g_0 = \frac{\varepsilon^2}{a} (ak)^2 \frac{2\sqrt{\pi}\Gamma(\kappa + 1.5)}{\Gamma(\kappa)(\kappa + 0.5)} \propto f^2; \quad ak \gg 1 \quad (10)$$

214 and for small  $ak$  ( $ak \ll 1$ ) as well:

$$g^* = g_0 = \frac{\varepsilon^2}{a} (ak)^4 \frac{8\sqrt{\pi}\Gamma(\kappa + 1.5)}{\Gamma(\kappa)} \propto f^4; \quad ak \ll 1 \quad (11)$$

215 The shape of the envelope is mainly determined by the transport scattering coefficient  
216  $g^*(f, z)$  and the absorption coefficient  $b(f, z)$  (Fig. 3). Due to trade-offs, it is not possible  
217 to determine the individual parameters  $\kappa$ ,  $a$ ,  $k$ , and  $\varepsilon$  for the same transport scattering  
218 coefficient (Wegler et al., 2006; Przybilla et al., 2009; Gaebler et al., 2015), so we  
219 fix the product of correlation length and wave number to six ( $ak = 6$ ) and thus primarily  
220 consider forward scattering (Sato et al., 2012, p. 132). The occurrence of scattering  
221 is determined by  $g_0 v(z) \Delta t > U_4$  with the random number  $U_4$  and the condition  $v(z) \Delta t \ll$   
222  $g_0^{-1}$  (Yoshimoto, 2000). If the particle is scattered, the new direction of the particle is  
223 calculated using the rejection method (Press et al., 1996; Wegler et al., 2006). The scattering  
224 incidence angle  $\theta_{sc}$  is calculated in a local coordinate system with the z-axis pointing  
225 in the direction of particle motion. First, we use equation 2 to generate a scattering  
226 angle  $\theta_{sc}$ . Additionally, another random number  $U_5$  is generated. We determine the  
227 normalized angular dependent scattering coefficient  $g(\theta_{sc})/g(0)$ :

$$g(\theta_{sc})/g(0) = \left( 1 + (2ak \sin(\theta_{sc}/2))^2 \right)^{-\kappa-1.5} \quad (12)$$

228 and if  $g(\theta_{sc})/g(0) > U_5$  the guessed angle  $\theta_{sc}$  is accepted, otherwise the process is re-  
229 peated with a new  $\theta_{sc}$  and  $U_5$  until an angle is accepted. This method is inefficient when  
230 there is strong forward scattering because the constant comparison function 1 in the forward  
231 direction greatly differs from  $g(\theta_{sc})/g(0)$ , leading to many incorrect guesses for the  
232 scattering angle. The azimuth angle is chosen from the rotational symmetry of the problem  
233 using equation 3 for  $\varphi_{sc}$ . Once the new direction of propagation is selected in the  
234 local coordinate system, an Euler rotation is applied to translate it to the original coordinate  
235 system. Incorporating anisotropic scattering into energy propagation simulations is critical in  
236 accurately representing the complex and inhomogeneous nature of the medium and understanding  
237 its effect on energy propagation.

238 By utilizing the 1-D symmetry, a torus volume can be used as the receiver volume  
239  $\Delta V$  (Fig. 2). The major radius of the torus is equal to the epicentral distance and the  
240 minor radius a given value. If the particle is inside the receiver volume during the simulation,  
241 the incoming energy is stored at time  $t$  and contributes to the envelope  $G_{MC}$ .

242 By simulating a total of  $N$  particles, the energy density  $E_{syn}(t)$  at the receiver at time  
 243  $t$  can be calculated:

$$E_{syn}(t) = \frac{WRG_{MC}(t)}{N\Delta V} \quad (13)$$

244 In contrast to isotropic scattering models, anisotropic scattering does not require a sep-  
 245 arate consideration of the direct S-wave, since envelope broadening results from the sim-  
 246 ulation (Przybilla et al., 2006; Wegler et al., 2006). The missing spectral S-wave source  
 247 energy of the event  $W$  and the energy site amplification of the station  $R$  cannot be de-  
 248 termined directly because there is a trade-off. Therefore, for each earthquake-station pair,  
 249 we compute the displacement factor  $c$  using least-squares so that the difference  $E_{obs} =$   
 250  $cE_{syn}$  is minimal. We obtain the linear equation system:

$$\ln(c_j) = \ln(W_e) + \ln(R_s) \quad (14)$$

251 with  $N_{obs}$  the number of station-earthquake pairs (index  $j$ ),  $N_e$  the number of events (in-  
 252 dex  $e$ ) and  $N_s$  the number of stations (index  $s$ ). Since not every station is present in ev-  
 253 ery event and  $N_{obs} > N_e + N_s$ , the system of equations is overdetermined and can be  
 254 solved using least-squares. We also assume that the site amplification of a station at one  
 255 frequency is the same for different events (Eulenfeld & Wegler, 2016). However, due to  
 256 the multicollinearity between  $W$  and  $R$ , an additional constraint is needed. To obtain  
 257 a reliable solution, we fix the geometric mean of all station site corrections  $W$  to 1. Fi-  
 258 nally, the intrinsic attenuation  $Q_i^{-1}$  and the scattering attenuation  $Q_{sc}^{-1}$  can be calcu-  
 259 lated:

$$Q_{sc}^{-1}(f, z) = \frac{v(z)g^*(f, z)}{2\pi f} \quad Q_i^{-1}(f, z) = \frac{b(f, z)}{2\pi f} \quad (15)$$

260 A power-law applies to the transport scattering coefficient  $g^*(f, z)$  and asserts that  $g^*(f, z)$   
 261 either remains constant or increases with frequency (Eq. 9). In nature, it is often ob-  
 262 served that a power-law is also applicable to intrinsic attenuation  $Q_i^{-1}$ . This frequency  
 263 dependence can be explained by a viscoelastic fractional Maxwell body (Mainardi, 2010).  
 264 Both power-laws can be described by the equation:

$$Q^{-1} = Q_0^{-1}f^{-\tau} \quad (16)$$

265 The power-law of  $Q_{sc}^{-1} \propto f^{-\tau}$  can be used to determine the Hurst exponent  $\kappa$  with  $\tau =$   
 266  $2\kappa$  (Eq. 9 and 15), which describes the roughness of a medium. The Hurst exponent  $\kappa$   
 267 ranges from 0 to 0.5, with small values representing higher roughness and vice versa.

268 The total attenuation  $Q_{tot}^{-1}$  corresponds to the sum of  $Q_{sc}^{-1}$  and  $Q_i^{-1}$ :

$$Q_{tot}^{-1} = Q_{sc}^{-1} + Q_i^{-1} \quad (17)$$

269 and the dominant term of  $Q_{tot}^{-1}$  can be determined using seismic albedo  $B_0$ :

$$B_0 = \frac{Q_{sc}^{-1}}{Q_{tot}^{-1}} \quad (18)$$

270  $B_0$  ranges from 0 to 1, and media with strong heterogeneity and weak intrinsic atten-  
 271 uation have higher  $B_0$  values ( $> 0.5$ ), while absorbing homogeneous media have zero.

## 272 2.2 Inversion for absorption and scattering coefficient

273 The data variance  $S$  (Menke, 2012, p. 39) is the sample wise difference between  
 274 the observed and the synthetic envelopes:

$$S = \frac{\sum_{i=1}^{N_{obs}} \sum_{t_{min}}^{t_{max}} (\log_{10}(E_{obs_i}(t)) - \log_{10}(E_{syn_i}(t)))^2}{N_{samp}} \quad (19)$$

275 with  $N_{obs}$  the number of station-earthquake pairs,  $t_{min}$  the starting point,  $t_{max}$  the end  
 276 point of the envelope time window and  $N_{samp}$  the total number of samples. The data

277 variance is normalized by dividing it by the total number of samples. This normaliza-  
 278 tion compensates for the varying number of data points across different frequencies, al-  
 279 lowing for a comparison of data variances. Using the logarithm of the envelope ensures  
 280 that the late low energy coda has a similar weight as the early high energy coda and di-  
 281 rect S-waves.

282 The model variance  $L$  (Menke, 2012, p. 43) is the sum of the differences between  
 283 two adjacent layers  $n$  and  $n + 1$  and can be described by:

$$L = \sum_{i=1}^{N_l-1} \left( \log_{10} \left( Q_{sc_{i+1}}^{-1} \right) - \log_{10} \left( Q_{sc_i}^{-1} \right) \right)^2 + \left( \log_{10} \left( Q_{i_{i+1}}^{-1} \right) - \log_{10} \left( Q_{i_i}^{-1} \right) \right)^2 \quad (20)$$

284 with  $N_l$  the number of layers in the 1-D model. Finally, the misfit function  $\phi$  can be de-  
 285 fined as (Menke, 2012, p. 55):

$$\phi = S + \lambda^2 L \quad (21)$$

286 with  $\lambda$  the inversion damping factor, also called the Tikhonov regularization parameter  
 287 (Tikhonov & Arsenin, 1977). The Tikhonov regularization parameter balances the in-  
 288 fluence of data and model variance and ensures a smooth depth dependency of the at-  
 289 tenuation model. The  $\lambda$  value can be determined by means of the L-curve test (Hansen,  
 290 1992). By varying the two layer-dependent inversion parameters  $g^*(f, z)$  and  $b(f, z)$  the  
 291 synthetic envelope  $E_{syn}$  can be fitted to the observed envelope  $E_{obs}$  by non-linear inver-  
 292 sion. The parameters  $v(z)$ ,  $\rho(z)$  and  $ak$  are assumed to be known (a priori information).

293 The overall goal of inversion is to minimize the misfit  $\phi$  so that the synthetic data  
 294 resembles the observed data while also maintaining a smooth model. To minimize  $\phi$ , we  
 295 utilize a genetic algorithm (Holland, 1992; Gad, 2021), which is a global optimization  
 296 method. This method is inspired by principles of natural selection and genetics and is  
 297 often used for solving complex problems. The genetic algorithm operates as follows: For  
 298 the first generation, a population is created that consists of both random and predeter-  
 299 mined starting models. Synthetic data is generated for each model and compared to the  
 300 observed data to calculate the misfit (Eq. 21). The population is evaluated, and the mod-  
 301 els are sorted based on their misfit. The inferior half of the models is discarded, and the  
 302 remaining models become parents. It is important to note that the best model with the  
 303 lowest misfit across all generations is always included in the parent pool. Mating occurs  
 304 through crossover and mutation based on the parents. Two parents are chosen chrono-  
 305 logically from the parent pool to produce an offspring. A random crossover point is then  
 306 chosen, which determines the point up to which the starting model parameters of one  
 307 parent are adopted. The remaining parameters are taken from the other parent. A mu-  
 308 tation is then applied to the newly obtained model, where a random parameter is replaced  
 309 by a randomly selected value within the inversion limits. The selection, crossover, and  
 310 mutation procedure is repeated until a new population of models forms the next gen-  
 311 eration. The parent pool is then discarded, and the new population is evaluated. This  
 312 process is repeated until a prescribed number of generations is reached or the misfit no  
 313 longer changes over a number of generations.

314 The inversion is performed in two steps. In the first step, the parameter search space  
 315 is kept very large, allowing for testing a large number of different models. Once the first  
 316 inversion is completed, the best-fit model is used and a second inversion is performed.  
 317 This time, the search space is smaller and limited to the vicinity of the best-fit model.  
 318 Since there is a trade-off between the parameters  $E_{syn}$ ,  $R$  and  $W$ , the values of  $R$  and  
 319  $W$  are only updated every 10th generation during the inversion.

### 320 2.3 Inversion for site amplification and source properties

321 The source displacement spectrum  $\omega M(f)$ , the seismic moment  $M_0$  and the mo-  
 322 ment magnitude  $M_w$  can be calculated from the spectral source energy  $W(f)$ . Accord-  
 323 ing to Sato et al. (2012, p. 188) the source displacement spectrum of a double-couple in

324 the far-field of an S-wave can be calculated with:

$$\omega M(f) = \sqrt{\frac{5\rho v W(f)}{2\pi f^2}} \quad (22)$$

325 The seismic moment  $M_0$ , the corner frequency  $f_c$  and the high-frequency fall-off  $n$  can  
 326 be inverted with the equation (Abercrombie, 1995) using non-linear least-square curve  
 327 fit (Virtanen et al., 2020):

$$\ln(\omega M(f)) = \ln(M_0) - \frac{1}{\gamma} \ln\left(1 + \left(\frac{f}{f_c}\right)^{\gamma n}\right) \quad (23)$$

328 assuming a Brune (Brune, 1970) source model ( $\gamma = 1$ ). The moment magnitude can  
 329 then be calculated using the seismic moment (Hanks & Kanamori, 1979):

$$M_w = \frac{2}{3} \log_{10}(M_0) - 6.07 \quad (24)$$

### 330 **3 Local earthquake data**

331 The method was applied to two different regions (Fig. 4), Insheim (INS) in the Up-  
 332 per Rhine Graben (URG) and the Leipzig-Regensburg fault zone (LRZ). The LRZ was  
 333 further divided into a northern (NLRZ) and a southern part (SLRZ), because previous  
 334 studies had already determined different attenuation values (Gaebler et al., 2015; van  
 335 Laaten et al., 2022). The earthquakes along the LRZ are of tectonic origin and occur at  
 336 various depths. The region consists mainly of metamorphic and igneous rocks. In con-  
 337 trast, Insheim is characterized by a sedimentary basin and shallow induced earthquakes  
 338 in the underlying crystalline rocks. Both regions are geologically distinct and provide  
 339 a good opportunity to study depth-dependent attenuation. During the simulation, sur-  
 340 face waves are neglected since the earthquakes used in this study do not generate direct  
 341 surface waves due to their depth. Additionally, seismic attenuation is only determined  
 342 at high frequencies, resulting in a small proportion of surface waves in the coda.

#### 343 **3.1 Leipzig-Regensburg fault zone**

344 The central part of the LRZ is visible as a seismically active north-south trending  
 345 band about 150 km long and 40 km wide (Bankwitz et al., 2003). The LRZ is crossed by  
 346 several NW-SE trending Hercynian fault zones (Pietzsch, 1963). Outside the intersec-  
 347 tion area, earthquakes on the Hercynian fault zones are rare. According to Ellenberg (1992),  
 348 one of the Hercynian fault zones, the Gera-Jáchymov fault zone, is aseismic and creep  
 349 outside the intersection prevents seismic activity. The largest historical earthquake in  
 350 the region was located near the intersection of the LRZ and the Gera-Jáchymov fault  
 351 zone and occurred on 6 March 1872 with an estimated moment magnitude of  $M_w = 5.2$ .  
 352 It was felt at a distance of several 100 km (von Seebach, 1873).

353 Along the LRZ, earthquakes change their characteristic (e.g. Neunhöfer et al., 1996;  
 354 Fischer et al., 2014; Dahm et al., 2018). Earthquakes in the southern part of the LRZ  
 355 are more frequent and occur at depths between 5 and 15 km. Further north the earth-  
 356 quakes become less frequent and deeper with focal depths between 10 and 25 km. Korn  
 357 et al. (2008) and Sonnabend (2022) analyzed the focal mechanisms of selected earthquakes  
 358 using first-arrival polarity and moment-tensor inversion along the LRZ. They concluded  
 359 that there are two preferred striking lineaments: NW-SE (Hercynian) and N-S (LRZ).  
 360 In the stress field inversion, these two groups of focal mechanisms were also determined,  
 361 with the number of N-S striking groups being slightly larger (Sonnabend, 2022). Since  
 362 no rupture direction is more likely than the other, we can assume that the different rup-  
 363 ture directions cross each other or that different focal planes are activated at different  
 364 depths and activating each other reciprocally (Sonnabend, 2022). In addition, several  
 365 earthquake swarm areas are located in the southern part of the LRZ, which are absent

366 in the north (Korn et al., 2008; van Laaten et al., 2023). Uprising mantle-derived mag-  
 367 matic fluids are suspected to be triggering the earthquake swarms in the southern part  
 368 (Špičák & Horálek, 2001; Weise et al., 2001; Hofmann et al., 2003; Bräuer et al., 2009;  
 369 Fischer et al., 2014; Mousavi et al., 2021; Vlček et al., 2022). A velocity reduction in a  
 370 1-D velocity model at a depth of 65 km is interpreted by Heuer et al. (2006) as partial  
 371 melting or an updoming of the asthenosphere, which is assumed to be the origin of the  
 372 magmatic fluids. The fluids are dissolved in the mantle to uprising melts and only sep-  
 373 arate in the crust above the updoming Moho beneath NW Bohemia/Vogtland (Geissler  
 374 et al., 2005). The exact structure of the LRZ is still controversial since no geological dis-  
 375 placement is visible at the surface. Previous studies (Bankwitz et al., 1979; Krull, 1984;  
 376 Grünthal et al., 1985; Bankwitz et al., 2003) based on photolineations of satellite images  
 377 claimed to observe the LRZ at the surface, but recent studies using modern satellite-based  
 378 data claimed that this was not sufficiently proven (Dahm et al., 2018; Grünthal et al.,  
 379 2018).

### 380 3.2 Insheim

381 Deep geothermal reservoirs such as Insheim are continuously monitored for induced  
 382 seismic activity in the sedimentary basins of the URG. The URG is a European Ceno-  
 383 zoic rift system (Ziegler, 1992) that stretches approximately 300 km in length and 40 km  
 384 in width, striking in a NNE-SSW direction. It reaches depths of up to 3.5 km (Derer et  
 385 al., 2005). Over time, the URG has undergone three major subsidence episodes since the  
 386 Eocene (Schumacher, 2002). Insheim is located near the southern transfer zone that sep-  
 387 arates the northern and southern part (Derer et al., 2005). The URG shows increased  
 388 seismic activity, with several events  $M_L > 5$  within the last 1000 years (Leydecker, 2011).  
 389 The largest known earthquake in the URG occurred in 1356 in Basel with an estimated  
 390 macroseismic intensity of IX and an estimated seismic moment magnitude of  $M_w \approx 6.7$ –  
 391 7.1 (Fäh et al., 2009).

392 The URG is of particular interest in terms of geothermal energy due to the pres-  
 393 ence of a geothermal anomaly at shallow depths. The top of the granite basement near  
 394 Insheim is situated at a depth of 3.6 km and at a depth of 3 km, the URG exhibits the  
 395 strongest thermal anomaly in Germany with temperatures exceeding  $>160^\circ\text{C}$ . Heat dis-  
 396 tribution in the sedimentary basin is primarily driven by fluids, which are likely trans-  
 397 ported along rift and fault zones (Pribnow & Schellschmidt, 2000). In 2008, drilling op-  
 398 erations commenced in Insheim and the first circulation tests for the geothermal power  
 399 plant were conducted in 2009. Induced seismicity can occur during hydraulic stimula-  
 400 tion and operational phases. The injection of fluids disturbs the subsurface and facili-  
 401 tates ruptures by shifting the stress state towards failure through poroelastic stress trans-  
 402 fer (e.g. Deng et al., 2016) or pore pressure increase (e.g. Martínez-Garzón et al., 2014).  
 403 An example of induced seismicity in Insheim is the strongest induced earthquake recorded  
 404 on April 9, 2010 at 10:52:22 UTC, measuring a magnitude of  $M_L = 2.4$  (Landeserdbebendienst  
 405 Rheinland-Pfalz, 2023).

### 406 3.3 Data selection and inversion setup

407 As described, the LRZ was divided into a northern and a southern part. Previous  
 408 studies (Gaebler et al., 2015; van Laaten et al., 2022) have shown that the attenuation  
 409 values for the two areas are different. The northern part covers the range from 12.0 to  
 410 12.8°E and 50.5 to 51.0°N while the southern part covers the range from 50.1 to 50.5°N.  
 411 We selected 12 and 9 earthquakes from the TH earthquake catalog (Thüringer Seismol-  
 412 ogisches Netz, 2022) to analyze the crustal structure for NLRZ and SLRZ, respectively.  
 413 For INS, we selected 1 tectonic and 8 induced earthquakes from the LGB-RLP catalog  
 414 (Landeserdbebendienst Rheinland-Pfalz, 2023). The magnitudes and focal depths range  
 415 from 1.3 to 2.4 and 5.25 to 21.58 km for NLRZ, 1.0 to 4.3 and 4.76 to 20.40 km for SLRZ  
 416 and 1.1 to 2.1 and 3.84 to 11.72 km for INS. All earthquakes were repicked with SeismicHan-

417 dler (Stammler, 1993) and relocated using HYPOINVERSE (Klein, 2002) with a local  
 418 1-D velocity model. The S-wave velocity and density models are shown in Fig. 5. For  
 419 the NRLZ region we use the 1-D velocity model of van Laaten et al. (2023), for SLRZ  
 420 the models are based on the study of Hrubcová and Geissler (2009) and for INS a sim-  
 421 plified version of the velocity model of Küperkoch et al. (2018) is used. The Moho was  
 422 set to 30, 29 and 27 km for NRLZ, SLRZ and INS, respectively. The density model was  
 423 calculated using the Gardner equation (Gardner et al., 1974).

424 For NRLZ and SLRZ we used a total of 61 openly available stations from the net-  
 425 works with network codes 7E, BW, CZ, GE, GR, SX, TH and Z3. All stations are equipped  
 426 with a 3-component seismometer and sample the data at either 100 or 200 Hz. The max-  
 427 imum epicentral distance was limited to  $1^\circ$ , to avoid first arrivals of Sn-waves. For INS,  
 428 we use a total of 19 stations from the LE and GR networks. The INS stations are also  
 429 equipped with 3-component seismometers and all stations sample at 200 Hz.

430 Prior to filtering, the traces were detrended. The data for NRLZ and SLRZ were  
 431 filtered using a two-corner Butterworth filter with zero shift in the frequency bands 2.8  
 432 - 5.6, 4.0 - 8.0, 5.6 - 11.3, 8.0 - 16.0, 11.3 - 22.6, 16.0 - 32.0 and 22.6 - 45.2 Hz with the  
 433 corresponding center frequencies 4.2, 6.0, 8.5, 12.0, 17.0, 24.0 and 33.9 Hz. Since the INS  
 434 stations have a higher sampling rate, we were able to analyze additional frequency bands  
 435 of 32.0 - 64.0 and 45.3 - 90.5 Hz with corresponding center frequencies of 48.0 and 67.9 Hz.  
 436 However, the lowest frequency of 4.2 Hz could not be analyzed for INS. After filtering,  
 437 we calculated seismogram envelopes using Hilbert transformation. The three-component  
 438 envelopes were then stacked to obtain the total energy envelope. To determine the noise  
 439 level of the total energy envelope at each central frequency, we averaged two time win-  
 440 dows: one from 10 s to 4 s before the origin time, and another from 4 to 0 s before the  
 441 origin time. A minimum signal-to-noise ratio of 2 was required for a station to be included  
 442 in the inversion. Additionally, for SLRZ and NRLZ, we set a minimum coda length of  
 443 30 s from the S-pick to avoid any influence of coda length on the result. For shorter time  
 444 windows, there is a trade-off between intrinsic attenuation and source displacement spec-  
 445 tra (van Laaten et al., 2022). For INS we use a minimum coda length of 4 s, as the sta-  
 446 tions are much more local (Eulenfeld & Wegler, 2016). To save computational time in  
 447 the Monte Carlo simulation, we set the maximum window length to 50 s for NRLZ and  
 448 SLRZ and 40 s for INS from the S-pick. The envelopes were then sampled down to the  
 449 time interval of the Monte Carlo simulation and smoothed over 2 s using a Bartlett win-  
 450 dows.

451 The Monte Carlo simulation was performed with a time interval of  $\Delta t = 0.2$  s.  
 452 The small radius of the receiver volume was set to 2 km for NRLZ and SLRZ and 1 km  
 453 for INS. The damping factor of the inversion  $\lambda$  (Fig. 6) was determined using the L-curve  
 454 test (Hansen, 1992) for one frequency band (12 Hz) and then applied to the remaining  
 455 frequency bands. We selected  $\lambda = 0.3$  for all three regions. The L-curve test of NRLZ  
 456 provided  $\lambda = 0.1$ , but the results varied greatly at this value and did not satisfy the  
 457 expected power-law (Eq. 16). Therefore, a higher  $\lambda$  value was chosen. A total of 8 mil-  
 458 lion particles were simulated and the synthetic envelopes were smoothed to compensate  
 459 for fluctuations in the coda. Absorption and scattering coefficients were tested in the range  
 460 of  $b = [10^{-4.5}, 10^{1.0}] \text{ s}^{-1}$  and  $g^* = [10^{-4.3}, 10^{-1.3}] \text{ km}^{-1}$  for NRLZ and SLRZ and  $b =$   
 461  $[10^{-2.5}, 10^{0.5}] \text{ s}^{-1}$  and  $g^* = [10^{-3.7}, 10^{-0.7}] \text{ km}^{-1}$  for INS. The initial values of scat-  
 462 tering and absorption, as well as the spectral source energy and energy site amplifica-  
 463 tion were determined with Qopen assuming depth independence and isotropic scatter-  
 464 ing (Eulenfeld & Wegler, 2016; Eulenfeld, 2020).

## 465 4 Results and discussion

466 We obtained the depth and frequency dependent scattering and intrinsic attenua-  
 467 tion which were the main scope of this study. Additionally, the site amplification of sta-  
 468 tions (Fig. S1-S3 in Supporting Information) and the source spectra of the earthquakes  
 469 for the regions NRLZ, SLRZ, and INS were also measured as byproduct but not ana-

470 lyzed in much detail. The misfit of the homogeneous attenuation model was reduced by  
 471 the inversion, and the 1-D attenuation model is able to better explain the data. Taking  
 472 INS at 17 Hz as an example (Fig. 7), the misfit  $\phi$  was decreased from 0.77 for the ho-  
 473 mogeneous model to 0.25 for the 1-D attenuation model. The inversion produced 20 model  
 474 updates over 300 generations, with each update having a smaller misfit than the previ-  
 475 ous best-fit model. It was found that a single iteration was not enough to find the min-  
 476 imum of the objective function. An overview of the model space is shown in Fig. 8. There  
 477 are multiple intersection points outside the global minimum leading to local minima, par-  
 478 ticularly in the transport scattering coefficient versus absorption coefficient. Therefore,  
 479 a method with global optimization is required. Additionally, the second optimization with  
 480 a narrow search range around the best-fit model has resulted in a refinement of the model.  
 481 A comparison of synthetic and observed envelopes is shown in Fig. 9, with one earthquake-  
 482 station combination from each region for three different frequencies. Further envelopes  
 483 can be found in the Supporting Information (Fig. S4 - S12).

484 The assumption of anisotropic scattering is necessary because isotropic scattering  
 485 cannot describe the envelope broadening of the direct wave with propagation distance  
 486 (Sato et al., 2012, p. 319 - 399). Another advantage of the QEST method is that the de-  
 487 termination of the site amplification and the source spectrum eliminates the need for coda  
 488 normalization that is often used. Coda normalization assumes that the focal mechanism  
 489 does not affect the late coda in the diffusion regime. To perform coda normalization, one  
 490 must determine the average energy of a time window positioned in the diffusion time win-  
 491 dow of the coda, i.e. the coda window position being as late as possible. However, de-  
 492 termining the start of the diffusion regime requires prior knowledge of the transport scat-  
 493 tering coefficient. Also, Heller et al. (2022) has shown that there are still differences in  
 494 the coda if, for example, a weakly scattering crust is assumed. By omitting coda nor-  
 495 malization, we can also simulate shorter envelopes and include them in the inversion, thereby  
 496 increasing the total amount of data.

497 The attenuation values for NLRZ and SLRZ are shown in Fig. 10 and for INS in  
 498 Fig. 11. The figures compare the homogeneous attenuation values of  $Q_{open}$  determined  
 499 with isotropic scattering with the frequency dependency of the attenuation in the dif-  
 500 ferent layers. The error bars on the values represent the estimated uncertainty, assum-  
 501 ing a 5% tolerance of the misfit of the best-fit model. The depth dependence of the three  
 502 regions for 12 Hz is shown in Fig. 12. The attenuation values shown in the figure are based  
 503 on the power-law. The power-law was determined separately for each layer, using weighted  
 504 least-squares with the slope of intrinsic and scattering attenuation versus frequency as  
 505 the basis and the inverse misfit as the weighting factor (see Fig. 10 and 11). It is impor-  
 506 tant to note that the depth-dependent model is not based on a single inversion, but rather  
 507 considers all inversion results from different frequency bands. Therefore, any anomalies  
 508 in the models do not originate from inaccuracies of a single frequency band. Selected depth-  
 509 dependent inversion results (Fig. S13 - S21) and all depth-dependent power-law mod-  
 510 els (Fig. S22 - S24) are given in Supporting Information.

#### 511 4.1 Leipzig-Regensburg fault zone

512 Scattering and intrinsic attenuation for NLRZ have already been determined by  
 513 van Laaten et al. (2022). The results are comparable to our homogeneous attenuation  
 514 values. For SLRZ, the attenuation values have already been determined by Gaebler et  
 515 al. (2015). Compared to the acoustic results of Gaebler et al. (2015), the homogeneous  
 516 attenuation values determined here are lower. This can be explained by a different se-  
 517 lection of earthquakes. Gaebler et al. (2015) selected only earthquakes from the NW-Bohemian  
 518 region, while in this study earthquakes north of this region were also used. The differ-  
 519 ence in attenuation can be attributed to the fact that the attenuation decreases north-  
 520 ward along the LRZ. The 1-D models of NRLZ and SLRZ show similar values for the  
 521 attenuation ( $Q_i^{-1}$  and  $Q_{sc}^{-1}$ ) in the homogeneous space. The only difference is observed  
 522 in the intrinsic attenuation  $Q_i^{-1}$  at low frequencies of NLRZ, which shows a stronger ab-

sorption. The result of the 1-D inversion is more consistent with the power-law compared to the homogeneous model. For NRLZ, there is a slight depth dependence of  $Q_{sc}^{-1}$  and  $Q_i^{-1}$  (Fig. 12 (d) and (e)). At 12 Hz the intrinsic attenuation  $Q_i^{-1}$  decreases slightly with depth. For SLRZ, the intrinsic attenuation  $Q_i^{-1}$  also decreases, but then increases below 12 km. Earthquakes in both regions occur preferentially in the region of low intrinsic attenuation  $Q_i^{-1}$ . The majority of earthquakes in the NRLZ are at depths greater than 12 km, while in the SLRZ most earthquakes are between 6 and 16 km depth. According to Mainardi (2010, p. 53), in a Maxwell body the intrinsic attenuation equals:

$$Q_i^{-1} = \frac{\mu}{\eta\omega}; \quad \omega \gg \mu/\eta \quad (25)$$

with  $\mu$  the shear modulus,  $\eta$  the viscosity and  $\omega$  the angular frequency. Therefore, the viscosity  $\eta$  is inversely proportional to the intrinsic attenuation  $Q_i^{-1}$ . A low  $Q_i^{-1}$ , as preferred for seismic depths of NRLZ and SLRZ, can be explained by a high viscosity  $\eta$ . At high viscosity  $\eta$ , the crust exhibits low anelasticity, leading to high friction and a lack of ductile properties during crustal relaxation. This, in turn, leads to stress concentration in the area with low intrinsic attenuation  $Q_i^{-1}$ , which is released in the form of earthquakes. According to laboratory experiments, above the seismogenic layer frictional sliding occurs, and below the Earth's crust plastically flows due to temperature rise preventing stress accumulation (Kohlstedt et al., 1995). A limitation of estimating viscosity from seismic wave attenuation is the different time scale of particle motion caused by seismic waves compared to motions related to crustal stress relaxation. Additionally, the exponent in Eq. 16 should be exactly  $\tau = 1$  for a Maxwell body. Observed values of this study are  $0.44 < \tau < 1.15$ , which is better explained by a fractional Maxwell model (Mainardi, 2010).

Eulenfeld (2020) has already interpreted from his inter-source interferometry analysis that the near-surface layer has a higher intrinsic attenuation. One side of the cross-correlation function was found to be dominant, indicating that the coda waves between two events with a low inclination angle consist of waves leaving the source in the downward direction. On the other hand, waves that travel upward and spend more time in the uppermost crust experience more attenuation (Eulenfeld, 2020). Therefore, we can partially confirm this observation. Another possible explanation for the effect observed by Eulenfeld (2020) could be the stronger transport scattering coefficient  $g^*$  in the layer 12 to 18 km. This ensures that the waves in this layer are scattered and change direction more frequently, causing them to move upwards. The higher intrinsic attenuation values  $Q_i^{-1}$  below 12 km of SLRZ compared to NRLZ can be explained by the presence of fluids or a significant increase in temperature.

Regarding scattering attenuation  $Q_{sc}^{-1}$ , there is a clear difference between the isotropic and anisotropic scattering in both regions. For NRLZ, the anisotropic scattering attenuation is stronger at low frequencies and weaker at higher frequencies, while for SLRZ, the scattering attenuation of the anisotropic scattering is consistently stronger than in the isotropic case. A similar observation was also made by Calvet et al. (2023), where the attenuation determined with anisotropic scattering was stronger than the attenuation determined with isotropic scattering. While the assumption of isotropic scattering is not incorrect (Gaebler et al., 2015), it is merely an approximation. Anisotropic scattering is more precise and the assumption of isotropic scattering is thus an oversimplification. This may lead to an underestimation of the scattering attenuation depending on the region. The depth dependence of the scattering attenuation  $Q_{sc}^{-1}$  shows a different behavior than the intrinsic attenuation  $Q_i^{-1}$ . Scattering attenuation  $Q_{sc}^{-1}$  increases with depth at 12 Hz for both NRLZ and SLRZ. It is worth noting that the transport scattering coefficient  $g^*$  decreases slightly in contrast to the scattering attenuation  $Q_{sc}^{-1}$ . Thus, the increase in scattering attenuation results from the increase in velocity with depth. The difference between the transport scattering coefficient  $g^*$  and scattering attenuation  $Q_{sc}^{-1}$  can be explained as follows. Scattering in the crust becomes less directional as depth increases, but there is a slight increase in energy loss due to scattering. In both regions  $\kappa$  increases with depth, in the case of NRLZ from 0.29 to 0.36 and for SLRZ from 0.03

576 to 0.08. This indicates that the subsurface of SLRZ is significantly rougher than that of  
577 NLRZ. Due to trade-off problems the correlation length  $a$  is not well constraint for the  
578 crust. However, we did not observe a kink in the frequency behavior of the transport scat-  
579 tering coefficient,  $g^*$  at low frequencies during the analysis, as shown in Fig. 1. There-  
580 fore, we can make a minimum estimate for the correlation length  $a$ . Since we are still  
581 in the forward scattering regime (Fig. 1),  $ak > 1$  applies. For the correlation length  
582  $a$  follows  $a > 1/k = v/f$ . The lowest frequency analyzed for NLRZ and SLRZ is 4.2 Hz.  
583 This results in a minimum correlation length  $a$  of the respective layers of the attenua-  
584 tion model: [0.8, 0.8, 0.8, 0.9, 1.0] km for NLRZ and [0.8, 0.8, 0.9, 0.9, 1.0] km for SLRZ.  
585 The seismic attenuation  $Q_{tot}^{-1}$  in both regions is dominated by the intrinsic attenuation  
586  $Q_i^{-1}$  (Fig. 12 (e)). However, in NLRZ, the dominance of intrinsic attenuation decreases  
587 slightly with depth as the albedo increases. In SLRZ, the albedo initially increases and  
588 then slightly decreases starting from 12 km. The low albedo value therefore implies that  
589 the attenuation reduces the amplitude of the entire signal. Overall, the crystalline rock  
590 in both NLRZ and SLRZ regions shows little depth dependence and the assumption of  
591 a homogeneous random medium for determining attenuation values is valid and yields  
592 similar results. The average high-frequency fall-off of earthquake source spectra is  $n =$   
593 2.3 for NLRZ (Fig. 13) and  $n = 1.9$  for SLRZ (Fig. S25 in Supporting Information),  
594 while the average corner frequency is  $f_c = 13.6$  Hz and  $f_c = 7.9$  Hz for NLRZ and SLRZ,  
595 respectively. Therefore, the fall-off for both regions corresponds to the omega-square model  
596 ( $n = 2$ ) and the corner frequency corresponds to the typical corner frequency of local  
597 earthquakes with magnitudes ranging from 1.3 to 2.4 for NLRZ and 1.0 to 4.3 for SLRZ,  
598 respectively. A comparison between the moment magnitude  $M_w$  and the local magni-  
599 tude  $M_L$  as well as the QEST moment magnitude and Qopen moment magnitude of the  
600 NLRZ and SLRZ earthquakes is provided in the in Supporting Information (Fig. S26  
601 - S27).

## 602 4.2 Insheim

603 The intrinsic and scattering attenuation in INS, assuming a homogeneous random  
604 medium, have been determined by Eulenfeld and Wegler (2016). The attenuation val-  
605 ues obtained here for the homogeneous space with isotropic scattering are comparable  
606 to the results of Eulenfeld and Wegler (2016). However, there is a noticeable difference  
607 between the depth-dependent attenuation values determined with anisotropic scatter-  
608 ing and the attenuation values of the homogeneous model with isotropic scattering. In  
609 contrast to NLRZ and SLRZ, the intrinsic attenuation  $Q_i^{-1}$  shows a clear depth depen-  
610 dence. The near-surface sediments are strongly absorbing and the intrinsic attenuation  
611  $Q_i^{-1}$  decreases with depth and is slightly weaker than the intrinsic attenuation of the ho-  
612 mogeneous model.

613 The scattering attenuation  $Q_{sc}^{-1}$  is stronger and slightly increases with depth com-  
614 pared to the scattering attenuation of the homogeneous model. In particular, the trans-  
615 port scattering coefficients  $g^*$  behaves differently. While a power-law applies to the scat-  
616 tering coefficient (see Eq. 16), the scattering coefficient in the homogeneous model does  
617 not exhibit this behavior. In fact, as the frequency increases, the scattering coefficient  
618 of the homogeneous model decreases. According to Eq. 7 the transport scattering co-  
619 efficient  $g^*$  is an integral over the power spectral density  $P$  of the random medium, where  
620  $P$  is always positive. Therefore  $g^*$  cannot decrease with increasing frequency. A power-  
621 law behavior of  $g^*$  is typically observed for the Earth's crust and corresponds to a von  
622 Kármán type random medium with  $ak \gg 1$  (Fig. 1 and Eq. 9).

623 On the other hand, the anisotropic transport scattering coefficient  $g^*$ , remains con-  
624 stant near the surface and slightly increases with depth. Unlike the scattering coefficient  
625 of the homogeneous model, the anisotropic transport scattering coefficient follows a power-  
626 law. Therefore, the assumption of isotropic scattering and depth independence is an over-  
627 simplification and cannot adequately explain the subsurface properties in the INS region.  
628 Another factor that may account for the difference in attenuation  $Q^{-1}$  is the 1-D veloc-

ity model used in our study. In the homogeneous model, there are no reflections and transmissions at layer boundaries. The absence of reflections and transmissions lead to a higher energy of the direct wave, which can in turn affect the attenuation values. Another peculiarity can be observed when comparing the transport scattering coefficient  $g^*$ , and the scattering attenuation  $Q_{sc}^{-1}$  or the inverse transport mean free time  $1/t^*$  ( $t^* = vg^*$ ). As the depth increases,  $g^*$  decreases, whereas  $Q_{sc}^{-1}$ , or  $1/t^*$ , initially decreases and then increases below 3 km depth. Therefore, on average, the wave scatters more frequently in layers near the surface, but it loses more energy at depth when a scattering event occurs. Also, the inverse absorption length  $1/l_i$  ( $l_i = b/v$ ) exhibits a greater dependence on depth compared to both the absorption coefficient  $b$  and intrinsic attenuation  $Q_i^{-1}$ . Therefore, when using the depth-dependent 1-D model, it is crucial to differentiate between  $g^*$  and  $1/t^*$ , as well as between  $b$  and  $1/l_i$ , since the S-wave velocity  $v$  is different in each layer.

In contrast to NLRZ and SLRZ, the Hurst exponent  $\kappa$  decreases from 0.51 at the surface to 0.44 in the crystalline rock of INS. The subsurface is characterized by a low roughness, which only slightly increases with depth. In contrast, the crystalline rocks of NLRZ and SLRZ are significantly rougher. As in NLRZ and SLRZ, a minimum estimate of the correlation length  $a$  can also be made for INS. Analogously, a minimum correlation length  $a$  results for INS for the respective layers of the attenuation model: [0.1, 0.2, 0.4, 0.5, 0.7] km. The total attenuation  $Q_{tot}^{-1}$  is dominated (Fig. 12 (f)) by the strong intrinsic attenuation  $Q_i^{-1}$  near the surface. As a result, the amplitude of the signal near the surface is strongly attenuated. In crystalline rock, the seismic albedo increases and the intrinsic attenuation loses influence, but is still the dominant term. Part of the energy of the direct wave is therefore transferred to the coda in the crystalline rock. The average fall-off of the earthquake source spectra in INS (Fig. S28 in Supporting Information) is  $n = 4.2$  and the average corner frequency is  $f_c = 14.2$ . Since the earthquakes of INS cover a similar magnitude range (1.1 to 2.1) as NLRZ, the average corner frequency is comparable and corresponds to the typical value of local earthquakes. However, the fall-off value is particularly high and the omega-square model is not applicable to the earthquakes. Eulenfeld and Wegler (2016) found fall-off values of 3 and attributed this to the reservoir-induced nature of the earthquakes. To achieve lower fall-off values, the slope of the source spectrum would need to be flatter and thus the transport scattering coefficient  $g^*$  would have to increase less with frequency. However, this would make the results similar to those of the homogeneous model, which violates the power-law behavior of the transport scattering coefficient  $g^*$ . Thus, the source spectra of the induced earthquakes here are peculiar and require further investigation. Another explanation for the high fall-off values  $n$  could be strong attenuation in the first few meters below the surface (Raghukanth & Somala, 2009). Higher frequencies are more sensitive to these layers compared to lower frequencies. As a result, the site amplification at high frequencies would be lower, leading to larger source spectrum values and a smaller  $n$ . However, the boundary condition that the geometric mean of all stations equals 1 requires larger station amplification values. A reference station on bedrock, such as the LE borehole stations, could be used for normalization. A comparison between the moment magnitude  $M_w$  and the local magnitude  $M_L$  as well as the QEST moment magnitude and Qopen moment magnitude of the INS earthquakes is given in Supporting Information (Fig. S29).

### 4.3 Outlook

The QEST method has potential for further development in various directions. One possibility is to use the elastic RTT instead of the acoustic RTT, as in Margerin et al. (2000); Sens-Schönfelder et al. (2009); Gaebler et al. (2015), to take P- and S-waves as well as body wave conversions into account. Additionally, integrating surface wave conversion into the Monte Carlo simulation, as in the studies of Maeda et al. (2008); Margerin et al. (2019) is beneficial.

681 Another main focus could be the source spectra of the earthquakes and the site am-  
 682 plification of the stations. The resolution of the source spectra and site amplifications  
 683 is increased by analyzing a large number of narrow frequency bands. This can be achieved  
 684 by using the power-law of intrinsic and scattered attenuation to interpolate attenuation  
 685 values. With the interpolated attenuation values, the source spectra and site amplifica-  
 686 tions of the new frequency bands can be determined by forward modeling for each fre-  
 687 quency band.

688 The next step towards spatial resolution would be a full 3-D attenuation tomog-  
 689 raphy, using the 1-D attenuation model obtained with QEST as the starting model. For  
 690 3-D, it is important to consider the focal mechanism of the earthquakes. Instead of us-  
 691 ing the torus receiver volume as in the 1-D case, a small half sphere volume must be used  
 692 at each station. The computational effort is also greater, as additional particles have to  
 693 be simulated due to the loss of azimuthal symmetry. The inversion is also more complex,  
 694 as more inversion parameters need to be accounted for.

## 695 5 Conclusion

696 In this study, we present an improved method of envelope fitting of seismic S-waves  
 697 to determine depth-dependent intrinsic and scattering attenuation. A key difference from  
 698 previous methods is that they often assume isotropic scattering in a homogeneous model.  
 699 In contrast, QEST assumes anisotropic scattering, which accurately describes the direct  
 700 S-wave in a multi-layer attenuation model that considers reflection and transmission at  
 701 layer boundaries of a 1-D velocity model. The code simultaneously inverts for the at-  
 702 tenuation and site amplification of stations, as well as the spectral source energy den-  
 703 sities of earthquakes using a global optimization method. Compared to coda normaliza-  
 704 tion, we are also able to simulate shorter envelopes. The depth-dependent attenuation  
 705 was determined for three regions: the northern and southern Leipzig-Regensburg fault  
 706 zone and Insheim in Germany. In all three regions, intrinsic attenuation  $Q_i^{-1}$  is domi-  
 707 nant. Depth dependence is only slightly present in the northern and southern Leipzig-  
 708 Regensburg fault zone. However, in Insheim the sedimentary basin absorbs and scatters  
 709 much more than the underlying crystalline rocks. Therefore, it is crucial to consider depth-  
 710 dependence depending on the region. This study also demonstrate that the assumption  
 711 of isotropic scattering can be an oversimplification in certain regions and can lead to an  
 712 underestimation of scattering attenuation. Therefore, caution is required when deter-  
 713 mining the spatial distribution of seismic attenuation under the assumption of isotropic  
 714 scattering. It is crucial to first verify whether isotropic scattering can be assumed. One  
 715 indication that attenuation is underestimated is the frequency behavior of the scatter-  
 716 ing coefficient. If the scattering coefficient contradicts the power-law and decreases with  
 717 increasing frequency instead of increasing or remaining constant, anisotropic scattering  
 718 may be necessary to explain the data. Otherwise, certain regions may be underestimated,  
 719 which could cause anomalies to appear or disappear. The earthquakes in the northern  
 720 and southern Leipzig-Regensburg fault zone are consistent with the omega-square model,  
 721 whereas Insheim exhibits significantly larger high-frequency fall-off values. Overall, the  
 722 method highlights the importance of a spatial examination of seismic attenuation.

## 723 6 Open Research

724 Data from the BGR, GEOFON, IRIS, LMU and ORFEUS archive with Federa-  
 725 tion of Digital Seismograph Networks (FDSN) network identifiers 7E (Wilde-Piórko et  
 726 al., 2006), BW (Department of Earth and Environmental Sciences, Geophysical Obser-  
 727 vatory, University of Munchen, 2001), CZ (Charles University in Prague (Czech) et al.,  
 728 1973), GR (Federal Institute for Geosciences and Natural Resources, 1976), LE (Erdbebendienst  
 729 Südwest Baden-Württemberg and Rheinland-Pfalz, 2009), SX (University of Leipzig, 2001),  
 730 TH (Institut fuer Geowissenschaften, Friedrich-Schiller-Universitaet Jena, 2009), Z3 (AlpArray  
 731 Seismic Network, 2015) were used in the creation of this manuscript. Data processing

732 and plotting were performed with Generic Mapping Tools (Wessel et al., 2013), Matplotlib  
 733 (Hunter, 2007), NumPy (Harris et al., 2020), ObsPy (Krischer et al., 2015), PyGAD (Gad,  
 734 2021), SciPy (Virtanen et al., 2020). The attenuation values are available at van Laaten  
 735 and Wegler (2023). QEST will be made available.

### 736 Acknowledgments

737 We would like to thank the operators of the different networks and data centers. Seis-  
 738 micHandler was funded by the German Research Foundation (DFG) within the frame-  
 739 work of SPP-1066. The computational experiments were performed on resources of Friedrich  
 740 Schiller University Jena supported in part by DFG grants INST 275/334-1 FUGG and  
 741 INST 275/363-1 FUGG. SEIGER was funded by the Federal Ministry for Economic Af-  
 742 fairs and Climate Action and the project executing organization Jülich grants 03EE4003A-  
 743 G. This work was supported by the Thüringer Landesamt für Umwelt, Bergbau und Naturschutz.

### 744 References

- 745 Abercrombie, R. (1995). Earthquake source scaling relationships from -1 to 5 ML  
 746 using seismograms recorded at 2.5-km depth. *J. Geophys. Res.*, *100*, 24015–  
 747 24036. doi: 10.1029/95JB02397
- 748 Aizawa, Y., Barnhoorn, A., Faul, U., Gerald, J., & Jackson, I. (2008). Seismic Prop-  
 749 erties of Anita Bay Dunite: an Exploratory Study of the Influence of Water. *J.*  
 750 *Petrol.*, *49*, 841–855. doi: 10.1093/petrology/egn007
- 751 Akande, W., De Siena, L., & Q., G. (2019). Three-dimensional kernel-based  
 752 coda attenuation imaging of caldera structures controlling the 1982-84  
 753 Campi Flegrei unrest. *J. Volcanol. Geotherm. Res.*, *381*, 273–283. doi:  
 754 10.1016/j.jvolgeores.2019.06.007
- 755 Aki, K., & Richards, R. (2002). *Quantitative Seismology*. Berlin: University Science  
 756 Books.
- 757 AlpArray Seismic Network. (2015). *Alparray seismic network (aasn) temporary com-*  
 758 *ponent*. AlpArray Working Group [Dataset]. Retrieved from [http://networks](http://networks.seismo.ethz.ch/networks/z3/)  
 759 [.seismo.ethz.ch/networks/z3/](http://networks.seismo.ethz.ch/networks/z3/) doi: 10.12686/ALPARRAY/Z3\_2015
- 760 Bankwitz, P., Bankwitz, E., & Frischbutter, A. (1979). Fototektonische Interpre-  
 761 tation von Mitteleuropa nach Aufnahmen der sowjetischen Wettersatelliten  
 762 Meteor 25 und 28. *Veröffentlichungen des Zentralinstituts für Physik der Erde,*  
 763 *Beiträge zur Fernerkundung*, 37–60. (in German)
- 764 Bankwitz, P., Schneider, G., Kämpf, H., & Bankwitz, E. (2003). Structural charac-  
 765 teristics of epicentral areas in Central Europe: study case Cheb basin (Czech  
 766 Republic). *J. Geodyn.*, *35*, 5–32. doi: 10.1016/S0264-3707(02)00051-0
- 767 Bräuer, K., Kämpf, H., & Strauch, G. (2009). Earthquake swarms in non-  
 768 volcanic regions: what fluids have to say. *Geophys. Res. Lett.*, *36*. doi:  
 769 10.1029/2009GL039615
- 770 Brune, J. (1970). Tectonic stress and the spectra of seismic shear waves from earth-  
 771 quakes. *J. Geophys. Res.*, *75*, 4997–5009. doi: 10.1029/JB075i026p04997
- 772 Calvet, M., & Margerin, L. (2013). Lapse-Time Dependence of Coda Q: Anisotropic  
 773 Multiple-Scattering Models and Application to the Pyrenees. *Bull. seism. Soc.*  
 774 *Am.*, *103*, 1993–2010. doi: 10.1785/0120120239
- 775 Calvet, M., Margerin, L., & Hung, S. (2023). Anomalous attenuation of high-  
 776 frequency seismic waves in Taiwan: observation, model and interpretation. *J.*  
 777 *Geophys. Res.*, *128*, e2022JB025211. doi: 10.1029/2022JB025211
- 778 Carcolé, E., & Sato, H. (2010). Spatial distribution of scattering loss and intrinsic  
 779 absorption of short-period S waves in the lithosphere of Japan on the basis of  
 780 the Multiple Lapse Time Window Analysis of Hi-net data. *Geophys. J. Int.*,  
 781 *180*, 268–290. doi: 10.1111/j.1365-246X.2009.04394.x
- 782 Chandrasekhar, S. (1960). *Radiative Transfer*. New York: Dover Publications.

- 783 Chapman, S., Tisato, N., Quintal, B., & Holliger, K. (2015). Seismic attenuation  
784 in partially saturated Berea sandstone submitted to a range of confining pres-  
785 sures. *J. Geophys. Res.*, *121*, 1664–1676. doi: 10.1002/2015JB012575
- 786 Charles University in Prague (Czech), Institute of Geonics, Institute of Geo-  
787 physics, Academy of Sciences of the Czech Republic, Institute of Physics  
788 of the Earth Masaryk University (Czech), & Institute of Rock Structure  
789 and Mechanics. (1973). *Czech Regional Seismic Network*. International  
790 Federation of Digital Seismograph Networks [Dataset]. Retrieved from  
791 <https://www.fdsn.org/networks/detail/CZ/> doi: 10.7914/SN/CZ
- 792 Dahm, T., Heimann, S., Funke, S., Wendt, S., Rappsilber, I., Bindi, D., . . . Cot-  
793 ton, F. (2018). Seismicity in the block mountains between Halle and Leipzig,  
794 Central Germany: centroid moment tensors, ground motion simulation, and  
795 felt intensities of two  $M \approx 3$  earthquakes in 2015 and 2017. *J. Seismol.*, *22*,  
796 985–1003. doi: 10.1007/s10950-018-9746-9
- 797 De Siena, L., Amoroso, A., Del Pezzo, E., Wakeford, Z., Castellano, M., & Crescen-  
798 tini, L. (2017). Space-weighted seismic attenuation mapping of the aseismic-  
799 source of Campi Flegrei 1983–1984 unrest. *Geophys. Res. Lett.*, *44*, 1740–1748.  
800 doi: 10.1002/2017GL072507
- 801 Del Pezzo, E., De La Torre, A., Bianco, F., Ibañez, J., Gabrielli, S., & De Siena,  
802 L. (2018). Numerically Calculated 3D Space-Weighting Functions to Image  
803 Crustal Volcanic Structures Using Diffuse Coda Waves. *Geosci. J.*, *8*, 175. doi:  
804 10.3390/geosciences8050175
- 805 Del Pezzo, E., Ibañez, J., Prudencio, J., Bianco, F., & De Siena, L. (2016). Ab-  
806 sorption and scattering 2-D volcano images from numerically calculated space-  
807 weighting functions. *Geophys. J. Int.*, *206*, 742–756. doi: 10.1093/gji/ggw171
- 808 Deng, K., Liu, Y., & Harrington, R. (2016). Poroelastic stress triggering of the  
809 December 2013 Crooked Lake, Alberta, induced seismicity sequence. *Geophys.*  
810 *Res. Lett.*, *43*, 8482–8491. doi: 10.1002/2016GL070421
- 811 Department of Earth and Environmental Sciences, Geophysical Observatory, Uni-  
812 versity of Munchen. (2001). *Bayernnetz*. International Federation of Digital  
813 Seismograph Networks [Dataset]. Retrieved from [https://www.fdsn.org/](https://www.fdsn.org/networks/detail/BW/)  
814 [networks/detail/BW/](https://www.fdsn.org/networks/detail/BW/) doi: 10.7914/SN/BW
- 815 Derer, C., Schumacher, M., & Schäfer, A. (2005). The northern Upper Rhine  
816 Graben: basin geometry and early syn-rift tectono-sedimentary evolution. *Int.*  
817 *J. Earth Sci.*, *94*, 640–656. doi: 10.1007/s00531-005-0515-y
- 818 Ellenberg, J. (1992). Recent fault tectonics and their relations to the seismicity of  
819 East Germany. *Tectonophysics*, *202*, 117–121. doi: 10.1016/0040-1951(92)  
820 90089-O
- 821 Erdbebendienst Südwest Baden-Württemberg and Rheinland-Pfalz. (2009). *Erd-  
822 bebendienst Südwest*. International Federation of Digital Seismograph Networks  
823 [Dataset]. Retrieved from <https://www.fdsn.org/networks/detail/LE/> doi:  
824 10.7914/SN/LE
- 825 Eulenfeld, T. (2020). Toward Source Region Tomography With Intersource Interfer-  
826 ometry: Shear Wave Velocity From 2018 West Bohemia Swarm Earthquakes.  
827 *J. Geophys. Res.*, *125*, e2020JB019931. doi: 10.1029/2020JB019931
- 828 Eulenfeld, T., Hillers, G., Vuorinen, T., & Wegler, U. (2023). Induced earthquake  
829 source parameters, attenuation, and site effects from waveform envelopes  
830 in the Fennoscandian Shield. *J. Geophys. Res.*, *128*, e2022JB025162. doi:  
831 10.1029/2022JB025162
- 832 Eulenfeld, T., & Wegler, U. (2016). Measurement of intrinsic and scattering atten-  
833 uation of shear waves in two sedimentary basins and comparison to crystalline  
834 sites in Germany. *Geophys. J. Int.*, *202*, 744–757. doi: 10.1093/gji/ggw035
- 835 Eulenfeld, T., & Wegler, U. (2017). Crustal intrinsic and scattering attenuation of  
836 high-frequency shear waves in the contiguous United States. *J. Geophys. Res.*,  
837 *122*, 4676–4690. doi: 10.1002/2017JB014038

- 838 Fähr, D., Gisler, M., Jaggi, B., Kästli, P., Lutz, T., Masciadri, V., ... Wenk, T.  
839 (2009). The 1356 Basel earthquake: an interdisciplinary revision. *Geophys. J.*  
840 *Int.*, *178*, 351–374. doi: 10.1111/j.1365-246X.2009.04130.x
- 841 Federal Institute for Geosciences and Natural Resources. (1976). *German Regional*  
842 *Seismic Network (GRSN)*. Bundesanstalt für Geowissenschaften und Rohstoffe  
843 [Dataset]. Retrieved from <https://www.seismologie.bgr.de/doi/grsn/> doi:  
844 10.25928/MBX6-HR74
- 845 Fehler, M., Hoshiaba, M., Sato, H., & Obara, K. (1992). Separation of scattering and  
846 intrinsic attenuation for the Kanto-Tokai region, Japan, using measurements of  
847 S-wave energy versus hypocentral distance. *Geophys. J. Int.*, *108*, 787–800. doi:  
848 10.1111/j.1365-246X.1992.tb03470.x
- 849 Fischer, T., Horálek, J., Hrubcová, P., Vavryčuk, V., Bräuer, K., & Kämpf, H.  
850 (2014). Intra-continental earthquake swarms in West-Bohemia and Vogtland: a  
851 review. *Tectonophysics*, *611*, 1–27. doi: 10.1016/j.tecto.2013.11.001
- 852 Gabrielli, S., Akinci, A., De Siena, L., Del Pezzo, E., Buttinelli, M., Maesano, F., &  
853 Maffucci, R. (2023). Scattering attenuation images of the control of thrusts  
854 and fluid overpressure on the 2016–2017 Central Italy seismic sequence. *Geo-*  
855 *phys. Res. Lett.*, *50*, e2023GL103132. doi: 10.1029/2023GL103132
- 856 Gabrielli, S., De Siena, L., Napolitano, F., & Del Pezzo, E. (2020). Understanding  
857 seismic path biases and magmatic activity at Mount St Helens volcano before  
858 its 2004 eruption. *Geophys. J. Int.*, *222*, 169–188. doi: 10.1093/gji/ggaa154
- 859 Gad, A. (2021). *PyGAD: An Intuitive Genetic Algorithm Python Library [Software]*.  
860 (arXiv: 2106.06158)
- 861 Gaebler, P., Bektas, H., Eulenfeld, T., Wegler, U., & Taymaz, T. (2019). Imaging  
862 of shear wave attenuation along the central part of the North Anatolian Fault  
863 Zone, Turkey. *J. Seismol.*, *23*, 913–927. doi: 10.1007/s10950-019-09842-1
- 864 Gaebler, P., Eulenfeld, T., & Wegler, U. (2015). Seismic scattering and ab-  
865 sorption parameters in the W-Bohemia/Vogtland region from elastic and  
866 acoustic radiative transfer theory. *Geophys. J. Int.*, *203*, 1471–1481. doi:  
867 10.1093/gji/ggv393
- 868 Gardner, G., Gardner, L., & A.R., G. (1974). Formation velocity and density; the  
869 diagnostic basics for stratigraphic traps. *Geophysics*, *39*, 770–780. doi: 10  
870 .1190/1.1440465
- 871 Geissler, W., Kämpf, H., Kind, R., Bräuer, K., Klinge, K., Plenefisch, T., ... Nehy-  
872 bka, V. (2005). Seismic structure and locations of a CO<sub>2</sub> source in the upper  
873 mantle of the western Eger (Ohře) Rift, central Europe. *Tectonophysics*, *24*,  
874 1–23. doi: 10.1029/2004TC001672
- 875 Giampiccolo, E., & Tuvè, T. (2018). Regionalization and dependence of coda Q on  
876 frequency and lapse time in the seismically active Peloritani region (northeast-  
877 ern Sicily, Italy). *J. Seismol.*, *22*, 1059–1074. doi: 10.1007/s10950-018-9750-0
- 878 Grünthal, G., Bankwitz, P., Bankwitz, E., Bednarek, J., Guterch, B., Schenk, V., ...  
879 Zeman, A. (1985). Seismicity and geological features of the eastern part of the  
880 West European Platform. *Gerlands Beiträge zur Geophysik*, *94*, 276–289.
- 881 Grünthal, G., Stromeyer, D., Bosse, C., Cotton, F., & Bindi, D. (2018). The prob-  
882 abilistic seismic hazard assessment of Germany—version 2016, considering the  
883 range of epistemic uncertainties and aleatory variability. *Bull. Earthq. Eng.*,  
884 *16*, 4339–4395. doi: 10.1007/s10518-018-0315-y
- 885 Gusev, A., & Abubakirov, I. (1996). Simulated envelopes of non-isotropically  
886 scattered body waves as compared to observed ones: another manifesta-  
887 tion of fractal heterogeneity. *Geophys. J. Int.*, *127*, 49–60. doi: 10.1111/  
888 j.1365-246X.1996.tb01534.x
- 889 Hanks, T., & Kanamori, H. (1979). A moment magnitude scale. *J. Geophys. Res.*,  
890 *84*, 2348–2349. doi: 10.1029/JB084iB05p02348
- 891 Hansen, P. (1992). Analysis of discrete ill-posed problems by means of the L-curve.  
892 *SIAM Rev.*, *34*, 561–580. doi: 10.1137/1034115

- 893 Harris, C., Millman, K., van der Walt, S., Gommers, R., Virtanen, P., Cournapeau,  
894 D., . . . T.E., O. (2020). Array programming with NumPy [Software]. *Nature*,  
895 *585*, 357–362. doi: 10.1038/s41586-020-2649-2
- 896 Hauksson, E., & P.M., S. (2006). Attenuation models ( $Q_P$  and  $Q_S$ ) in three dimen-  
897 sions of the southern California crust: Inferred fluid saturation at seismogenic  
898 depths. *J. Geophys. Res.*, *111*, B05302. doi: 10.1029/2005JB003947
- 899 Heller, G., Margerin, L., Sèbe, O., Mayor, J., & Calvet, M. (2022). Revisiting  
900 multiple-scattering principles in a crustal waveguide: equipartition, depolar-  
901 ization and coda normalization. *Pure Appl. Geophys.*, *179*, 2031–2065. doi:  
902 10.1007/s00024-022-03063-3
- 903 Heuer, B., Geissler, W., Kind, R., & Kämpf, H. (2006). Seismic evidence for as-  
904 thenospheric updoming beneath the western Bohemian Massif, central Europe.  
905 *Geophys. Res. Lett.*, *33*, L05311. doi: 10.1029/2005GL025158
- 906 Hirose, T., Nakahara, H., & Nishimura, T. (2019). A Passive Estimation Method  
907 of Scattering and Intrinsic Absorption Parameters From Envelopes of Seis-  
908 mic Ambient Noise Cross-Correlation Functions. *Geophys. Res. Lett.*, *46*,  
909 3634–3642. doi: 10.1029/2018GL080553
- 910 Hofmann, Y., Jahr, T., & Jentzsch, G. (2003). Three-dimensional gravimetric mod-  
911 elling to detect the deep structure of the region Vogtland/NW-Bohemia. *J.*  
912 *Geodyn.*, *35*, 209–220. doi: 10.1016/S0264-3707(02)00063-7
- 913 Holland, J. (1992). *Adaptation in natural and artificial systems*. Cambridge, Mas-  
914 sachusetts: The MIT Press.
- 915 Hoshiya, M. (1991). Simulation of multiple-scattered coda wave excitation based on  
916 the energy conservation law. *Phys. Earth planet. Inter.*, *67*, 123–136. doi: 10  
917 .1016/0031-9201(91)90066-Q
- 918 Hrubcová, P., & Geissler, W. (2009). The crust-mantle transition and the Moho  
919 beneath the Vogtland/West Bohemian region in the light of different seismic  
920 methods. *Stud. Geophys. Geod.*, *53*, 275–294. doi: 10.1007/s11200-009-0018-6
- 921 Hunter, J. (2007). Matplotlib: A 2D Graphics Environment [Software]. *Comput. Sci.*  
922 *Eng.*, *9*, 90–95. doi: 10.1109/MCSE.2007.55
- 923 Ibañez, J., Castro-Melgar, I., Cocina, I., Zuccarello, L., Branca, S., Del Pezzo, E., &  
924 Prudencio, J. (2020). First 2-D intrinsic and scattering attenuation images of  
925 Mt Etna volcano and surrounding region from active seismic data. *Geophys. J.*  
926 *Int.*, *220*, 267–277. doi: 10.1093/gji/ggz450
- 927 Institut fuer Geowissenschaften, Friedrich-Schiller-Universitaet Jena. (2009).  
928 *Thüringer Seismologisches Netz*. International Federation of Digital Seismo-  
929 graph Networks [Dataset]. Retrieved from [https://www.fdsn.org/networks/  
930 detail/TH/](https://www.fdsn.org/networks/detail/TH/) doi: 10.7914/SN/TH
- 931 Jackson, I., Gerald, J., Faul, U., & Tan, B. (2002). Grain-size-sensitive seismic wave  
932 attenuation in polycrystalline olivine. *J. Geophys. Res.*, *107*, 2360. doi: 10  
933 .1029/2001JB001225
- 934 Karato, S. (1996). Importance of anelasticity in the interpretation of seismic tomog-  
935 raphy. *Geophys. Res. Lett.*, *20*, 1623–1626. doi: 10.1029/93GL01767
- 936 Klein, F. (2002). *User’s Guide to HYPOINVERSE-2000, a Fortran Program to*  
937 *Solve for Earthquake Locations and Magnitudes* (Tech. Rep. Nos. 02–171). U.S.  
938 Geological Survey, Washington, D.C. (Open File Rep.) doi: 10.13140/2.1.4859  
939 .3602
- 940 Kohlstedt, D., Evans, B., & Mackwell, S. (1995). Strength of the lithosphere:  
941 Constraints imposed by laboratory experiments. *J. Geophys. Res.*, *100*, 17587–  
942 17602. doi: 10.1029/95JB01460
- 943 Korn, M., Funke, S., & Wendt, S. (2008). Seismicity and seismotectonics of  
944 West Saxony, Germany - new insights from recent seismicity observed with  
945 the Saxonian seismic network. *Stud. Geophys. Geod.*, *52*, 479–492. doi:  
946 10.1007/s11200-008-0033-z
- 947 Krischer, L., Megies, T., Barsch, R., Beyreuther, M., Lecocq, T., Caudron, C.,

- 948 & Wassermann, J. (2015). ObsPy: a bridge for seismology into scientific Python ecosystem [Software]. *Comput. Sci. Discov.*, 8, 014003. doi: 10.1088/1749-4699/8/1/014003
- 949
- 950
- 951 Krull, P. (1984). Kosmotektonisches Schema des Territoriums der Deutschen Demokratischen Republik. *Z. Angew. Geol.*, 30, 190–194. (in German)
- 952
- 953 Küperkoch, K., Olbert, K., & Meier, T. (2018). Long-Term Monitoring of Induced Seismicity at the Insheim Geothermal Site, Germany. *Bull. seism. Soc. Am.*, 108, 3668–3683. doi: 10.1785/0120170365
- 954
- 955
- 956 Lacombe, C., Campillo, M., Paul, A., & Margerin, L. (2003). Separation of intrinsic absorption and scattering attenuation from Lg coda decay in central France using acoustic radiative transfer theory. *Geophys. J. Int.*, 154, 417–425. doi: 10.1046/j.1365-246X.2003.01976.x
- 957
- 958
- 959
- 960 Landeserdbebendienst Rheinland-Pfalz. (2023). *Earthquake list, accessed June 26, 2023*. ([https://www.lgb-rlp.de/fachthemen/landeserdbebendienst/erdbebenereigniselokal.html?no\\_cache=1](https://www.lgb-rlp.de/fachthemen/landeserdbebendienst/erdbebenereigniselokal.html?no_cache=1))
- 961
- 962
- 963 Leydecker, G. (2011). *Erdbebenkatalog für Deutschland mit Randgebieten für die Jahre 800 bis 2008*. Stuttgart, Germany: Schweizerbart Science Publishers. (in German)
- 964
- 965
- 966 Maeda, T., Sato, H., & Nishimura, T. (2008). Synthesis of coda wave envelopes in randomly inhomogeneous elastic media in a half-space: single scattering model including Rayleigh waves. *Geophys. J. Int.*, 172, 130–154. doi: 10.1111/j.1365-246X.2007.03603.x
- 967
- 968
- 969
- 970 Mainardi, F. (2010). *Fractional Calculus and Waves in Linear Viscoelasticity*. Imperial College Press.
- 971
- 972 Margerin, L., Bajas, A., & Campillo, M. (2019). A scalar radiative transfer model including the coupling between surface and body waves. *Geophys. J. Int.*, 219, 1092–1108. doi: 10.1093/gji/ggz348
- 973
- 974
- 975 Margerin, L., Campillo, M., & van Tiggelen, B. (1998). Radiative transfer and diffusion of waves in a layered medium: new insight into coda Q. *Geophys. J. Int.*, 134, 596–612. doi: 10.1111/j.1365-246X.1998.tb07142.x
- 976
- 977
- 978 Margerin, L., Campillo, M., & van Tiggelen, B. (2000). Monte Carlo simulation of multiple scattering of elastic waves. *J. Geophys. Res.*, 105, 7873–7892. doi: 10.1029/1999JB900359
- 979
- 980
- 981 Martínez-Garzón, P., Kwiatak, G., Sone, H., Bohnhoff, M., Dresen, G., & Hartline, C. (2014). Spatiotemporal changes, faulting regimes, and source parameters of induced seismicity: A case study from The Geysers geothermal field. *J. Geophys. Res.*, 119, 8378–8396. doi: 10.1002/2014JB011385
- 982
- 983
- 984
- 985 Mayor, J., Calvet, M., Margerin, L., Vanderhaeghe, O., & Traversa, P. (2016). Crustal structure of the Alps as seen by attenuation tomography. *Earth & Planet. Sci. Lett.*, 439, 71–80. doi: 10.1016/j.epsl.2016.01.025
- 986
- 987
- 988 Menke, W. (2012). *Geophysical Data Analysis: Discrete Inverse Theory (Third Edition)*. Boston: Academic Press.
- 989
- 990 Mousavi, S., Bauer, K., Korn, M., & Hejrani, B. (2021). Seismic tomography reveals a mid-crustal intrusive body, fluid pathways and their relation to the earthquake swarms in West Bohemia/Vogtland. *Geophys. J. Int.*, 225, 589–607. doi: 10.1093/gji/ggaa606
- 991
- 992
- 993
- 994 Mousavi, S., Haberland, C., Bauer, K., Hejrani, B., & Korn, M. (2017). Attenuation tomography in West Bohemia/Vogtland. *Tectonophysics*, 695, 64–75. doi: 10.1016/j.tecto.2016.12.010
- 995
- 996
- 997 Neunhöfer, H., Studinger, M., & Tittel, B. (1996). Erdbeben entlang der Finne- und Gera-Jachimov-Störung in Thüringen und Sachsen, Fallbeispiel: Das Beben am 28.09.1993 bei Gera. *Z. angew. Geol.*, 42, 57–61. (in German)
- 998
- 999
- 1000 Ogiso, M. (2019). A method for mapping intrinsic attenuation factors and scattering coefficients of S waves in 3-D space and its application in southwestern Japan. *Geophys. J. Int.*, 216, 948–957. doi: 10.1093/gji/ggy468
- 1001
- 1002

- 1003 Paaschens, J. (1997). Solution of the time-dependent Boltzmann equation. *Phys.*  
 1004 *Ref. E.*, *56*, 1135–1141. doi: 10.1103/PhysRevE.56.1135
- 1005 Pietzsch, K. (1963). *Geologie von Sachsen*. Berlin: Dt. Verl. Wiss. (in German)
- 1006 Press, W., Flannery, B., Teukolsky, S., & Vetterling, W. (1996). *Numerical Recipes*  
 1007 *in Fortran 77: The Art of Scientific Computing*. Cambridge: Cambridge Uni-  
 1008 versity Press.
- 1009 Pribnow, D., & Schellschmidt, R. (2000). Thermal tracking of upper crustal fluid  
 1010 flow in the Rhine graben. *Geophys. Res. Lett.*, *27*, 1957–1960. doi: 10.1029/  
 1011 2000GL008494
- 1012 Przybilla, J., & Korn, M. (2008). Monte Carlo simulation of radiative en-  
 1013 ergy transfer in continuous elastic random media-three-component en-  
 1014 velopes and numerical validation. *Geophys. J. Int.*, *173*, 566–576. doi:  
 1015 10.1111/j.1365-246X.2008.03747.x
- 1016 Przybilla, J., Korn, M., & Wegler, U. (2006). Radiative transfer of elastic waves ver-  
 1017 sus finite difference simulations in two-dimensional random media. *J. Geophys.*  
 1018 *Res.*, *111*, B04305. doi: 10.1029/2005JB003952
- 1019 Przybilla, J., Wegler, U., & Korn, M. (2009). Estimation of crustal scattering  
 1020 parameters with elastic radiative transfer theory. *Geophys. J. Int.*, *178*, 1105–  
 1021 1111. doi: 10.1111/j.1365-246X.2009.04204.x
- 1022 Raghukanth, S., & Somala, S. (2009). Modeling of Strong-Motion Data in North-  
 1023 eastern India: Q, Stress Drop, and Site Amplification. *Bull. seism. Soc. Am.*,  
 1024 *99*, 705–725. doi: 10.1785/0120080025
- 1025 Rayleigh, L. (1899). XXXIV. On the transmission of light through an atmosphere  
 1026 containing small particles in suspension, and on the origin of the blue of the  
 1027 sky. *Philos. Mag.*, *47*, 375–384. doi: 10.1080/14786449908621276
- 1028 Rietbrock, A. (2001). P wave attenuation structure in the fault area of the  
 1029 1995 Kobe earthquake. *J. Geophys. Res.*, *106*, 4141–4154. doi: 10.1029/  
 1030 2000JB900234
- 1031 Ryzhik, L., Papanicolaou, G., & Keller, J. (1996). Transport equations for elastic  
 1032 and other waves in random media. *Wave Motion*, *24*, 237–370. doi: 10.1016/  
 1033 S0165-2125(96)00021-2
- 1034 Sato, H. (2019). Isotropic scattering coefficient of the solid earth. *Geophys. J. Int.*,  
 1035 *218*, 2079–2088. doi: 10.1093/gji/ggz266
- 1036 Sato, H., Fehler, M., & Maeda, T. (2012). *Seismic wave propagation and scattering*  
 1037 *in the heterogeneous Earth*. Berlin: Springer.
- 1038 Schumacher, M. (2002). Upper Rhine Graben: Role of preexisting structures during  
 1039 rift evolution. *Tectonics*, *21*, 6-1-6-17. doi: 10.1029/2001TC900022
- 1040 Sens-Schönfelder, C., Margerin, L., & Campillo, M. (2009). Laterally heteroge-  
 1041 neous scattering explains Lg blockage in the Pyrenees. *J. Geophys. Res.*, *114*,  
 1042 B07309. doi: 10.1029/2008JB006107
- 1043 Sens-Schönfelder, C., & Wegler, U. (2006). Radiative transfer theory for estimation  
 1044 of seismic moment. *Geophys. J. Int.*, *167*, 1363–1372. doi: 10.1111/j.1365-246X  
 1045 .2006.03139.x
- 1046 Shearer, P., & Earle, P. (2004). The global short-period wavefield modelled with a  
 1047 Monte Carlo seismic phonon method. *Geophys. J. Int.*, *158*, 1103–1117. doi:  
 1048 10.1111/j.1365-246X.2004.02378.x
- 1049 Shito, A., Matsumoto, S., Ohkura, T., Shimizu, H., Sakai, S., Iio, Y., . . . Asano,  
 1050 Y. (2020). 3-D Intrinsic and Scattering Seismic Attenuation Structures  
 1051 Beneath Kyushu, Japan. *J. Geophys. Res.*, *125*, e2019JB018742. doi:  
 1052 10.1029/2019JB018742
- 1053 Sketsiou, P., De Siena, L., Gabrielli, S., & Napolitano, F. (2021). 3-D attenua-  
 1054 tion image of fluid storage and tectonic interactions across the Pollino fault  
 1055 network. *Geophys. J. Int.*, *226*, 536–547. doi: 10.1093/gji/ggab109
- 1056 Sonnabend, L. (2022). *Neotektonik und Seismizität in Westsachsen und Nord-*  
 1057 *westböhmen* (PhD dissertation). Leipzig, Germany. (in German)

- 1058 Špičák, A., & Horálek, J. (2001). Possible role of fluids in the process of earth-  
 1059 quake swarm generation in the West Bohemia/Vogtland seismoactive region.  
 1060 *Tectonophysics*, *336*, 151–161. doi: 10.1016/S0040-1951(01)00099-3
- 1061 Stammler, K. (1993). SeismicHandler: programmable multichannel data handler  
 1062 for interactive and automatic processing of seismological analyses. *Comput.*  
 1063 *Geosci.*, *19*, 135–140. doi: 10.1016/0098-3004(93)90110-Q
- 1064 Thüringer Seismologisches Netz. (2022). *Institut für Geowissenschaften,*  
 1065 *Friedrich-Schiller-Universität Jena - Earthquake list, accessed July 10,*  
 1066 *2021.* ([http://www.erdbebenwahrnehmung-thueringen.uni-jena.de/](http://www.erdbebenwahrnehmung-thueringen.uni-jena.de/aktuelleEreignisse/Bulletin.archiv.txt)  
 1067 [aktuelleEreignisse/Bulletin.archiv.txt](http://www.erdbebenwahrnehmung-thueringen.uni-jena.de/aktuelleEreignisse/Bulletin.archiv.txt))
- 1068 Tikhonov, A., & Arsenin, V. (1977). *Solution of Ill-Posed Problems.* New York: Wi-  
 1069 ley.
- 1070 University of Leipzig. (2001). *SXNET Saxon Seismic Network.* International Feder-  
 1071 ation of Digital Seismograph Networks [Dataset]. Retrieved from [https://www](https://www.fdsn.org/networks/detail/SX/)  
 1072 [.fdsn.org/networks/detail/SX/](https://www.fdsn.org/networks/detail/SX/) doi: 10.7914/SN/SX
- 1073 van Dinther, C., Margerin, L., & Campillo, M. (2015). Laterally varying scatter-  
 1074 ing properties in the North Anatolian Fault Zone from ambient noise cross-  
 1075 correlations. *Geophys. J. Int.*, *203*, 1113–1127. doi: 10.1093/gji/ggv338
- 1076 van Laaten, M., Eulenfeld, T., & Wegler, U. (2022). Comparison of Multiple Lapse  
 1077 Time Window Analysis and Qopen to determine intrinsic and scattering atten-  
 1078 uation. *Geophys. J. Int.*, *228*, 913–926. doi: 10.1093/gji/ggab390
- 1079 van Laaten, M., & Wegler, U. (2023). *Non-linear inversion for a multi-layer seis-*  
 1080 *mic S-wave attenuation model using radiative transfer theory.* [Dataset]. Zen-  
 1081 odo. doi: <https://doi.org/10.5281/zenodo.8282669>
- 1082 van Laaten, M., Wegler, U., & Eulenfeld, T. (2023). On the trail of flu-  
 1083 ids in the northernmost intracontinental earthquake swarm areas of the  
 1084 Leipzig-Regensburg fault zone, Germany. *J. Seismol.*, *27*, 573–597. doi:  
 1085 10.1007/s10950-023-10146-8
- 1086 Virtanen, P., Gommers, R., Oliphant, T., Haberland, M., Reddy, T., Cournapeau,  
 1087 D., ... SciPy 1.0 Contributors (2020). SciPy 1.0: Fundamental Algorithms for  
 1088 Scientific Computing in Python [Software]. *Nature Methods*, *17*, 261–272. doi:  
 1089 10.1038/s41592-019-0686-2
- 1090 Vlček, J., Beránek, R., Fischer, T., & Vilhelm, J. (2022). Earthquake swarms in  
 1091 West Bohemia are most likely not rain triggered. *J. Geodyn.*, *150*, 101908. doi:  
 1092 10.1016/j.jog.2022.101908
- 1093 von Seebach, K. (1873). *Das Mitteldeutsche Erdbeben vom 6. März 1872.* Leipzig,  
 1094 Germany: Verlag von H. Haessel. (in German)
- 1095 Wang, W., & Shearer, P. (2017). Using direct and coda wave envelopes to resolve  
 1096 the scattering and intrinsic attenuation structure of Southern California. *J.*  
 1097 *Geophys. Res.*, *122*, 7236–7251. doi: 10.1002/2016JB013810
- 1098 Wegler, U., Korn, M., & Przybilla, J. (2006). Modeling Full Seismogram Envelopes  
 1099 Using Radiative Transfer Theory with Born Scattering Coefficients. *Pure Appl.*  
 1100 *Geophys.*, *163*, 503–531. doi: 10.1007/s00024-005-0027-5
- 1101 Weise, S., Bräuer, K., Kämpf, H., Strauch, G., & Koch, U. (2001). Transport of  
 1102 mantle volatiles through the crust traced by seismically released fluids: a natu-  
 1103 ral experiment in the earthquake swarm area Vogtland/NW Bohemia, Central  
 1104 Europe. *Tectonophysics*, *336*, 137–150. doi: 10.1016/S0040-1951(01)00098-1
- 1105 Wessel, P., Smith, W., Scharroo, R., Luis, J., & Wobbe, F. (2013). Generic Map-  
 1106 ping Tools: Improved Version Released [Software]. *Eos, Transactions American*  
 1107 *Geophysical Union*, *94*, 409–410. doi: 10.1002/2013EO450001
- 1108 Wilde-Piórko, M., Geissler, W., Plomerová, J., Knapmeyer-Endrun, B., Grad, M.,  
 1109 Babuška, V., ... Wiejacz, P. (2006). *PASSEQ 2006-2008: Passive Seismic*  
 1110 *Experiment in Trans-European Suture Zone.* GFZ Data Services [Dataset].  
 1111 Retrieved from <http://geofon.gfz-potsdam.de/doi/network/7E/2006> doi:  
 1112 10.14470/2R383989

- 1113 Wu, R. (1985). Multiple scattering and energy transfer of seismic waves — separa-  
1114 tion of scattering effect from intrinsic attenuation — I. Theoretical modelling.  
1115 *Geophys. J. Int.*, *82*, 57–80. doi: 10.1111/j.1365-246X.1985.tb05128.x
- 1116 Wu, R., & Aki, K. (1988). Introduction: Seismic wave scattering in three-  
1117 dimensionally heterogeneous earth. *PAGEOPH*, *128*, 1–6. doi: 10.1007/  
1118 BF01772587
- 1119 Yoshimoto, K. (2000). Monte Carlo simulation of seismogram envelopes in scattering  
1120 media. *J. Geophys. Res.*, *105*, 6153–6161. doi: 10.1029/1999JB900437
- 1121 Zeng, Y., Su, F., & Aki, K. (1991). Scattering wave energy propagation in a random  
1122 isotropic scattering medium: 1. Theory. *J. Geophys. Res.*, *96*, 607–619. doi: 10  
1123 .1029/90JB02012
- 1124 Zhang, T., Sens-Schönfelder, C., Epple, N., & Niederleithinger, E. (2022). Imaging  
1125 of Small-Scale Heterogeneity and Absorption Using Adjoint Envelope To-  
1126 mography: Results From Laboratory Experiments. *J. Geophys. Res.*, *127*,  
1127 e2022JB024972. doi: 10.1029/2022JB024972
- 1128 Zhang, T., Sens-Schönfelder, C., & Margerin, L. (2021). Sensitivity kernels for  
1129 static and dynamic tomography of scattering and absorbing media with elas-  
1130 tic waves: a probabilistic approach. *Geophys. J. Int.*, *225*, 1824–1853. doi:  
1131 10.1093/gji/ggab048
- 1132 Ziegler, P. (1992). European Cenozoic rift system. *Tectonophysics*, *208*, 91–111. doi:  
1133 10.1016/0040-1951(92)90338-7

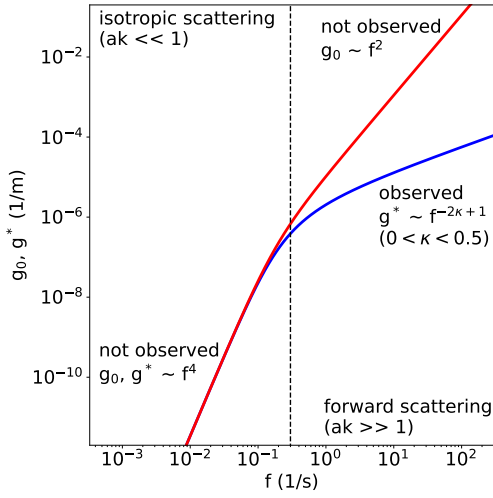


**Figure 1.** Frequency dependency of the total scattering coefficient  $g_0$  and transport scattering coefficient  $g^*$  for a von Kármán type random medium with  $0 < \kappa < 0.5$ . The frequency dependence shown by the blue line corresponds to the observed frequency dependence of scattering coefficients for crustal material. The theoretical frequency dependence shown by the red lines has not been observed for crustal material.

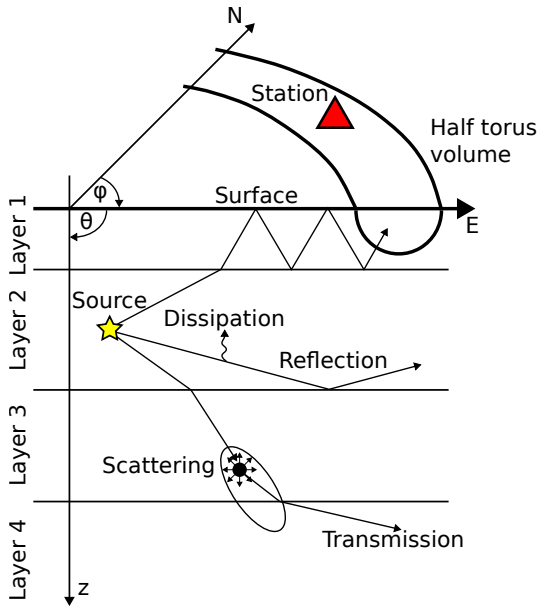


**Figure 2.** Schematic illustration of the Monte Carlo simulation. Particles are emitted from a point source. The simulation takes into account scattering and attenuation by dissipation, as well as reflection and transmission at layer boundaries. Different layers have different physical properties. A half torus volume below the surface serves as the receiver volume of the station.

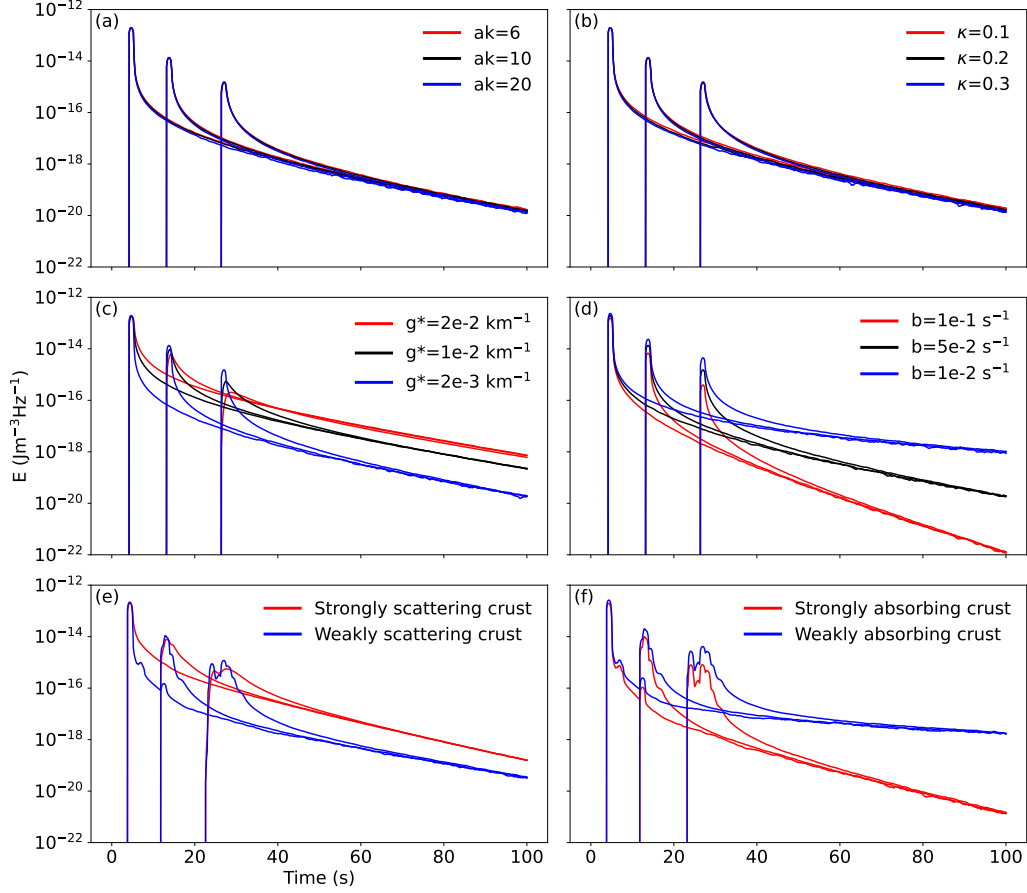


**Figure 3.** Envelopes for three stations at 10, 40, and 80 km distance in a homogeneous (a - d) and three-layer (e, f) random medium and different attenuation values. For the same  $g^*$ , different values of  $a, k, \varepsilon, \kappa$  in the top row do not affect the shape of the envelope ( $ak \gg 1$ ). Individual parameters cannot be determined because there is a trade-off between them. The middle row shows the effects of scattering and absorption. Scattering determines the absolute energy level of the coda and affects the shape of the first arrival, while absorption determines the decay of the coda. The bottom row shows the influence of a three-layer medium, once for a weakly and strongly scattering crust ( $g^*=[2e-3, 1e-3, 2e-4] \text{ km}^{-1}$  and  $g^*=[2e-2, 1e-2, 2e-3] \text{ km}^{-1}$ ) and once for a weakly and strongly absorbing crust ( $b=[1e-2, 5e-3, 1e-3] \text{ s}^{-1}$  and  $b=[1e-1, 5e-2, 1e-2] \text{ s}^{-1}$ ). The bumps in the early coda are caused by reflection and transmission at layer boundaries due to velocity and density changes.

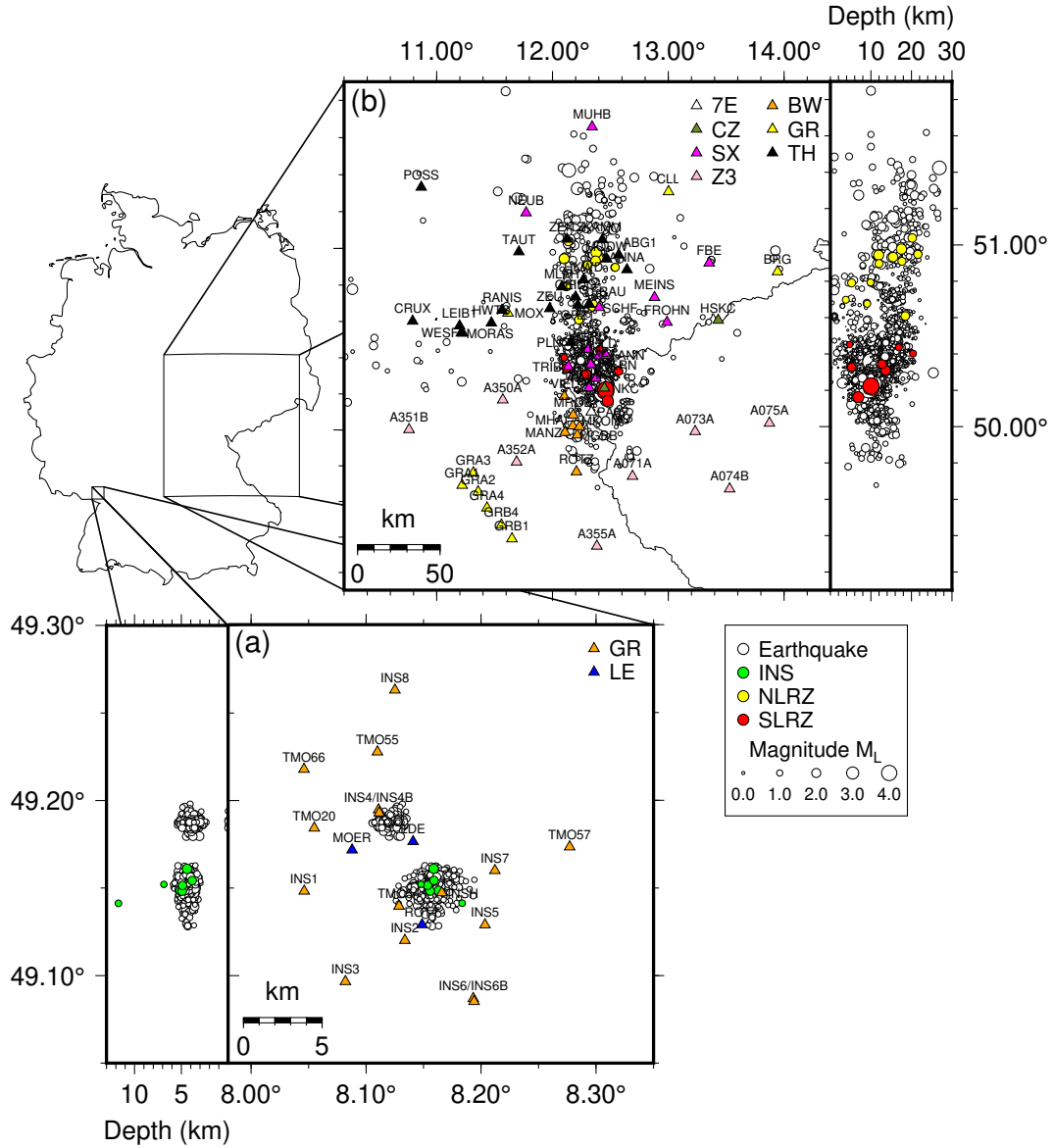


**Figure 4.** Map of Germany and locations of the two study areas Insheim (a) and Leipzig-Regensburg fault zone (b). Depending on the network (network codes 7E, BW, . . . , Z3), the stations used for the 1-D attenuation inversion are shown in color and earthquakes in relation to their magnitude. Earthquakes used for the inversion are highlighted and color-coded.

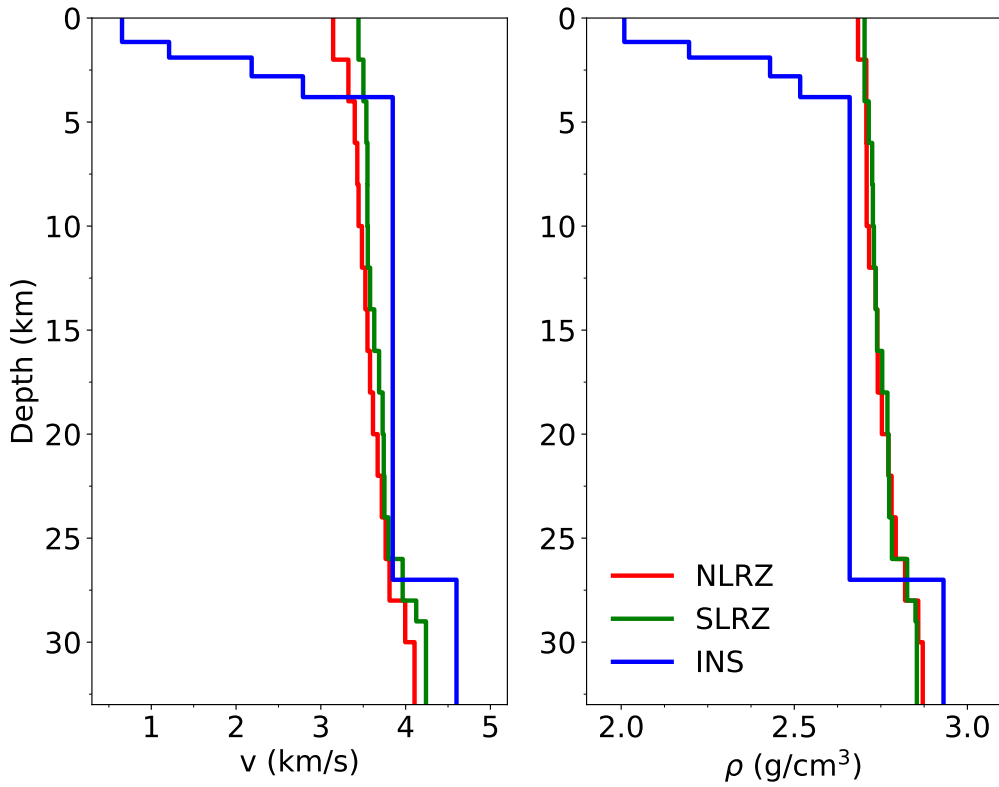


**Figure 5.** 1-D S-wave velocity models (left) and density models (right) used in the Monte Carlo simulations for each region.

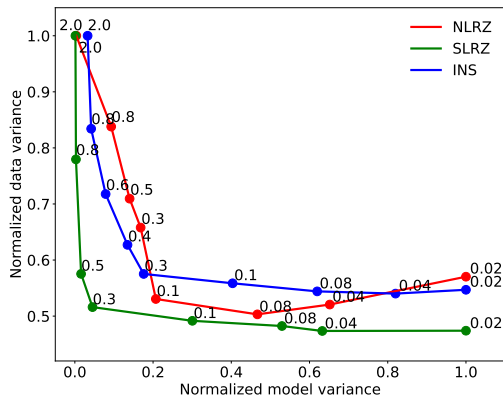


**Figure 6.** L-curve test to determine the Tikhonov regularization parameter  $\lambda$  for the three regions at 12 Hz. The lambda values corresponding to each point are displayed adjacent to them. The axes were normalized based on the respective maximum value. A value of 0.3 was chosen for all regions.

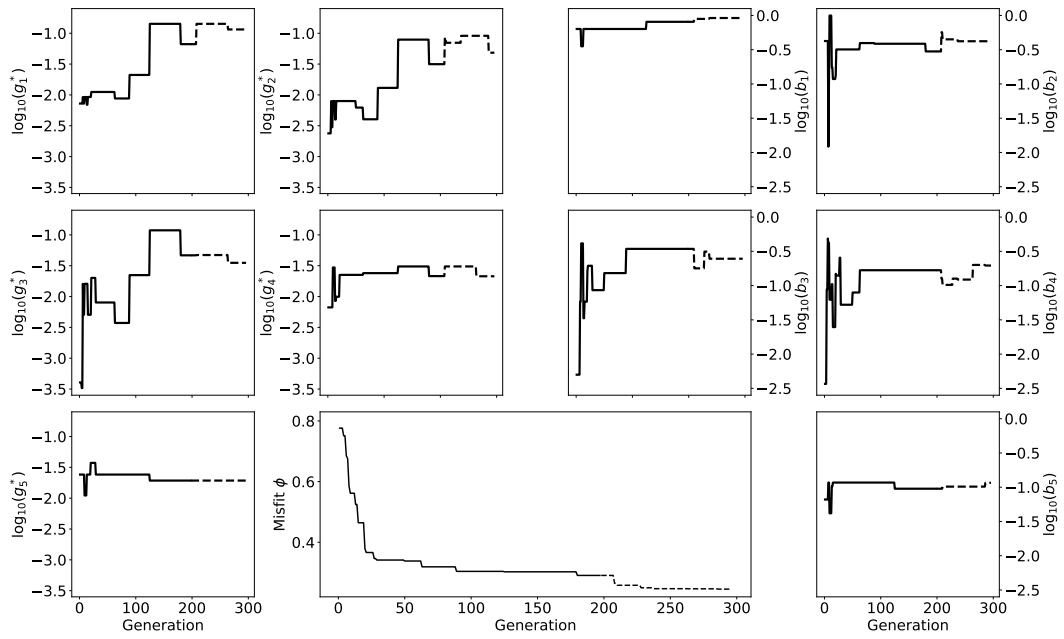


**Figure 7.** Scattering and absorption parameters of the best-fit model for the five individual layers as a function of generation and the misfit reduction during the inversion of INS at 17 Hz. Dashed lines indicate the 2nd step of the inversion with smaller search radii.

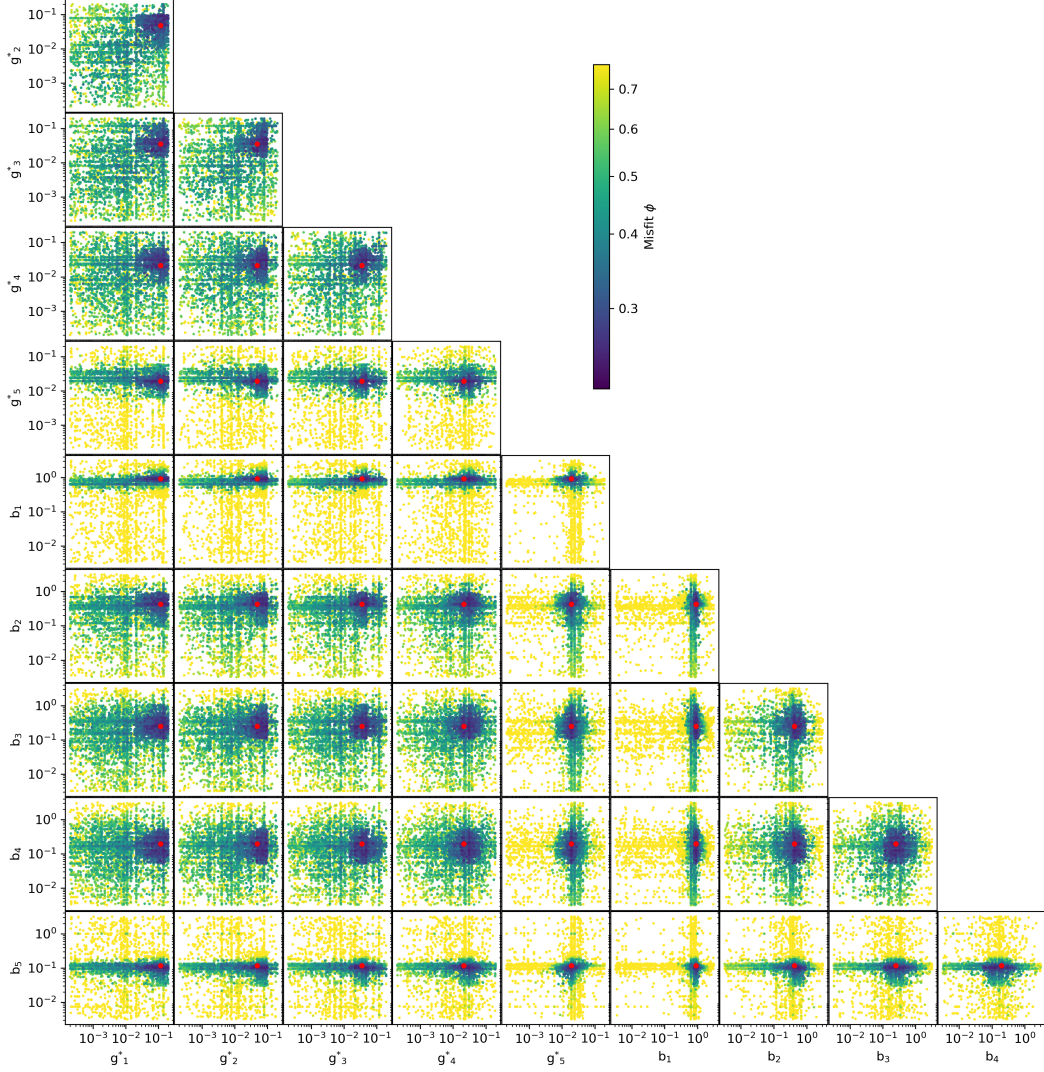


**Figure 8.** Model space sampling of all inversion parameter combinations for INS at 17 Hz. The best-fitting model is marked with a red dot. The maximum of the logarithmic color scale corresponds to the misfit of the homogeneous model from Qopen and the minimum corresponds to the misfit of the best-fit model. In addition to the global minimum, local minima can also be recognized as intersections, especially between the individual transport scattering and absorption coefficients. These local minima have slightly higher misfit values than the best-fit model.

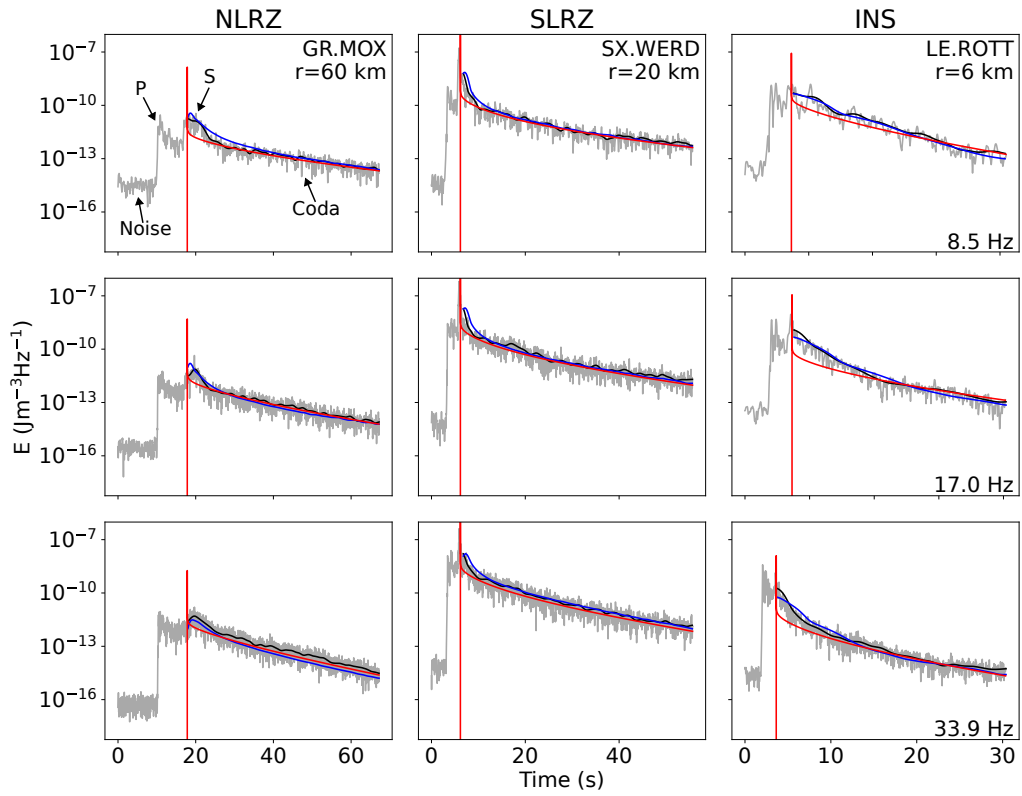


**Figure 9.** Exemplary fit of one station from each region between observed data (gray), smoothed observed data (black), synthetic data of the inversion with QEST (blue) and with Qopen (red). The different regions are shown in the three columns for three different frequencies (rows).

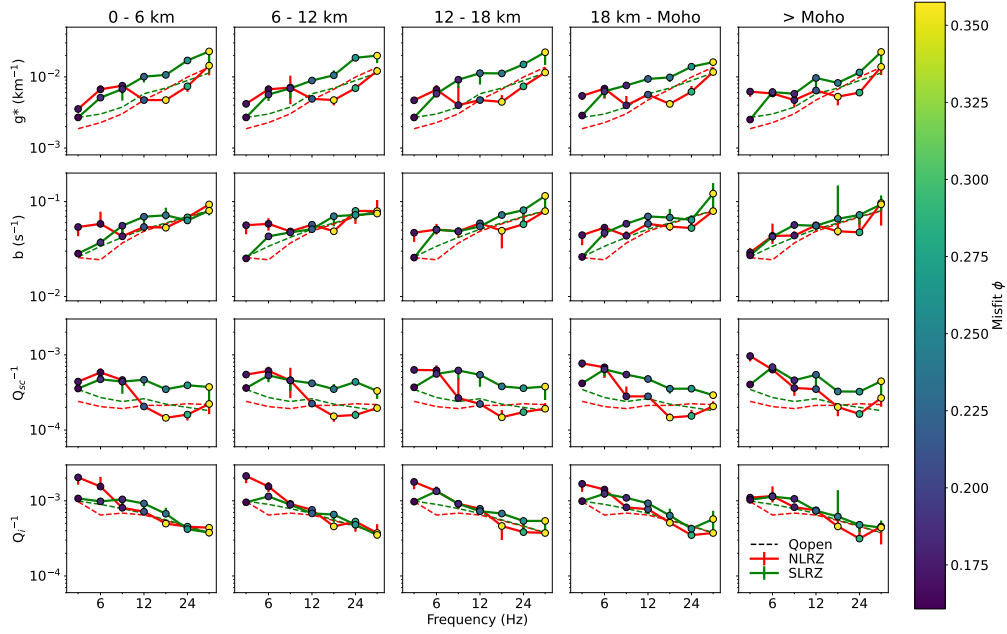


**Figure 10.** Frequency dependence of the attenuation parameters (rows) in each layer (column) of NLRZ (red line) and SLRZ (green line). The color of the points is displayed depending on the misfit. The error bars represents the range of models if a 5% error of the best-fit misfit is assumed. The corresponding homogeneous  $Q_{open}$  values (dashed line) are identical in each layer.

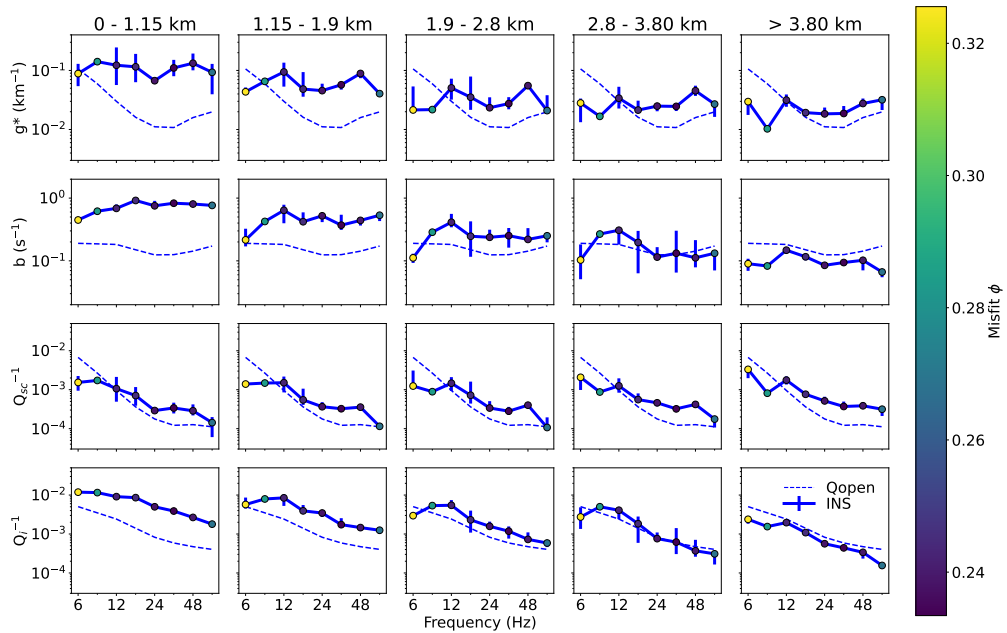


**Figure 11.** Frequency dependence of the attenuation parameters (rows) in each layer (column) of INS (blue line). The color of the points is displayed depending on the misfit. The error bars represents the range of models if a 5% error of the best-fit misfit is assumed. The corresponding homogeneous  $Q_{open}$  values (dashed line) are identical in each layer.

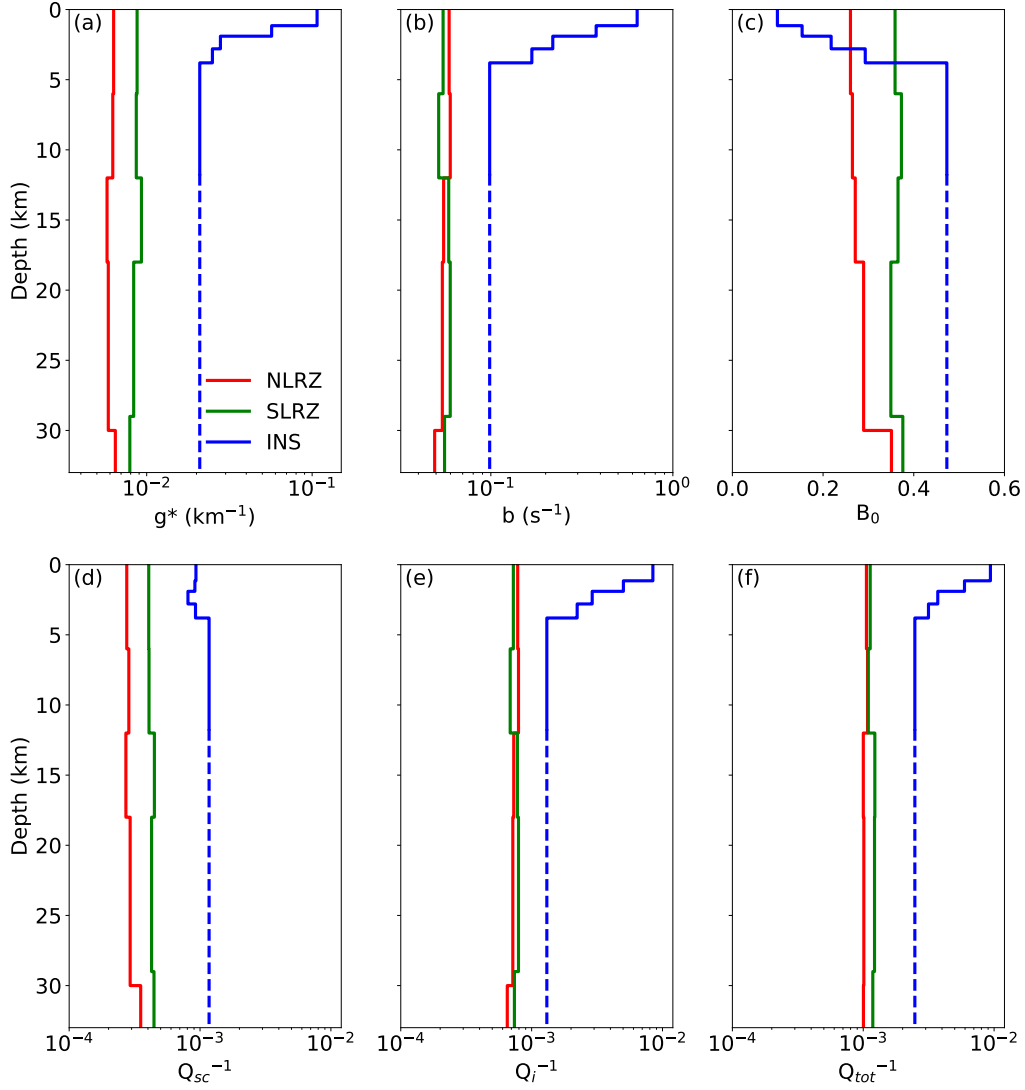


**Figure 12.** Depth-dependent 1-D attenuation models of the three regions at 12 Hz. Since we do not invert deep structures in INS, the values below the deepest earthquake are displayed as a dashed line. The models are based on the power-law fitted to the frequency dependence shown in Fig. 10 and Fig. 11.

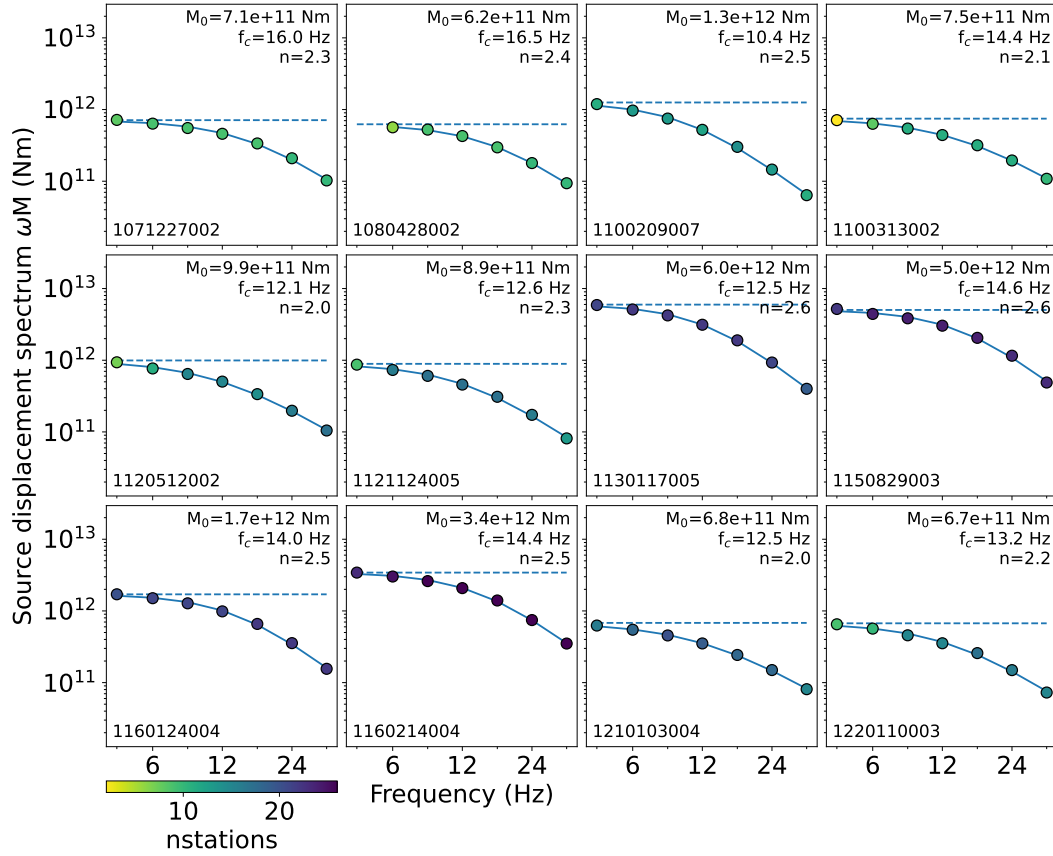


**Figure 13.** Observed source displacement spectra, displayed as circles depending on the number of observations ( $n_{stations}$ ) and the fitted source model (blue lines) for the NLRZ events. The seismic moment  $M_0$ , the corner frequency  $f_c$  and the high-frequency fall-off  $n$  were also determined.

# Supporting Information for ”Non-linear inversion for a multi-layer seismic S-wave attenuation model using radiative transfer theory”

Marcel van Laaten<sup>1</sup>, Ulrich Wegler<sup>1</sup>

<sup>1</sup>Institute of Geosciences, Friedrich Schiller University Jena, Burgweg 11, 07749 Jena, Germany

## Contents of this file

1. Table S1
2. Figures S1 to S29

---

**Table S1.** The following list summarises the variables used in the study.

| Symbol                                | Unit         | Description   |
|---------------------------------------|--------------|---|
| $a$                                   | $km$         | Correlation length  |
| $b$                                   | $1/s$        | Absorption coefficient  |
| $B_0$                                 | -            | Seismic albedo  |
| $c$                                   | $J/(m^3 Hz)$ | Displacement factor   |
| $E_{syn}, E_{obs}$                    | $J/(m^3 Hz)$ | Synthetic/Observed energy density   |
| $f_c, f$                              | $Hz$         | (Corner) Frequency  |
| $g$                                   | -            | Normalized angular dependent scattering coefficient                             |
| $g_0, g^*$                            | $1/km$       | Total/transport scattering coefficient  |
| $G$                                   | $J/(m^3 Hz)$ | Energy density Green's function   |
| $G_{MC}$                              | $J/(m^3 Hz)$ | Monte-Carlo envelope  |
| $j$                                   | -            | Angle of incidence  |
| $k$                                   | $1/km$       | Wave number   |
| $l_i$                                 | $1/km$       | Absorption length   |
| $l_0, l^*$                            | $1/km$       | Total/transport mean free path  |
| $L$                                   | -            | Model variance  |
| $M_0$                                 | $Nm$         | Seismic moment  |
| $M_L, M_w$                            | -            | Local/moment magnitude  |
| $n$                                   | -            | High-frequency fall-off   |
| $N, N_e, N_l, N_s, N_{samp}, N_{obs}$ | -            | Number of particles/events/layers/<br>stations/samples/station-earthquake pairs |
| $P$                                   | $km^3$       | Power spectral density function   |
| $Q, Q_0$                              | -            | Quality factor (at 1 Hz)  |
| $Q_i, Q_{sc}, Q_{tot}$                | -            | Intrinsic/scattering/total attenuation  |
| $R$                                   | -            | S-wave energy site amplification  |
| $R_c$                                 | -            | Energy reflection coefficient   |
| $S$                                   | $J/(m^3 Hz)$ | Data variance   |
| $t$                                   | $s$          | Time  |
| $t^*$                                 | $s$          | Transport mean free time  |
| $U_1, U_2$                            | -            | Random number for takeoff incidence/azimuthal angle                             |
| $U_3$                                 | -            | Random number for transmission/reflection                                       |
| $U_4$                                 | -            | Random number for scattering  |
| $U_5$                                 | -            | Random number for the rejection method  |
| $v$                                   | $km/s$       | S-wave velocity   |
| $W$                                   | $Nm$         | Spectral S-wave source energy   |
| $z$                                   | $km$         | Depth   |
| $\Gamma$                              | -            | Gamma function  |
| $\Delta t$                            | $s$          | Time step   |
| $\Delta V$                            | $km^3$       | Receiver volume   |
| $\Delta x$                            | $km$         | Travel distance   |
| $\varepsilon$                         | -            | Standard deviation  |
| $\eta$                                | $Pa s$       | Viscosity   |
| $\theta, \theta_{sc}$                 | -            | takeoff/scattering incidence angle  |
| $\kappa$                              | -            | Hurst exponent  |
| $\lambda$                             | -            | Inversion damping factor  |
| $\lambda_w$                           | -            | Wavelength  |
| $\mu$                                 | $Pa$         | Shear modulus   |
| $\rho$                                | $g/cm^3$     | Density   |
| $\tau$                                | -            | Power-law exponent  |
| $\varphi, \varphi_{sc}$               | -            | takeoff/scattering azimuthal angle  |
| $\phi$                                | $J/(m^3 Hz)$ | Misfit function   |
| $\omega$                              | -            | Angular frequency   |

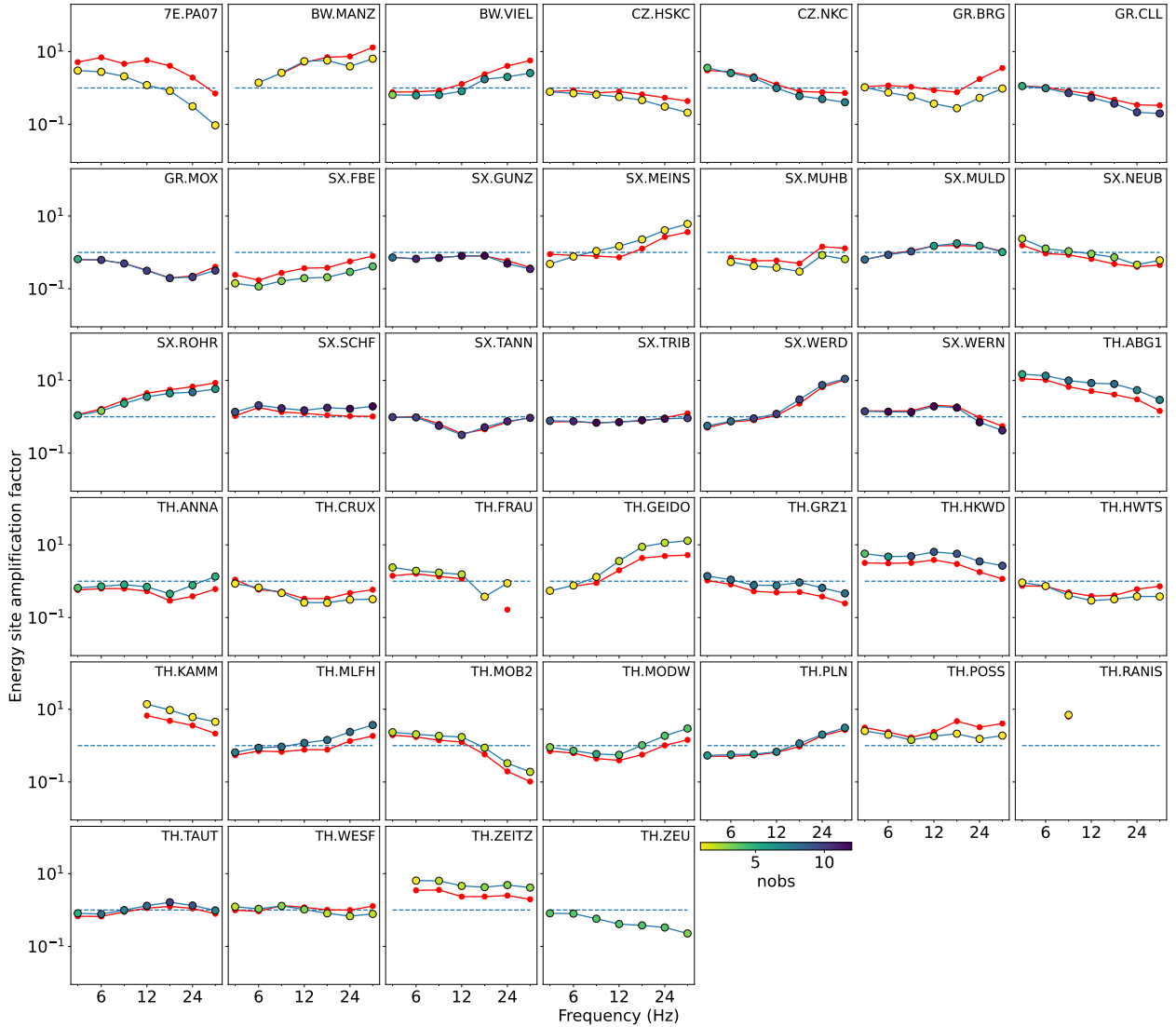


**Figure S1.** Inverted frequency-dependent site amplification of each seismic stations used for NLRZ. The coloured circles represent the number of events used in the corresponding frequency. Reference site amplification values of 1 is indicated by horizontal gray lines. For comparison, the Open results are shown as red dots.

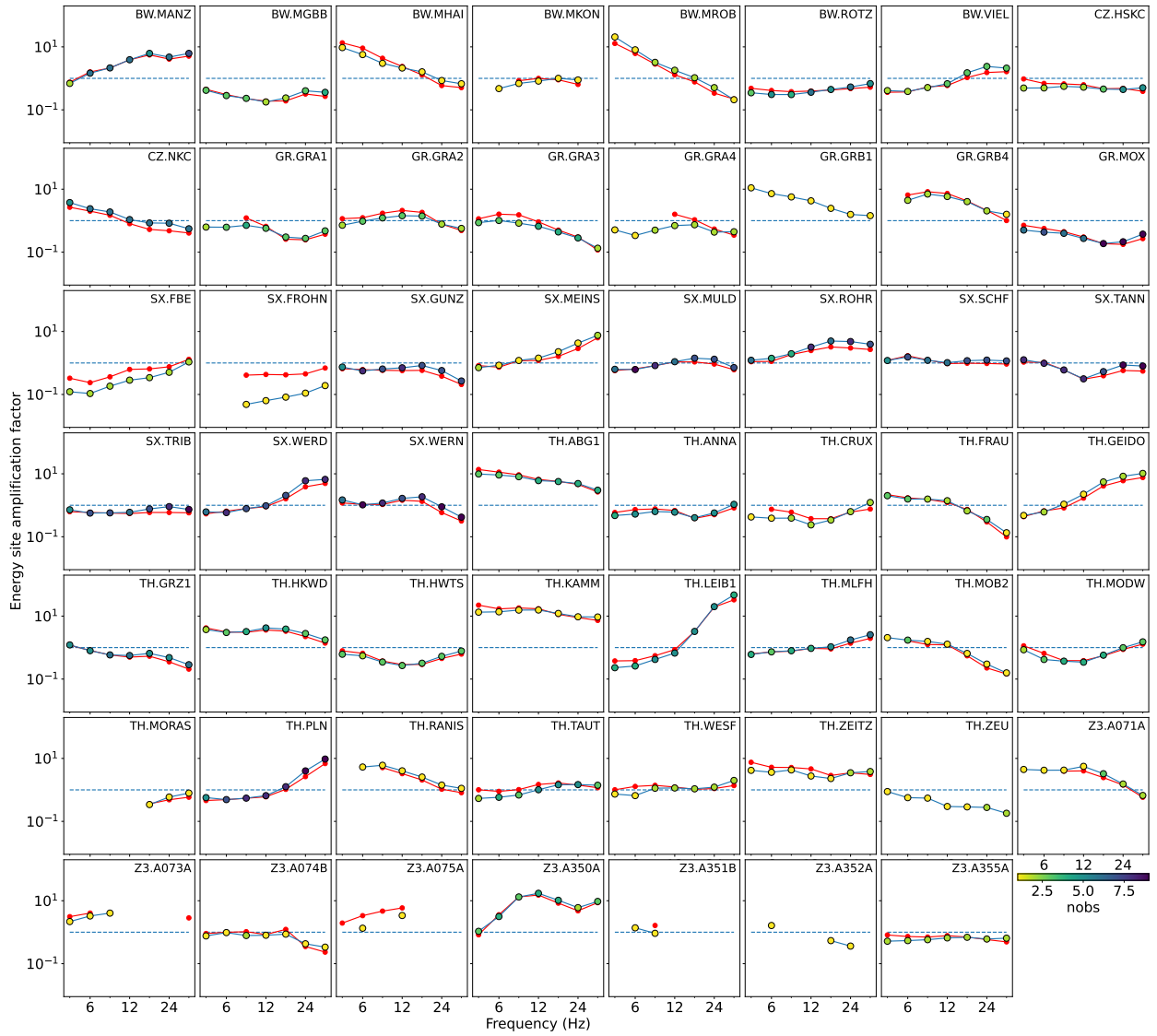
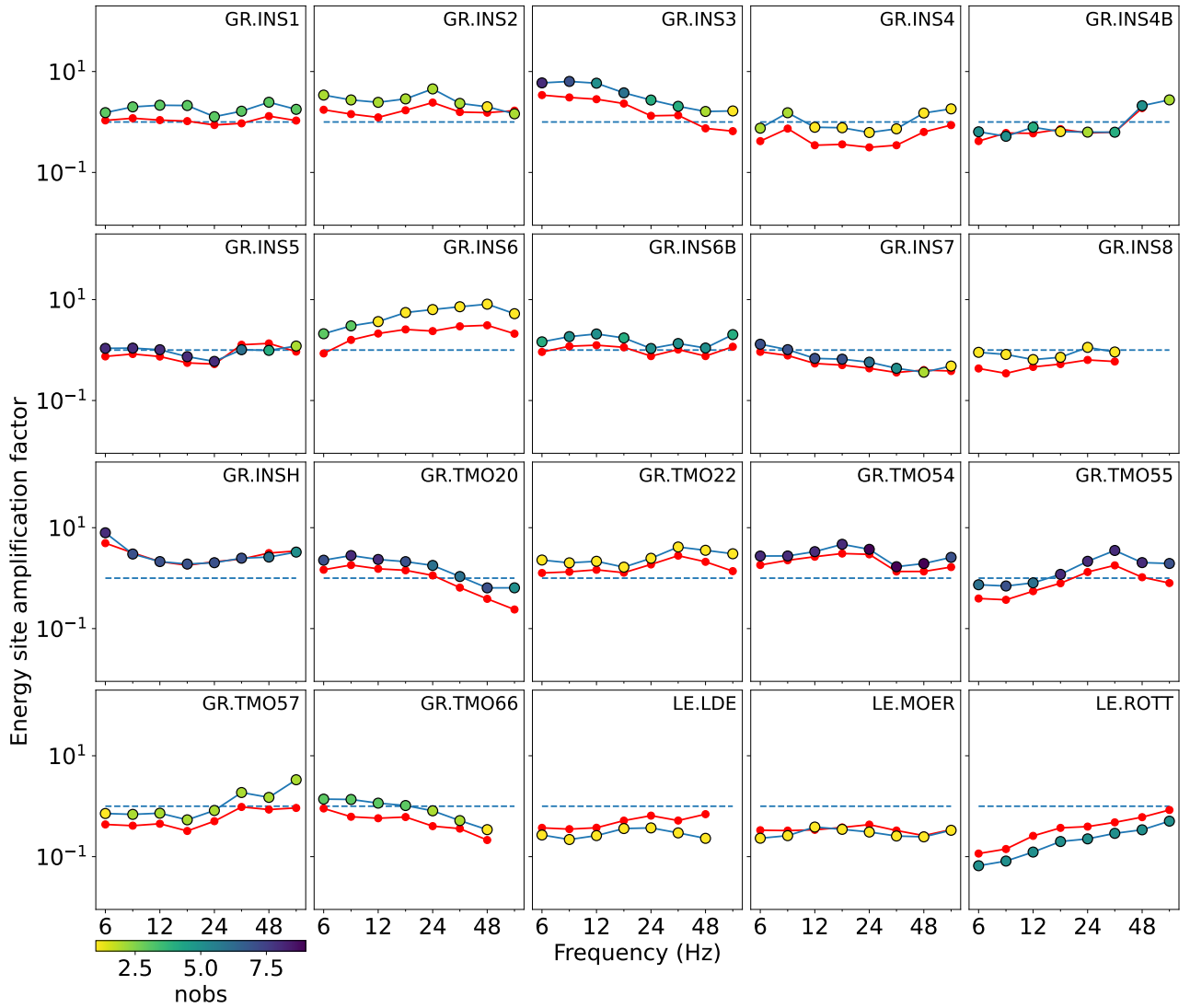
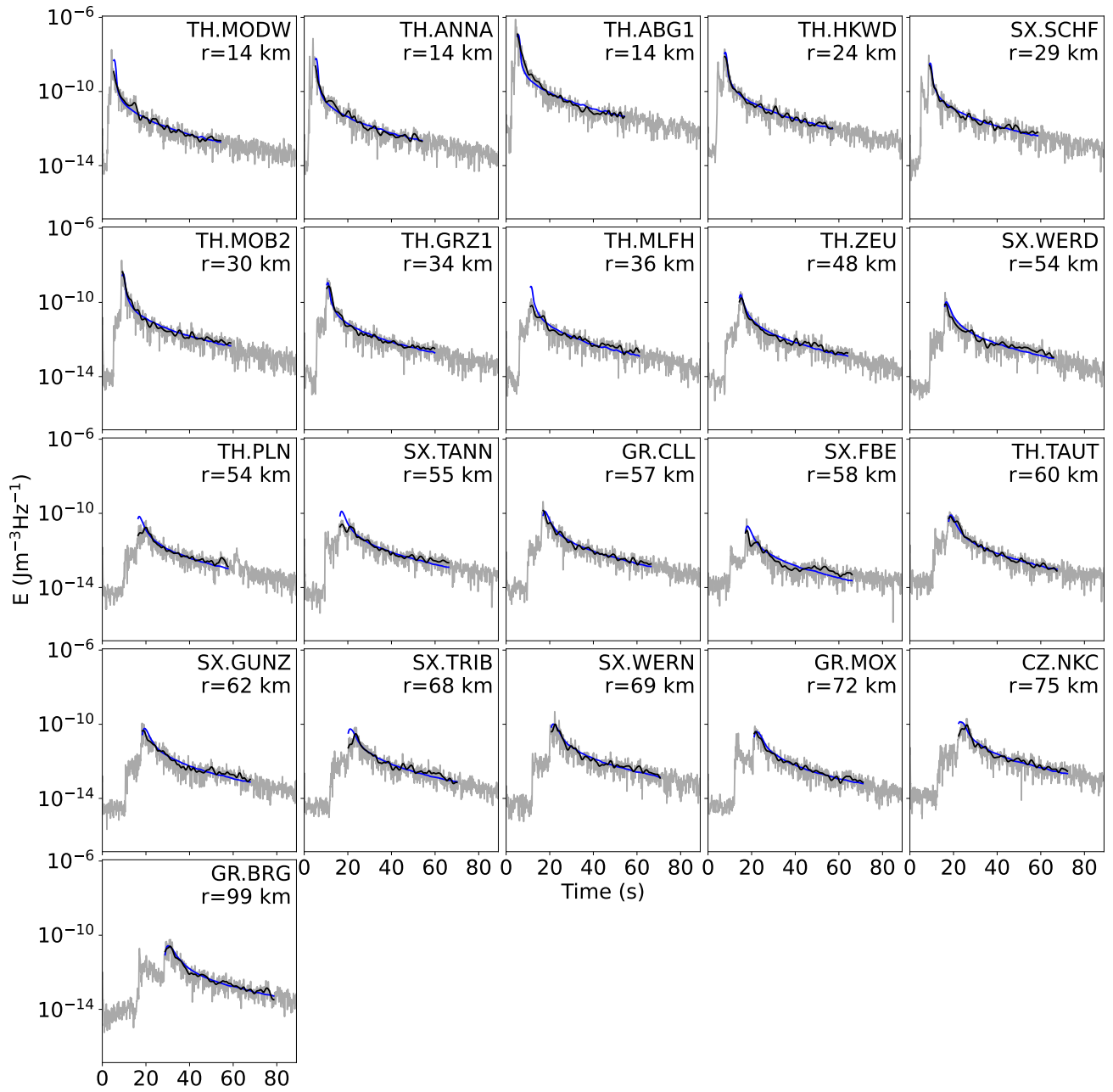


Figure S2. Same as Figure S1, but for SLRZ.



**Figure S3.** Same as Figure S1, but for INS.



**Figure S4.** Observed and synthetic envelopes for each station of an NLRZ event for the central frequency 6 Hz. Observed envelopes are shown with gray lines, smoothed envelopes are shown with black lines and synthetic envelopes are shown with blue lines.

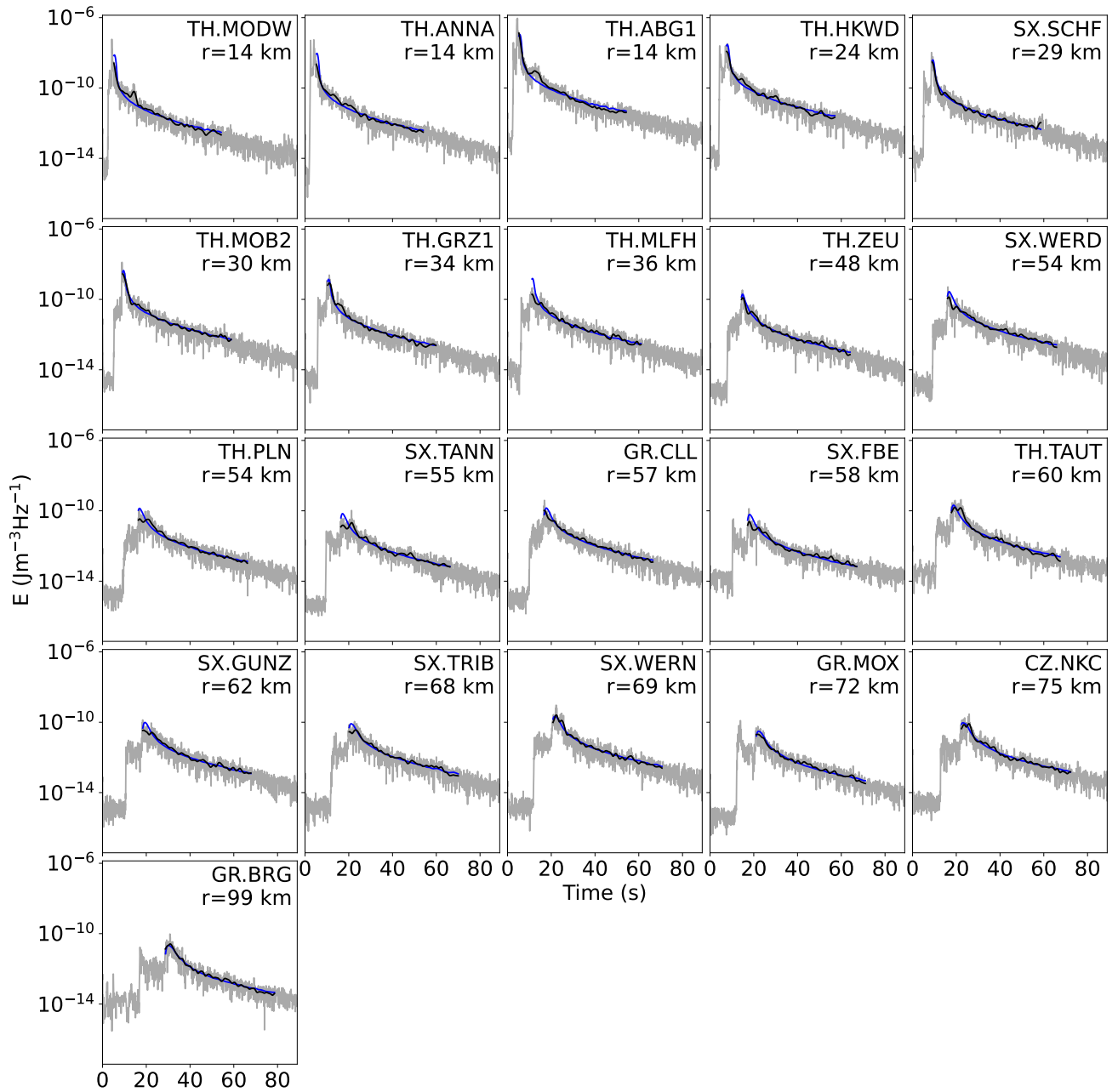


**Figure S5.** Same as Figure S4, but for the central frequency 12 Hz.

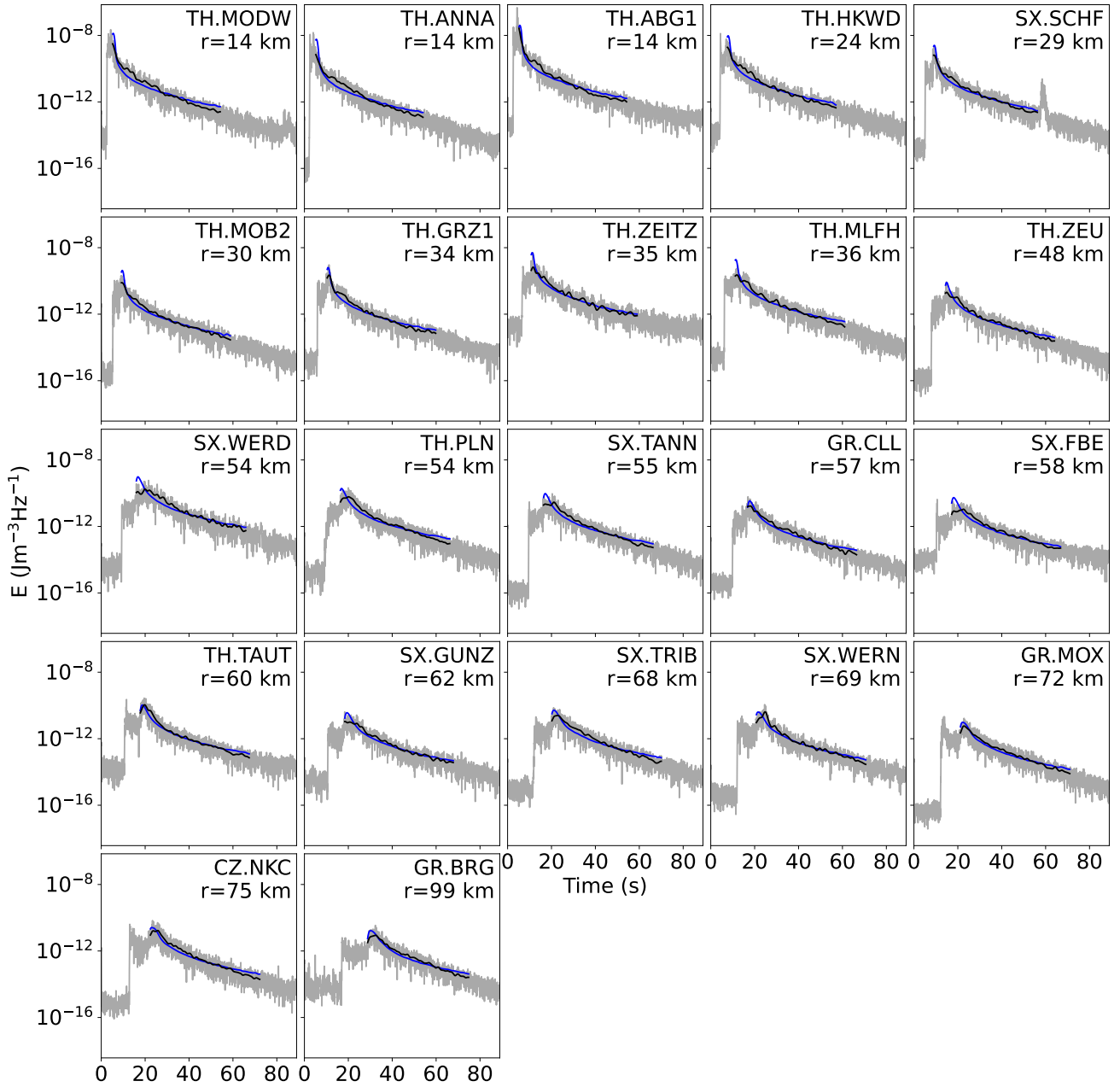


**Figure S6.** Same as Figure S4, but for the central frequency 24 Hz.

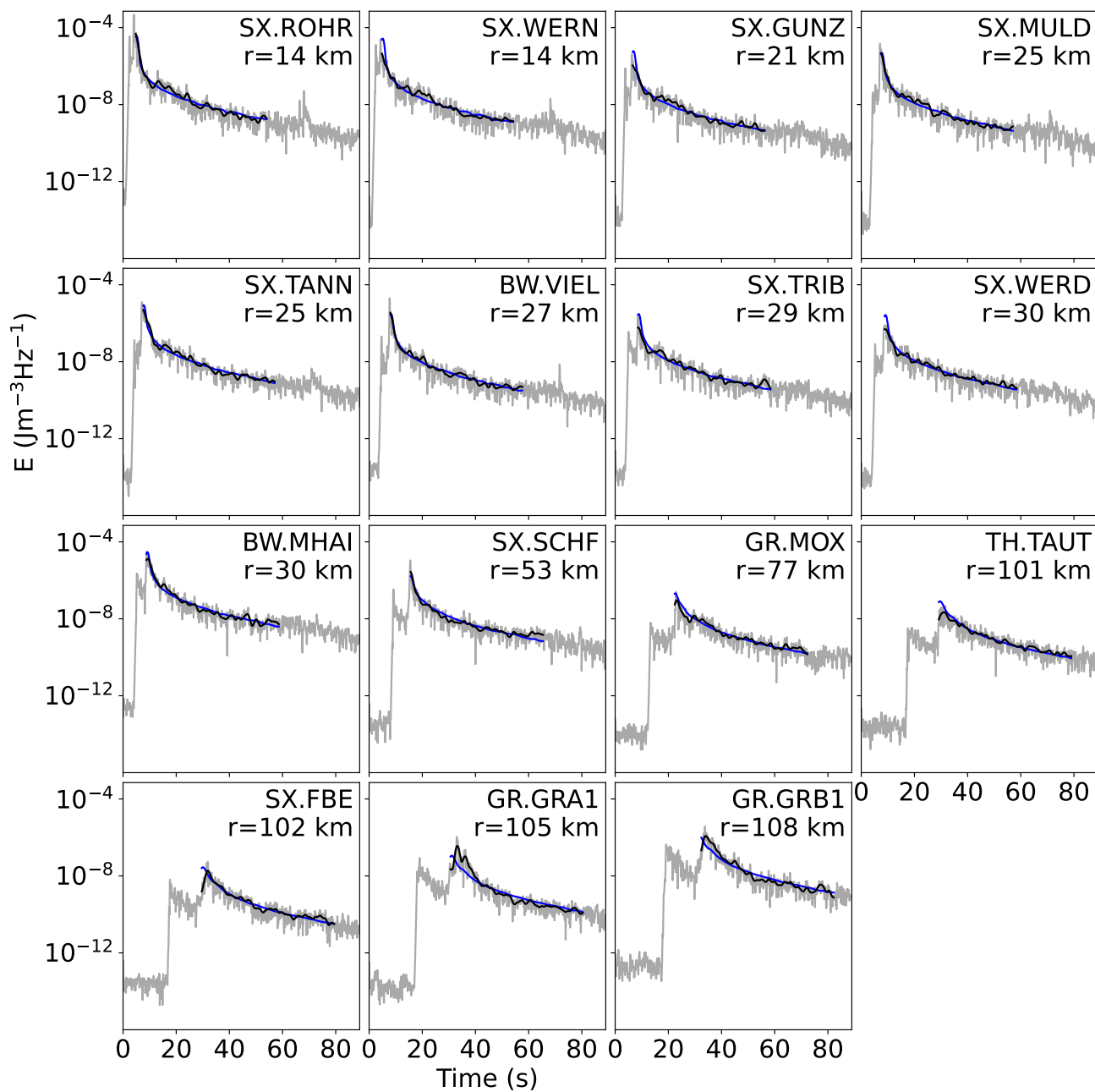


**Figure S7.** Same as Figure S4, but for an SLRZ event and the central frequency 6 Hz.

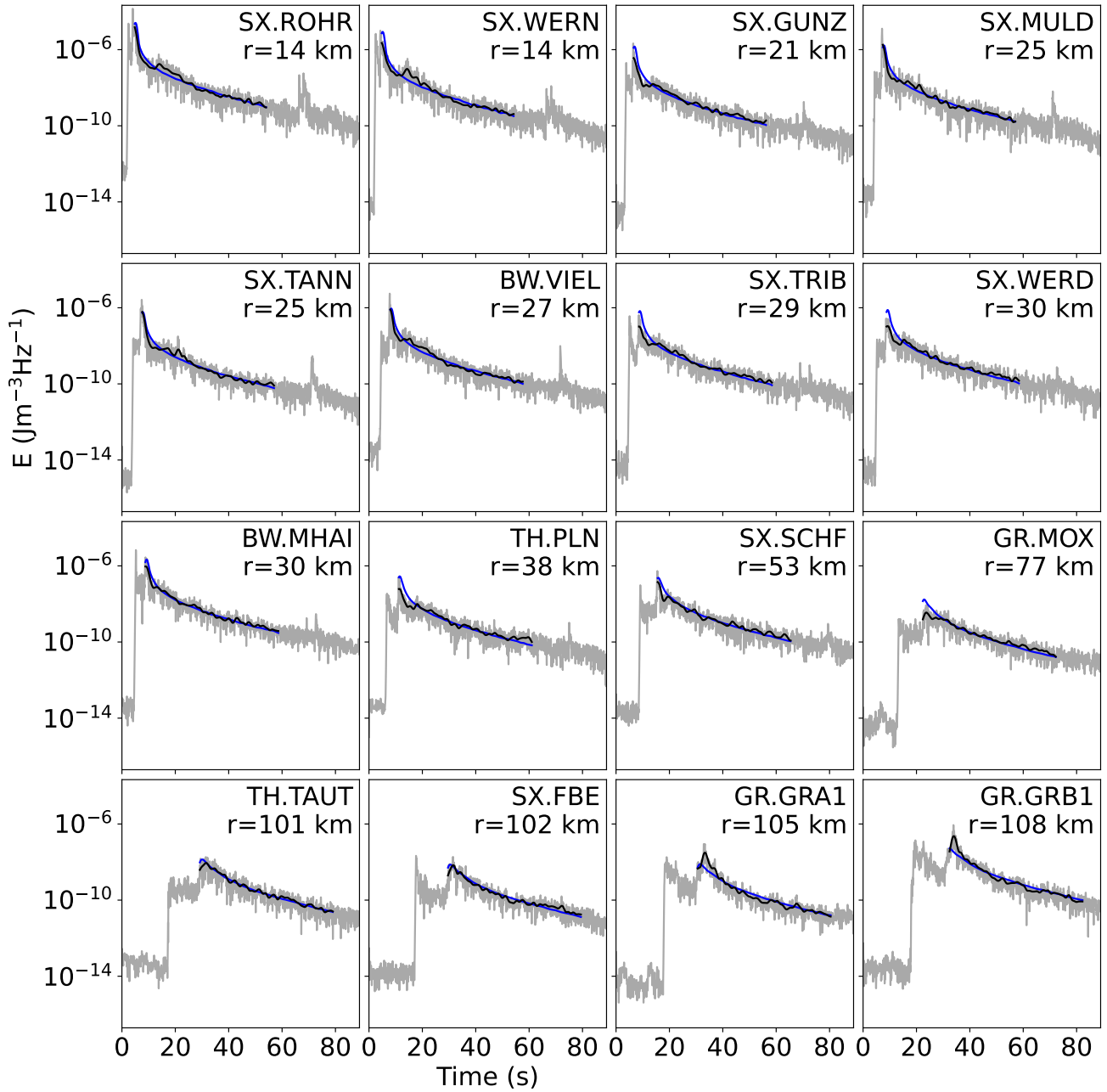


**Figure S8.** Same as Figure S4, but for an SLRZ event and the central frequency 12 Hz.

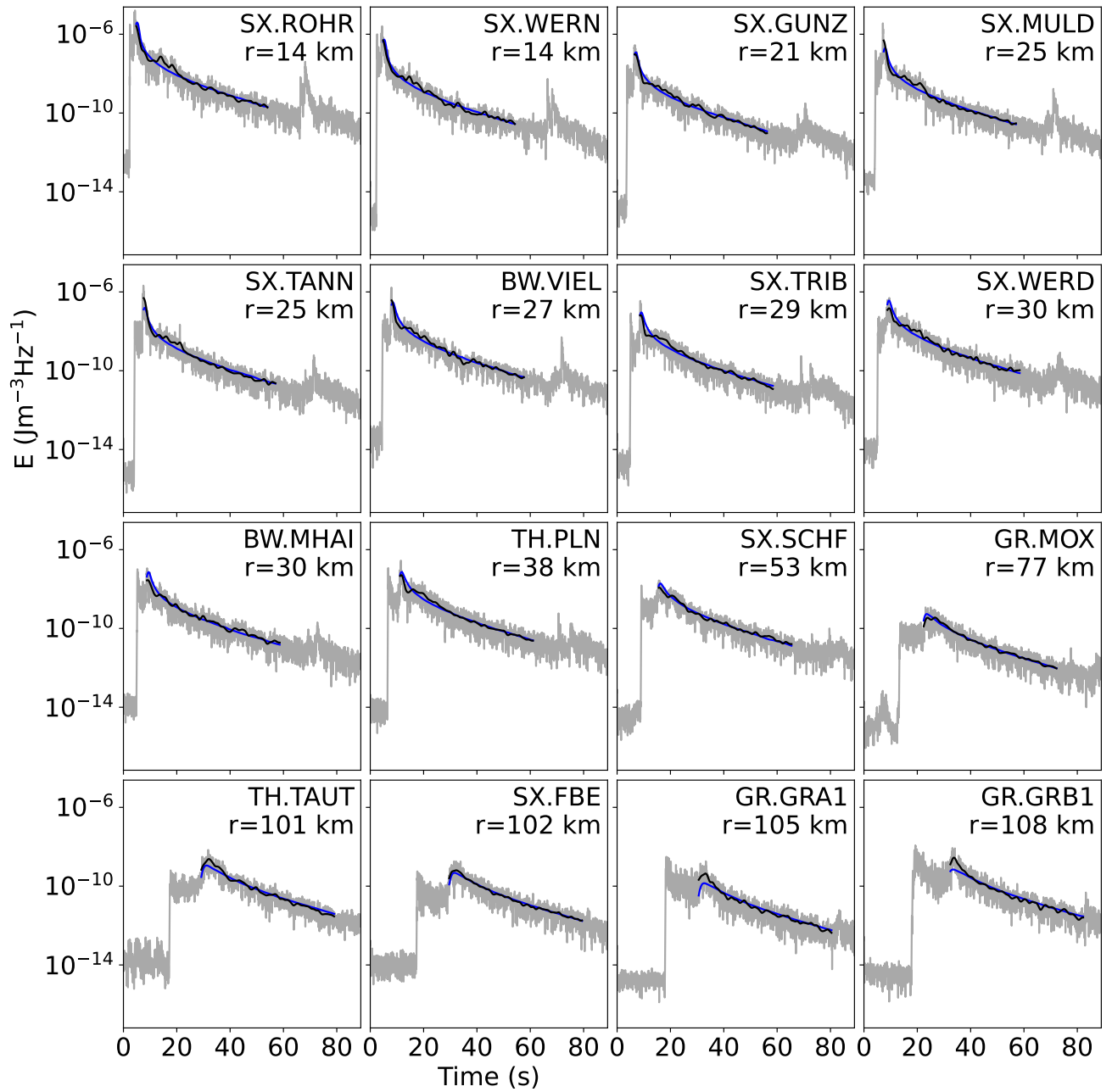


**Figure S9.** Same as Figure S4, but for an SLRZ event and the central frequency 24 Hz.

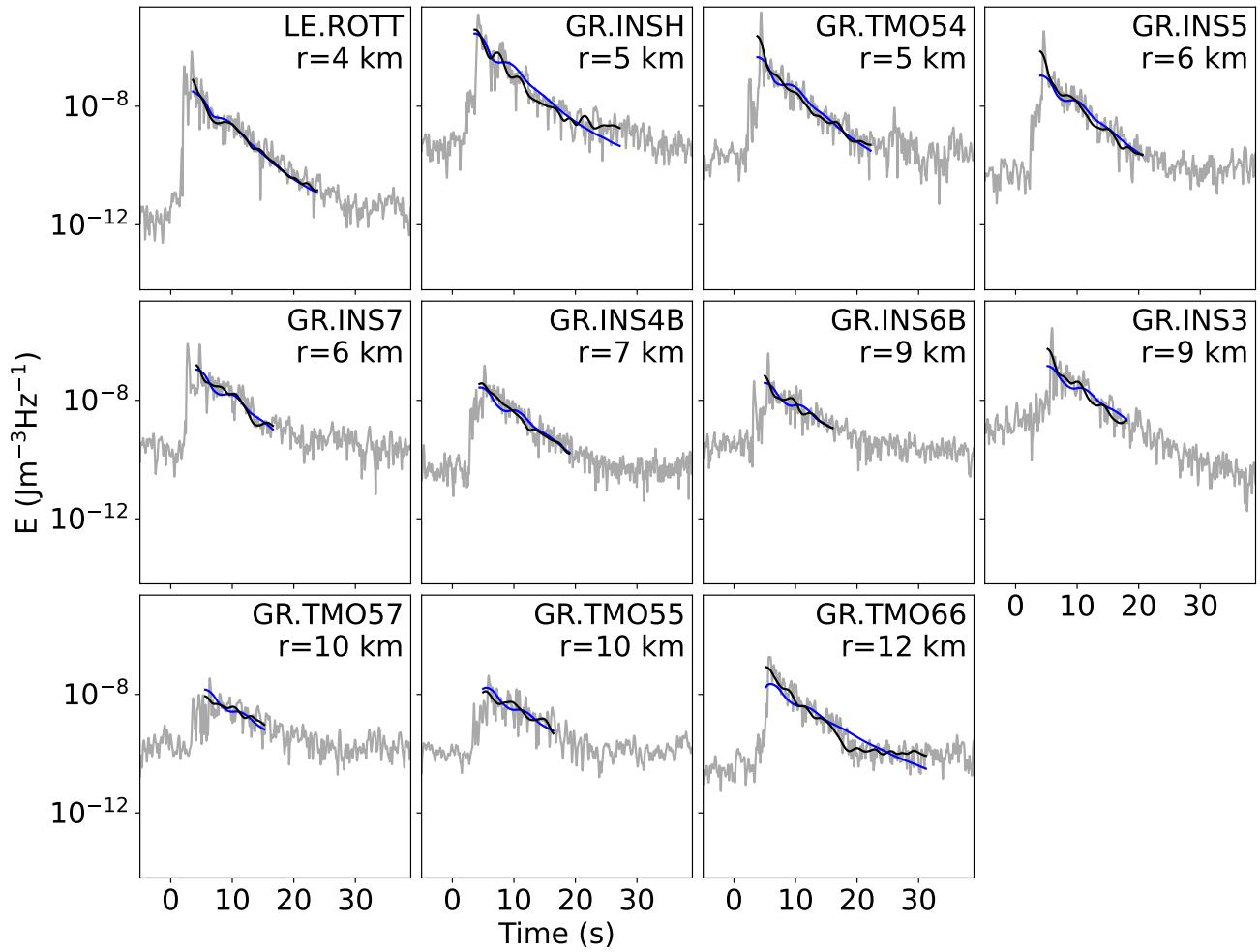


**Figure S10.** Same as Figure S4, but for an INS event and the central frequency 6 Hz.

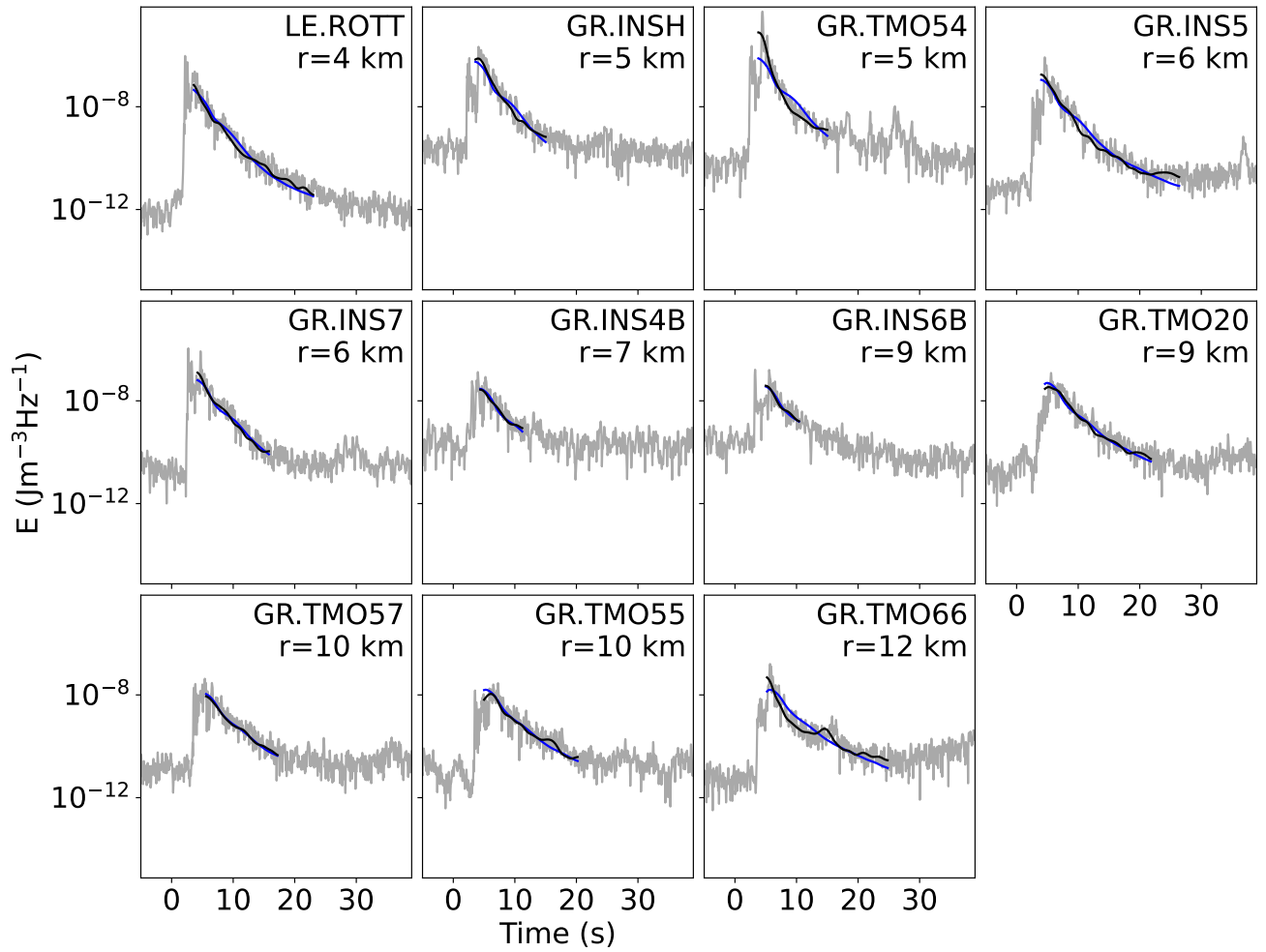


**Figure S11.** Same as Figure S4, but for an INS event and the central frequency 12 Hz.

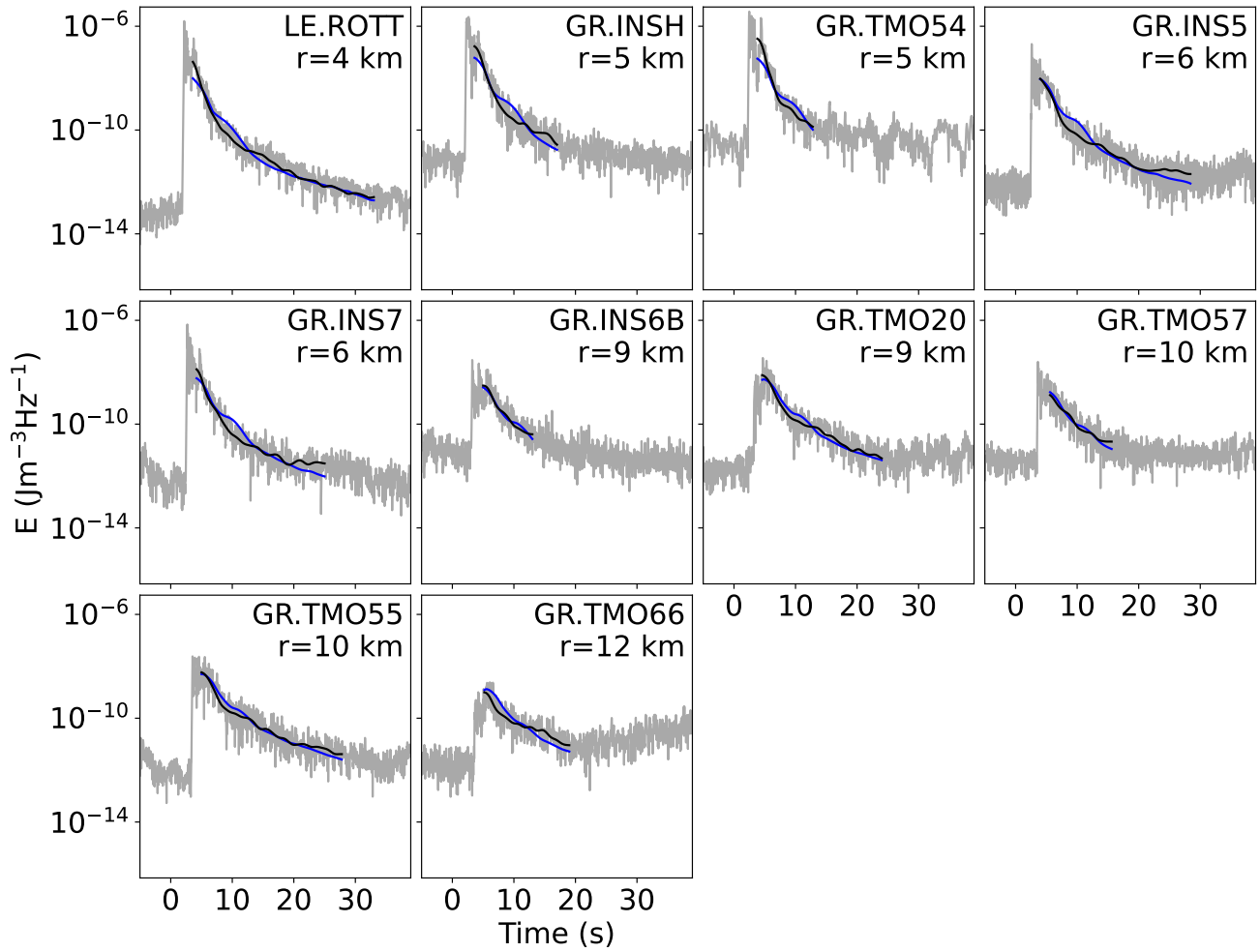


**Figure S12.** Same as Figure S4, but for an INS event and the central frequency 24 Hz.

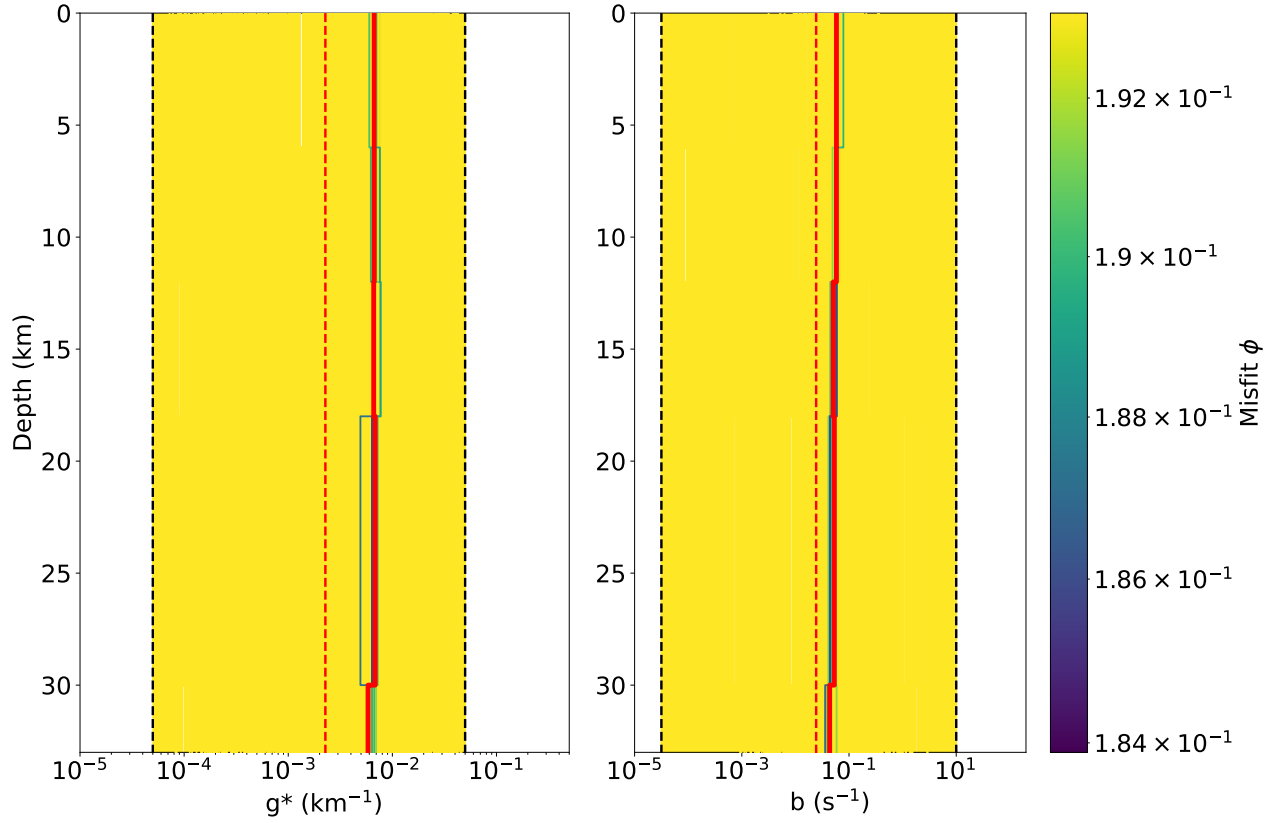


**Figure S13.** Inverted 1-D attenuation models of NLRZ for the central frequency 6 Hz as a function of misfit. The color scale ranges from the misfit of the best model at the minimum to a 5% error tolerance at the maximum. The best model is shown as a red line, the homogeneous Qopen model as a red dashed line and the allowed minimum and maximum values of the inversion as a black dashed line.

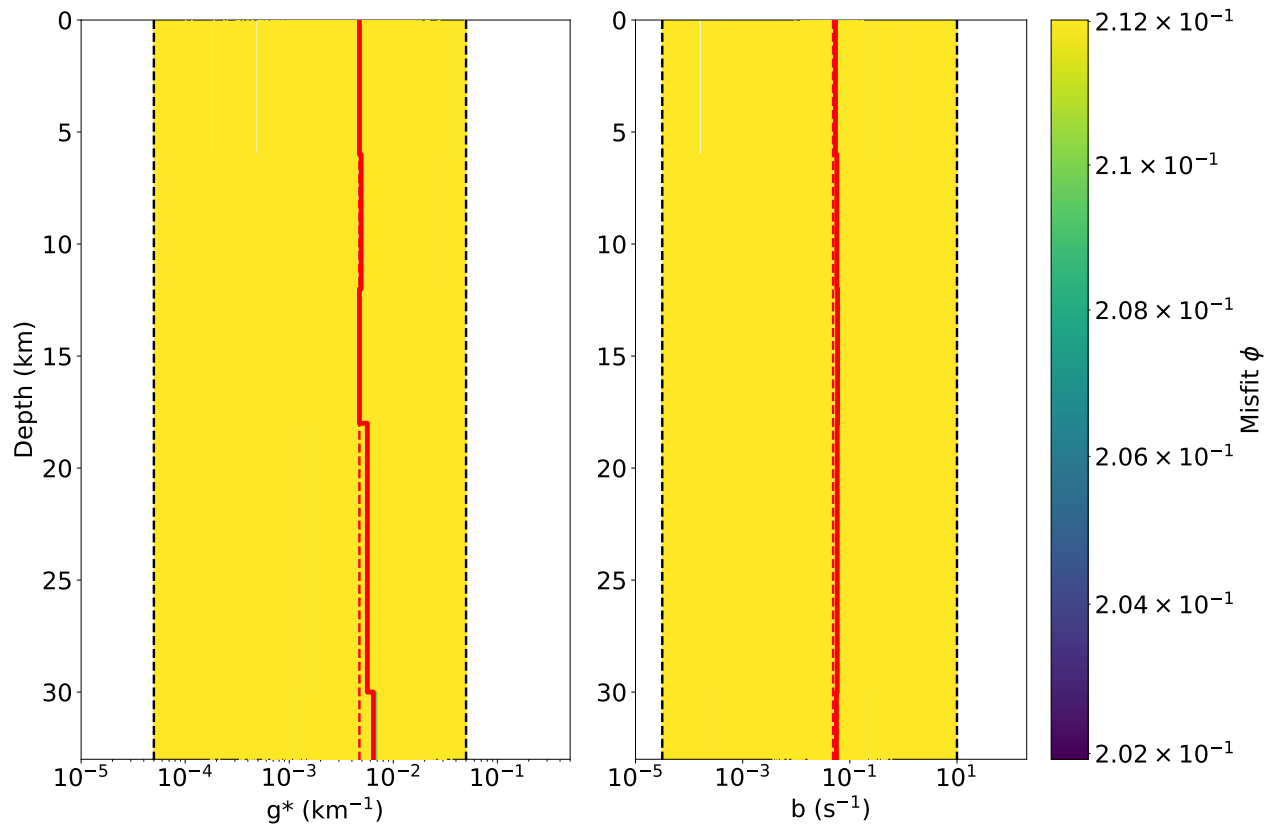


**Figure S14.** Same as Figure S13, but for the central frequency 12 Hz.

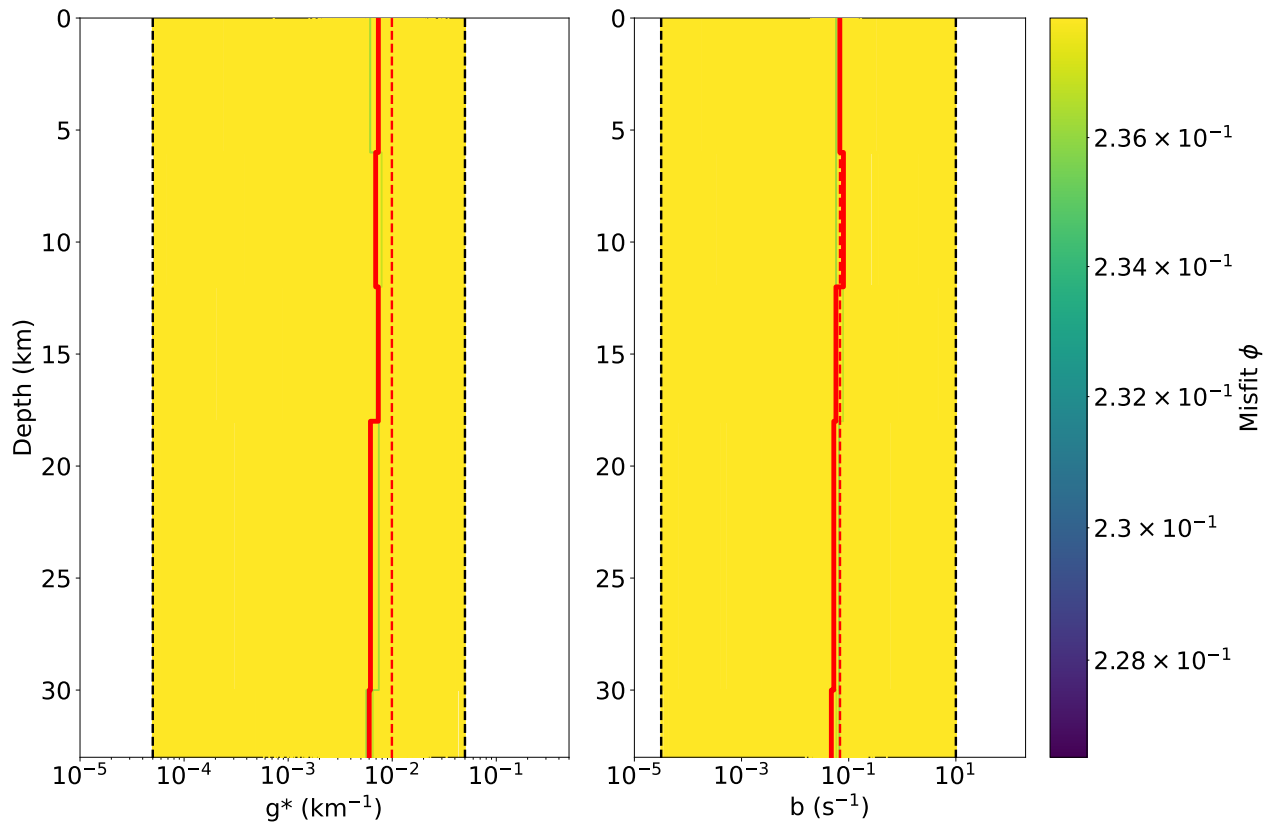


**Figure S15.** Same as Figure S13, but for the central frequency 24 Hz.

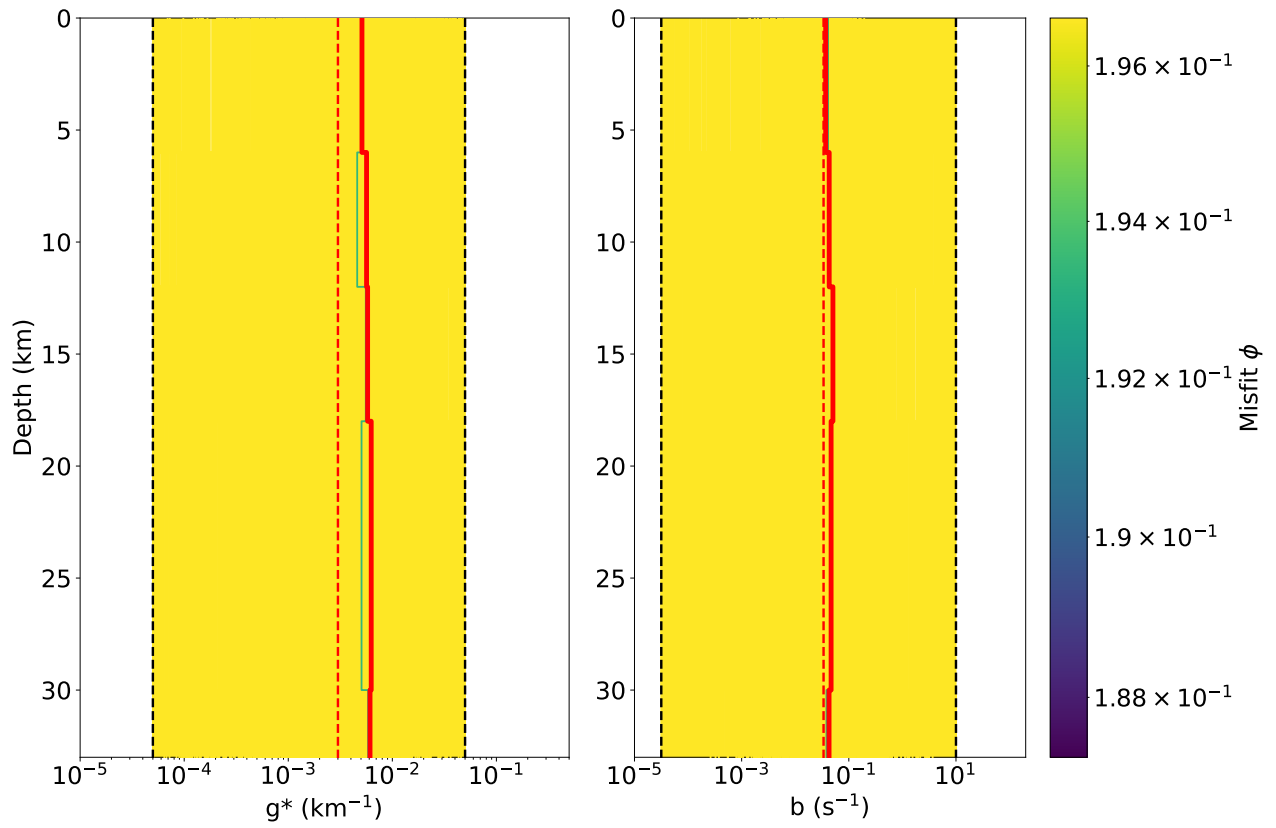


**Figure S16.** Same as Figure S13, but for an SLRZ event and the central frequency 6 Hz.

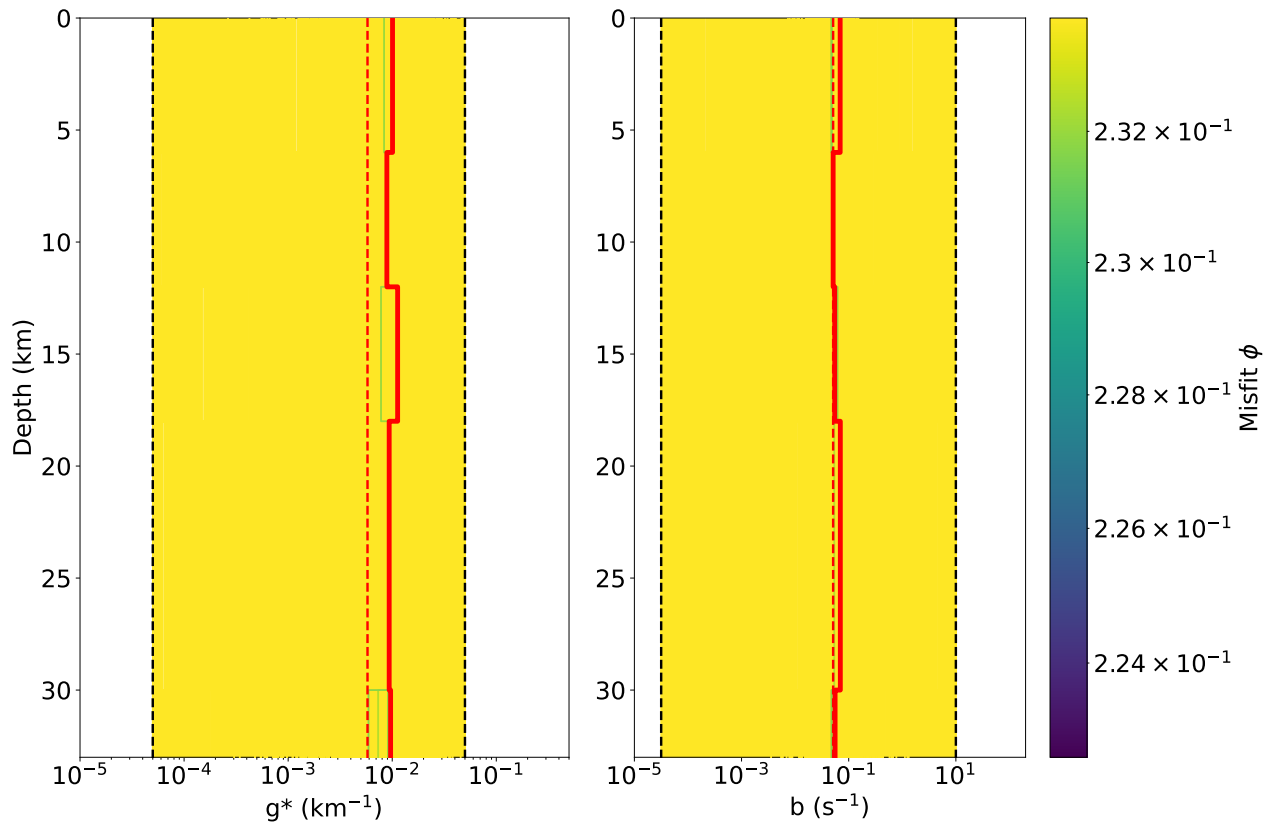


**Figure S17.** Same as Figure S13, but for an SLRZ event and the central frequency 12 Hz.

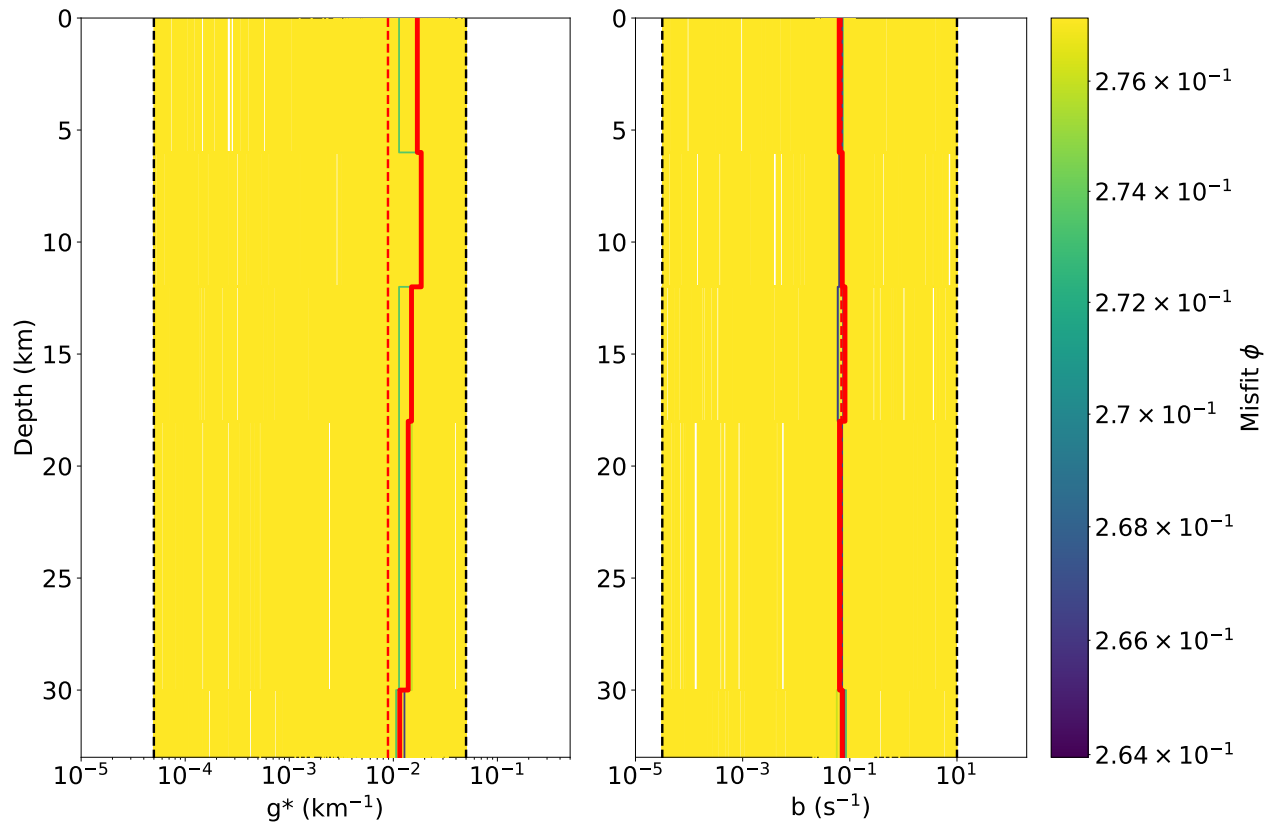


**Figure S18.** Same as Figure S13, but for an SLRZ event and the central frequency 24 Hz.

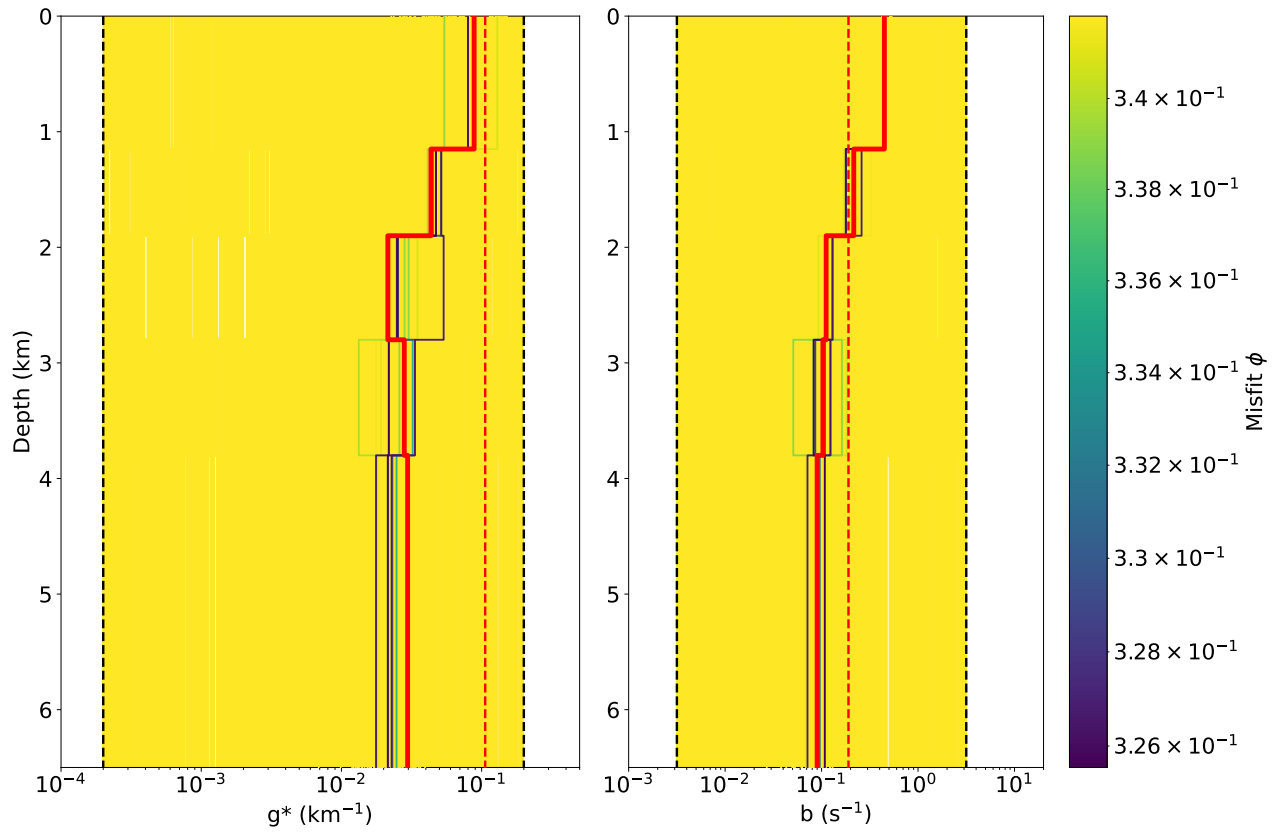


**Figure S19.** Same as Figure S13, but for an INS event and the central frequency 6 Hz.

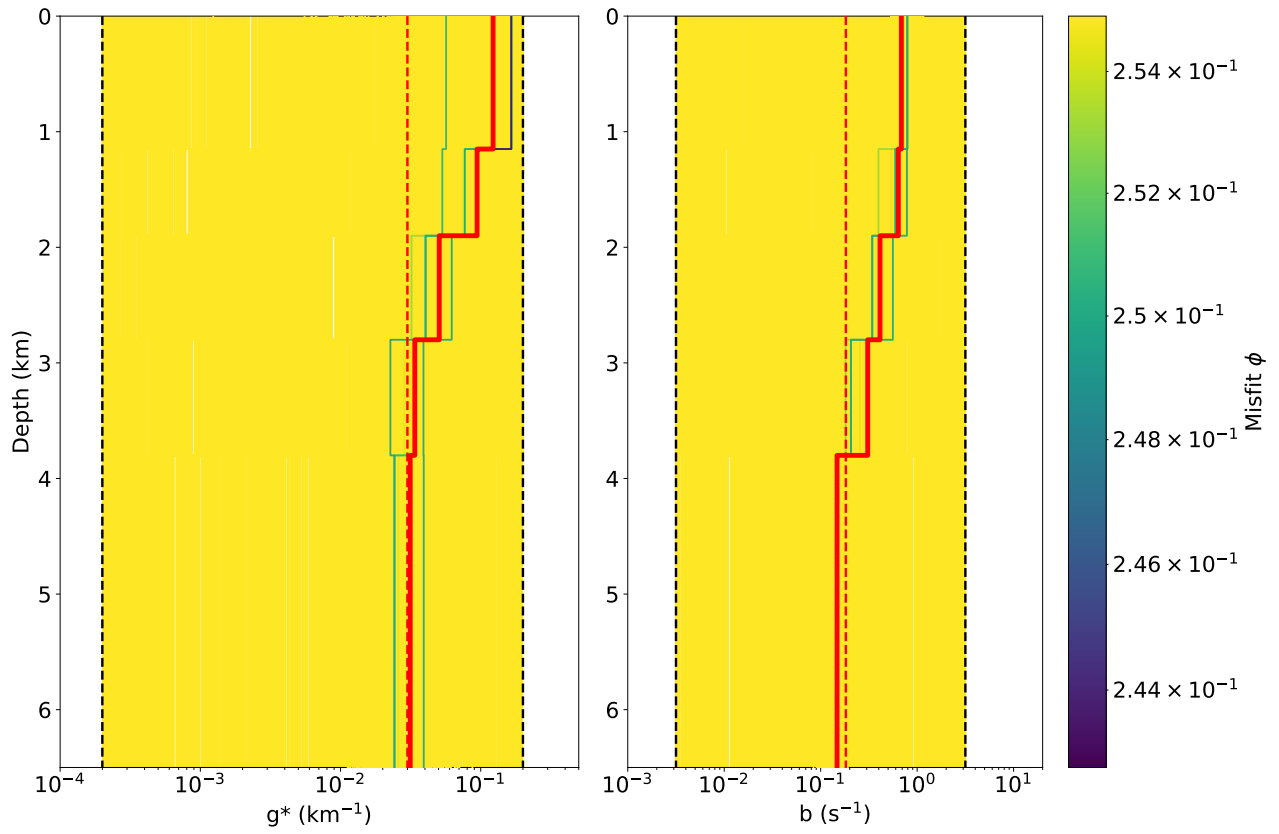


**Figure S20.** Same as Figure S13, but for an INS event and the central frequency 12 Hz.

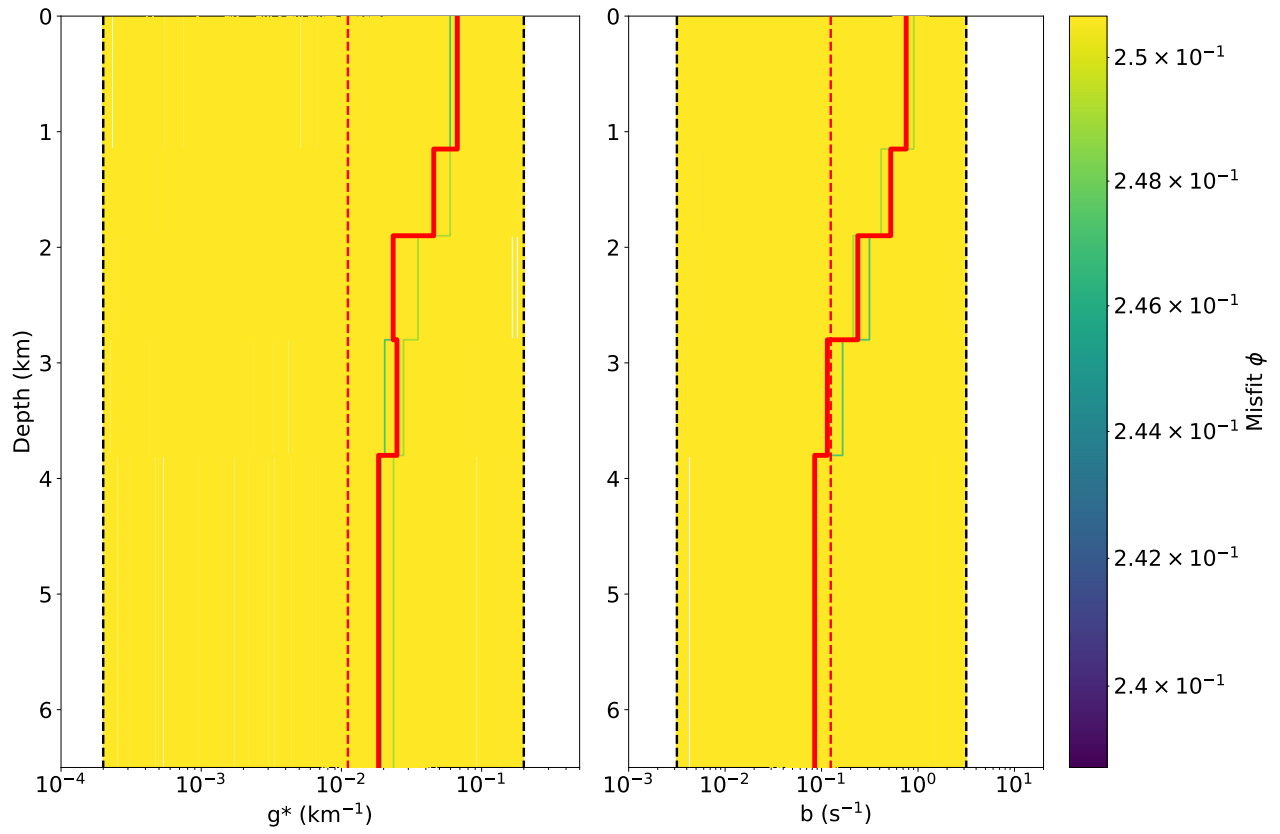


**Figure S21.** Same as Figure S13, but for an INS event and the central frequency 24 Hz.

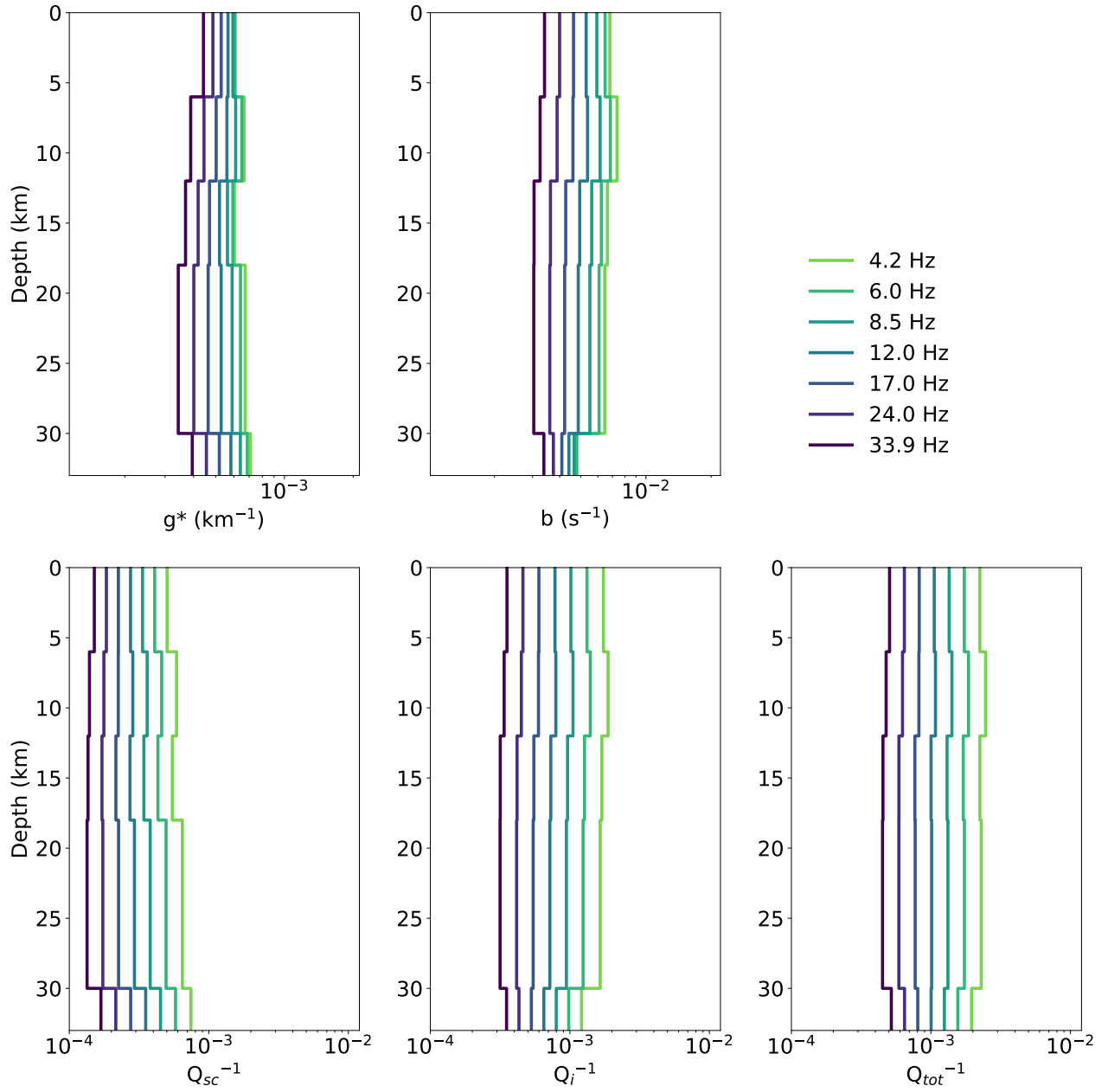


**Figure S22.** Depth-dependent 1-D attenuation models of NLRZ as a function of frequency.

The models are based on the power-law.

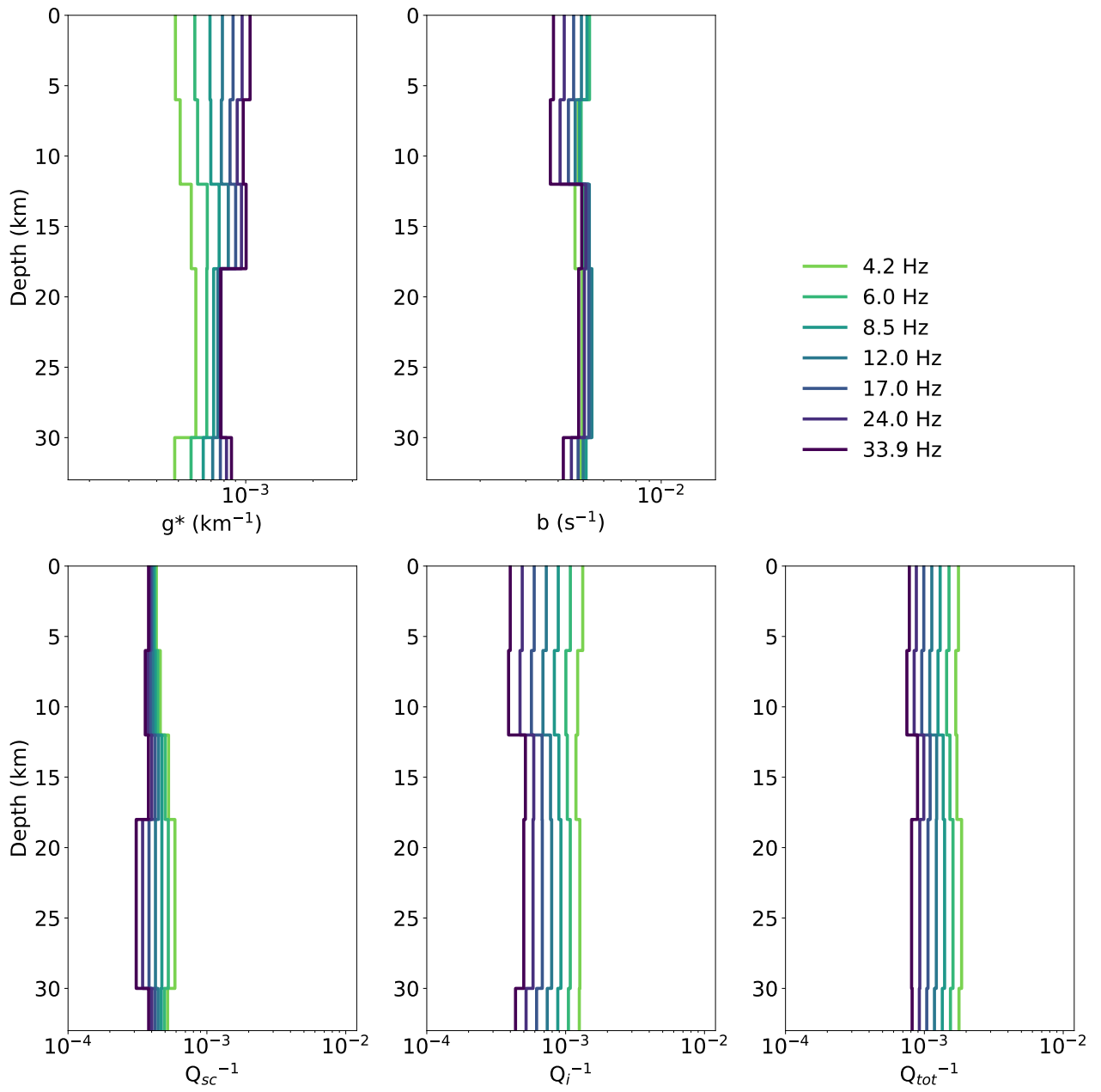


**Figure S23.** Same as Figure S22, but for SLRZ.

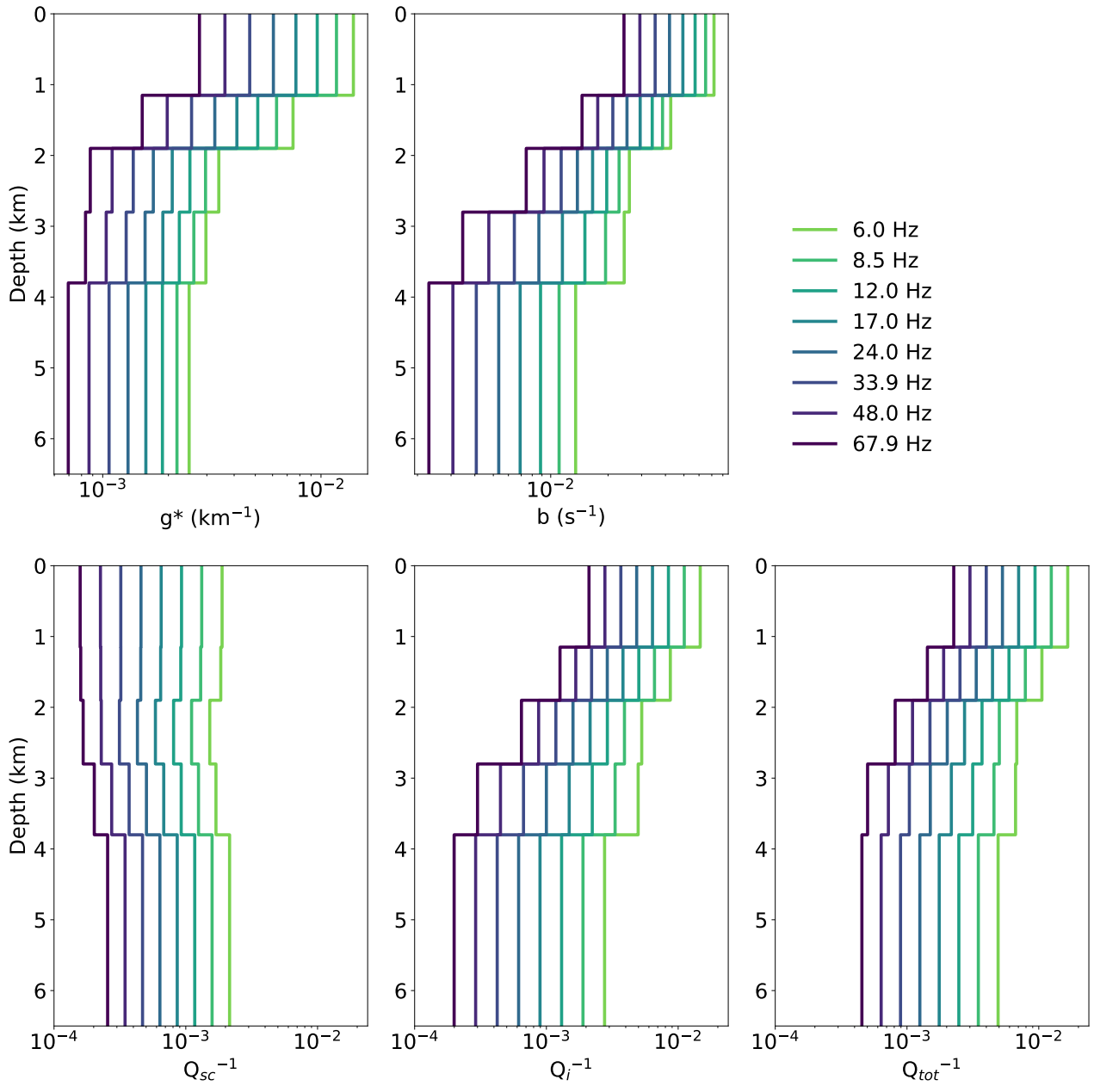


**Figure S24.** Same as Figure S22, but for INS.

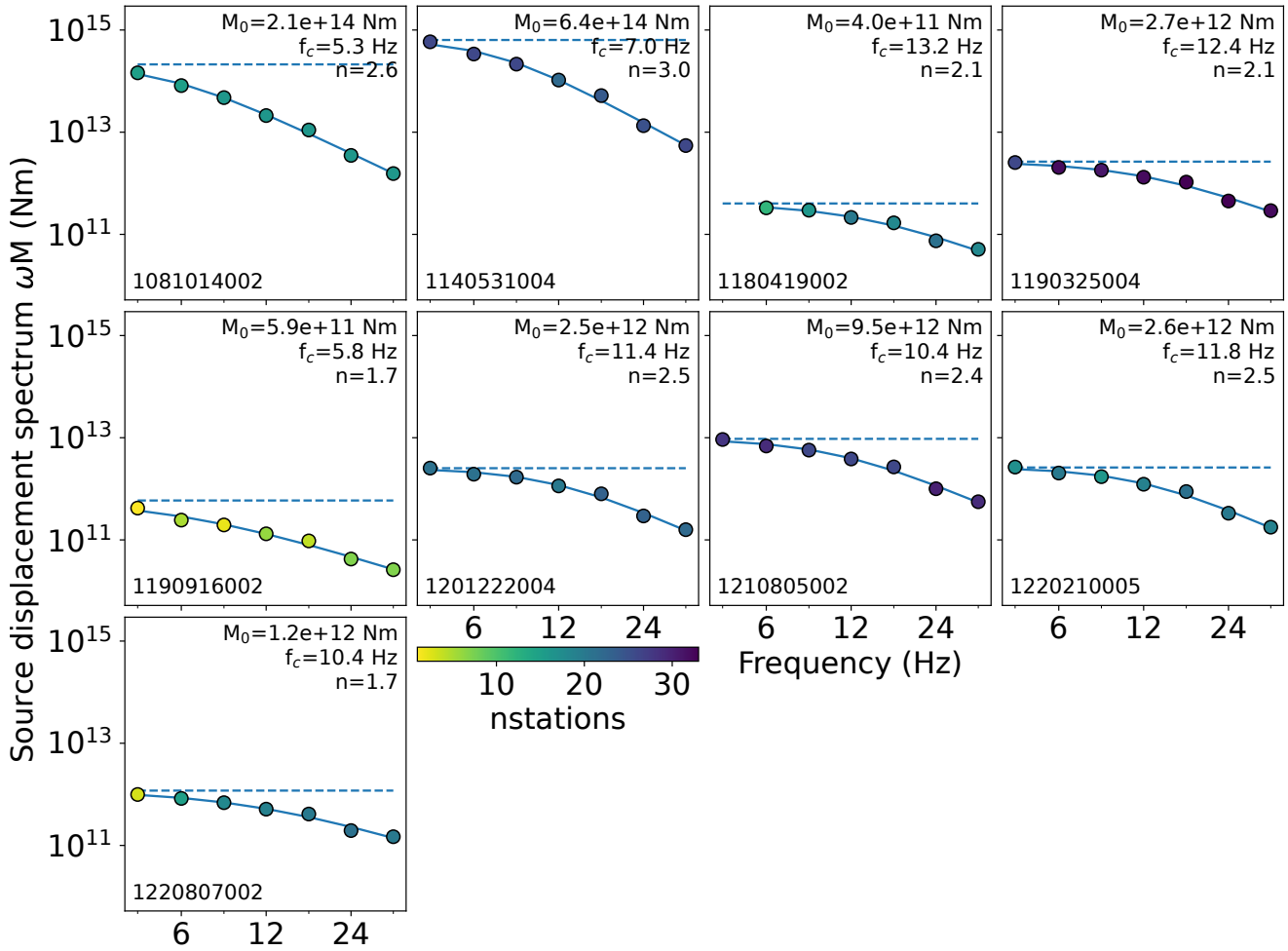


**Figure S25.** Observed source displacement spectra, displayed as circles depending on the number of observations ( $n_{stations}$ ) and the fitted source model (blue lines) for the SLRZ events. The seismic moment  $M_0$ , the corner frequency  $f_c$  and the high-frequency fall-off  $n$  were also determined.

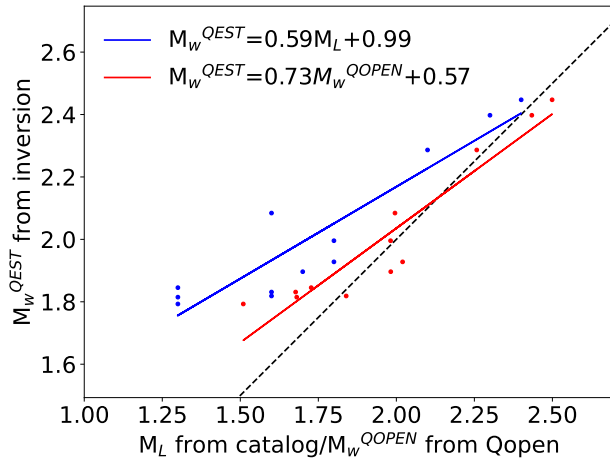


**Figure S26.** Comparison of catalogue local magnitude  $M_L$  and moment magnitude  $M_w$  estimated during the inversion (blue), as well as the estimated moment magnitude  $M_w$  from Qopen and QEST (red) in NLRZ. The black dashed line represents the one-to-one ratio. The least-squares fit to the data is indicated with a blue and red line, respectively.

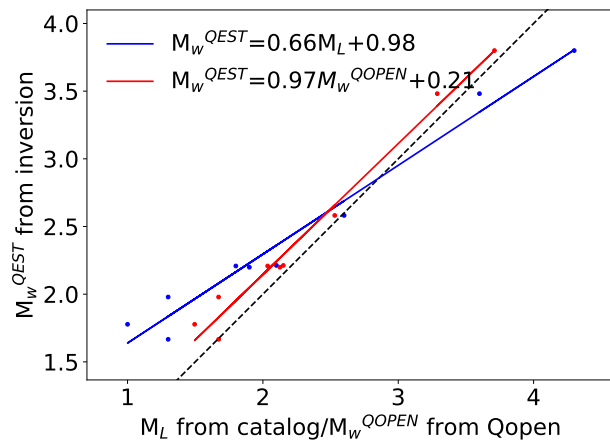


**Figure S27.** Same as Figure S26, but for SLRZ.

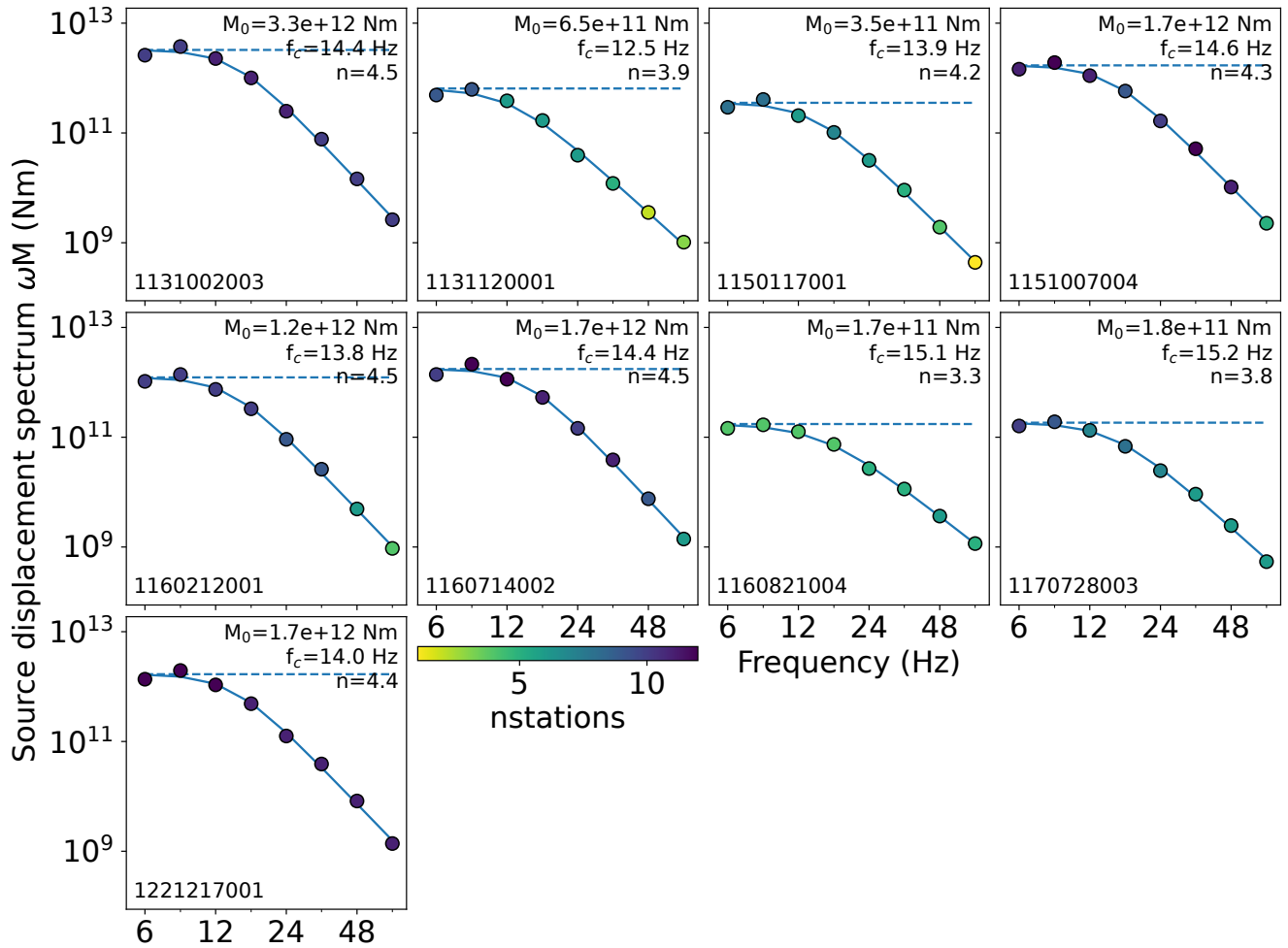
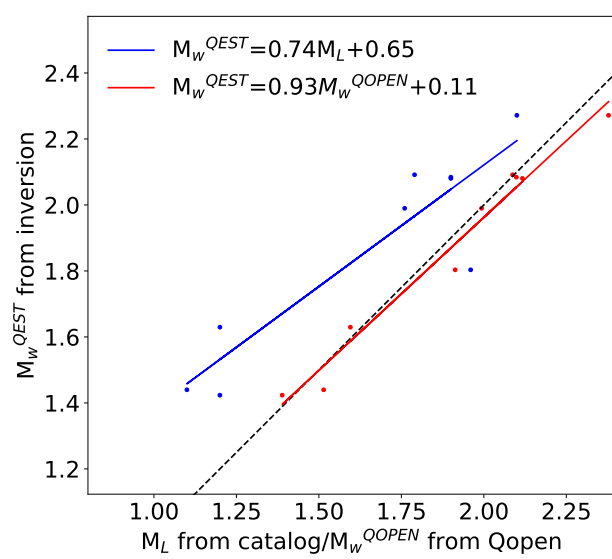


Figure S28. Same as Figure S25, but for INS.



**Figure S29.** Same as Figure S26, but for INS.

## 7 | Results and discussion

The research questions were investigated in three publications by analyzing the seismic velocity and attenuation along the LRZ. The most significant results of the publications are discussed and summarized below. A detailed description of all results can be found in the respective publications.

### 7.1 Fluids and their origin

The cause of the earthquake swarms in Schöneck and Werdau was previously unknown, as there was no evidence of fluids in either area. In contrast, in NW-Bohemia/Vogtland there are mofettes where fluids emerge at the surface, providing direct evidence of fluid movements in the subsurface. Given the proximity of Schöneck and Werdau to NW-Bohemia/Vogtland and the occurrence of earthquake swarms in Schöneck and Werdau, it was postulated that fluids must also be present in this area. It was hypothesized that the fluids would travel along fault intersections, such as the GJZ and LRZ intersection (Hemmann et al., 2003). To identify potential areas in the crust that contain fluids, traveltimes tomography was carried out (van Laaten et al., 2023). The obtained velocity model shows areas with increased  $v_p/v_s$  values, indicating the presence of fluids. A narrow fluid path that traverses the Schöneck and Werdau earthquake swarm areas could not be imaged with tomography, possibly due to the limited resolution. Nevertheless, given the occurrence of earthquake swarms, fluids must traverse these areas. It remains unclear what happens to the fluids once they have passed the earthquake swarm areas. There is no evidence of concentrated fluid leakage at the surface, like mofettes, in the Schöneck and Werdau area. Thus, uprising fluids might be distributed diffusely through the crust. Intrinsic attenuation, which is sensitive to fluids, provides further indications of the presence of fluids in the crust. For the homogeneous model (van Laaten et al., 2022), the intrinsic attenuation is stronger in NW-Bohemia. This difference could indicate a higher concentration of fluids in the southern region.

The question of the origin of the fluids for the Schöneck and Werdau earthquake swarm areas could be clarified using receiver functions (van Laaten et al., 2022). At a depth of  $68 \pm 2$  km, there is a velocity discontinuity that has been identified as the source of the fluids. This is

the same source that Heuer et al. (2006) have already identified below NW-Bohemia/Vogtland, but unlike Heuer et al. (2006), we were able to trace the discontinuity further north. The velocity discontinuity can be explained by a  $3.7 \pm 1\%$  decrease in velocity at a depth of 65 km, or by a 5 km thick gradual velocity decrease between 65 and 70 km (Heuer et al., 2006). According to Heuer et al. (2006), the discontinuity is possibly a local updoming of the lithosphere-asthenosphere boundary caused by partial melting. The uprising fluids are caused by mantle degassing. Plomerová et al. (2007) were able to rule out a plume beneath NW-Bohemia/Vogtland using teleseismic P-velocity tomography. The tomography showed no narrow anomaly in the upper mantle, as would be expected for a plume and is visible below the Eifel (Ritter et al., 2001). According to Babuška and Plomerová (2010), the most likely source of the fluids is also an uplift of the asthenosphere. The northern extent of the partial melt's lateral extension could also be determined (van Laaten et al., 2023), reaching just before the Werdau earthquake swarm area. After that, it is bound by a dipping seismic reflector. Geissler et al. (2005) interpret the second, more shallow discontinuity as the base of a metasomatic uppermost mantle containing a few percent melt.

## 7.2 Schöneck and Werdau earthquake swarms

Seismic traveltime tomography was used to investigate whether the crust in the earthquake swarm regions of Schöneck and Werdau has a structure similar to that of the NW-Bohemia/Vogtland region (van Laaten et al., 2023). Potential areas containing fluids were also identified in the crust of Schöneck and Werdau, similar to those in NW-Bohemia/Vogtland. Both earthquake swarm regions are located near intersections. In the case of Werdau, the GJZ and LRZ, while in the case of Schöneck, the BKZ and LRZ intersection. Therefore, the assumption of uprising fluids along the intersection by Hemmann et al. (2003) is likely correct. The different strike directions cause stress to accumulate in the intersection area. When the stress reaches a critical point, earthquakes are triggered. In the case of the Schöneck and Werdau earthquake swarm area, the presence of an intrusive body in the crust in the immediate vicinity can be inferred from the low  $v_p/v_s$ -ratio. The velocities indicate that the intrusive body may be a quartz-rich granitic intrusion. The location of the intrusive body near the intersection could lead to additional stress accumulation, further pro-

moting earthquakes. In this context, parallels can be drawn to the earthquake swarms in NW-Bohemia/Vogtland, where the combination of fluids, faults and intrusive bodies is also believed to be the trigger of the earthquake swarms (Mousavi et al., 2015). However, the crust around the earthquake swarms in NW-Bohemia/Vogtland has a different structure. An analysis of the Hurst exponent indicates that the crust in the southern area is significantly rougher ( $\kappa \approx 0.06$ ) than the northern part of the LRZ ( $\kappa \approx 0.33$ ) (van Laaten & Wegler, 2024). Furthermore, the absence of other earthquake swarm areas north of Werdau could be attributed to the fact that the Werdau earthquake swarm area is situated at the boundary of partial melting in the asthenosphere (van Laaten et al., 2023). Further north, there are no uprising fluids that could potentially trigger earthquake swarms.

### 7.3 Earthquakes along the LRZ

The earthquake behavior along the LRZ changes. Seismic events are observed at greater depths in the northern part of the LRZ than in the southern part. This suggests that the brittle-ductile boundary of the crust along the LRZ is not at a uniform depth. The brittle-ductile transition zone is defined as the transition from the upper, more brittle crust to the lower, more ductile crust. Depending on the mineral composition of the crust, the transition zone lies at different depths (Fig. 7.1). In quartz-rich crusts, the transition is at around 300°C, while in feldspar-rich crusts the transition is at around 450°C. Below the brittle-ductile transition zone, the probability of ductile deformation of the rock through creep is higher than that of fracture formation. This prevents the accumulation of stress and the occurrence of earthquake. The exact depth of the brittle-ductile transition zone is influenced by various factors including strain rate, temperature gradient, crustal composition, fluid content, or the age of the crust. Earthquakes also rarely occur near the surface, because frictional sliding prevents stress accumulation. The uplift of the Moho from 31 km to approximately 27 km below NW-Bohemia/Vogtland results in a stronger temperature gradient and increased fluid flow in the crust due to magmatic processes (Bräuer et al., 2008). These processes also impact the depth of the brittle-ductile transition zone. Based on the depth of the earthquakes, it can be concluded that the transition in the southern part of the LRZ is shallower than in the northern part. Intrinsic attenuation can be used for an explanation.

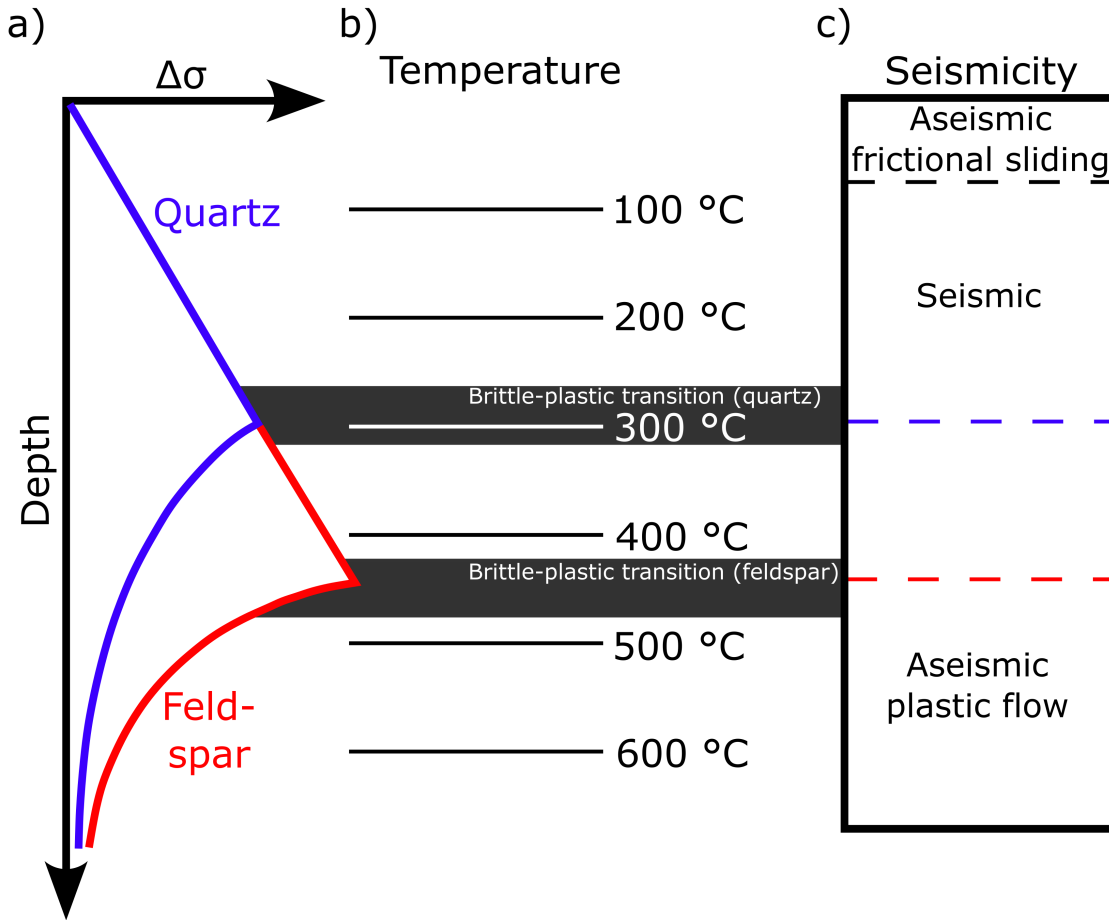


Figure 7.1: Schematic differential stress profile of the crust. Depending on the heat flow, temperature and material properties of quartz and feldspar minerals the brittle-ductile transition lies at different depths. Seismicity is coupled with the differential stress profile. Near the surface, frictional sliding prevents earthquakes and at greater depths, below the brittle-plastic transition, plastic flow prevents earthquakes. The seismogenic zone lies in between, where larger differential stresses are necessary to leave the stable regime.

Assuming that the crust behaves like a Maxwell body, intrinsic attenuation is anti-proportional to the viscosity ( $Q_i^{-1} \propto 1/\eta$ ). In Fig. 7.2, the power-law of van Laaten and Wegler (2024) was used to show the frequency-dependent depth profiles for SLRZ and NLRZ. The intrinsic attenuation is compared with the depth distribution of earthquakes from the respective study area. In SLRZ, most earthquakes occur at depths where intrinsic attenuation is lowest. In the layers above and below, the intrinsic attenuation increases, while the number of earthquakes decreases. Due to frictional sliding or plastic flow, earthquakes in these layers are rather unlikely. The intrinsic attenuation exhibits an inverse relationship with the differential stress profile. Areas with high viscosity (low  $Q_i^{-1}$ ) correspond to the areas where high differential stress is needed to reach the brittle domain. In general, NLRZ also aligns with this ob-

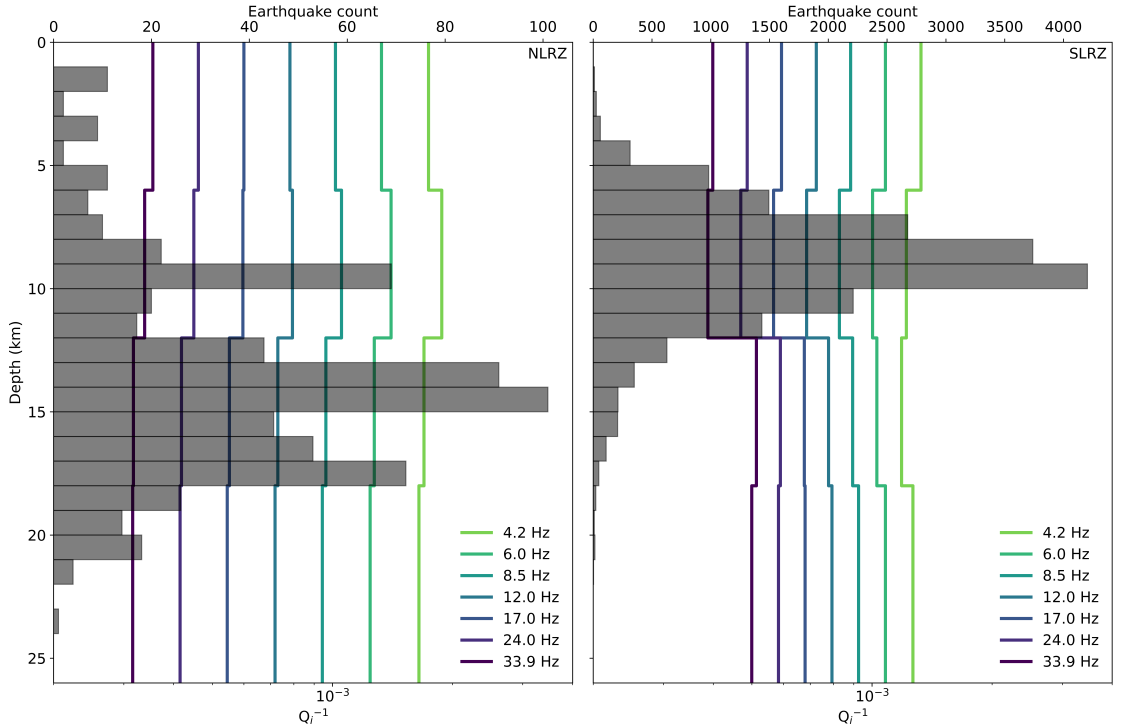


Figure 7.2: Earthquake depth distribution in the northern (NLRZ, left) and southern part of the LRZ (SLRZ, right) and depth profiles of the intrinsic attenuation from van Laaten and Wegler (2024). The depth profiles are shown in color as a function of frequency.

ervation and there are few earthquakes near the surface. The peak at 9 km is an exception to this rule, as it represents the earthquake swarm of 2016 that occurred northwest of Werdau. The swarm represents a local peculiarity that cannot be properly described with the assumption of a 1-D crust. However, most earthquakes in NLRZ are located at a depth between 12 and 18 km, where the intrinsic attenuation is also low. The layer below has even lower intrinsic attenuation, but it is possible that stresses cannot accumulate here due to the depth condition. In principle, intrinsic attenuation follows the inverse differential stress profile, except that this time the maximum strength is not visible.

## 7.4 Stress drop

The radiative transfer equation can be used to determine the attenuation properties of the subsurface, as well as S-wave source displacement spectrum of earthquakes. The spectrum provides valuable information about earthquake characteristics, including the seismic moment, corner frequency and high-frequency fall-off. Seismic moment is a measure of the energy released by an earthquake and can be used to calculate the

moment magnitude  $M_w$ . The moment magnitude is a superior measure of earthquake strength compared to the local magnitude  $M_L$ , which is based on an empirically derived formula and often underestimates the strength of smaller earthquakes ( $M_L < 2$ ) (Bethmann et al., 2011; Deichmann, 2006). This phenomenon is evident when comparing the moment magnitude of the earthquake with the local magnitude (van Laaten & Wegler, 2024). For earthquakes with a magnitude of two or higher, the difference between the local and moment magnitude is minimal. However, for earthquakes with a local magnitude of less than two, there are significant discrepancies. As a result, smaller earthquakes are systematically underestimated with the local magnitude, impacting seismic hazard analyses, such as the b-value of the Gutenberg-Richter law. The b-value is a ratio of small to large earthquakes and is an important parameter for the probabilistic seismic hazard estimation (e.g. Smith, 1981). The assumption of a homogeneous subsurface and isotropic scattering is sufficient to determine the moment magnitude (van Laaten et al., 2022). The use of a depth-dependent attenuation model only slightly improves this determination (van Laaten & Wegler, 2024).

The corner frequency corresponds to the duration of an earthquake, while the high-frequency fall-off value describes overall properties of a seismic source. The high-frequency fall-off values for NLRZ and SLRZ correspond to  $n = 2.3$  and  $n = 1.9$ , respectively. These values are in agreement with the frequently used omega-square model ( $n = 2$ ). The determined corner frequencies also correspond to typical values of local earthquakes with corresponding magnitude.

The S-wave source displacement spectrum of several earthquakes with different magnitudes can be used to determine the stress drop of a region. It is an important factor in ground motion prediction and hazard assessment scenarios. The stress drop is the amount of shear stress released along the rupture during an earthquake and can be calculated using the circular fault mode of Madariaga (1976):

$$\Delta\sigma = \frac{7}{16}M_0 \left( \frac{f_c}{kv_s} \right)^3 \quad \text{with } k = 0.21 \quad (7.1)$$

A constant stress drop, which is independent of magnitude, corresponds to a proportionality of  $M_0 \propto f^{-3}$  for the omega-square model (Brune, 1970). In order to better estimate the stress drop along the LRZ and as an outlook for a further study, the source spectra of a few earthquakes

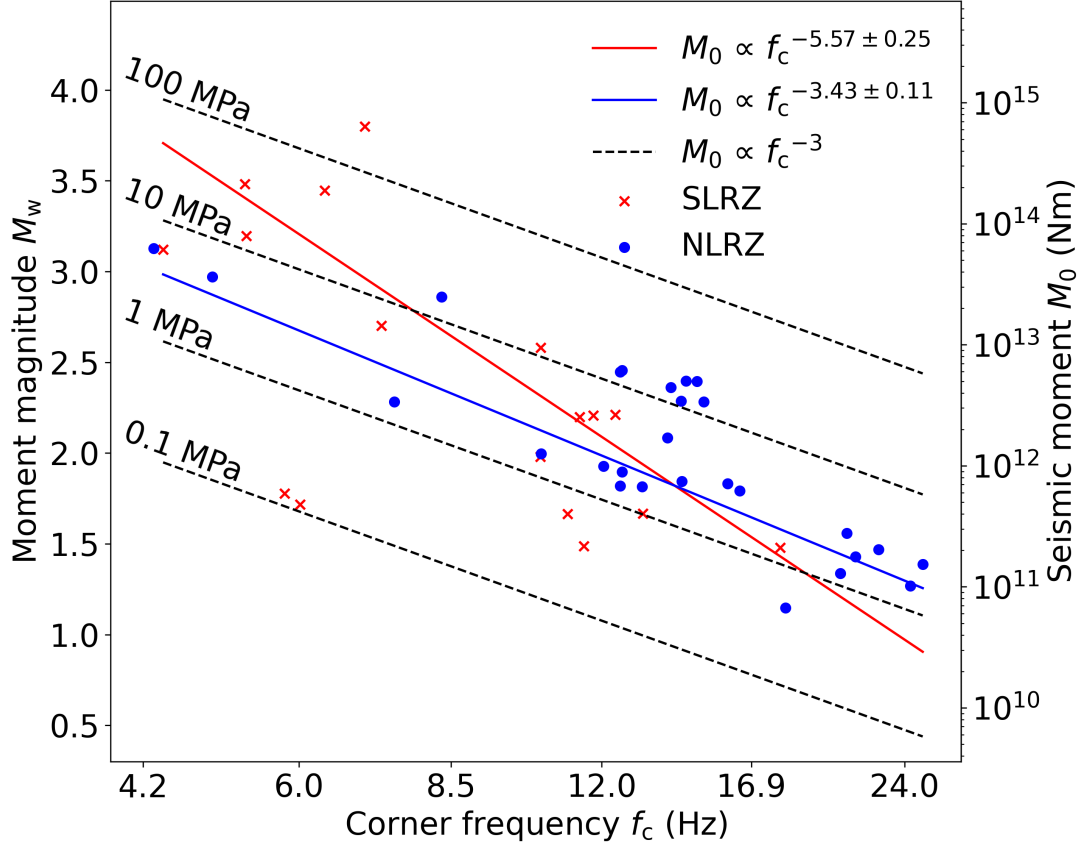


Figure 7.3: Relation between corner frequency and moment magnitude. Constant stress drops of 0.1, 1, 10 and 100 MPa corresponds to a scaling  $M_0 \propto f_c^{-3}$  (Madariaga, 1976) and are indicated with black dashed lines. Continuous lines were fitted with RANSAC algorithm (Fischler & Bolles, 1981) between moment magnitude and logarithmic corner frequency.

from the respective regions were determined. The depth-dependent attenuation model and site amplification of the stations of van Laaten and Wegler (2024) were utilized to determine the source spectra of the earthquakes. Fig. 7.3 shows the stress drop for the southern (SLRZ) and northern part of the LRZ (NLRZ). In total, the source spectra of 27 earthquakes were determined for NLRZ and 17 source spectra for SLRZ. Due to the limited sample size and magnitude range, the stress drop can only be estimated.

The NLRZ region shows a constant stress drop with magnitudes in the narrow magnitude range analyzed, thus self-similarity can be assumed for the region. In contrast, the SLRZ region does not exhibit self-similarity. Stronger earthquakes tend to larger stress drop. Studies by Eulenfeld et al. (2021) and Michálek and Fischer (2013) have also quantified the stress drop for SLRZ. For an earthquake with a seismic moment of  $10^{13}$  Nm, a stress drop of approximately 1.8 MPa and 10 MPa

was determined in their respective studies. Here a stress drop of 8.8 MPa for SLRZ for the same seismic moment was found. Consequently, the value is situated between the two studies, although it is considerably closer to the findings of Michálek and Fischer (2013). In order to improve stress drop estimation, it is necessary to analyze a greater number of earthquakes and a wider range of magnitudes, which will be addressed in a future work.

## 8 | Conclusions

This thesis examines the crust and the presence of fluids along the Leipzig-Regensburg fault zone. Seismic velocity and seismic attenuation were determined using traveltimes tomography, receiver function analysis and the radiative transfer theory. By determining these two material properties, new insights were gained in the area of the Leipzig-Regensburg fault zone.

The presence of fluids in the northern area of the fault zone was partially confirmed. The question of why Werdau is the northernmost earthquake swarm region of the Leipzig-Regensburg fault zone can also be answered. Due to the extension of the partial melt in the asthenosphere below NW-Bohemia/Vogtland, there is no fluid source in the northern part of the fault zone system and thus earthquake swarms cannot be triggered. The triggering mechanisms of the Schöneck and Werdau earthquake swarm region are analogous to those of the NW-Bohemia/Vogtland earthquakes swarm. A combination of fluids, fault zones and presence of an intrusive body is likely responsible for the triggering of earthquake swarms. However, a narrow fluid path, as observed in the NW-Bohemia/Vogtland region, could not be imaged in the vicinity of Schöneck and Werdau.

Another noteworthy finding is a possible explanation for the earthquake depth distribution. Earthquakes are more likely to occur in areas with lower intrinsic attenuation, explaining the more shallow earthquakes in the southern part and deeper earthquakes in the northern part of the Leipzig-Regensburg fault zone. The results of the 1-D attenuation depth profile already provide new insights into crustal tectonic processes and represent a preliminary step towards a 3-D frequency-dependent scattering and intrinsic attenuation tomography. Spatial imaging of frequency-dependent seismic attenuation is essential to gain further insights.

Stress drop estimates were made for both the southern and northern parts of the Leipzig-Regensburg fault zone. Earthquakes in the northern part exhibit self-similarity, resulting in a constant stress drop regardless of magnitude. This does not apply to the earthquakes in the south. In NW-Bohemia/Vogtland region, stronger earthquakes tend to exhibit a larger stress drop than smaller earthquakes. In conclusion, the findings of this study have the potential to greatly enhance future research efforts concerning seismic hazards.



# References

- Abubakirov, I. & Gusev, A. (1990). Estimation of scattering properties of lithosphere of Kamchatka based on Monte-Carlo simulation of record envelope of a near earthquake. *Phys. Earth Planet. Inter.*, *64*, 52–67. doi: [https://doi.org/10.1016/0031-9201\(90\)90005-I](https://doi.org/10.1016/0031-9201(90)90005-I)
- Aizawa, Y., Barnhoorn, A., Faul, U., Gerald, J. & Jackson, I. (2008). Seismic Properties of Anita Bay Dunitite: an Exploratory Study of the Influence of Water. *J. Petrol.*, *49*, 841–855. doi: [10.1093/petrology/egn007](https://doi.org/10.1093/petrology/egn007)
- Aki, K. & Chouet, B. (1975). Origin of coda waves: Source, attenuation, and scattering effects. *J. Geophys. Res.*, *80*, 3322–3342. doi: [10.1029/JB080i023p03322](https://doi.org/10.1029/JB080i023p03322)
- Apresyan, L. & Kravtsov, Y. (1996). *Radiation Transfer*. London: CRC Press.
- Babuška, V. & Plomerová, J. (2010). Mantle lithosphere control of crustal tectonics and magmatism of the western Ohře (Eger) Rift. *J. Geosci.*, *55*, 171–186. doi: [doi.org/10.3190/jgeosci.070](https://doi.org/10.3190/jgeosci.070)
- Bankwitz, P. & Bankwitz, E. (1994). *Crustal Structure of the Erzgebirge*. doi: [10.13140/RG.2.1.3390.9607](https://doi.org/10.13140/RG.2.1.3390.9607)
- Bankwitz, P., Schneider, G., Kämpf, H. & Bankwitz, E. (2003). Structural characteristics of epicentral areas in Central Europe: study case Cheb basin (Czech Republic). *J. Geodyn.*, *35*, 5–32. doi: [10.1016/S0264-3707\(02\)00051-0](https://doi.org/10.1016/S0264-3707(02)00051-0)
- Behr, H., Conrad, W., Müller, A. & Trzebski, R. (2002). Compilation, Linsser filtering and interpretation of the gravity map of Germany and adjacent regions at a scale of 1:1,000,000. *Z. geol. Wiss.*, *30*, 385–402. doi: [10.1007/s10950-018-9746-9](https://doi.org/10.1007/s10950-018-9746-9)
- Bethmann, F., Deichmann, N. & Mai, P. (2011). Scaling Relations of Local Magnitude versus Moment Magnitude for Sequences of Similar Earthquakes in Switzerland. *Bull. seism. Soc. Am.*, *101*, 515–534. doi: [10.1785/0120100179](https://doi.org/10.1785/0120100179)
- Bleibinhaus, F., Stich, D., Simon, M. & Gebrande, H. (2003). New results from amplitude preserving prestack depth migration of the Münchberg/Vogtland segment of the MVE deep seismic survey. *J. Geodyn.*, *35*, 33–43. doi: [10.1016/S0264-3707\(02\)00052-2](https://doi.org/10.1016/S0264-3707(02)00052-2)
- Bostock, M., Hyndman, R., Rondenay, S. & Peacock, S. (2002). An inverted continental Moho and serpentinization of the forearc mantle. *Nature*, *417*, 536–538. doi: [10.1038/417536a](https://doi.org/10.1038/417536a)
- Bram, K. & Hirschmann, G. (Eds.). (1992). *KTB Report 92-3: Ergebnisse geowissenschaftlicher Umfelduntersuchungen* (Vol. 92-3). Stuttgart: Schweizerbart. (Editor: Projektleitung Kontinentales Tiefbohrprogramm der Bundesrepublik Deutschland, in German.) doi: [10.2312/ktb.92-3](https://doi.org/10.2312/ktb.92-3)
- Bräuer, K., Kämpf, H., Niedermann, S., Strauch, G. & Tesař, J. (2008). Natural laboratory NW Bohemia: Comprehensive fluid studies between 1992 and 2005 used to trace geodynamic processes. *Geochem. Geophys. Geosyst.*, *9*, Q04018. doi: [10.1029/2007GC001921](https://doi.org/10.1029/2007GC001921)
- Bräuer, K., Kämpf, H. & Strauch, G. (2009). Earthquake swarms in nonvolcanic regions: what fluids have to say. *Geophys. Res. Lett.*, *36*, L17309. doi: [10.1029/2009GL039615](https://doi.org/10.1029/2009GL039615)
- Brune, J. (1970). Tectonic stress and the spectra of seismic shear waves from earthquakes. *J. Geophys. Res.*, *75*, 4997–5009. doi: [10.1029/JB075i026p04997](https://doi.org/10.1029/JB075i026p04997)

- Chandrasekhar, S. (1960). *Radiative Transfer*. New York: Dover Publications.
- Chapman, S., Tisato, N., Quintal, B. & Holliger, K. (2015). Seismic attenuation in partially saturated Berea sandstone submitted to a range of confining pressures. *J. Geophys. Res.*, *121*, 1664–1676. doi: 10.1002/2015JB012575
- Conrad, W., Haupt, M. & Bölsche, J. (1994). Interpretation des tiefenseismischen Regionalprofils EV 01 - EV 02/1978 - Vogtland - Erzgebirge - Lausitz (Adorf - Bautzen) mit Hilfe der Gravimetrie und Magnetik. *Z. geol. Wiss.*, *22*, 603–615. (in German)
- Credner, H. (1876). Das vogtländisch-erzgebirgische Erdbeben vom 23. November 1875. *Z. geol. Wiss.*, *48*, 246–269. (in German)
- Dahm, T., Heimann, S., Funke, S., Wendt, S., Rappsilber, I., Bindi, D., ... Cotton, F. (2018). Seismicity in the block mountains between Halle and Leipzig, Central Germany: centroid moment tensors, ground motion simulation, and felt intensities of two  $M \approx 3$  earthquakes in 2015 and 2017. *J. Seismol.*, *22*, 985–1003. doi: 10.1007/s10950-018-9746-9
- Deichmann, N. (2006). Local Magnitude, a Moment Revisited. *Bull. seism. Soc. Am.*, *96*, 1267–1277. doi: 10.1785/0120050115
- DEKORP Research Group. (1994). The deep reflection seismic profiles DEKORP 3/MVE-90. *Z. geol. Wiss.*, *22*, 627–828.
- Eberhart-Phillips, D. (1986). Three-dimensional velocity structure in the northern California Coast Ranges from inversion of local earthquake arrival times. *Bull. Seismol. Soc. Am.*, *76*, 1025–1052. doi: 10.1785/BSSA0760041025
- Eberhart-Phillips, D. (1993). Local earthquake tomography: Earthquake source regions. In *Seismic tomography: Theory and practice* (pp. 613–643). New York: Chapman and Hall. Retrieved from <https://pubs.usgs.gov/publication/70186523>
- Ehlers, J., Gibbard, P. & Hughes, P. (2011). Chapter 13 - pleistocene glaciations of north germany—new results. In *Quaternary glaciations - extent and chronology* (Vol. 15, pp. 149–162). Elsevier. doi: 10.1016/B978-0-444-53447-7.00013-1
- Eissmann, L. (1987). Lagerungsstörungen im Lockergebirge. Exogene und endogene Tektonik im Lockergebirge des nördlichen Mitteleuropas. *Geophysikalische Veröffentlichungen der KMU Leipzig*, *3*, 7–77.
- Eissmann, L. (1996). *Das Quartär Deutschlands*. Stuttgart, Germany: Schweizerbart Science Publishers. (in German)
- Eissmann, L. (2002). Quaternary geology of eastern Germany (Saxony, Saxon-Anhalt, South Brandenburg, Thuringia), type area of the Elsterian and Saalian Stages in Europe. *Quaternary Science Reviews*, *21*, 1275–1346. doi: 10.1016/S0277-3791(01)00075-0
- Ellenberg, J. (1992). Recent fault tectonics and their relations to the seismicity of East Germany. *Tectonophysics*, *202*, 117–121. doi: 10.1016/0040-1951(92)90089-O
- Enderle, U. (1998). *Signaturen in refraktionsseismischen Daten als Abbild geodynamischer Prozesse* (PhD thesis). Karlsruhe, Germany. (in German)
- Enderle, U., Schuster, K., Prodehl, C., Schulze, A. & Bribach, J. (1998). The refraction seismic experiment GRANU95 in the Saxothuringian belt, southeastern Germany. *Geophys. J. Int.*, *133*, 245–259. doi: 10.1046/j.1365-246X.1998.00462.x

- Eulenfeld, T., Dahm, T., Heimann, S. & Wegler, U. (2021). Fast and Robust Earthquake Source Spectra and Moment Magnitudes from Envelope Inversion. *Bull. seism. Soc. Am.*, *112*, 878–893. doi: 10.1785/0120210200
- Fehler, M., Hoshiya, M., Sato, H. & Obara, K. (1992). Separation of scattering and intrinsic attenuation for the Kanto-Tokai region, Japan, using measurements of S-wave energy versus hypocentral distance. *Geophys. J. Int.*, *108*, 787–800. doi: 10.1111/j.1365-246X.1992.tb03470.x
- Fischer, T., Horálek, J., Hrubcová, P., Vavryčuk, V., Bräuer, K. & Kämpf, H. (2014). Intra-continental earthquake swarms in West-Bohemia and Vogtland: a review. *Tectonophysics*, *611*, 1–27. doi: 10.1016/j.tecto.2013.11.001
- Fischler, M. & Bolles, R. (1981). Random sample consensus: a paradigm for model fitting with applications to image analysis and automated cartography. *Commun. ACM*, *24*, 381–395. doi: 10.1145/358669.358692
- Franke, W. (2000). The mid-european segment of the variscides: tectonostratigraphic units, terrane boundaries and plate tectonic evolution. *Geological Society, London, Special Publications*, *179*, 35–61. doi: 10.1144/GSL.SP.2000.179.01.05
- Geissler, W., Kämpf, H., Kind, R., Bräuer, K., Klinge, K., Plenefisch, T., ... Nehybka, V. (2005). Seismic structure and locations of a CO<sub>2</sub> source in the upper mantle of the western Eger (Ohře) Rift, central Europe. *Tectonophysics*, *24*, 1–23. doi: 10.1029/2004TC001672
- Geissler, W., Sodoudi, F. & Kind, R. (2010). Thickness of the central and eastern European lithosphere as seen by S receiver functions. *Geophys. J. Int.*, *181*, 604–634. doi: 10.1111/j.1365-246X.2010.04548.x
- Grünthal, G. (1989). About the history of seismic activity in the focal region Vogtland/Western Bohemia. In P. Bormann (Ed.), *Monitoring and analysis of the earthquake swarm 1985/86 in the region Vogtland/Western Bohemia* (pp. 30–34). Zentralinstitut für Physik der Erde.
- Grünthal, G., Bankwitz, P., Bankwitz, E., Bednarek, J., Guterch, B., Schenk, V., ... Zeman, A. (1985). Seismicity and geological features of the eastern part of the West European Platform. *Gerlands Beiträge zur Geophysik*, *94*, 276–289.
- Grünthal, G., Bosse, C. & Stromeyer, D. (2009). *Die neue Generation der probabilistischen seismischen Gefährdungseinschätzung der Bundesrepublik Deutschland : Version 2007 mit Anwendung für die Erdbeben-Lastfälle der DIN 19700:2004-07 Stauanlagen* (Vol. 09/07; Scientific Technical Report STR). Potsdam: Deutsches GeoForschungsZentrum. (in German) doi: 10.2312/GFZ.b103-09076
- Grünthal, G., Mayer-Rosa, D. & Lenhardt, W. (1998). Abschätzung der Erdbebengefährdung für die D-A-CH-Staaten - Deutschland, Österreich, Schweiz. *Bautechnik.*, *10*, 19–33. (in German)
- Grünthal, G., Stromeyer, D., Bosse, C., Cotton, F. & Bindi, D. (2018). The probabilistic seismic hazard assessment of Germany-version 2016, considering the range of epistemic uncertainties and aleatory variability. *Bull. Earthq. Eng.*, *16*, 4339–4395. doi: 10.1007/s10518-018-0315-y
- Gusev, A. & Abubakirov, I. (1996). Simulated envelopes of non-isotropically scattered body waves as compared to observed ones: another manifestation of fractal heterogeneity. *Geophys. J. Int.*, *127*, 49–60. doi: 10.1111/

j.1365-246X.1996.tb01534.x

- Haslinger, F. (1998). *Velocity structure, seismicity and seismotectonics of North-western Greece between the Gulf of Arta and Zakynthos* (PhD thesis). Zürich, Switzerland.
- Heinicke, J., Woith, H., Alexandrakis, C., Buske, S. & Telesca, L. (2017). Can hydroseismicity explain recurring earthquake swarms in NW-Bohemia? *Geophys. J. Int.*, *212*, 211–228. doi: 10.1093/gji/ggx412
- Hemmann, A., Meier, T., Jentzsch, G. & Ziegert, A. (2003). Similarity of waveforms and relative relocalisation of the earthquake swarm 1997/1998 near Werdau. *J. Geodyn.*, *35*, 191–208. doi: 10.1016/S0264-3707(02)00062-5
- Heuer, B., Geissler, W., Kind, R. & Kämpf, H. (2006). Seismic evidence for asthenospheric updoming beneath the western Bohemian Massif, central Europe. *Geophys. Res. Lett.*, *33*, L05311. doi: 10.1029/2005GL025158
- Hofmann, Y. (2003). *Gravimetrische und geodynamische Modellierungen in der Schwarmbeben-Region Vogtland/NW-Böhmen* (PhD thesis). Jena, Germany. (in German)
- Hofmann, Y., Jahr, T. & Jentzsch, G. (2003). Three-dimensional gravimetric modelling to detect the deep structure of the region Vogtland/NW-Bohemia. *J. Geodyn.*, *35*, 209–220. doi: 10.1016/S0264-3707(02)00063-7
- Hoshiaba, M. (1991). Simulation of multiple-scattered coda wave excitation based on the energy conservation law. *Phys. Earth planet. Inter.*, *67*, 123–136. doi: 10.1016/0031-9201(91)90066-Q
- Hounsfeld, G. (1973). Computerized transverse axial scanning (tomography): Part 1. Description of system. *Br. J. Radiol.*, *46*, 1016–1022. doi: 10.1259/0007-1285-46-552-1016
- Hrubcová, P., Geissler, W., Bräuer, K., Vavryčuk, V., Tomek, C. & Kämpf, H. (2017). Active Magmatic Underplating in Western Eger Rift, Central Europe. *Tectonics*, *36*, 2846–2862. doi: 10.1002/2017TC004710
- Hrubcová, P., Šroda, P., Špičák, A., Guterch, A., Grad, M., Keller, G., ... Thybo, H. (2005). Crustal and uppermost mantle structure of the Bohemian Massif based on CELEBRATION 2000 data. *J. Geophys. Res.*, *110*, B11305. doi: 10.1029/2004JB003080
- Hubbert, M. & Rubey, W. (1959). ROLE OF FLUID PRESSURE IN MECHANICS OF OVERTHRUST FAULTING: I. MECHANICS OF FLUID-FILLED POROUS SOLIDS AND ITS APPLICATION TO OVERTHRUST FAULTING. *GSA Bulletin*, *70*, 115–166. doi: 10.1130/0016-7606(1959)70[115:ROFPIM]2.0.CO;2
- Iyer, H. & Hirahara, K. (1993). *Seismic tomography : theory and practice*. London, England: Chapman and Hall.
- Jackson, I., Gerald, J., Faul, U. & Tan, B. (2002). Grain-size-sensitive seismic wave attenuation in polycrystalline olivine. *J. Geophys. Res.*, *107*, 2360. doi: 10.1029/2001JB001225
- Kämpf, H., Franzke, H., Neunhöfer, H., Märtens, P., Röllig, G. & Schauer, M. (1991). *Zur strukturellen Bedeutung der Nord-Süd-Bruchstörungszone Plauen/Klingenthal - Altenberg/Gera - Leipzig/Halle - Dessau/Bernburg*. (in: Geologisch-tektonischer Bau der Gera-Jachymov (Joachimsthal)-Störungszone und die daran gebundenen Uranlagerstätten - Kurzfassungen der Vorträge und

- Poster, 12-13, in German)
- Kennett, B. & Engdahl, E. (1991). Traveltimes for global earthquake location and phase identification. *Geophys. J. Int.*, *105*, 429–465. doi: 10.1111/j.1365-246X.1991.tb06724.x
- Kind, R., Yuan, X., Saul, J., Nelson, D., Sobolev, S., Mechie, J., ... Jiang, M. (2002). Seismic images of crust and upper mantle beneath Tibet: Evidence for Eurasian plate subduction. *Science*, *298*, 1219–1221. doi: 10.1126/science.1078115
- Kissling, E. (1988). Geotomography with local earthquake data. *Rev. Geophys.*, *26*, 659–698. doi: <https://doi.org/10.1029/RG026i004p00659>
- Kley, J. & Voigt, T. (2008). Late Cretaceous intraplate thrusting in central Europe: Effect of Africa-Iberia-Europe convergence, not Alpine collision. *Geology*, *36*, 839–842. doi: 10.1130/G24930A.1
- Korn, M., Funke, S. & Wendt, S. (2008). Seismicity and seismotectonics of West Saxony, Germany - new insights from recent seismicity observed with the Saxonian seismic network. *Stud. Geophys. Geod.*, *52*, 479–492. doi: 10.1007/s11200-008-0033-z
- Kossmat, F. (1927). *Gliederung des varistischen Gebirgsbaues*. G. A. Kaufmann's Buchhandlung.
- Krull, P. (1984). Kosmotektonisches Schema des Territoriums der Deutschen Demokratischen Republik. *Z. Angew. Geol.*, *30*, 190–194. (in German)
- Kumar, P., Kind, R. & Yuan, X. (2010). Receiver function summation without deconvolution. *Geophys. J. Int.*, *180*, 1223–1230. doi: 10.1111/j.1365-246X.2009.04469.x
- Leydecker, G. (2011). *Erdbebenkatalog für Deutschland mit Randgebieten für die Jahre 800 bis 2008*. Stuttgart, Germany: Schweizerbart Science Publishers. (in German)
- LfULG - Sächsisches Landesamt für Umwelt, Landwirtschaft und Geologie. (2018). *Digitales geologisches und seismologisches Kartenmaterial des Freistaates Sachsen*. (<https://www.lfulg.sachsen.de/karten-und-daten-13433.html>)
- Linnemann, U. & Romer, R. (2010). *Pre-mesozoic geology of saxo-thuringia*. Stuttgart, Germany: Schweizerbart Science Publishers.
- Madariaga, R. (1976). Dynamics of an expanding circular fault. *Bull. seism. Soc. Am.*, *66*, 639–666. doi: 10.1785/BSSA0660030639
- McCann, T. (2008). *The Geology of Central Europe, Volume 1 - Precambrian and Palaeozoic*. London: The Geological Society.
- McKerrow, W., Mac Niocaill, C. & Dewey, J. (2000). The Caledonian Orogeny redefined. *J. Geol. Soc.*, *157*, 1149–1154. doi: 10.1144/jgs.157.6.1149
- Meschede, M. (2018). *Geologie Deutschlands*. Heidelberg, Germany: Springer Spektrum Berlin. (in German)
- Michálek, H. & Fischer, T. (2013). Source parameters of the swarm earthquakes in West Bohemia/Vogtland. *Geophys. J. Int.*, *195*, 1196–1210. doi: 10.1093/gji/ggt286
- Mousavi, S., Bauer, K., Korn, M. & Hejrani, B. (2015). Seismic tomography reveals a mid-crustal intrusive body, fluid pathways and their relation to the earthquake swarms in West Bohemia/Vogtland. *Geophys. J. Int.*, *203*, 1113–1127. doi: 10.1093/gji/ggv338

- Müller, K. (2022). *Palaeoseismological analyses of northern and central Germany*. (PhD thesis, Hannover, Germany). doi: 10.15488/11972
- Murphy, J., Strachan, R. & Quesada, C. (2021). Pannotia to Pangaea: Neoproterozoic and Paleozoic Orogenic Cycles in the Circum-Atlantic Region: A celebration of the career of Damian Nance. *Geological Society, London, Special Publications*, 503, 1–11. doi: 10.1144/SP503-2020-213
- Nance, R., Evans, D. & Murphy, J. (2022). Pannotia: To be or not to be? *Earth-Science Reviews*, 232, 104128. doi: 10.1016/j.earscirev.2022.104128
- Nickschick, T., Kämpf, H. & Jahr, T. (2014). The “Triasscholle” near Greiz, Germany—a volcanic origin? *Bull. Volcanol.*, 76, 806. doi: 10.1007/s00445-014-0806-x
- Nolet, G. (1987). Seismic wave propagation and seismic tomography. In *Seismic Tomography: With Applications in Global Seismology and Exploration Geophysics* (pp. 1–23). Dordrecht: Springer Netherlands. doi: 10.1007/978-94-009-3899-1\_1
- Paaschens, J. (1997). Solution of the time-dependent Boltzmann equation. *Phys. Ref. E.*, 56, 1135–1141. doi: 10.1103/PhysRevE.56.1135
- Pälchen, W. (2009). *Geologie von Sachsen II*. Stuttgart, Germany: Schweizerbart Science Publishers.
- Pälchen, W. & Walter, H. (2008). *Geologie von Sachsen*. Stuttgart, Germany: Schweizerbart Science Publishers.
- Plomerová, J., Achauer, U., Babuška, V., Vecsey, L. & working group, B. (2007). Upper mantle beneath the Eger Rift (Central Europe): plume or asthenosphere upwelling? *Geophys. J. Int.*, 169, 675–682. doi: 10.1111/j.1365-246X.2007.03361.x
- Pohl, D., Wetzel, H.-U. & Grünthal, G. (2006). Tektonische Untersuchung im Raum Vogtland-Leipzig mit Hilfe von Fernerkundung. In E. Seyfert (Ed.), *Geoinformatik und Erdbeobachtung : Vorträge ; 26. Wissenschaftlich-Technische Jahrestagung der DGPF, 11. - 13.09.2006 in Berlin* (pp. 277–286). Deutschen Gesellschaft für Photogrammetrie, Fernerkundung und Geoinformation (DGPF) e.V.
- Rappsilber, I. (2003). *Struktur und Entwicklung des nördlichen Saale-Beckens (Sachsen-Anhalt): Geophysik und Geologie* (PhD thesis, Halle, Germany). (in German) doi: 10.25673/3234
- Rietbrock, A. (2001). P wave attenuation structure in the fault area of the 1995 Kobe earthquake. *J. Geophys. Res.*, 106, 4141–4154. doi: 10.1029/2000JB900234
- Ritter, J., Jordan, M., Christensen, U. & Achauer, U. (2001). A mantle plume below the eifel volcanic fields, germany. *Earth Planet. Sci. Lett.*, 186, 7–14. doi: 10.1016/S0012-821X(01)00226-6
- Sato, H. (1989). Broadening of seismogram envelopes in the randomly inhomogeneous lithosphere based on the parabolic approximation: southeastern Honshu, Japan. *J. Geophys. Res.*, 94, 17735–17747. doi: 10.1029/JB094iB12p17735
- Sato, H., Fehler, M. & Maeda, T. (2012). *Seismic wave propagation and scattering in the heterogeneous Earth*. Berlin: Springer.
- Schimschal, S. (2013). *Abbildung der Krustenstruktur im Bereich Münchberg/Vogtland/Erzgebirge durch Reprozessierung des tiefenseismischen MVE90-Profiles* (Master’s thesis). TU Bergakademie Freiberg, Germany. (in

- German)
- Schneider, M., Cotton, F. & Schweizer, P.-J. (2023). Criteria-based visualization design for hazard maps. *Nat. Hazard Earth Sys.*, *23*, 2505–2521. doi: 10.5194/nhess-23-2505-2023
- Schuster, A. (1905). Radiation Through a Foggy Atmosphere. *Astrophys. J.*, *21*, 1–22. doi: 10.1086/141186
- Seismoverbund Mitteldeutschland. (2024). *Kartendienst Antares - Seismologie in Mitteldeutschland*. (<https://tlubn.thueringen.de/kartendienst>)
- Smith, W. (1981). The b-value as an earthquake precursor. *Nature*, *289*, 136–139. doi: 10.1038/289136a0
- Sonnabend, L. (2022). *Neotektonik und Seismizität in Westsachsen und Nordwestböhmen* (PhD dissertation). Leipzig, Germany. (in German)
- Spakman, W., Wortel, M. & Vlaar, N. (1988). The Hellenic Subduction Zone: A tomographic image and its geodynamic implications. *Geophys. Res. Lett.*, *15*, 60–63. doi: 10.1029/GL015i001p00060
- Špičák, A. & Horálek, J. (2001). Possible role of fluids in the process of earthquake swarm generation in the West Bohemia/Vogtland seismoactive region. *Tectonophysics*, *336*, 151–161. doi: 10.1016/S0040-1951(01)00099-3
- Stewart, R. (1991). *Exploration Seismic Tomography: Fundamentals*. Tulsa, Oklahoma: Society of Exploration Geophysicists. (Vol. 3, pp. 189)
- Švancara, J., Havíř, J. & Conrad, W. (2008). Derived gravity field of the seismogenic upper crust of se germany and west bohemia and its comparison with seismicity. *Stud. Geophys. Geod.*, *52*, 567–588. doi: 10.1007/s11200-008-0038-7
- Thurber, C. (1983). Earthquake locations and three-dimensional crustal structure in the Coyote Lake area, central California. *J. Geophys. Res.*, *88*, 8226–8236. doi: 10.1029/JB088iB10p08226
- Thurber, C. (1993). *Local earthquake tomography: velocities and Vp/Vs - theory*. New York: Chapman and Hall.
- Tomek, Č., Dvorakova, V. & Vrána, S. (1997). Geological interpretation of the 9HR and 503M seismic profiles in western Bohemia. *Jour. Geol. Sci.*, *47*, 43–50.
- Um, J. & Thurber, C. (1987). A fast algorithm for two-point seismic ray tracing. *Bull. Seismol. Soc. Am.*, *77*, 972–986. doi: 10.1785/BSSA0770030972
- van Laaten, M., Eulendorf, T. & Wegler, U. (2022). Comparison of Multiple Lapse Time Window Analysis and Qopen to determine intrinsic and scattering attenuation. *Geophys. J. Int.*, *228*, 913–926. doi: 10.1093/gji/ggab390
- van Laaten, M. & Wegler, U. (2024). *Non-linear inversion for a multi-layer seismic S-wave attenuation model using radiative transfer theory*. (submitted to *J. Geophys. Res.*)
- van Laaten, M., Wegler, U. & Eulendorf, T. (2023). On the trail of fluids in the northernmost intracontinental earthquake swarm areas of the Leipzig-Regensburg fault zone, Germany. *J. Seismol.*, *27*, 573–597. doi: 10.1007/s10950-023-10146-8
- Vlček, J., Beránek, R., Fischer, T. & Vilhelm, J. (2022). Earthquake swarms in west bohemia are most likely not rain triggered. *J. Geodyn.*, *150*, 101908. doi: doi.org/10.1016/j.jog.2022.101908
- von Seebach, K. (1873). *Das Mitteldeutsche Erdbeben vom 6. März 1872*. Leipzig, Germany: Verlag von H. Haessel. (in German)

- Vrána, S. & Štědrá, V. (1998). Crustal structure of the western part of the Bohemian Massif, Czech Republic - A summary of the project Geological model of western Bohemia, related to the deep borehole KTB in Germany. *Episodes*, *21*, 241–247. doi: 10.18814/epiiugs/1998/v21i4/005
- Weinlich, F., Bräuer, K., Kämpf, H., Strauch, G., Tesař, J. & Weise, S. (1999). An active subcontinental mantle volatile system in the western Eger rift, Central Europe: Gas flux, isotopic (He, C, and N) and compositional fingerprints. *Geochim. Cosmochim. Acta*, *63*, 3653–3671. doi: 10.1016/S0016-7037(99)00187-8
- Weise, S., Bräuer, K., Kämpf, H., Strauch, G. & Koch, U. (2001). Transport of mantle volatiles through the crust traced by seismically released fluids: a natural experiment in the earthquake swarm area Vogtland/NW Bohemia, Central Europe. *Tectonophysics*, *336*, 137–150. doi: 10.1016/S0040-1951(01)00098-1
- Wolfgang, F., Cocks, L. & Torsvik, T. (2017). The Palaeozoic Variscan oceans revisited. *Gondwana Res.*, *48*, 257–284. doi: 10.1016/j.gr.2017.03.005
- Wu, R. (1985). Multiple scattering and energy transfer of seismic waves — separation of scattering effect from intrinsic attenuation — I. Theoretical modelling. *Geophys. J. Int.*, *82*, 57–80. doi: 10.1111/j.1365-246X.1985.tb05128.x
- Zeng, Y., Su, F. & Aki, K. (1991). Scattering wave energy propagation in a random isotropic scattering medium: 1. Theory. *J. Geophys. Res.*, *96*, 607–619. doi: 10.1029/90JB02012
- Zhang, J. & Toksöz, M. (1998). Nonlinear refraction travelttime tomography. *Geophysics*, *63*, 1726–1737. doi: 10.1190/1.1444468

# Acknowledgments

This thesis would not have been possible without a large number of people and I would like to thank everyone who supported me.

First of all, there is my supervisor Prof. Dr. Ulrich Wegler. Thank you very much for giving me the opportunity to write this doctoral thesis. It has been a long journey during which I have learned an incredible amount from you. You have always been patient and given me the time and space to develop and pursue my own ideas. I am incredibly grateful for your many suggestions and critical discussions. Without your support this thesis would not have been possible.

Many thanks also go to Prof. Dr. Michael Korn for his patience and for his second review of this work.

Special thanks to Dr. Tom Eulendorf. Thank you for always having an open ear and being supportive. Discussions with you have been incredibly helpful and it has been a pleasure to work with you.

I would also like to thank my (former) colleagues in geophysics for their time and support: Dr. Thomas Burghardt, Jozef Müller, Roman Esefelder, Dr. Andreas Goepel, Dr. Thomas Jahr, Valentin Kasburg, Dr. Cornelius Schwarze and Anne Schulz.

Furthermore, many thanks to Andreas Hoffmann, Christine Luge, Christina Mohr, Dirk Schönwald, Janet Kreßler, Matthias Meininger, Volker Schwarz and Frank Buchwald for their administrative, technical and craftsmanship support of all kinds.

The last few lines are dedicated to my friends and family. Thank you for always having my back and being there for me! I would especially like to thank my wife Neele, who has been with me through all the ups and downs, and my daughter Finja, who has helped me to enjoy life alongside my work. Many, many thanks!



# Curriculum Vitae